


# GAS ADSORPTION AND SELECTIVITY STUDIES FOR POROUS METAL-ORGANIC FRAMEWORKS

Shan Gao, MSc

Thesis submitted to The University of Nottingham

for the degree of Doctor of Philosophy

August 2016

# Declaration

Except where specific reference is made to other sources, the work presented in this thesis is the original work of the author. It has not been submitted, in whole or in part, for any other degree. Some of the results have already been published.

Signed: Shan Gao

Date:

## Acknowledgements

Firstly, I would like to express my sincere gratitude to my supervisor, Professor Martin Schröder, for the opportunity of working in his group and for his continuous support in my PhD. I am also grateful to Dr Sihai Yang for his guidance, patience and motivation with my project.

Secondly, I would like to sincerely thank Dr Yong Yan for his kind help with the lab work and patient discussions with my research. I would also like to thank Dr Timothy Easun, for his immense knowledge of chemistry and supervision during the first two years of my PhD. In particular, I appreciate the friendship and kindness of my colleagues: Dr Mathew Savage, Dr Cristina Perez Krap, Dr Florian Moreau, Dr Stephen Argent, Dr Tamoghna Mitra, Dr Magdalene Chong, Dr William Trenholme, Dr Martyn Brown, Dr Simona Pili, Dr Zhenzhong Lu, Dr Lei Li, Christopher Morris, Xinran Zhang, Jennifer Eyley, Adam Nevin, Harry Godfrey, Christopher Marsh, Lydia Briggs, Gemma Smith, Nicholas Jacques, Thien Duong, Peter Rought, Jack Humby and all other colleagues. I would also like to thank my project students, Andrew Valentine and Rosie Magnall for their help with the lab work.

Thirdly, I would like thank Professor Sandy Blake and Dr William Lewis for their help with crystallography; Professor Mark Thomas for the discussions with gas sorption; Chiu Tang and Claire Murray for the Diamond experiments; Catherine Dejoie, Carlotta Giacobbe and Andrew Fitch for the ESRF experiments; Mark Guyler for the technical help.

Fourthly, I would also like to sincerely thank China Scholarship Council for the CSC Research Excellence Scholarship and EPSRC for the experimental funding.

In the end, I would like to thank my family and friends for their support and concerns.

# Abstract

This thesis describes research on the preparation and characterisation of porous metal-organic framework (MOF) materials for gas storage and separation applications, with particular focus on light hydrocarbons. This work is of great importance in the structural flexibility studies of MOF materials upon the physisorption of gas molecules. It also involves comprehensive gas sorption and separation studies of a Zr-based MOF, MFM-601, with a pioneering investigation for $NH_3$ uptakes for this species of MOFs.

Chapter 1 outlines the background and reasons for designing the targeted MOFs in this work. It reviews a series of porous materials on their general syntheses, structures, properties and potential applications. Among these porous materials, MOFs are highlighted, with reviews mainly focusing on design of flexible MOFs and isostructural MOFs due to their important applications. In addition, this chapter summarises the importance and interests of porous materials for light hydrocarbon sorption and separation, toxic gas storage and carbon capture.

Chapter 2 describes and discusses a comprehensive study of a flexible MOF, MFM-202a, in the applications of light hydrocarbon ($CH_4$, $C_2H_2$, $C_2H_4$, $C_2H_6$, $C_3H_6$ and $C_3H_8$) sorption and separation. MFM-202a is known to be a flexible crystalline material that shows dramatic structural flexibility upon adsorption of $CO_2$ and $SO_2$ gases, which is indicated by the stepwise adsorption and hysteretic desorption. Interestingly, the light hydrocarbon sorption of this flexible MOF also exhibits stepwise adsorption and hysteretic desorption isotherms for $C_2H_2$, $C_2H_4$ and $C_3H_6$ at ~195 K. However, for the saturated hydrocarbons, such as $CH_4$, $C_2H_6$ and $C_3H_8$, no correlated hysteresis is observed. To gain insights into the structural change for the $C_2$ hydrocarbons, *in situ* synchrotron power diffraction (*in situ* PXRD) experiments have been carried out. The results suggest that MFM-202a again exhibits structural flexibility upon the sorption of $C_2$ hydrocarbons. Le Bail refinements have been performed to give the specific unit cell parameters upon sorption of the three $C_2$ hydrocarbons. In addition, MFM-202a shows very high uptakes of $C_2H_2$ (18.3 mmol $g^{-1}$) and $C_2H_4$ (14.8 mmol $g^{-1}$) and $C_3$s (11.9 mmol $g^{-1}$) at 195 K, compared with other MOFs.

The isotherms of these light hydrocarbons at 273−303 K have also been carried out and show remarkable differences in sorption capacities, suggesting potential hydrocarbon separation applications. In this chapter, two methods have been adopted in the calculations of selectivities, dual-site Langmuir Freundlich-Ideal adsorbed solution theory (DSLF-IAST) and numerical integration-IAST (NI-IAST). MFM-202a exhibits excellent selectivities for $C_2$s/$CH_4$ (~7−12), $C_3$s/$CH_4$ (~63−105) and an inverse selectivity for $C_2H_4/C_2H_6$ (~0.7).

Chapter 3 describes the uptake of $NH_3$ for MFM-202a at 293 K over multiple cycles. In the first cycle, MFM-202a exhibits a high uptake capacity of 8.5 mmol $g^{-1}$. However, in the second cycle, the uptake shows a dramatic decrease. As $NH_3$ is a polar molecule, it may interact strongly with the framework and lead to a possible structural change. To investigate the structural response upon $NH_3$ adsorption of MFM-202a, *in situ* PXRD and *in situ* X-ray pair distribution function (PDF) experiments have been carried out for MFM-202a during the adsorption and desorption of $NH_3$. Interestingly, the time-dependent *in situ* PXRD patterns of the $NH_3$-loaded MFM-202a shows a gradual loss of peaks, indicating the loss of crystallinity upon interaction with $NH_3$. However, after a very short time period, new diffraction peaks appear which differ from the peaks of the activated material. This suggests that the framework undergoes a fast rearrangement of the structure after the collapse of the original structure upon adsorption of $NH_3$. Upon desorption, the *in situ* PXRD patterns of the new phase is retained, indicating an irreversible phase transition upon the uptake of $NH_3$.

Chapter 4 presents the synthesis and characterisation of four novel Zr- and Hf-based MOFs. The two Hf-based MOFs have been synthesised using the strategy of isostructural MOF design. $Zr_6(L^1)_2(\mu_3\text{-}O)_4(\mu_3\text{-}OH)_4(OH)_4(H_2O)_4$ and its isostructural $Hf_6(L^1)_2(\mu_3\text{-}O)_4(\mu_3\text{-}OH)_4(OH)_4(H_2O)_4$ are synthesised from the linker of biphenyl-3,3',5,5'-tetra-(phenyl-4-carboxylic acid) ($H_4L^1$) and both crystallise in space group *Fmmm*. In comparison, the $Zr_6(L^2)_2(\mu_3\text{-}O)_4(\mu_3\text{-}OH)_4(OH)_4(H_2O)_4$ (denoted MFM-601) is synthesised from the amine-functionalised linker of 4,4'-diamino-3,3',5,5'-tetra(4-carboxyphenyl)biphenyl ($H_4L^2$) and crystallises in *Cmmm* space group. The difference in structure owes to the different conformation of the two linkers. $H_4L^1$ adopts a twisted conformation for the two internal phenyl rings whereas $H_4L^2$ adopts a flat style. With similar porosity to MFM-202a, MFM-601 has also

been investigated for a series of gas storage and separation applications. Light hydrocarbon adsorption measurements carried out at low temperature show dramatic stepwise adsorption, which could be due to the mesopore effect. Remarkably, MFM-601 shows even higher uptakes of $C_2H_2$, $C_2H_4$, $C_2H_6$, $C_3H_6$ and $C_3H_8$ than MFM-202a at ~195 K. Furthermore, the hydrocarbon uptakes at 293 K also exhibit significant difference in the capacities. DSLF-IAST has been adopted to calculate the selectivities. It shows high selectivity for $C_2$s/$CH_4$ and $C_3$s/$CH_4$. In addition to the light hydrocarbon sorption, $CO_2$ adsorption for MFM-601 has also been carried out, which shows very high $CO_2$ storage (31.3 mmol $g^{-1}$) at ~198 K, with stepwise adsorption and hysteretic desorption. This has been further studied by *in situ* PXRD experiments to observe structural changes during the adsorption of $CO_2$. The $CO_2$-loaded PXRD patterns show significant peak shifts compared with the bare material, confirming the structural change upon the adsorption of $CO_2$. In addition, as a pioneering study of $NH_3$ sorption on a Zr-based MOF, MFM-601 exhibits reasonable repeatability in multiple cycles.

Chapter 5 summarises the experimental results and conclusions of the thesis and gives the perspectives for future investigations of the work.

# Abbreviations

| | |
|---|---|
| Å | Angstroms (1 Å = $10^{-10}$ m) |
| δ | Chemical shift |
| Δ | Shift, Change |
| λ | Wavelength of X-ray |
| θ | Diffraction angles of X-ray |
| ΔS | Entropy of adsorption |
| 1D | One dimension or one dimensional |
| 2D | Two dimension or two dimensional |
| 3D | Three dimension or three dimensional |
| atm | Atmospheres |
| bar | Unit of pressure, 1 bar = $10^5$ Pa |
| bdc | Benzenedicarbonxylate |
| BET | Brunauer-Emmett-Teller |
| BPDC | [1,1'-biphenyl]-4,4'-dicarboxylic acid |
| $C_2$s | $C_2H_2$, $C_2H_4$ and $C_2H_6$ |
| $C_3$s | $C_3H_6$ and $C_3H_8$ |
| ca. | Circa, approximately |
| CHN | Elemental analysis |
| CIF | Crystallographic Information File |
| cm | Centimetres |
| COF | Covalent-organic framework |
| conc. | Concentrated |
| ESRF | European Synchrotron Radiation Facility |
| DEF | Diethylformamide |
| DMF | Dimethylformamide |
| $Dobdc^{4-}$ | 2,5-dioxido-1,4-benzenedicarboxylate |
| DOE | US Department of Energy |
| DSLF | Dual-site Langmuir-Freaudlich |
| FWHM | Full width at half maximum |
| g | Gram |
| HPDC | 4,5,9,10-tetrahydropyrene-2,7-dicarboxylic acid |
| IAST | Ideal Adsorbed Solution Theory |
| IGA | Intelligent Gravimetric Analyser |
| IRMOF | Isoreticular MOF |

| | |
|---|---|
| IUPAC | International Union of Pure and Applied Chemistry |
| K | Kelvin |
| kg | Kilogram |
| kJ | Kilojoule |
| L | Ligand or Litre, according to the context |
| NI | Numerical Integration |
| m | Multiplet (NMR) or metre |
| M | Metal |
| $m^{-2}$ | Per square meter |
| $m^{-3}$ | Per cubic meter |
| mbar | Milli bar |
| M | Metal |
| MeOH | Methanol |
| EtOH | Ethanol |
| MHz | Mega Hertz |
| MIL | Material of the Lavoisier Institute |
| mins | Minutes |
| MOF | Metal-Organic Framework |
| mol | Moles |
| $mol^{-1}$ | Per mole |
| MPa | Mega pascal |
| MS | Mass Spectrometry |
| m/z | Mass to Charge Ratio |
| n | Normal |
| nm | Nanometres |
| NMR | Nuclear Magnetic Resonance |
| P | Pressure |
| PDC | pyrene-2,7-dicarboxylic acid |
| PDF | Pair distribution function |
| ppm | Part per Million |
| PXRD | Powder X-ray Diffraction |
| q | Quartet (NMR) |
| $Q_{st}$ | Heats of Adsorption |
| R | Universal constant, J $mol^{-1}$ $K^{-1}$ |
| R.T. | Room temperature, 298 K |
| s | Singlet (NMR) OR Seconds, according to context |

| | |
|---|---|
| t | Triplet |
| T | Temperature |
| TGA | Thermal Gravimetric Analysis |
| THF | Tetrahydrofuran |
| TPDC | [1,1':4',1"-terphenyl]-4,4"-dicarboxylic acid |
| UV | Ultraviolet |
| vis | Visible |
| wt% | Weight percentage |
| ZIF | Zeolitic imidazolate frameworks |

# List of contents

Declaration ..... i
Acknowledgements ..... ii
Abstract ..... iii
Abbreviations ..... vi
List of contents ..... ix
Chapter 1 Introduction ..... 1
1.1 MOF development ..... 1
1.1.1 Porous materials ..... 1
1.1.2 General synthetic route of MOFs ..... 4
1.2 MOF design ..... 5
1.2.1 Isoreticular design of MOFs ..... 5
1.2.2 Flexible MOFs ..... 8
1.3 Gas separation and storage of MOFs ..... 10
1.3.1 Hydrocarbon separation and sorption studies of MOFs ..... 10
1.3.2 Storage of other gases in MOFs ..... 13
1.4 Aims of the work ..... 13
References ..... 15
Chapter 2 Hydrocarbon sorption and selectivity studies for MFM-202a ..... 24
2.1 Introduction of MOFs in hydrocarbon sorption and separation ..... 24
2.2 Aims of this work ..... 29
2.3 Gas uptake and selectivity studies for MFM-202a ..... 30
2.3.1 Flexible MFM-202a ..... 30
2.3.2 Gas uptake and selectivity studies for MFM-202a at 273–303 K ..... 30
2.3.3 $Q_{st}$ and $\Delta S$ calculations and discussions ..... 36
2.3.4 Equimolar binary gas mixture uptakes and selectivity calculations ..... 38
2.3.5 Low temperature uptake of hydrocarbons ..... 48
2.3.6 *In situ* synchrotron powder X-ray diffraction analysis and discussions ..... 51
2.4 Experimental section ..... 55
2.4.1 Materials and techniques ..... 55
2.4.2 *In situ* PXRD experiments ..... 55
2.4.3 Calculation of the isosteric heats of adsorption and entropy ..... 56
2.4.4 Calculation of selectivity ..... 56
2.5 Conclusions ..... 62
References ..... 63

Chapter 3 *In situ* PXRD studies for $NH_3$-loaded MFM-202a ..... 66
3.1 Introduction ..... 66
3.1.1 $NH_3$ sorption ..... 66
3.1.2 *In situ* PXRD studies of gas induced structural flexibility and phase change for MFM-202a with hysteretic isotherms ..... 69
3.1.2.1 Hysteretic uptake of $CO_2$ and *in situ* PXRD investigation ..... 69
3.1.2.2 Hysteretic uptake of $SO_2$ and *in situ* PXRD investigation ..... 69
3.1.2.3 Hysteretic uptakes of unsaturated hydrocarbons and *in situ* PXRD investigations ..... 70
3.2 Aims of this work ..... 74
3.3 $NH_3$ sorption in MFM-202a ..... 74
3.4 *In situ* PXRD and PDF studies of $NH_3$-dosed MFM-202a ..... 75
3.4.1 *In situ* PXRD *vs in situ* PDF experiments ..... 75
3.4.2 *In situ* PXRD studies of $NH_3$-dosed MFM-202a ..... 75
3.4.3 *In situ* PDF studies of $NH_3$-dosed MFM-202a ..... 78
3.5 Experimental section ..... 82
3.5.1 Materials and techniques ..... 82
3.5.2 High resolution synchrotron X-ray powder diffraction ..... 82
3.5.3 High resolution synchrotron PDF experiment ..... 83
3.6 Conclusions ..... 84
References ..... 85
Chapter 4 Gas uptake and selectivity studies on Zr- and Hf-based MOFs ..... 87
4.1 Introduction ..... 87
4.1.1 Development of Zr(IV)- and Hf(IV)-based MOFs ..... 87
4.1.2 Introduction of a flexible ligand ..... 89
4.2 Aims of the work ..... 91
4.3 Studies of Zr- and Hf-based MOFs ..... 92
4.3.1 Crystallographic studies of Zr- and Hf-based MOFs ..... 92
4.3.1.1 Crystallographic study of $Zr_6(L^1)_2(\mu_3\text{-}O)_4(\mu_3\text{-}OH)_4(OH)_4(H_2O)_4$ and $Hf_6(L^1)_2(\mu_3\text{-}O)_4(\mu_3\text{-}OH)_4(OH)_4(H_2O)_4$ ..... 92
4.3.1.2 Crystallographic study of MFM-601 and $Hf_6(L^2)_2(\mu_3\text{-}O)_4(\mu_3\text{-}OH)_4(OH)_4(H_2O)_4$ ..... 95
4.3.1.3 Comparison of ligands conformation for $L^1$ and $L^2$ in $Zr_6(L^1)_2(\mu_3\text{-}O)_4(\mu_3\text{-}OH)_4(OH)_4(H_2O)_4$ and MFM-601, respectively ..... 97
4.3.2 PXRD and TGA results ..... 98
4.3.2.1 PXRD and TGA discussions for $Zr_6(L^1)_2(\mu_3\text{-}O)_4(\mu_3\text{-}OH)_4(OH)_4(H_2O)_4$ and $Hf_6(L^1)_2(\mu_3\text{-}O)_4(\mu_3\text{-}OH)_4(OH)_4(H_2O)_4$ ..... 98
4.3.2.2 PXRD and TGA results for MFM-601 and $Hf_6(L^2)_2(\mu_3\text{-}O)_4(\mu_3\text{-}OH)_4(OH)_4(H_2O)_4$ ..... 101
4.4 Gas sorption and separation investigations ..... 104

4.4.1 Activation for $Zr_6(L^1)_2(\mu_3\text{-}O)_4(\mu_3\text{-}OH)_4(OH)_4(H_2O)_4$/ $Hf_6(L^1)_2(\mu_3\text{-}O)_4(\mu_3\text{-}OH)_4(OH)_4(H_2O)_4$/ $Hf_6(L^2)_2(\mu_3\text{-}O)_4(\mu_3\text{-}OH)_4(OH)_4(H_2O)_4$ ..... 104
4.4.2 Gas sorption and separation investigations for MFM-601 ..... 104
4.4.2.1 $N_2$ sorption studies ..... 104
4.4.2.2 Hydrocarbon sorption and separation investigations ..... 105
4.4.2.2.1 Hydrocarbon sorption and separation investigations at 273–303 K ..... 105
4.4.2.2.2 Hydrocarbon sorption investigations at low temperature ..... 111
4.4.2.3 Other gas sorption and separation investigations ..... 113
4.4.2.3.1 $CO_2$ sorption ..... 113
4.4.2.3.2 *In situ* PXRD investigations of $CO_2$-loaded MFM-601 ..... 115
4.4.2.3.3 $NH_3$ sorption ..... 116
4.4.3 Selectivity between hydrocarbons ..... 117
4.4.4 Calculations of isosteric heats of adsorption and entropy ..... 127
4.5 Experimental section ..... 132
4.5.1 Materials and techniques ..... 132
4.5.2 Ligand preparation ..... 132
4.5.3 Syntheses of MOFs ..... 135
4.5.4 Single crystal X-ray structure ..... 137
4.5.5 Calculation of selectivities ..... 137
4.6 Conclusions ..... 139
References ..... 141
Chapter 5 Conclusions ..... 144
Appendices ..... 147
Publications ..... 148

# Chapter 1 Introduction

## 1.1 MOF development

### 1.1.1 Porous materials

A porous material is a solid material containing voids and pores which can be used as a medium to carry gases, liquids and solids. According to the radius of the pore defined by IUPAC, these materials can be categorised as macroporous (> 500 Å), mesoporous (20–500 Å) and microporous (< 20 Å). There are natural porous substances such as rocks, soil, zeolites, *etc.*, as well as synthetic porous materials, such as activated carbons (ACs), covalent-organic frameworks (COFs) and metal-organic frameworks (MOFs). Owing to their designability and versatility, significant development of such materials has occurred in the last two decades.

**Activated carbons**

Activated carbon (AC), also termed as activated charcoal, is a processed form of carbon with a BET surface area of 500–2000 $m^2$ $g^{-1}$.[1] ACs are the oldest adsorbents known.[1] There are several thousand kinds of activated carbons that can be classified by a variety of methods. For example, based on their shapes, the activated carbons are generally classified as powdered activated carbon, granular activated carbon, cylindrical activated carbon and spherical activated carbon. Activated carbons have been investigated for many applications, including gas storage and purification, metal extraction and sewage treatment.[2]. For example, two types of activated carbon, BAX 1100 and LAC 30–57, have been reported for the adsorption of propylene and propane. BAX 1100 exhibits propylene adsorption capacity of 4.9 mmol $g^{-1}$ and propane uptake of 4.4 mmol $g^{-1}$ at 303 K and 1 bar, whereas LAC activated carbon shows propylene uptake of 5.5 mmol $g^{-1}$ and propane uptake of 4.8 mmol $g^{-1}$ at 303 K and 1 bar.[3]

**Zeolites**

Zeolites, also known as molecular sieves, are microporous aluminosilicate mineral species made from interlinked tetrahedra of alumina ($AlO_4$) and silica ($SiO_4$), which can accommodate a variety of cations, such as $Na^+$, $K^+$, $Mg^{2+}$ and others. There are common natural mineral zeolites such as heulandite, stibnite, chabazite and clinoptilolite. They can also be produced synthetically, particularly from aqueous basic aluminosilicate precursor gels under hydrothermal conditions at elevated teperatures.[4] The best known synthetic zeolites are zeolite A, zeolites X and Y and ZSM-5 (Zeolite Socony Mobil-5). Zeolites have been used as adsorbents and catalysts owing to their uniformly sized pores throughout the crystal structure, selectivity, thermal and chemical stability.[5] For example, Hyun et al. have studied a 13X molecular sieve material for the adsorption of ethane, ethylene, carbon dioxide and binary mixtures of *i*-$C_4H_{10}$-$C_2H_4$, *i*-$C_4H_{10}$-$C_2H_6$ and $C_2H_4$-$CO_2$.[5] Cooney et al. have designed and operated a system for the continuous removal of ammonium ions from sewage using natural Australian zeolite (clinoptilolite).[6]

**ZIFs**

Zeolitic imidazolate frameworks (ZIFs) are a class of metal-organic frameworks synthesised by introducing organic units and transition metals into the backbone of the zeolites.[7-8] ZIFs are topologically isomorphic with zeolites, since the bridging angle of M-Im-M (M= Zn, Co and Im= imidazolate) fragment is coincident with that of Si-O-Si in zeolites (145$^o$).[9] Yaghi et al. have undertaken extensive work on this new type of porous materials and many ZIFs have been synthesised and reported in the investigations of gas storage and separation. For example, one of the most commonly studied ZIF material, ZIF-8 ($Zn(MeIM)_2$, MeIM = 2-methylimidazole) is able to adsorb gas molecules as large as 7.6 Å due to the flexible aperture of the pore.[10-11] Relevant studies of $CH_4$, $C_2$s, $C_3$s, $C_4$s and $CO_2$ sorption of ZIF-8 have been carried out in recent years.[10-12] Another widely-studied ZIF material is ZIF-7, which is formed by connecting Zn(II) metal clusters with benzimidazole (BIM) likers. It shows selective $C_2H_6$ adsorption over $C_2H_4$ through the gate-opening mechanism owing to the rotational freedom of the linker.[13]

**COFs**

Covalent-organic frameworks (COFs) are made of organic components which are interlinked into a periodic framework. COF materials are generally synthesised through the boronate anhydride formation, boronate ester formation, borosilicate formation, nitrile cyclotrimerization, imine formation and hydrazine formation reactions.[14-15] Yaghi et al. developed the first COF materials, such as COF-1 and COF-5. COF-1 is synthesised by a condensation reaction of phenyl diboronic acid in a mesitylene-dioxane solution. The structure of COF-1 can be derived from graphite, in that there are 2D sheets, with C replaced by a $B_3O_3$ unit and a ditopic phenylene unit. The structure has 1D pores in each layer with an aperture of 7.0 Å. Under similar reaction condition, COF-5 is synthesised by the condensation reaction of phenyl diboronic acid and hexahydroxytriphenylene, with an eclipsed graphitic structure.[14] Apart from the 2D-sheet stacking structures, there are also a number of 3D COF materials, such as COF-102, COF-103, COF-105 and COF-108. Of these, COF-105 and COF-108 have been predicted to show very high hydrogen uptakes of 18–19wt% at 77 K and 100 bar.[16,17]

**MOFs**

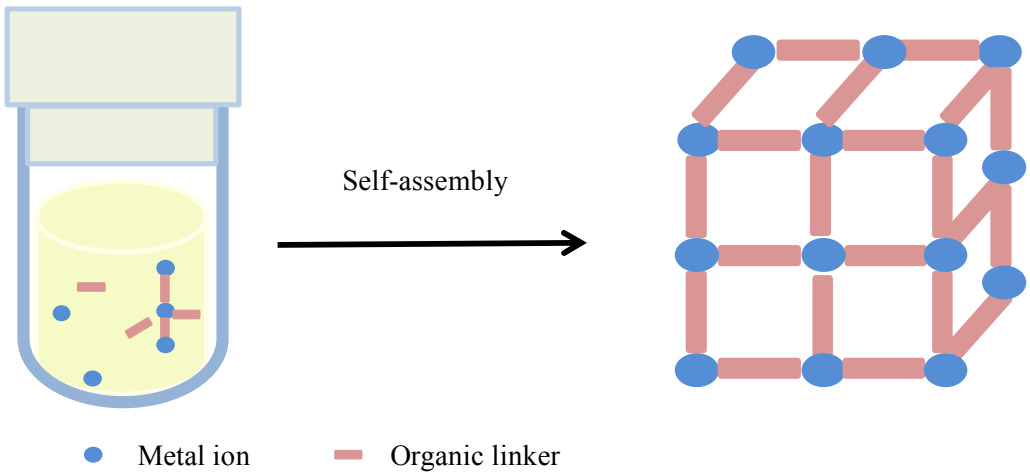
Metal-organic frameworks (MOFs) are well-ordered crystalline hybrid materials constructed from metal centres or clusters and organic linkers. MOFs comprise porous coordination polymers (PCPs) and nonporous coordination polymers.[18] Approximately half of the metals in the periodic table have been used to synthesise MOF materials up to now. The organic linkers can also be designed to introduce a variety of functionalities, giving rise to thousands of ligands. MOFs can be prepared using solvothermal reactions or even hydrothermal reactions, making them green synthesis products. MOFs are considered as promising candidates in a variety of applications, including gas sorption and separation,[19-22] catalysis,[23] sensing,[24] proton-conducting[25] and drug delivery.[26]

In summary, ZIFs, COFs and MOFs are all crystalline materials but built with different components. COFs are constructed from organic compounds only, while MOFs are synthesised with metal unit and organic ligand unit. ZIFs can be viewed as a special category of MOFs, among which transition metal ions are linked by substituted imidazolate ions with zeolite or zeolite-like structures. Owing to the

excellent tunability and versatility, MOF materials have developed fast in recent years, with significant advanced technologies in their synthesis, design and functionality.

### 1.1.2 General synthetic route of MOFs

MOFs are generally synthesised at high temperature in a sealed pressure vessel (pressure tube, pressure flask, vials, autoclaves and so forth), with all the reagents mixed well in a high-boiling-point solvents (DMF, DEF, water, dioxane, ethanol, *etc.*). There are a number of heating methods employed in their synthesis, such as traditional oil-bath heating, microwave-assisted heating, sonochemical heating, electrochemical heating and mechanochemical heating.[27-33] MOFs can form by self-assembly in a timescale ranging from a few minutes to a couple of days. The crude solid products normally contain the unreacted organic linkers, metal ions or the solvent molecules that are trapped in the pores of the frameworks after the reaction. To remove these impurities, the raw products are washed with fresh solvent and then soaked into low boiling-point solvent, such as acetone and methanol, which are easily removed by activation at high temperature. In some cases, the solvent molecules play an important role in the stabilisation of the structure. Thus these MOFs tend to collapse after the removal of solvent molecules in vacuum. One alternative for the unstable MOFs is to adopt a supercritical $CO_2$ ($scCO_2$) drying method.




Scheme 1.1 Schematic representation of the synthesis of MOF materials using a pressure tube.

**$ScCO_2$ drying**

$ScCO_2$ drying is an alternative to the conventional activation procedures, aiming to activate the framework by continuously flowing $CO_2$ into the sample to remove the solvent molecules in the pores. The $ScCO_2$ drying process allows the sample to be dried without any surface tension, thus reducing the likelihood of stiction.

## 1.2 MOF design

As reports of MOF material have continued to emerge, researchers have suggested a number of principles for the targeted design of novel MOFs. This includes the design of isoreticular structures in self-assembly process and the design of structural flexibility in response to a stimulus. In terms of the targeted design of isoreticular structures, there are many reported strategies illustrating the syntheses either by altering metal ions or functionalising the linkers.[34-38] On the other hand, with respect to the flexible MOFs, the stimuli consist of temperature, pressure, light, guest molecules and so forth. Due to the flexibility of the structure, the MOF material can undergo a breathing effect or phase transition upon the stimuli.[39-45]

### 1.2.1 Isoreticular design of MOFs

MOF-5 (IRMOF-1) series can be considered as a typical example of systematic synthesis of isoreticular MOFs with varied pore size and functionality.[34] The rules to design targeted isoreticular structures were discovered by Yaghi et al., comprising three aspects, i) the starting building blocks should have the necessary attributes to assemble the skeleton of the desired structure, ii) the synthesis must be adaptable to use derivatives of the building blocks to synthesise the same structure with distinct dimensions and functionalities; iii) the products should be highly crystalline to be characterised by X-ray diffraction (XRD) techniques.[34] Constructed by $Zn_4O$ tetrahedra and 1,4-benzenedicarboxylate linkers, MOF-5 crystallises in *Fm*-3*m* space group.[46] Figure 1.1 shows 11 isostructures of MOF-5. They are synthesised using similar conditions to that of MOF-5 but instead with extended or functionalised linkers. Among these linkers, BPDC, HPDC, PDC and TPDC (corresponding to IRMOF-9, -11, -13 and -15, respectively) give rise to doubly interpenetrated structures. This phenomenon also happens to the

primitive cubic system that form interpenetrated structure with elongated linkers.[47] However, Yaghi and co-workers designed a method to avoid the interpenetration by using more dilute conditions, thus non-interpenetrated isoreticular IRMOF-10, -12, -14, and -16 have been successfully prepared, as shown in Figure 1.1. With the strategy of growing isoreticular structures from different linkers, the free volume percent shows remarkable increase from 55.8% (MOF-5) to 91.1% (IRMOF-16), and with a variety of pore sizes and functionalities, which can be adapted to different requirements.

Another typical example for the isoreticular structural design of MOFs is the UiO-66 series, which reveals that the cage in the framework can be readily expanded by elongating the linkers as shown in Figure 1.2. UiO-66 is synthesised from $ZrCl_4$ and benzenedicarbonxylate (bdc) linker using DMF as the solvent. The length of the ligand is increased by adding one more phenyl group and under similar conditions; UiO-67 can be easily prepared which possesses a larger pore size than UiO-66. In addition, UiO-68 has also been successfully synthesised using the same approach but with two more phenyl rings added to the linker as shown in Figure 1.2.[38]

There are other examples of isoreticular MOFs which are synthesised by systematic modification of organic ligands.[38] Likewise, by substitution of the metal ions with other metals with similar coordination and properties, new isostructural MOFs also can be produced; for example, the M-MOF-74 series (also named as CPO-27-M or M/dobdc), where M = Fe, Co, Mg, Zn and Ni.[48] Compared with modifying the organic linkers, metal ion substitution introduces minor structural change in terms of unit cell size and functionality. However, such minor changes could bring about significant improvements for applications in gas uptake and catalysis. For example, Mg-MOF-74 outperforms the other isostructures of Fe-MOF-74, Co-MOF-74, Ni-MOF-74 and Zn-MOF-74 in the adsorption of $CO_2$ at R.T. and 1 bar. In particular, the uptake capacity of Mg-MOF-74 is double the values of other MOF-74 series at 0.1 bar.[38, 48-49] Another example is the isostructures of Zr-NU-1000 and Hf-NU-1000. By comparing the enthalpies of typical Hf–O (802 kJ $mol^{-1}$) and Zr–O (776 kJ $mol^{-1}$) bonds,

Beyzavi et al. speculated that Hf is more oxophilic than Zr and thus acts as a stronger Brønsted acid, which was verified by the catalytic cycloaddition reactions of $CO_2$ with epoxides.[50]

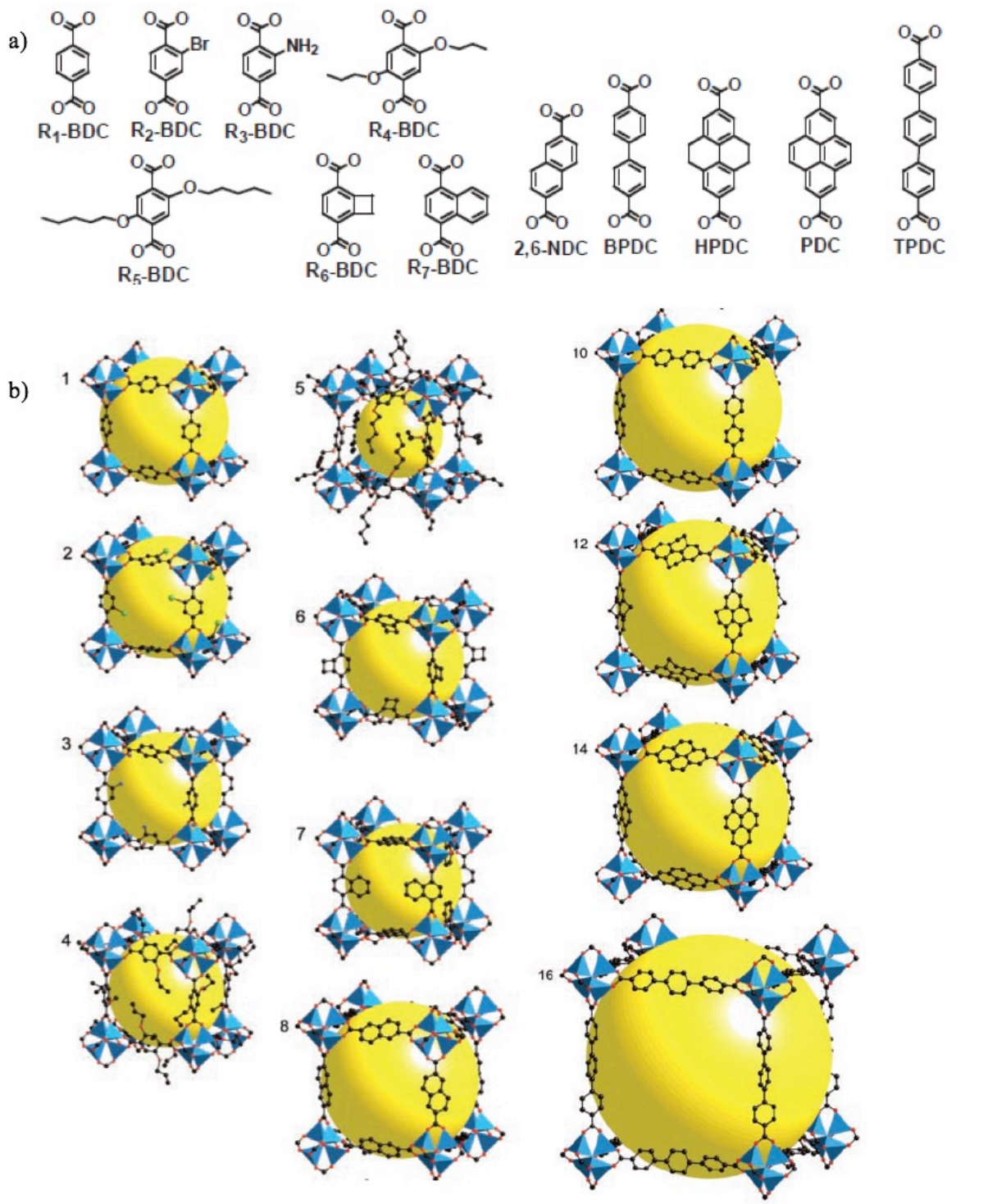



Figure 1.1 a): scheme of the linkers used for the synthesis of IRMOFs; b): the single crystal X-ray structures of IRMOF-n (n = 1–7, 8, 10, 12, 14 and 16). Zn: blue tetrahedra, O: red, C: black, Br, green, amino-groups: blue. Reproduced from Ref. 34.

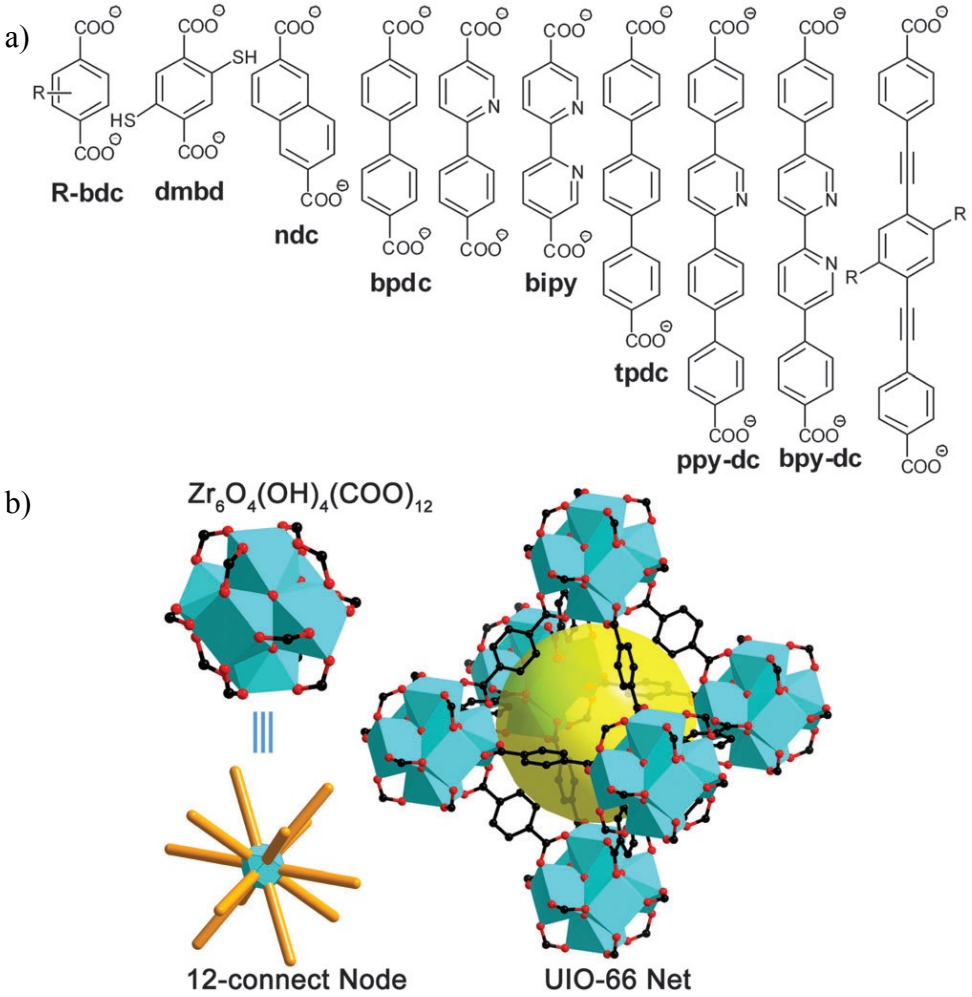



Figure 1.2 a): linkers used to synthesise isoreticular UiO-66 series; b): single crystal structure of UiO-66. Zr: turquoise, O: red, C: black. Reproduced from Ref. 38.

### 1.2.2 Flexible MOFs

Flexible MOFs are also referred to as soft porous crystals, which combines the ordering of the underlying coordination networks with cooperative structural transformability.[51] These materials can respond to physical and chemical stimuli in a tuneable fashion by self-assembly *in situ*, such as the so-called breathing or swelling effect and phase transition. General characterisation techniques involve the use of *in situ* analyses,[51] using such techniques as powder X-ray diffraction,[52-53] neutron diffraction,[54] single crystal X-ray diffraction,[55] $^{129}$Xe NMR,[56] Raman spectroscopy and IR spectroscopy.[57-58]

A well-known flexible MOF material is MIL-53(Al, Cr), which is constructed from infinite chains of corner-sharing $MO_4(OH)_2$ (M = Al, Cr) octahedra interconnected by the bdc linker, giving a 3D porous crystalline structure.[59] This flexibility can be triggered by temperature, the guest molecules and pressure

stimuli.[56, 60-61] The as-synthesised MIL-53 crystallises in the *Pnma* space group with the channels occupied by the uncoordinated disordered terephthalic acid molecules. By removing all the molecules from the pores *via* calcination at 330 °C, the material undergoes a phase transition and recrystallises in the *Imma* space group, also named as the dehydrated phase or high temperature (HT) phase. However, after water adsorption, MIL-53 transforms into another crystalline structure in the *C*2/*c* space group, known as the hydrated phase or low temperature (LT) phase, as shown in Figure 1.3b. The reason for the naming of HT and LT phase of MIL-53 is derived from similar structure transitions between the two phases upon the temperature change which has been confirmed *via* neutron powder diffraction.[63] The transition from the LT to the HT phase occurs by heating the sample to a temperature range of 325−375 K, while the HT to the LT phase transition occurs by cooling the sample to a temperature range of 125−150 K.

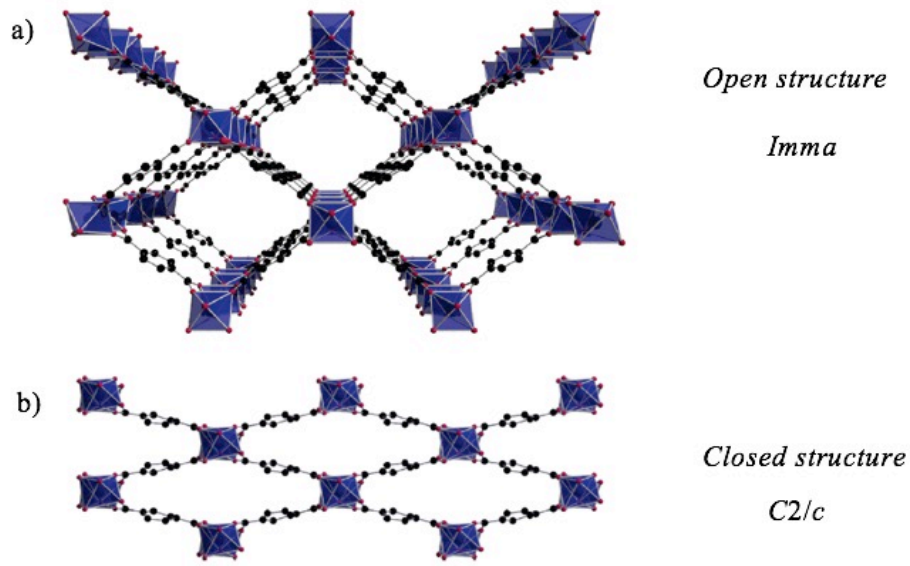



Figure 1.3 Schematic representation of the breathing effect of MIL-53 (Al) in the hydration and dehydration processes. Top: High temperature phase of MIL-53, bottom: low temperature phase of MIL-53. Reproduced from Ref. 62.

The hydrated phase of MIL-53(Cr) as the adsorbent shows dramatic improvement in the adsorption selectivity of $CO_2$ over $CH_4$ compared with the dehydrated phase.[64] It is interesting to note that at 15 bar, the $CO_2$ adsorption involves a complete phase transition to the open structure (space group *Imcm*) with cell parameters close to the dehydrated form of MIL-53, as evidenced by *in situ* synchrotron X-

ray diffraction experiments. This open structure changes back to the closed structure by desorption, giving a reversible structure change during the sorption and desorption. Apart from $CO_2$ gas stimulus, there are also hydrocarbon molecules, such as hexanes and nonanes, which have been confirmed using PXRD to induce a phase transition for MIL-53.[65]

## 1.3 Gas separation and storage of MOFs

Gas separation has been considered as one of the most promising industrial applications to be realised in MOF materials.[66] It is also one of the most widely-studied research fields in the area of MOF materials. The gas separation application of MOFs mainly concentrates on the isolation of a single component from the hydrocarbon mixtures.[67-68] Furthermore, MOFs have been investigated intensively for gas storage, such as $CO_2$, $H_2$ and $C_2H_2$, especially showing great potential in the fuel gas storage of methane.[69-70]

### 1.3.1 Hydrocarbon separation and sorption studies of MOFs

The separation of light hydrocarbons is one of the most crucial and difficult processes in the petrochemical industry. Traditionally, the separation of ethylene and propylene from mixtures of light gases involves low-temperature distillation and extractive distillation as shown in Figure 1.4. The former is performed at elevated pressures in traditional trayed fractionators. This method is highly heat extensive with a cascaded ethylene/propylene refrigeration system as the source of low temperature cooling, which is expensive to build and operate. The extractive distillation uses an extractive distillation column, where the high-boiling point polar solvent enters and its amount is reduced by the reflux of the overhead product.[71] Therefore, physical adsorption and chemical adsorption methods have been developed as alternatives to overcome the harsh conditions and high-cost problems brought about by the distillation techniques.[72-75]

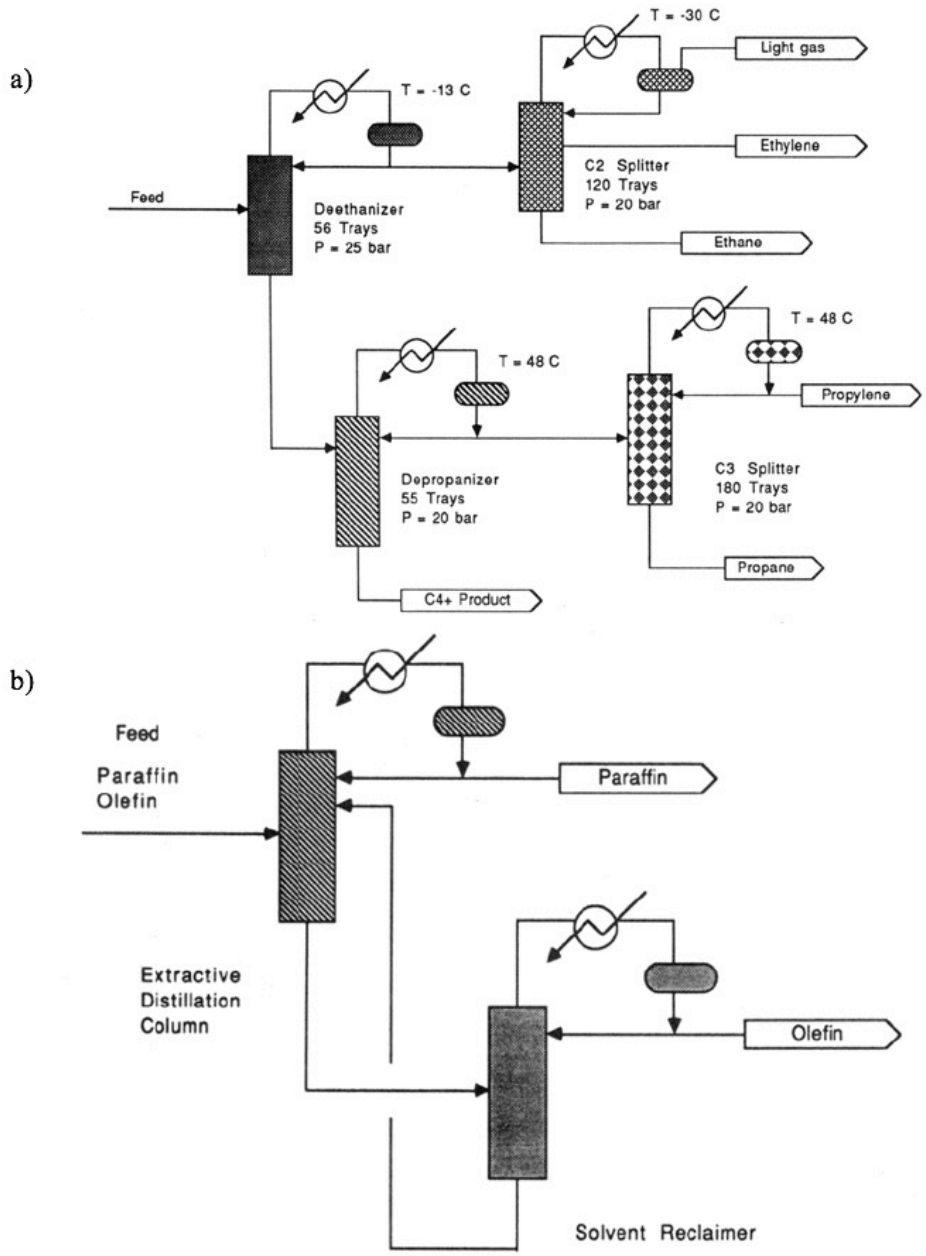



Figure 1.4 Shematic representation of the conventional low temperature distillation process for olefin/parafin separation (a) and typical extractive distillation process (b). Reproduced from Ref. 71.

Chemical adsorption methods are generally based on the interaction between the olefin π bonds and the metal σ and π bonds, which are commonly copper and silver ions.[71] Compared with chemical adsorption, physical sorption methods provide greater diversity in choosing the candidates. Among those materials, MOFs show remarkable chemical tunability of the pore geometry and surface functionality within the networks, which can facilitate control over adsorption selectivity. In addition, there are numerous MOFs with high porosity to give large separation working capacity.[76] Gas separation in MOFs generally

depends on two aspects, one is pore dimension combined with affinity of frameworks; and the other is the gas molecules having distinct physical properties, such as the quadruple moment and polarizability that result in higher adsorption enthalpy.[25,67]

**$CH_4$ purification and storage in MOFs**

As an alternative high-density fuel source to hydrogen and gasoline, natural gas plays an important role in power generation, domestic cooking and heating and transportation. As a much cleaner and highly efficient energy source, it is aiming to gradually replace the traditional gasoline and diesel fuels. However, while crude natural gas primarily consists of methane (over 70%), it also contains $CO_2$ and a series of other light hydrocarbons, such as ethane and propane. The presence of impurities reduces the energy content of the natural gas and could lead to pipeline corrosion and damage.[77] Additionally, to meet the requirements, natural gas must comply with the strict $CO_2$ concentration limits of 2% in the pipeline.[77] Hence, the separation of higher hydrocarbons and $CO_2$ from $CH_4$ has attracted much research interest recently.

A number of MOFs have been investigated for the purification and storage of methane. As one of the pioneers to investigate this subject, Snurr et al. reported a MOF material, $Zn_2(NDC)_2(DPNI)$ (NDC = 2,6-naphthalenedicarboxylate, DPNI = *N*, *N*'-di-(4-pyridyl)-1,4,5,8-naphthalene tetracarboxydiimide) synthesised using a microwave-assisted method. It exhibits an average $CO_2/CH_4$ selectivity of 4 below 2 bar at 296 K.[77] Additionally, more MOF materials have been reported which show an improving $CO_2/CH_4$ selectivity in recent years.[78-79]

**$C_2H_4/C_2H_6$ separation**

Ethylene is primarily generated from crude oil refineries, with large quantities produced globally. However, as ethane is an important feedstock for ethylene production, the raw product often contains ethane as an impurity due to the incomplete conversion. Thus the separation between $C_2H_4$ and $C_2H_6$ is required, which has been studied widely in MOF systems.[80-82]

In addition, the separations of $C_3H_6/C_3H_8$, $C_2H_4/C_3H_6$ and $C_2H_6/C_3H_8$ in MOF materials have been intensively investigated and reported in recent years, with promising progress being made.[76,83]

### 1.3.2 Storage of other gases in MOFs

#### $NH_3$ in MOFs

Ammonia is an important feedstock for the production of ammonium salts, metal nitrate salts, nitric acid and other nitrogenous reagents which are widely used in the chemical industry. However, ammonia is a noxious gas that causes serious damage to human health when the level reaches 50−100 ppm in the environment.[84] MOF materials have been studied in the applications of $NH_3$ storage and removal. Recently, Dincă et al. reported a series of isostructural mesoporous azolate MOFs, $M_2Cl_2(BTDD)\text{-}(H_2O)_2$ (M = Mn, Co, Ni), which show high ammonia uptakes of 17.9, 12.4 and 12.4 mmol $g^{-1}$, respectively. Compared with MOFs that partially decompose due to contact with ammonia, these MOF materials show reversible ammonia uptakes in the multiple cycles experiments.[85]

#### Carbon capture in MOF materials

The topic of carbon capture using MOFs has been developing for many years, with the key aim of reducing the amount of green-house gas released to the open environment. Numerous studies of porous MOFs have been reported and reviewed for $CO_2$ capture with remarkable progress. Materials with $CO_2$ adsorbed would then be subjected to permanent sequestration into underground geological formations like depleted oil reservoirs and salt water aquifers.[86-88] These studies show great potential in the application of carbon capture and sequestration (CCS) technologies. In particular, large porosity and functionality play a significant role in terms of carbon capture.[89-90]

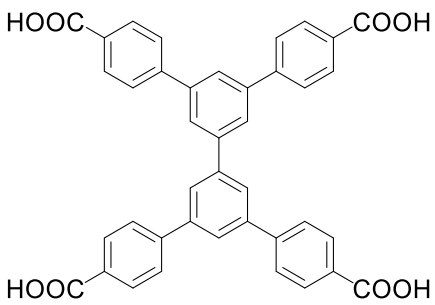
## 1.4 Aims of the work

In this thesis, two linkers are designed for the syntheses of porous MOFs, with detailed discussions for their conformations when coordinated to different metal ions. $H_4L^1$ has been previously reported for the synthesis of MFM-202 (also known as NOTT-202), ZJU-30 and a Ba-based MOF.[91-94] Among these three MOFs, MFM-202 exhibits the highest BET surface area (2220 $m^2$ $g^{-1}$) and interesting flexibility

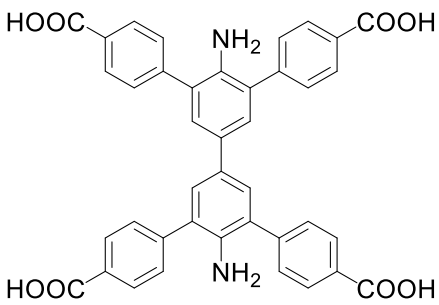
in the uptakes of $CO_2$ and $SO_2$, and thus was chosen for further studies with respect to the hydrocarbon separation and ammonia storage.[91-92] In addition, due to the high chemical stability of Zr-based MOFs, this linker has also been used for the synthesis of Zr MOFs. However, this work has been confirmed to parallel the work of another research group.[95] Matzger et al. introduced this MOF regarding to the structure and topology in May, 2016. In this work, further characterisation of this new MOF has been detailed in Chapter 4.

The modification for functionalising $H_4L^1$ with two amine groups is due to the proven enhancement in $CO_2$ capture with amine-functionalised materials.[67] In this work, this linker has been reacted with Zr(IV) and Hf(IV) ions to give rise to two new isostructural MOFs.

In this work, the design and characterisation of porous MOFs are aimed for applications in light hydrocarbon separation and storage, $NH_3$ storage and carbon capture. The corresponding characterisation techniques involved in this work include PXRD experiments, TGA and *in situ* PXRD experiments.




$H_4L^1$




$H_4L^2$

## References

1. Suhas, P. J. M. Carrott and M. M. L. Ribeiro Carrott, Lignin – from natural adsorbent to activated carbon: A review. *Bioresour. Technol.* **2007**, *98*, 2301–2312.

2. Bhatia, S. K.; Liu, F. and Arvind, G. Effect of pore blockage on adsorption isotherms and dynamics: anomalous adsorption of iodine on activated carbon. *Langmuir*. **2000**, *16,* 4001–4008.

3. Mofarahi, M.; Sadrameli, M. and Towfighi, J. Characterization of activated carbon by propane and propylene adsorption. *J. Chem. Eng. Data*. **2003**, *48,* 1256–1261.

4. Mintova, S.; Olson, N. H.; Valtchev, V. and Bein, T.. Mechanism of zeolite A nanocrystal growth from colloids at room temperature. *Science* **1999**, *283*, 958–960.

5. Hyun, S. H. and Danner, R. P. Equilibrium adsorption of ethane, ethylene, isobutane, carbon dioxide, and their binary mixtures on 13X molecular sieves. *J. Chem. Eng. Data*. **1982**, *27*, 196–200.

6. Cooney, E. L.; Booker, N. A.; Shallcross, D. C. and Stevens, G. W. Ammonia removal from wastewaters using natural Australian zeolite. II. Pilot-scale study using continuous packed column process. *Sep. Sci. Technol.* **1999**, *34*, 2741–2760.

7. Yamamoto, K.; Sakata, Y.; Nohara, Y.; Takahashi, Y. and Tatsumi, T. Organic-inorganic hybrid zeolites containing organic frameworks. *Science* **2003***, 300*, 470–472.

8. Hayashi, H.; Côté, A. P.; Furukawa, H.; O′Keeffe, M. and Yaghi, O. M. Zeolite A imidazolate frameworks. *Nat. Mater*. **2007**, *6*, 501−506.

9. Phan, A.; Doonan, C. J.; Uribe-Romo, F. J.; Knobler, C. B.; O'Keeffe, M. and Yaghi, O. M. Synthesis, structure, and carbon dioxide capture properties of zeolitic imidazolate frameworks. *Acc. Chem. Res.* **2010**, *43*, 58−67.

10. Zhang, C. and Koros, W. J. Zeolitic imidazolate framework-enabled membranes: challenges and opportunities. *J. Phys. Chem. Lett.* **2015**, *6*, 3841−3849.

11. Zhang, K.; Lively, R. P.; Zhang, C.; Chance, R. R.; Koros, W. J.; Sholl, D. S.; Nair, S. Exploring the framework hydrophobicity and flexibility of ZIF-8: From biofuel recovery to hydrocarbon separations. *J. Phys. Chem. Lett.* **2013**, *4*, 3618−3622.

12. Luebber, M. T.; Wu, T.L Shen, L. and Masel, R. I. Effects of molecular sieving and electrostatic enhancement in the adsorption of organic compounds on the zeolitic imidazolate framework ZIF-8. *Langmuir*. **2010**, *26*, 15625–15633.

13. Gücüyener, C.; van den Bergh, J.; Gascon, J. and Kapteijn, F. Ethane/ethene separation turned on its head: selective ethane adsorption on the metal-organic framework ZIF-7 through a gate-opening mechanism. *J. Am. Chem. Soc.* **2010**, *132*, 17704–17706.

14. Côté, A. P., Benin, A. I., Ockwig, N. W., O'Keeffe, M.,A.; Matzger, J. and Yaghi, O. M. Porous, crystalline, covalent organic frameworks. *Science* **2005**, *310*, 1166–1170.

15. Ding, S. Y. and Wang, W. Covalent organic frameworks (COFs): from design to applications. *Chem. Soc. Rev.* 2013, **42**, 548–568.

16. Han, S. S.; Furukawa, H.; Yaghi, O. M. and Goddard III, W. A. Covalent organic frameworks as exceptional hydrogen storage materials. *J. Am. Chem. Soc.* **2008**, *130*, 11580–11581.

17. El-Kaderi, H. M.; Hunt, J. R.; Mendoza-Cortés, J. L. Côté, A. P.; Taylor, R. E.; O'Keeffe, M. and Yaghi, O. M. Designed Synthesis of 3D Covalent Organic Frameworks. *Science* **2007**, *310*, 268–272.

18. Zhang, J. P.; Zhang, Y -B.; Lin, J –B. and Chen X. M. Metal Azolate Frameworks: From Crystal Engineering to Functional Materials. *Chem. Rev.* **2012**, *112*, 1001–1033.

19. Nijem, N.; Fürsich, K.; Bluhm, H. L.; Leone, S. R.; Gilles and M. K. Ammonia adsorption and co-adsorption with water in HKUST-1: spectroscopic evidence for cooperative interactions. *J. Phys. Chem. C.* **2015**, *119*, 24781−24788.

20. Asadi, T.; Ehsani, M. R.; Ribeiro, A. M.; Loureiro, J. M. and Rodrigues, A. E. CO2/CH4 Separation by Adsorption using Nanoporous Metal Organic Framework Copper-benzene-1,3,5-tricarboxylate Tablet. *Chem. Eng. Technol.* **2013**, *36*,1231–1239.

21. An, J. and Rosi, R. L. Tuning MOF $CO_2$ adsorption properties via cation exchange. *J. Am. Chem. Soc.* 2010, 132, 5578–5579.

22. Barea, E.; Montoro, C. and Navarro, J. A. R. Toxic gas removal – metal–organic frameworks for the capture and degradation of toxic gases and vapours. *Chem. Soc. Rev.* **2014**, *43*, 5419–5430.

23. Lee, J.; Farha, O. K.; Roberts, J.; Scheidt, K. A.; Nguyen S. T. and Hupp J. T. Metal–organic framework materials as catalysts. *Chem. Soc. Rev.* **2009**, *38*, 1450–1459.

24. Kreno,L. E.; Leong, K.; Farha, O. K.; Allendorf, M.; Van Duyne, R. P. and Hupp, J. T. Metal–organic framework materials as chemical sensors. *Chem. Rev.* **2012**, *112*, 1105–1125.

25. Furukawa, H.; Cordove, K. E.; O'Keeffe, M. and Yaghi, O. M. The chemistry and applications of metal-organic frameworks. *Science.* **2013**, *341*, 1230444-1–1230444-12.

26. Férey, G. Hybrid porous solids: past, present, future. *Chem. Soc. Rev.* **2008**, *37*, 191–214.

27. Lee, Y. –R.; Kim J. and Ahn, W. –S. Synthesis of metal-organic frameworks: a mini review. *Krean J. Chem. Eng.* **2013**, *30*, 1667–1680.

28. Bai, Y.; Dou Y.; Xie, L., Rutledge, W.; Li, J. and Zhou, H. Zr-based metal–organic frameworks: design, synthesis, structure, and applications. *Chem. Soc. Rev.* **2016**, *45*, 2327–2367.

29. Han, S. S.; Deng, W. Q. and Goddard, W. A. III. Improved Designs of Metal–Organic Frameworks for Hydrogen Storage. *Angew. Chem. Int. Ed.* **2007**, *46*, 6289-6292.

30. McDonald, T.; Lee, W. R.; Mason, J. A.; Wiers, B. M.; Hong, C. S. and Long, J. R. Capture of carbon dioxide from air and flue gas in the alkylamine-appended metal–organic framework mmen-$Mg_2$(dobpdc). *J. Am. Chem. Soc.* **2012**, *134*, 7056–7065.

31. Son, W. –J.; Kim, J.; Kim, J. and Ahn, W. –S. Sonochemical synthesis of MOF-5. *Chem. Commun.* **2008**, 6336–6338.

32. Mueller, U.; Puetter, H.; Hesse, M. Schuber, M. and Wessel, H. Method for electrochemical production of a crystalline porous metal organic skeleton material. *PCT Patent*. **2005**, 049892.

33. Pichon, A.; Lazuen-Garay, A. and James, S. L. Solvent-free synthesis of a microporous metal–organic framework. *Cryst. Eng. Comm*. **2006**, *8*, 211–214.

34. Eddaoudi, M.; Kim, J.; Rosi, N.; Vodak, D.; Wachter, J.; O'Keeffe, M. and Yaghi, O. M. Systematic design of pore size and functionality in isoreticular MOFs and their application in methane storage. *Science* **2002**, *295*, 469–472.

35. Wang, T. C.; Vermeulen, N. A.; Kim, I. S.; Martinson, A. B. F.; Stoddart, J. F.; Hupp, J. T. and Farha, O. K. Scalable synthesis and post-modification of a mesoporous metal-organic framework called NU-1000. *Nat. Protoc.* **2016**, *11*, 149–162.

36. Xydias, P.; Spanopoulos, S.; Klontzas, E.; Froudakis, G. E. and Trikalitis, P. N. Drastic enhancement of the $CO_2$ adsorption properties in sulfone-functionalized Zr- and Hf-UiO-67 MOFs with hierarchical mesopores. *Inorg. Chem.* **2014**, *53*, 679−681.

37. Dietzel, P. D. C.; Georgiev, P. A.; Eckert, J.; Blom, R.; Strässle, T. and Unruh, T. Interaction of hydrogen with accessible metal sites in the metal–organic frameworks $M_2$(dhtp) (CPO-27-M; M = Ni, Co, Mg). *Chem. Commun.* **2010**, *46*, 4962–4964.

38. Lu, W.; Wei, Z.; Gu, Z. –Y.; Liu T. –Fu.; Park, J.; Park, J.; Tian, J.; Zhang, M.; Zhang, Q.; Gentle III, J.; Bosch, M. and Zhou, H. –C. Tuning the structure and function of metal–organic frameworks via linker design. *Chem. Soc. Rev.* **2014**, *43*, 5561−5593.

39. Moggach, S. A.; Bennett, T. D. and Cheetham, A. K. The Effect of Pressure on ZIF-8: Increasing Pore Size with Pressure and the Formation of a High-Pressure Phase at 1.47 GPa. *Angew. Chem. Int. Ed.* **2009**, *48*, 7087 –7089.

40. Serre, C.; Millange, F.; Thouvenot, C.; Noguès, M.; Marsolier, G.; Louër, D. and Férey, G. Very large breathing effect in the first nanoporous chromium(III)-based solids: MIL-53 or $Cr^{III}(OH)\cdot\{O_2C\text{-}C_6H_4\text{-}CO_2\}\cdot\{HO_2C\text{-}C_6H_4\text{-}CO_2H\}_x\cdot H_2O_y$. *J. Am. Chem. Soc.* **2002**, *124*, 13519–13526.

41. Alhamami, M.; Doan, H. and Cheng, C. –H. A review on breathing behaviors of metal-organic-frameworks (MOFs) for gas adsorption. *Materials.* **2014**, *7*, 3198−3250.

42. Bueken, B.; Vermoortele, F.; Cliffe, M. J.; Wharmby, M. T.; Foucher, D.; Wieme, J.; Vanduyfhuys, L.; Martineau, C.; Stock, N.; Taulelle, F.; Speybroeck, V. V.; Goodwin, A. L. and Vos, D. D. A breathing zirconium metal–organic framework with reversible loss of crystallinity by correlated nanodomain formation. *Chem. Eur. J.* **2016**, *22*, 3264–3267.

43. Shi, D.; Zeng, L.; Ming, Z.; He, C.; Meng, C. and Duan, C. A breathing MOF: direct crystallographic observation of the site-selective C($sp^3$)–H functionalization. *RSC Adv.* **2016**, *6*, 51936−51940.

44. Serre, B.; Bourrelly, S.; Vimont, A.; Ramsahye, N. A.; Maurin, G.; Llewellyn, P. L.; Daturi, M.; Filinchuk, Y.; Leynaud, O.; Barnew, P. and Férey, G. An explanation for the very large breathing effect of a metal–organic framework during $CO_2$ adsorption. *Adv. Mater.* **2007**, *19*, 2246–2251.

45. Gong, L. L.; Feng, X. F. and Luo, F. Novel azo-metal−organic framework showing a 10-connected bct Net, breathing behavior, and unique photoswitching behavior toward $CO_2$. *Inorg. Chem.* **2015**, *54*, 11587−11589.

46. Li, H.; Eddaoudi, M.; O'Keeffe, M. and Yaghi, O. M. Design and synthesis of an exceptionally stable and highly porous metal-organic framework. *Nature.* **1999**, *402*, 276–279.

47. Reineke, T. M.; Eddaoudi, M.; Moler, D.; O'Keeffe, M. and Yaghi, O. M. Large free volume in maximally interpenetrating networks: The role of secondary building units exemplified by $Tb_2(ADB)_3[(CH_3)_2SO]_4{\cdot}16[(CH_3)_2SO]$. *J. Am. Chem. Soc.* **2000**, *122*, 4843–4844.

48. Caskey, S. R.; Wong-Foy, A. G. and Matzger, A. J. Dramatic Tuning of Carbon Dioxide Uptake via Metal Substitution in a Coordination Polymer with Cylindrical Pores. *J. Am. Chem. Soc.* **2008**, *130*, 10870–10871.

49. Lou, W.; Yang, J.; Li, L. and Li, J. Adsorption and separation of CO2 on Fe(II)-MOF-74: Effect of the open metal coordination site. *J. Solid State Chem.* **2014**, *213*, 224–228.

50. Beyzavi, M. H.; Klet, R. C.; Tussupbayev, S.; Borycz, J.; Vermeulen, N. A.; Cramer, C. J.; Stoddart, J. F.; Hupp, J. T. and Farha, O. K. A hafnium-based metal−organic framework as an efficient and multifunctional catalyst for facile $CO_2$ fixation and regioselective and enantioretentive epoxide activation. *J. Am. Chem. Soc.* **2014**, *136*, 15861–15864.

51. Schneemann, A.; Bon, V.; Schwedler, I.; Senkovska, I.; Kaskel, S. and Fischer, R. A. Flexible metal–organic frameworks. *Chem. Soc. Rev.* **2014**, *43*, 6062–6096.

52. Yang, S.; Liu, L.; Sun, J.; Thomas, K. M.; Davies, A. J.; George, M. W.; Blake, A. J.; Hill, A. H.; Fitch, A. N.; Tang, C. C.; Schröder, M. Irreversible network transformation in a dynamic porous host catalyzed by sulfur dioxide. *J. Am. Chem. Soc.* **2013**, *135*, 4954–4957.

53. Kubota,Y.; Takata, M.; Matsuda, R.; Kitaura, R.; Kitagawa, S. and Kobayashi,T. C. *Angew. Chem. Int. Ed.* **2006**, *45*, 4932–4936.

54. Yang, W.; Davies, A. J.; Lin, X.; Suyetin, M.;. Matsuda, R.; Blake, A. J.; Wilson, C.; Lewis, W.; Parker, J. E.; Tang, C. C.; George, M. W.; Hubberstey, P.; Kitagawa, S.; Sakamoto, H.; Bichoutskaia, E.; Champness, N. R.; Yang, S. and Schroder, M. Selective $CO_2$ uptake and inverse $CO_2/C_2H_2$ selectivity in a dynamic bifunctional metal–organic framework. *Chem. Sci.* **2012**, *3*, 2993–2999.

55. Allan, P. K.; Xiao, B.; Teat, S. J.; Knight, J. W. and Morris, R. E. *In situ* single-crystal diffraction studies of the structural transition of metal−organic framework copper 5-sulfoisophthalate, Cu-SIP-3. *J. Am. Chem. Soc.* **2010**, *132*, 3605−3611.

56. Springuel-Huet, M. –A.; Nossov, A.; Adem, Z.; Guenneau, F.; Volkringer, C.; Loiseau, T.; Férey, G. and Gédéon, A. 129Xe NMR study of the framework flexibility of the porous hybrid MIL-53(Al). *J. Am. Chem. Soc.* **2010**, *132*, 11599–11607.

57. Seo, J.; Bonneau, C.; Matsuda, R.; Takata, M. and Kitagawa, S. Soft secondary building unit: dynamic bond rearrangement on multinuclear core of porous coordination polymers in gas media. *J. Am. Chem. Soc.* **2011**, *133*, 9005–9013.

58. Salles, F.; Maurin, G.; Serre, C.; Llewellyn, P. L.; Knofel, C.; Choi, H. J.; Filinchuk, Y.; Oliviero, L.; Vimont, A.; Long, J. R. and Ferey ,G. Multistep $N_2$ breathing in the metal−organic framework Co(1,4-benzenedipyrazolate). *J. Am. Chem. Soc.* **2010**, *132*, 13782–13788.

59. Millange, F.; Serre, C. and Férey, G. Synthesis, structure determination and properties of MIL-53as and MIL-53ht: the first $Cr^{III}$ hybrid inorganic–organic microporous solids: $Cr^{III}(OH)\cdot\{O_2C–C_6H_4–CO_2\}\cdot\{HO_2C–C_6H_4–CO_2H\}x$. *Chem. Commun.* **2002**, 822–823.

60. Fe´rey, G.; Latroche, M.; Serre, C.; Millange, F.; Loiseau, T.; Percheron-Guegan, Hydrogen adsorption in the nanoporous metal-benzenedicarboxylate $M(OH)(O_2C–C_6H_4–CO_2)$ ($M = Al^{3+}$, $Cr^{3+}$), MIL-53A. *Chem. Commun.* **2003**, 2976–2977.

61. Bourrelly, S.; Llewellyn, P. L.; Serre, C.; Millange, F.; Loiseau, T.; Fe´rey, G. Different adsorption behaviors of methane and carbon dioxide in the isotypic nanoporous metal terephthalates MIL-53 and MIL-47. *J. Am. Chem. Soc.* **2005**, *127*, 13519–13521.

62. Mendt, M.; Jee, B.; Stock, N.; Ahnfeldt, T.; Hartmann, M.; Himsl, D. and Pöppl, A. Structural phase transitions and thermal hysteresis in the metal-organic framework compound MIL-53 as studied by electron spin resonance spectroscopy. *J. Phys. Chem. C.* **2010**, *114*, 19443–19451.

63. Liu, Y. Her, J. –H.; Dailly, A.; Ramirez-Cuesta, A. J.; Neumann, D. A. and Brown, C. M. *J. Am. Chem. Soc.* **2008**, *130*, 11813–11818.

64. Llewellyn, P. L. and Bourrelly, S. How hydration drastically improves adsorption selectivity for $CO_2$ over $CH_4$ in the flexible chromium terephthalate MIL-53. *Angew. Chem. Int. Ed.* **2006**, *45*, 7751 – 7754.

65. Trung, T. K.; Trens, P.; Tanchoux, N.; Bourrelly, S.; Llewellyn, P. L.; Loera-Serna, S.; Serre, C.; Loiseau, T.; Fajula, F. and Férey, G. Hydrocarbon adsorption in the flexible metal organic frameworks MIL-53(Al, Cr). *J. Am. Chem. Soc.* **2008**, *130*, 16926–16932.

66. Czaja, A. U.; Trukhan, N.; Müller, U. Industrial applications of metal-organic frameworks. *Chem. Soc. Rev.* **2009**, *38*, 1284–1293.

67. Sumida, K.; Rogow, D. L.; Jarad, A. M.; McDonald, T. M.; Bloch, E. D.; Herm, Z. R.; Bae, T. –H. and Long, J. R. Carbon dioxide capture in metal organic frameworks. *Chem. Rev.* **2012**, *112*, 724–781.

68. Geier, S. J.; Mason, J. A.; Bloch, E. D.; Queen, W. L.; Hudson, M. R.; Brown, C. M.; Long, J. R. Selective adsorption of ethylene over ethane and propylene over propane in the metal-organic frameworks $M_2$(dobdc) (M = Mg, Mn, Fe, Co, Ni, Zn). *Chem. Sci.* **2013**, *4*, 2054–2061.

69. He, Y.; Zhou, W.; Qian, G. and Chen, B. Methane storage in metal–organic frameworks. *Chem. Soc. Rev.* **2014**, *43*, 5657−5678.

70. Peng, Y.; Krungleviciute, V.; Eryazici, I.; Hupp, J. T., Farha, O. K. and Yildirim, T. Methane Storage in Metal−Organic Frameworks: Current Records, Surprise Findings, and Challenges. *J. Am. Chem. Soc.* **2013**, *135*, 11887−11894.

71. Eldridge, R. B. Olefin/Paraffin Separation Technology: A Review. *Ind. Eng. Chem. Res.* **1993**, *32*, 2208–2212.

72. Shu, C. M.; Kulvaranon, S.; Findley, M. E.; Liapis, A. T. Experimental and computational studies of propane-propylene separation by adsorption and variable-temperature stepwise desorption. *Sep. Technol.* **1990**, *1*, 18–28.

73. Peralta, D.; Chaplais, G.; Simon-Masseron, A.; Barthelet, K.; Chizallet, C.; Quoineaud, A. –A. and Pirngruber, G. D. Comparison of the behavior of metal−organic frameworks and zeolites for hydrocarbon separations. *J. Am. Chem. Soc.* **2012**, *134*, 8115−8126.

74. Gao, S.; Morris, C. G.; Lu, Z.; Yan, Y.; Godfrey, H. G. W.; Murray, C.; Tang, C. C.; Thomas, K. M.; Yang, S. and Schröder, M. *Chem. Mater.* **2016**, *28*, 2331−2340.

75. Hirai, H.; Kurima, K.; Komiyama, M. Selected solid ethylene adsorption composed of copper (I) chloride and polystyrene resin having amino groups. *Polym. Mater. Sci. Eng.* **1986a**, *55*, 464–468.

76. Herm, Z. R.; Bloch, E. D. and Long, J. R. Hydrocarbon separations in metal−organic frameworks. *Chem. Mater.* **2014**, *26*, 323−338.

77. Bae, Y. –S.; Mulfort, K. L.; Frost, H.; Ryan, P.; Punnathanam, S.; Broadbelt, L. J.; Hupp, J. T. and Snurr, R. Q. Separation of $CO_2$ from $CH_4$ using mixed-ligand metal-organic frameworks. *Langmuir.* **2008**, *24*, 8592–8598.

78. Jeazet, H. B. T.; Sorribas, S.; Román- Marín, J. M.; Zornoza, B.; Téllz, C.; Coronas, J. and Janiak, C. Increased selectivity in $CO_2/CH_4$ separation with mixed-matrix membranes of polysulfone and mixed-MOFs MIL-101(Cr) and ZIF-8. *Eur. J. Inorg. Chem.* **2016**, *DOI: 10.1002/ejic.20160019.*

79. Dorosti, F.; Omidkhah, M. and Abedini, R. Enhanced $CO_2/CH_4$ separation properties of asymmetric mixed matrix membrane by incorporating nano-porous ZSM-5 and MIL-53 particles into Matrimid®5218. *Journal of Natural Gas Science and Engineering.* **2015**, *25*, 88–102.

80. Wang, Q. M.; Shen, D. M.; Bülow, M.; Lau, M. L.; Deng, S. G.; Fitch, F. R.; Lemcoff, N. O.; Semanscin, *J. Microporous Mesoporous Mater*. **2002**, *55*, 217.

81. Bao, Z.; Alnemrat, S.; Yu, L.; Vasiliev, I.; Ren, Q.; Lu, X.; Deng, S. *Langmuir.* **2011**, *27*, 13554.

82. Zhang, C.; Lively, R. P.; Zhang, K.; Johnson, J. R.; Karvan, O.; Koros, W. J. *J. Phys. Chem. Lett.* **2012**, *3*, 2130.

83. Bloch, E. D.; Queen, W. L.; Krishna, R.; Zadrozny, J. M.; Brown, C. M.; Long, J. R. Hydrocarbon separations in a metal-organic framework with open iron(II) coordination sites. *Science*. **2012**, *335*, 1606–1610.

84. Ghauri, M.; Tahir, M.; Abbas, T.; Khurram, S. and Shehzad, K. Adsorption studies for the removal of ammonia by thermally activated carbon. *Sci. Int.* **2012**, *24*, 411–414.

85. Rieth, A. J.; Tulchinsky, Y. and Dincă, M. High and reversible ammonia uptake in mesoporous zzolate metal−organic frameworks with open Mn, Co, and Ni sites. *J. Am. Chem. Soc.* **2016**, *138*, 9401−9404.

86. Sumida, K.; Rogow, D. L.; Mason, J. A.; McDonald, T. M.;Bloch, E. D.; Herm, Z. R.; Bae, T. –H. and Long, J. R. Carbon Dioxide Capture in MetalOrganic Frameworks. *Chem. Rev.* **2012**, *112*, 724–781.

87. Zhang, Z.; Zhao, Y.; Gong, Q.; Li, Z. and Li, J. MOFs for CO2 capture and separation from flue gas mixtures: the effect of multifunctional sites on their adsorption capacity and selectivity. *Chem. Commun.* **2013**, *49*, 653–661.

88. Bae, Y. –S. and Snurr, R. Q. Development and evaluation of porous materials for carbon dioxide separation and capture. *Angew. Chem. Int. Ed.* **2011**, *50*, 11586 – 11596.

89. Millward, A. R. and Yaghi, O. M. Metal-organic frameworks with exceptionally high capacity for storage of carbon dioxide at room temperature. *J. Am. Chem. Soc.* **2005**, *127*, 17998–17999.

90. Hamon, L.; Serre, C.; Devic, T.; Loiseau, T.; Millange, F.; Férey, G. and Weireld, G. D. Comparative Study of Hydrogen Sulfide Adsorption in the MIL-53(Al, Cr, Fe), MIL-47(V), MIL-

100(Cr), and MIL-101(Cr) Metal-Organic Frameworks at Room Temperature. *J. Am. Chem. Soc.* **2009**, *131*, 8775−8777.

91. Yang, S.; Lin, X.; Lewis, W.; Suyetin, M.; Bichoutskaia, E.; Parker, J. E.; Tang, C. C.; Allan, D. R.; Rizkallah, P. J.; Hubberstey, P.; Champness, N. R.; Thomas, K. M.; Blake, A. J.; Schröder, M. A partially interpenetrated metal-organic framework for selective hysteretic sorption of carbon dioxide. *Nature Mater.* **2012**, *11*, 710−716.

92. Chen, X.; He, S.; Chen, F. and Feng, Y. Synthesis, characterization, and luminescence modulation of a rare barium-tetracarboxylate framework with $I^2O^1$ connectivity. *CrystEngComm.* **2014**, *16*, 8706-8709.

93. Chang, G.; Li, B.; Wang, H.; Hu, T.; Bao, Z. and Chen, B. Control of interpenetration in a microporous metal–organic framework for significantly enhanced $C_2H_2/CO_2$ separation at room temperature. *Chem. Commun.* **2016**, *52*, 3494-3496.

94. Cai, J; Yu, J.; Xu, H.; He, Y.; Duan, X.; Cui, Y.; Wu, C. and Chem, B. A doubly interpenetrated metal–organic framework with open metal sites and suitable pore sizes for highly selective separation of small hydrocarbons at room temperature. *Cryst. Growth Des.* **2013**, *13*, 2094–2097.

95. Ma, J.; Tran, L. D. and Matzger, A. J. Toward topology prediction in Zr-Based microporous coordination polymers: the role of linker geometry and flexibility. *Cryst. Growth Des.* **2016**, *16*, 4148−4153.

# Chapter 2 Hydrocarbon sorption and selectivity studies for MFM-202a

## 2.1 Introduction of MOFs in hydrocarbon sorption and separation

The separation of small hydrocarbon gaseous mixtures is an important industrial purification and refinery process. For example, the separation of propane-propene mixtures is one of the most significant and challenging process in petrochemical industry. The mixture is usually obtained from the thermal or catalytic cracking of heavy hydrocarbons. After separation, pure gaseous propene in contact with solid catalyst can be used to produce the important industrial chemical polypropene, which is a thermoplastic polymer used in a wide variety of applications, such as packaging, textiles and stationery. On the other hand, pure liquefied propane can be used as a fuel for engines, portable stoves and residential central heating. In industry, the separation is commonly associated with intensive energy and high costs, owing to the traditional cryogenic distillation method. The difficulty for the separation of these hydrocarbons originates from their similar chemical constitution, chemical structure and properties as shown in Figure 2.1 and Table 2.1.

As one of the pioneers seeking for an alternative method of small hydrocarbon separation, Long's group proposed a novel idea of using highly porous MOFs (for example, $Fe_2$(dobdc), Figure 2.2) to separate ethene/ethane, acetylene/ethene and propylene/propane and fractionation of methane/ethane/ethene/acetylene mixtures.[1] The MOF material contains coordinatively unsaturately divalent iron sites, with high surface density of 2.9 Fe(II) coordination sites per 100 $Å^2$ on its surface. Neutron powder diffraction experiments confirmed that the open iron sites serve as the main binding sites for the hydrocarbon molecules, and also showed different binding modes in saturated and unsaturated hydrocarbons. The saturated hydrocarbon molecules interact with the exposed Fe sites through ion-induced dipole interaction, whereas the unsaturated hydrocarbons binds to the open Fe sites through a side-on binding mode. In terms of hydrocarbon separation, they found that the MOF exhibits higher uptakes of unsaturated propene, acetylene and ethene compared with their saturated counterparts. To give a quantitative idea of how good the separation property is for hydrocarbons, they adopted Ideal adsorbed solution theory (IAST) coupled with dual-site Langmuir-Freundlich fittings of the isotherms

to obtain the selectivity values between two different hydrocarbons.[2] For example, the selectivity calculated for $C_3H_6/C_3H_8$ equimolar binary mixture is approximately 13–15 at 1 bar and 318 K, comparable to zeolite ITQ-12 (selectivity = 15).[1,3]

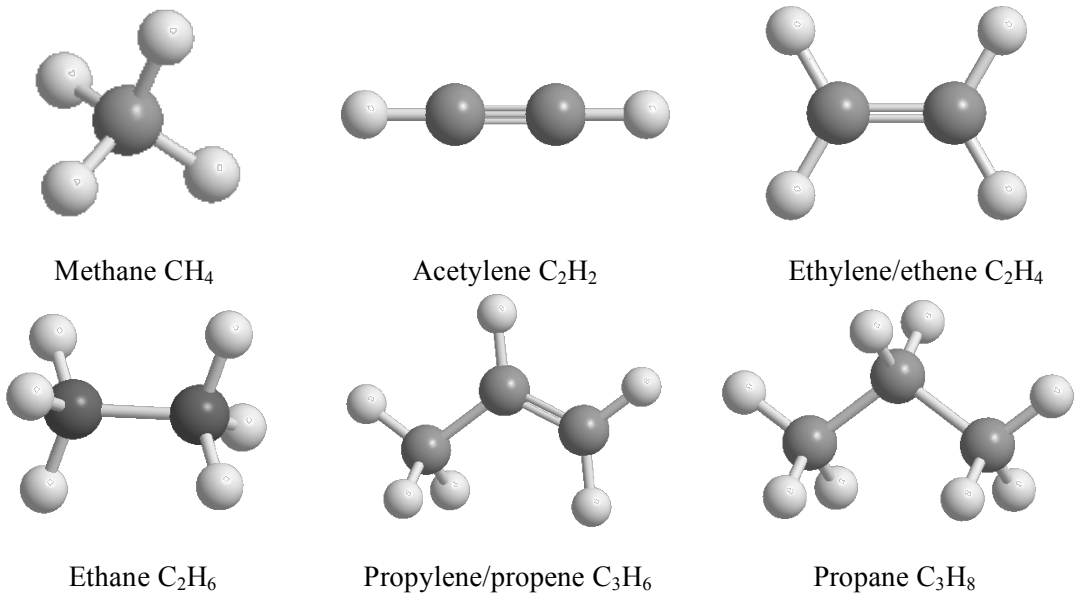



Figure 2.1 Molecular structurers of small hydrocarbon molecules. Dark grey: carbon; light grey: hydrogen.

Table 2.1 Summary of physical parameters of light hydrocarbons. [4,5]

| Gas | Kinetic diameter (Å) | Critical temp (°C) | Boiling points at 1.013 bar (°C) | Liquid density at 1.013 bar and boiling point (kg $m^{-3}$) | Molecular weight (g $mol^{-1}$) | Polarizability (× $10^{-25}$ $cm^3$) |
|---|---|---|---|---|---|---|
| $CH_4$ | 3.758 | -82.60 | -161.48 | 422.36 | 16.043 | 25.93 |
| $C_2H_2$ | 3.3 | 35.75 | -84.7 | 729 (solid) | 26.037 | 33.3–39.3 |
| $C_2H_4$ | 4.163 | 9.2 | -103.77 | 567.65 | 28.05 | 42.52 |
| $C_2H_6$ | 4.4443 | 32.17 | -88.58 | 543.83 | 30.069 | 44.3–44.7 |
| $C_3H_6$ | 4.678 | 91.06 | -47.62 | 610.06 | 42.08 | 62.6 |
| $C_3H_8$ | 4.3–5.118 | 96.7 | -42.11 | 580.88 | 44.096 | 62.9–63.7 |

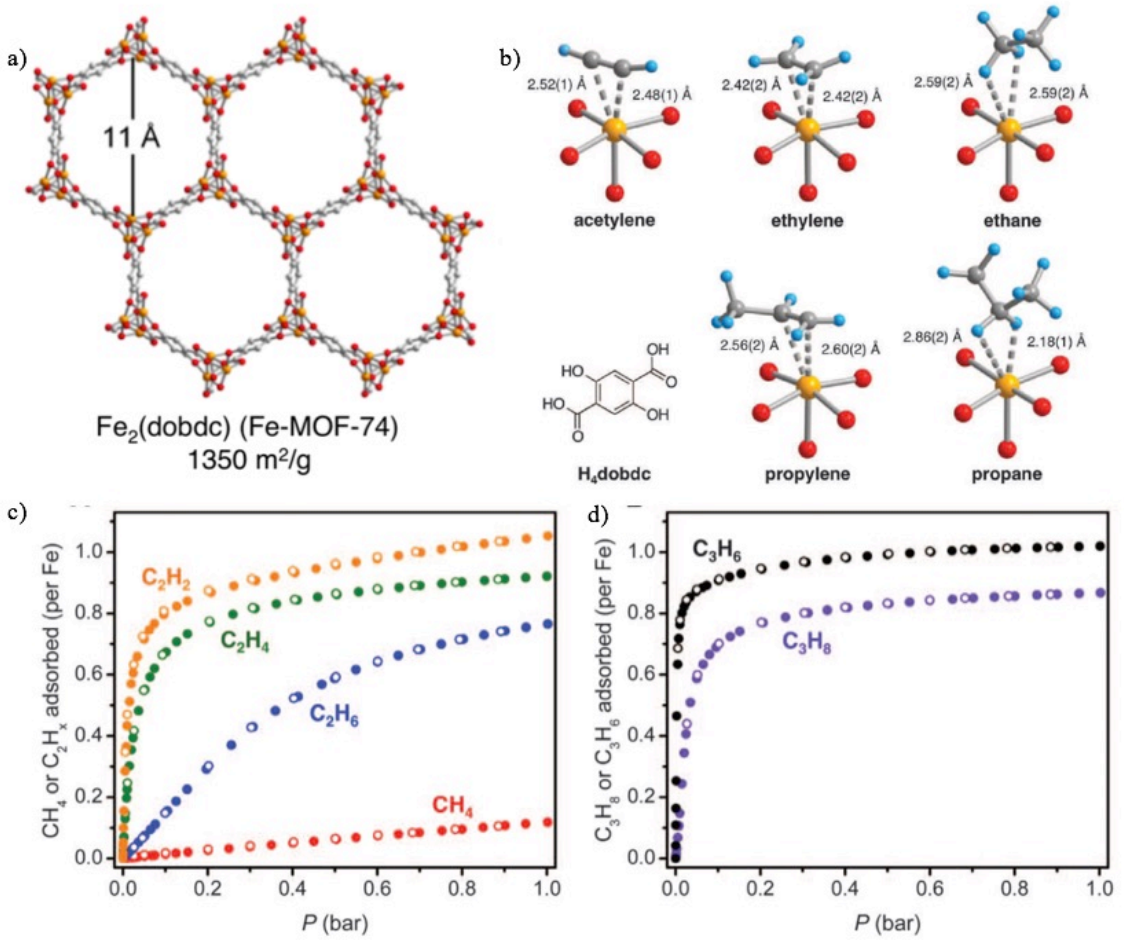



Figure 2.2 a) Crystal structure of $Fe_2$(dobdc), b) $H_4$(dobdc) ligand and the first coordination spheres for the iron centres in the solid-state structures obtained upon dosing acetylene, ethene, ethane, propene and propane. c,d) Hydrocarbon isotherms at 318 K. Reproduced from Ref. 1.

The hydrocarbon sorption and separation studies have also been carried out for flexible MOFs, MIL-53 series.[6] MIL-53 has been recognised as a typical crystalline material with a flexible structure, showing breathing effect upon the sorption/desorption of guest molecules. Specifically, it exhibits a contracting structure upon the sorption of water at R.T. Upon heating above 100 °C (to remove the water molecules in the pores), the structure transfers to a swelling mode as shown in Figure 2.3.[7] Férey *et al.* studied the adsorption of *n*-alkanes for MIL-53 (Al, Cr) and discovered that the short alkanes, $CH_4$ and $C_2H_6$, exhibited type I isotherms. However, longer alkyl chains induced apparent substeps in the sorption as shown in Figure 2.4. The substeps were discussed to have two possible mechanisms, one was the successive adsorption by inorganic and organic sites and the other was the breathing effect which was previously observed from the water containing structure. They subsequently carried out *in situ* PXRD experiments of the *n*-hexane and nonane loaded MIL-53 (Al) and *ex situ* XRD analyses to investigate

the cell parameters, which confirmed that the substeps were associated with the breathing phenomenon, as shown in Figure 2.5.

In this chapter, a typical flexible MOF material MFM-202a[8] was investigated for the sorption of a series of light hydrocarbons, coupled with the *in situ* PXRD analyses and the IAST calculation for the selectivities between two distinct hydrocarbons.

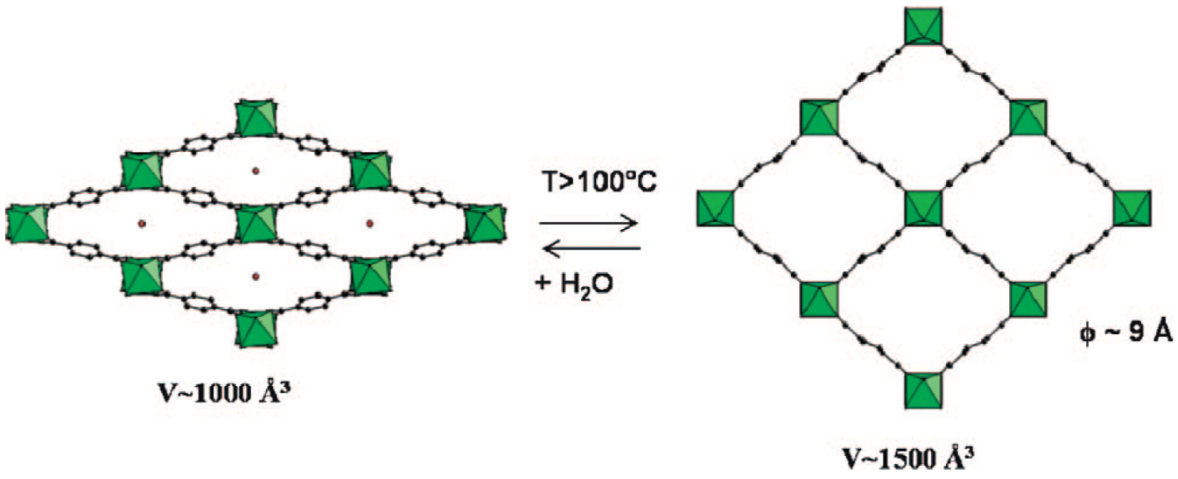



Figure 2.3 Schematic view of the structural change of MIL-53 (Al, Cr) along c axis upon adsorption-desorption of water. Left: hydrated; right: dehydrated. Picture reproduced from Ref. 6.

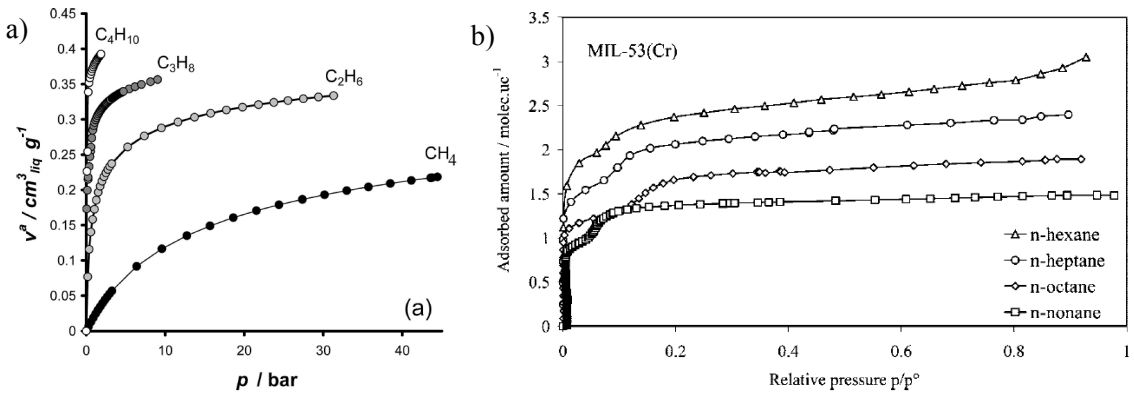



Figure 2.4 Adsorption of n-alkanes of MIL-53 (Cr) at 303 K for $C_1$-$C_4$ alkanes (a) and 313 K for $C_6$-$C_8$ alkanes (b). Picture reproduced from Ref. 6.

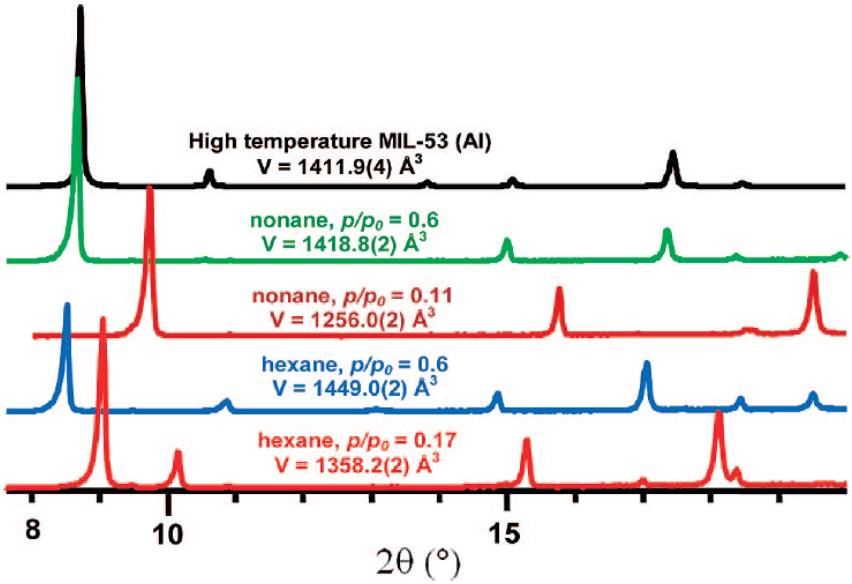



Figure 2.5 XRD patterns of MIL-53 (Al) dosed with *n*-hexane or *n*-nonane. Picture reproduced from Ref. 6.

## 2.2 Aims of this work

The aims of this work are to synthesise a flexible metal organic framework MFM-202a (Figure 2.6) and investigate the effect of hydrocarbon molecules on the structure during the sorption and desorption processes, together with the calculation and discussion of the selectivity between small hydrocarbon uptakes based on the isotherms at 293 K via both DSLF-IAST and Numerical Integration-IAST methods. Additionally, the heats of adsorption ($Q_{st}$) and entropies ($\Delta S$) for each hydrocarbon as a function of gas uptake amount are discussed.

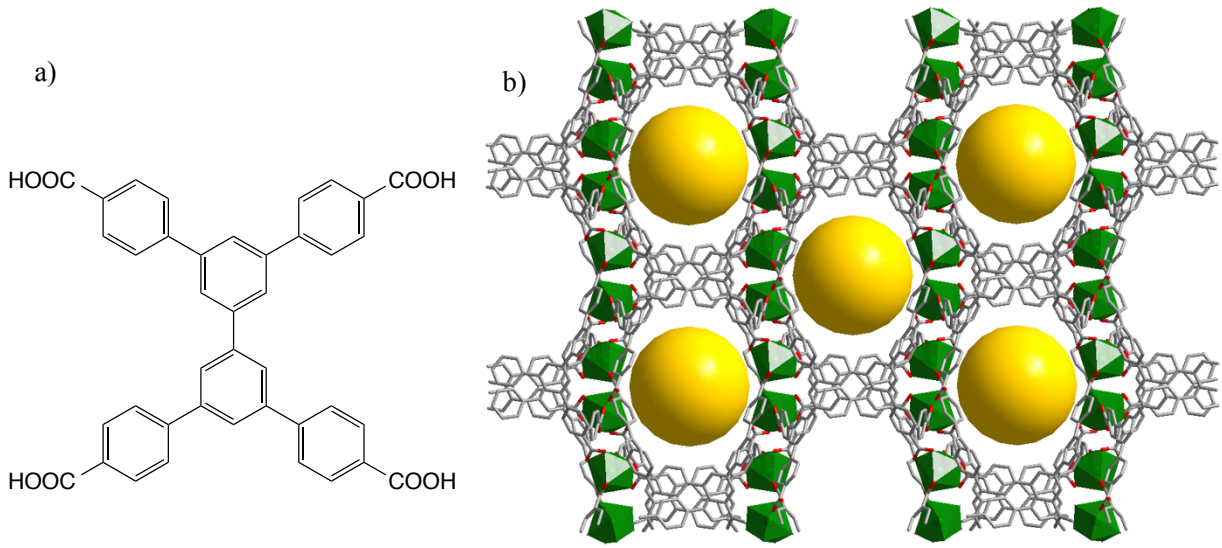



Figure 2.6 (a) View of $H_4L^1$ (5',5"-bis(4-carboxyphenyl)-[1,1':3',1":3",1"'-quaterphenyl]-4,4"'-dicarboxylic acid) used to construct MFM-202a. (b) View of channels running along c axis for MFM-202a. (Indium: green polyhedron; oxygen: red; carbon: grey; hydrogen is omitted for clarity; pore space (9 × 9 Å) is highlighted by yellow balls). Picture reproduced from Ref.8.

## 2.3 Gas uptake and selectivity studies for MFM-202a

### 2.3.1 Flexible MFM-202a

MFM-202a (also known as NOTT-202a) is the activated material from MFM-202 (NOTT-202, $(Me_2NH_2)_{1.75}[In(L)]_{1.75}(DMF)_{12}(H_2O)_{10}$).[8,9] It has a doubly interpenetrated 4,4-diamondoid structure, one network of which is approximately ~75% occupied owing to the conflicting steric requirements of the linker, resulting in a defect structure. The anionic framework is constructed from mononuclear $[In(O_2CR)_4]$ centres and the ligand (shown in Figure 2.6) in ratio of 1:1, with $(Me_2NH_2)$ as counter ion. The desolvated MFM-202a has a pore size of ~9 x 9 Å, a BET surface area of 2220 $m^2$ $g^{-1}$, a total micropore volume of 0.953 $cm^3$ $g^{-1}$ and a large pore void of ~70% of the cell volume as estimated by PLATON/SOLV.[10]

### 2.3.2 Gas uptake and selectivity studies for MFM-202a at 273–303 K

Four isotherms of $CH_4$ were measured at 273−303 K and the uptake capacities of MFM-202a below 20 bar are shown in Figure 2.7. The material shows reversible near-linear sorption/desorption profiles at the four temperatures below 1 bar, but non-linear sorption/desorption profiles at 20 bar. The adsorption amounts at 1 bar and 20 bar and various temperatures are listed in Table 2.2. The uptake at 20 bar shows almost a linear drop of 0.6~0.7 mmol $g^{-1}$ when the temperature increases every 10 K. This is probably attributed to the thermodynamics of the interaction between the framework and $CH_4$ molecules.

Compared with the $CH_4$ uptake in $Fe_2$(dobdc), which exhibits 0.77 mmol $g^{-1}$ at 318 K and 1 bar,[1] MFM-202a has a moderate adsorption capacity of $CH_4$ of 0.39 mmol $g^{-1}$ at 303 K and 1 bar. This is attributed to the nature of the binding between $CH_4$ and the framework, which arises from the linker-gas intermolecular interactions in the absence of strong open metal sorption sites and functional group sorption sites.

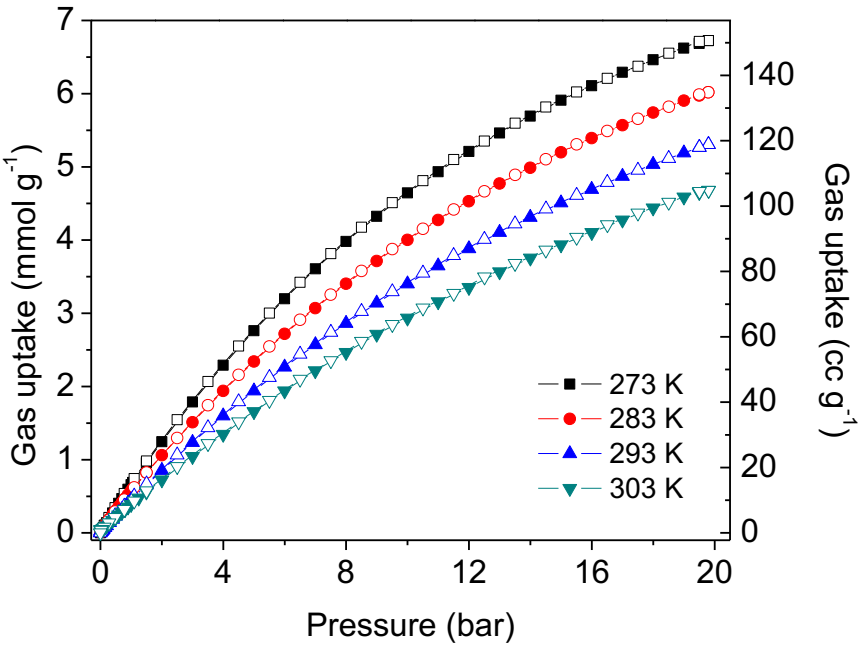



Figure 2.7 $CH_4$ sorption isotherms for MFM-202a at various temperatures. Solid symbols: adsorption, open symbols: desorption.

Table 2.2 $CH_4$ uptake capacities of MFM-202a at 1 bar and 20 bar bar and various temperatures.

| **Temperature (K)** | **273** | | **283** | | **293** | | **303** | |
|---|---|---|---|---|---|---|---|---|
| **Pressure (bar)** | **1** | **20** | **1** | **20** | **1** | **20** | **1** | **20** |
| **Uptakes (mmol $g^{-1}$)** | **0.69** | **6.73** | **0.60** | **6.02** | **0.45** | **5.31** | **0.39** | **4.68** |

The four isotherms of $C_2H_2$ exhibit reversible near-linear sorption/desorption profiles. However, the increment at low temperature is larger than that at higher temperature, as shown in Figure 2.8. For example, the uptake at 273 K is 1.83 mmol $g^{-1}$ higher than that at 283 K. However, the uptake at 293 K is only 0.86 mmol $g^{-1}$ higher than that at 303 K. Compared with the $CH_4$ uptakes, which show increases of equal increment, this is probably attributed to the molecular properties of the guest molecule $C_2H_2$, which contains π electrons that may bind to the framework through π - π interaction. The uptake amounts at various temperatures are shown in Table 2.3.

MOFs with small pore/window size or with strong binding sites (for example, open metal sites) generally reach saturation at 1 bar above 273 K.[1,11] For example, MFM-300 (~6.5 × 6.5 Å), of which the uptake of $C_2H_2$ reached saturation at 1 bar, showing 6.34 mmol $g^{-1}$ capacity at 293 K.[11] Furthermore,

$Fe_2$(dobdc) exhibits steep uptake profile at low pressure and reaches saturation of 6.89 mmol $g^{-1}$ at 1 bar and 318 K.[1] In contrast, MOFs with large pore windows and without strong binding sites, often show near-linear unsaturated uptake profiles at 1 bar. At 293 K, MFM-202a shows moderate uptake of $C_2H_2$ and is approximately 3.44 mmol $g^{-1}$.

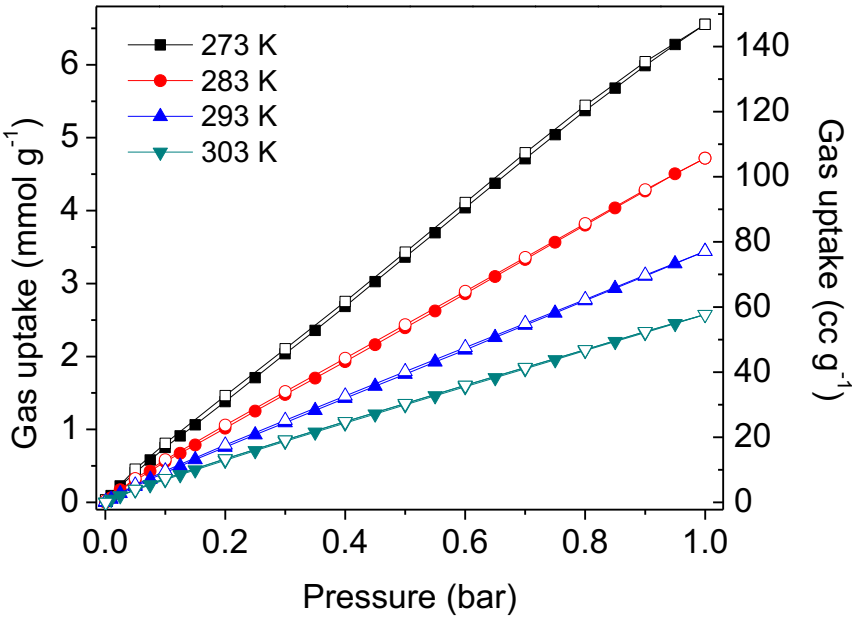



Figure 2.8 $C_2H_2$ sorption isotherms for MFM-202a at various temperatures. Solid symbols: adsorption, open symbols: desorption.

Table 2.3 $C_2H_2$ uptake capacities of MFM-202a at 1 bar and various temperatures.

| **Temperature (K)** | **273** | **283** | **293** | **303** |
|---|---|---|---|---|
| **Uptake (mmol $g^{-1}$)** | 6.55 | 4.72 | 3.44 | 2.58 |

The uptake of $C_2H_4$ shows similar near-linear fully reversible sorption/desorption profiles as that of $C_2H_2$, despite lower uptake capacities than $C_2H_2$ at the four temperatures. At 273 K and 293 K, the uptakes of $C_2H_4$ are 1.48 mmol $g^{-1}$ and 0.54 mmol $g^{-1}$ lower than $C_2H_2$ respectively. This trend is consistent with most of the reported MOF materials.[11-13] It also exhibits a larger uptake increment at low temperature than at high temperature which is similar to that of $C_2H_2$. The uptake capacities of $C_2H_4$ at 1 bar and various temperatures are shown in Table 2.4.

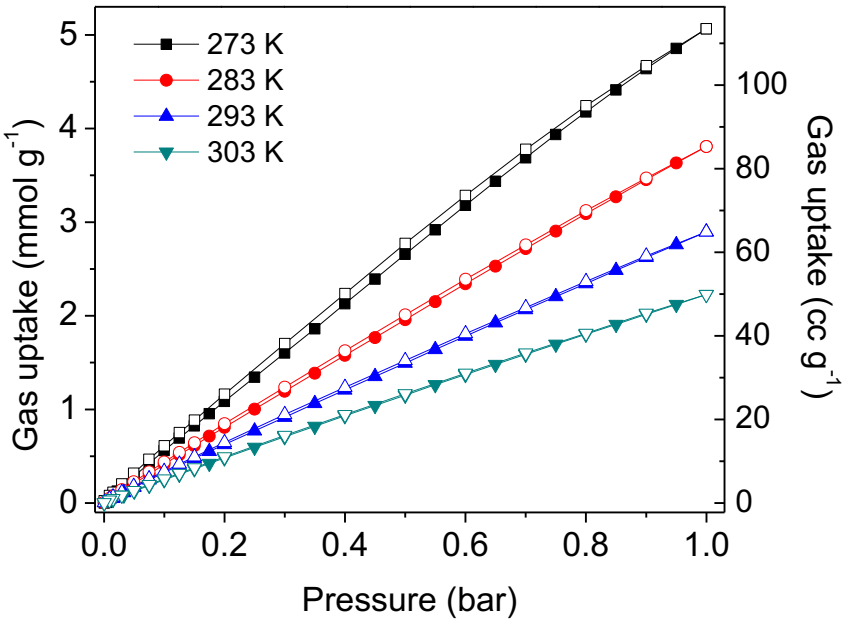



Figure 2.9 $C_2H_4$ sorption isotherms for MFM-202a at various temperatures. Solid symbols: adsorption, open symbols: desorption.

Table 2.4 $C_2H_4$ uptake capacities of MFM-202a at 1 bar and various temperatures.

| **Temperature (K)** | **273** | **283** | **293** | **303** |
|---|---|---|---|---|
| **Uptake (mmol $g^{-1}$)** | 5.07 | 3.81 | 2.90 | 2.23 |

Unlike $C_2H_2$ and $C_2H_4$ isotherms, which are measured up to 1 bar, the measurements of $C_2H_6$ uptakes were performed up to 10 bar to give the saturation uptake amounts at various temperatures, shown in Figure 2.10. Compared with the isotherms of $C_2H_2$ and $C_2H_4$ at 1 bar, $C_2H_6$ also shows similar near-

linear profiles at 293 K and 303 K. However, at lower temperatures of 273 K and 283 K, the shapes are not linear as shown in the embedded figure of Figure 2.10. Interestingly, unlike the trend of the reported uptakes of $C_2H_2 > C_2H_4 > C_2H_6$, MFM-202a shows an inverse sequence, with the uptake of $C_2H_6$ higher than the other two.[1] At 273 K and 293 K, the uptakes of $C_2H_6$ are 10.05 mmol $g^{-1}$ and 9.13 mmol $g^{-1}$ respectively, which are comparable to other best-performing MOFs.[1] The summary of uptakes is shown in Table 2.5.

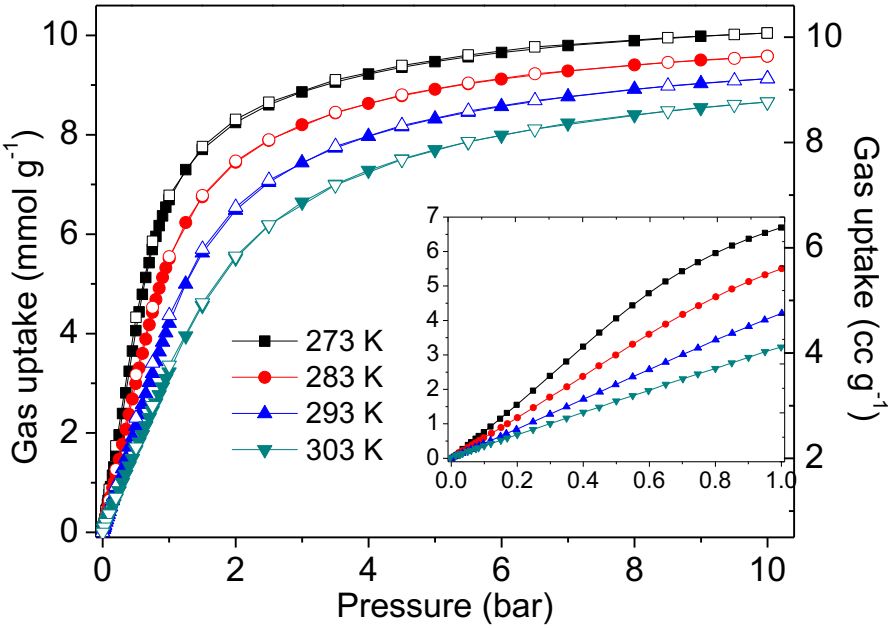



Figure 2.10 $C_2H_6$ sorption isotherms for MFM-202a at various temperatures. Solid symbols: adsorption, open symbols: desorption.

Table 2.5 $C_2H_6$ uptake capacities of MFM-202a at 1 bar and 10 bar and various temperatures.

| **Temperature (K)** | **273** | | **283** | | **293** | | **303** | |
|---|---|---|---|---|---|---|---|---|
| **Pressure (bar)** | 1 | 10 | 1 | 10 | 1 | 10 | 1 | 10 |
| **Uptake (mmol $g^{-1}$)** | 6.69 | 10.05 | 5.51 | 9.58 | 4.21 | 9.13 | 3.23 | 8.66 |

Compared with $CH_4$ and $C_2$ hydrocarbon uptakes, the $C_3$s also show fully reversible sorption/desorption profiles at 1 bar and 273–303 K, but with much higher gravimetric uptake capacities than $CH_4$ and $C_2$s,

owing to the stronger intermolecular interaction of larger size and polarizability of the gas molecule. Furthermore, unlike the near-linear isotherms of $CH_4$ and $C_2$s, the uptakes of $C_3H_6$ and $C_3H_8$ show steep uptakes at low pressure and reach saturation at 1 bar. Compared with the linear increments for $C_3H_8$ uptakes, the unsaturated $C_3H_6$ shows non-linear uptake increments from 303 K to 273 K. For example, the sorption of $C_3H_6$ shows an increment of 0.53 mmol $g^{-1}$ from 303 K to 293 K and 0.46 mmol $g^{-1}$ from 293 K to 283 K, but a much larger increment of 0.95 mmol $g^{-1}$ from 283 K to 273 K. However, the sorption of $C_3H_8$ shows equal increments of 0.38–0.41 mmol $g^{-1}$ from 303 K to 273 K.

Compared with $Fe_2$(dobdc), which uptakes 6.66 mmol $g^{-1}$ ($C_3H_6$) and 5.67 mmol $g^{-1}$ ($C_3H_8$) at 318 K and 1 bar respectively, MFM-202a shows comparable uptake amounts of $C_3H_6$ (6.72 mmol $g^{-1}$) and $C_3H_8$ (6.35 mmol $g^{-1}$) at 303 K and 1 bar, and a higher uptake of $C_3H_8$ than the flexible MIL-53(Fe) (3 mmol $g^{-1}$) at 303 K and 1 bar.[1,14]

Table 2.6 $C_3H_6$ uptake capacities of MFM-202a at 1 bar and various temperatures.

| **Temperature (K)** | **273** | **283** | **293** | **303** |
|---|---|---|---|---|
| **Uptake (mmol $g^{-1}$)** | 8.66 | 7.71 | 7.18 | 6.72 |

Table 2.7 $C_3H_8$ uptake capacities of MFM-202a at 1 bar and various temperatures.

| **Temperature (K)** | **273** | **283** | **293** | **303** |
|---|---|---|---|---|
| **Uptake (mmol $g^{-1}$)** | 7.54 | 7.16 | 6.76 | 6.35 |

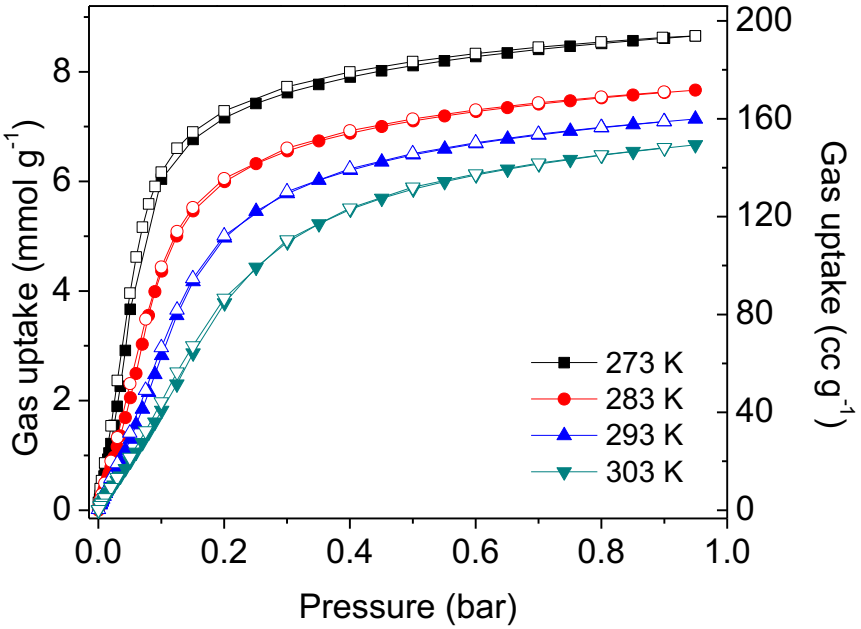



Figure 2.11 $C_3H_6$ sorption isotherms for MFM-202a at various temperatures. Solid symbols: adsorption, open symbols: desorption.

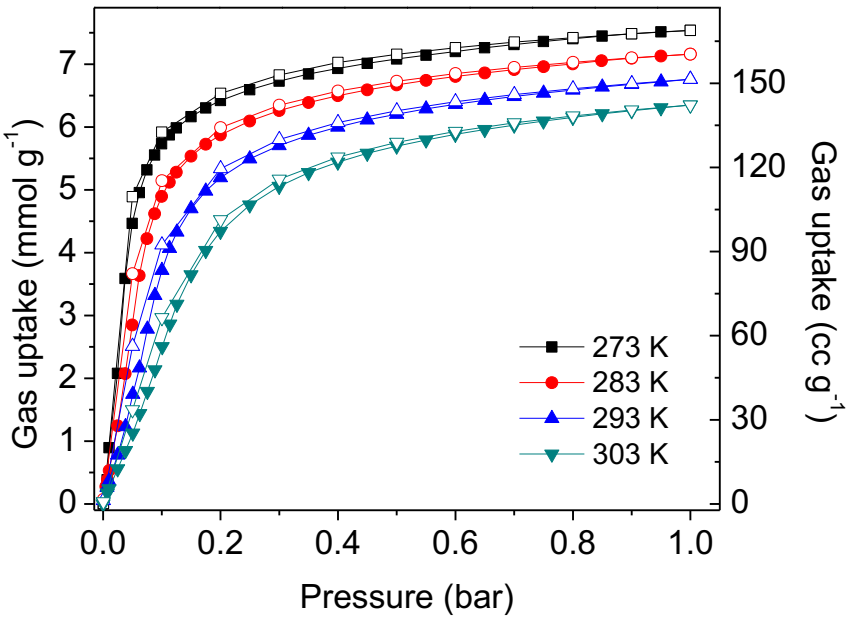



Figure 2.12 $C_3H_8$ sorption isotherms for MFM-202a at various temperatures. Solid symbols: adsorption, open symbols: desorption.

### 2.3.3 $Q_{st}$ and $\Delta S$ calculations and discussions

To assess the binding energy for each light hydrocarbon, the isosteric heats of adsorption ($Q_{st}$) were calculated by the Clausius-Clapeyron equation as a function of absolute loadings from the single gas

adsorption isotherms at 273, 283, 293 and 303 K. Additionally, the equation also gives the adsorption entropy (ΔS), which reflects the microscopic configurations and disordering of the gas molecules during the sorption process.

The values of heats of adsorption for $CH_4$ lie in the range 12–22 kJ $mol^{-1}$ from zero surface coverage up to 4.7 mmol $g^{-1}$ (20 bar) following a trend of gradual increase with the uptake amount. Similarly, the $Q_{st}$ values of $C_2H_4$ (17.5–20 kJ $mol^{-1}$) and $C_2H_6$ (14–33 kJ $mol^{-1}$) also generally increase with the gas loading despite a few fluctuations. However, the isosteric heats of adsorption for $C_2H_2$ decrease initially from 23.3 kJ $mol^{-1}$ to 21.9 kJ $mol^{-1}$ between loadings of 0.4 mmol $g^{-1}$and 1.3 mmol $g^{-1}$ and reaches plateau afterwards. Compared with $CH_4$ and $C_2$, $C_3$ hydrocarbons have higher adsorption enthalpy values (27–50 kJ $mol^{-1}$ for $C_3H_6$; 27–39 kJ $mol^{-1}$ for $C_3H_8$,). The binding energy order for saturated hydrocarbons is $C_3H_8$ (27–39 kJ $mol^{-1}$) > $C_2H_6$ (15–22 kJ $mol^{-1}$) > $CH_4$ (12–15 kJ $mol^{-1}$), which is consistent with the increased molecular size and polarizability that contributes to the molecular interaction with the framework. For the three unsaturated hydrocarbons, the interaction strength sequence is $C_3H_6$ > $C_2H_2$ > $C_2H_4$, which is consistent with the order of uptake capacities at 1 bar. It is also noticeable that the uptake of $C_3H_6$ exceeded that of $C_3H_8$ at ~5.7 mmol $g^{-1}$, where the $Q_{st}$ of $C_3H_6$ exhibits a dramatic increase but $C_3H_8$ almost reaches plateau. The entropies for $CH_4$, $C_2$s, and $C_3H_6$ all follow a trend of gradual decreasing (corresponding to the continuous ordering of the system), except that the $C_3H_8$ shows a fluctuation below the uptake of approximately 1mmol $g^{-1}$ and thereafter decreases gradually.

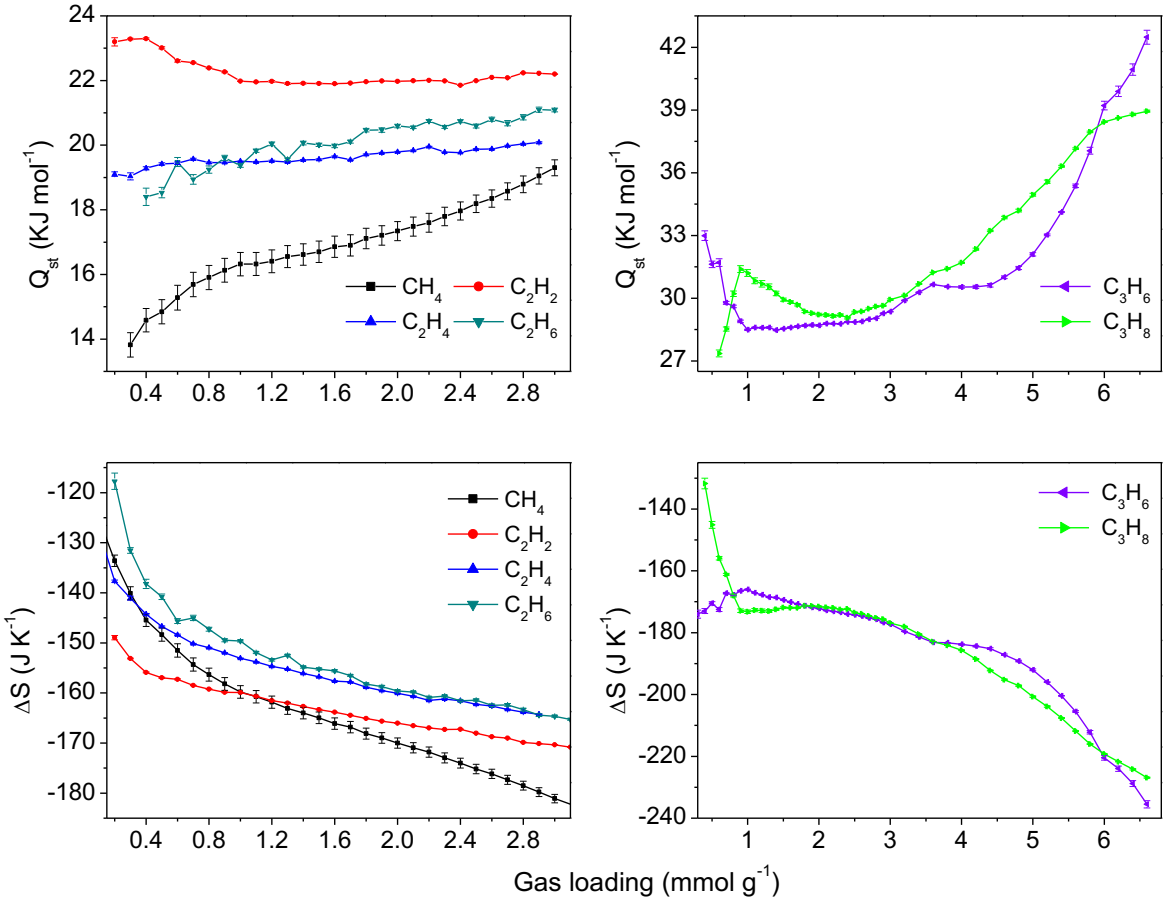



Figure 2.13 Variation of the thermodynamic parameters $Q_{st}$ and $\Delta S$ with error bars for MFM-202a as a function of hydrocarbon uptake.

### 2.3.4 Equimolar binary gas mixture uptakes and selectivity calculations

The selectivities between these light hydrocarbons have been calculated by both DSLF-IAST and NI-IAST methods. By comparison with experimental equimolar binary gas mixture measurements, it gives insights to the reliability and availability of the two theoretical predictions.

Industrial separation and purification processes for hydrocarbons involve dealing with mixtures of these with widely differing compositions. To simplify the procedure, here all the mixed gases experiments and theoretical calculations are set and defined as a 1:1 equimolar ratio binary gas mixture. In addition, all the calculations of selectivities are based on the single component isotherms measured at 293 K and 1 bar, as shown in Figure 2.14. The equimolar binary mixture uptake measurements were all carried out at 293 K and 1 bar which is consistent with the single pure component isotherms. By comparing the theoretical models with the experimental equimolar binary mixture uptakes, it can provide an insight into their differences quantitatively.

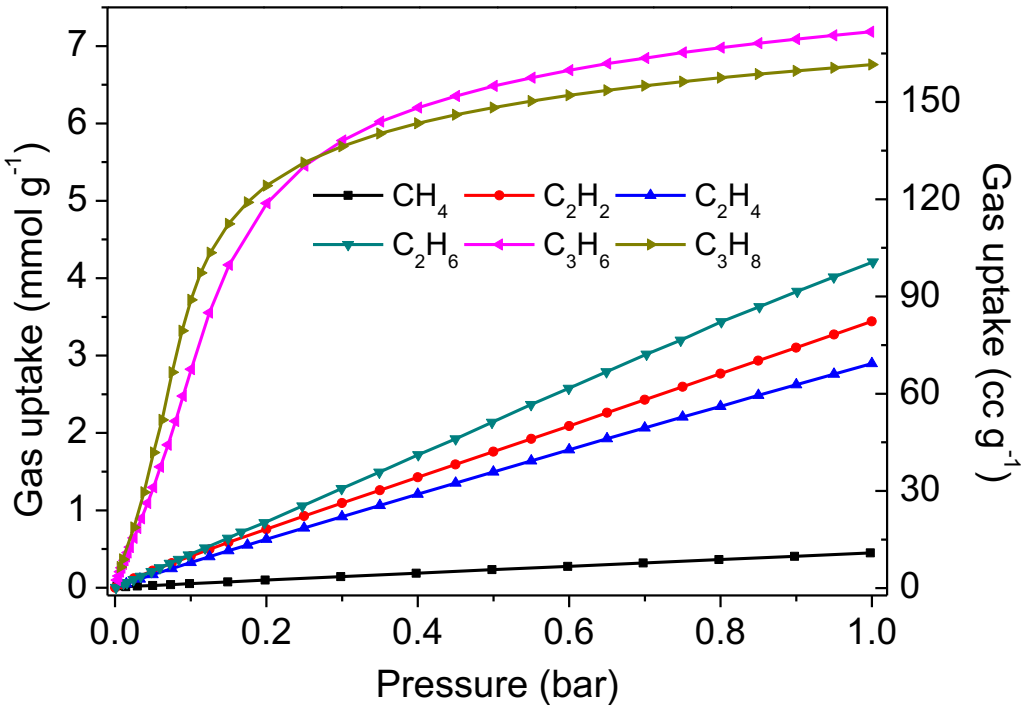



Figure 2.14 Hydrocarbon isotherms for MFM-202a measured at 293 K.

The separations of $C_2H_4/C_2H_6$, $C_2H_4/C_3H_6$ and $C_2H_6/C_3H_8$ for MFM-202a have been studied, as shown in Figure 2.15–17. The solid symbols represent the experimental gas uptakes, for example, $C_2H_4$: black squares, $C_2H_6$: red squares and equimolar mixture uptakes: blue triangles. The solid blue and cyan lines represent equimolar mixture uptake predicted by DSLF-IAST and NI-IAST methods respectively; solid black/grey lines and solid red/orange lines represent the calculated contribution of each gas in the predicted binary uptakes. The dashed lines represent the corresponding extrapolations beyond the isotherm experimental range.

The predicted equimolar $C_2H_4/C_2H_6$ mixture isotherm exhibits some features of interest. Firstly, it shows the same shape of profile as the two single uptake isotherms, which are both near-linear. Secondly, the binary isotherm lies in between the two single uptake isotherms and slightly closer to the isotherm with lower uptake ($C_2H_4$).

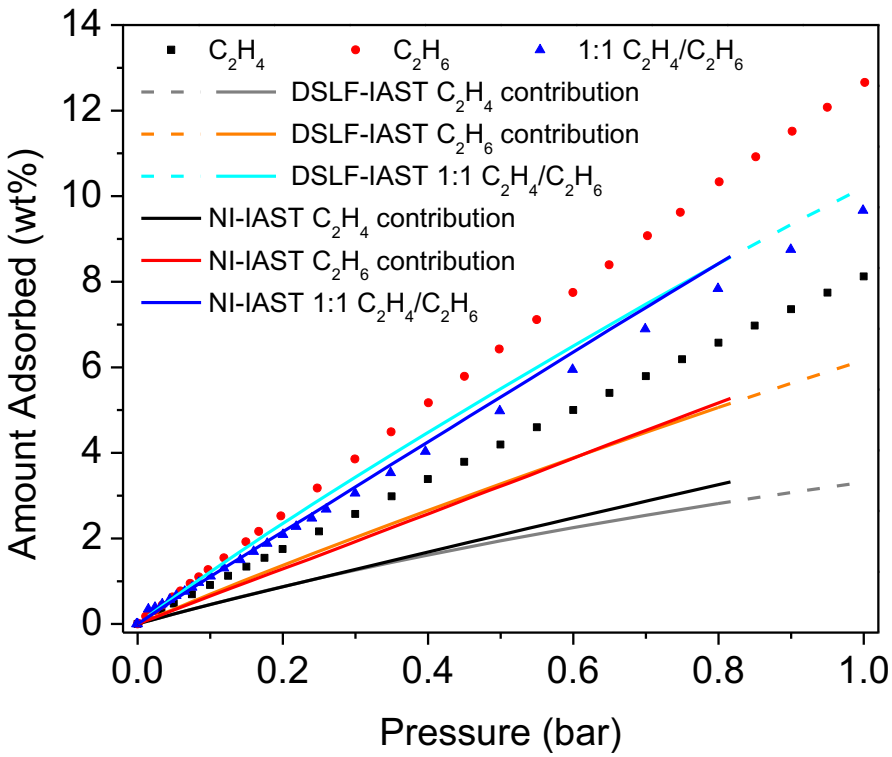



Figure 2.15 Comparison between experimental equimolar binary hydrocarbons mixture uptakes and theoretical (IAST) prediction from the pure components of $C_2H_4$ and $C_2H_6$.

Compared with the DSLF-IAST method, NI-IAST shows a limited prediction range of pressure, which is determined by the spreading pressure of the gas component with lower adsorption capacity (here determined by $C_2H_4$). DSLF-IAST is able to predict the binary uptake at any pressure, though the prediction beyond the spreading pressure is considered as an extrapolation. At lower pressure range of $C_2H_4/C_2H_6$ mixture, the NI-IAST shows better agreement with the experimental data than DSLF-IAST prediction. However, the divergence between NI-IAST and the experimental data increases as the pressure increases. The discrepancies at 0.8 bar of the two models have been calculated to show 7.8% (NI-IAST) and 7.4% (DSLF-IAST) higher than the experimental data. At 1 bar, the weight contribution of $C_2H_4$ reaches 40% and the contribution of $C_2H_6$ reaches 60% as calculated from DSLF-IAST in the extrapolation.

Conversely to the calculation of $C_2H_4/C_2H_6$, of which the two pure components both exhibit near-linear uptake profiles, the calculation of $C_2H_4/C_3H_6$ is based on two isotherms with distinct types of profiles, one near-linear isotherm ($C_2H_4$) and the other near-saturation isotherm ($C_3H_6$). The equimolar mixture uptake shows a similar shape of isotherm to $C_3H_6$, with the inflection point shifting slightly to higher pressure as shown in Figure 2.16. Moreover, the mixture isotherm is closer to the component with higher uptake ($C_3H_6$), which is different from that of $C_2H_4/C_2H_6$ mixture isotherm.

Both DSLF-IAST and NI-IAST shows slightly lower uptake values than the experimental data at low pressure range of 0–0.1 bar. However, the extrapolation of DSLF-IAST shows excellent agreement with the binary mixture uptakes, especially at 1 bar, with the discrepancy calculated being only 5.8% as shown in Table 2.8.

Due to the similar single gas isotherm shapes and uptake amounts to $C_2H_4$ and $C_3H_6$ respectively, the $C_2H_6/C_3H_8$ mixture shows similar features to those of $C_2H_4/C_3H_6$ experiments and calculations results. For example, the shape of the binary mixture isotherm is closer to the single gas isotherm of higher uptake (here is $C_3H_8$), with an inflection point shifting slightly to the high pressure region. Both models show slightly lower uptakes than the experimental mixture isotherm at low pressure and the extrapolation of DSLF-IAST fits very well with the experimental data, as shown in Figure 2.17.

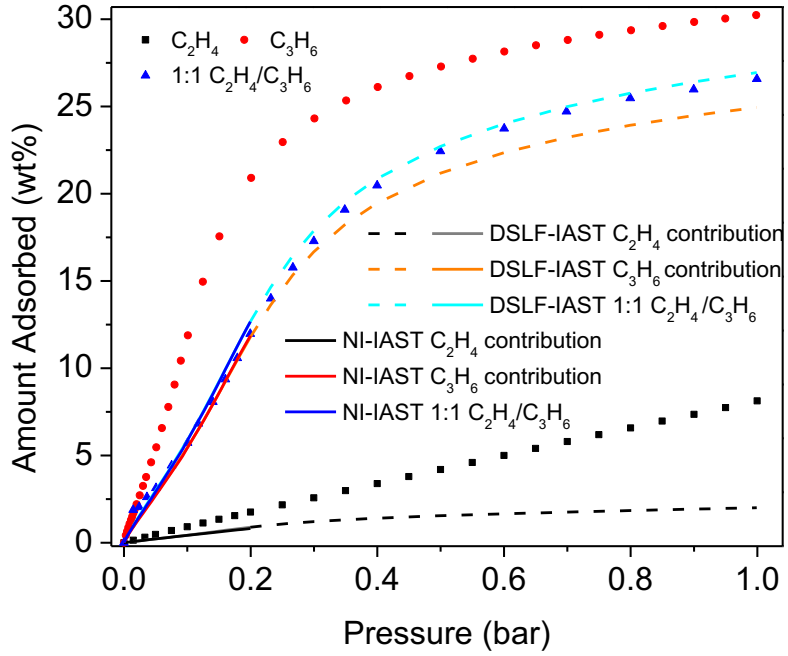



Figure 2.16 Comparison between experimental equimolar binary hydrocarbons mixture uptakes and theoretical (IAST) prediction from the pure components of $C_2H_4$ and $C_3H_6$.

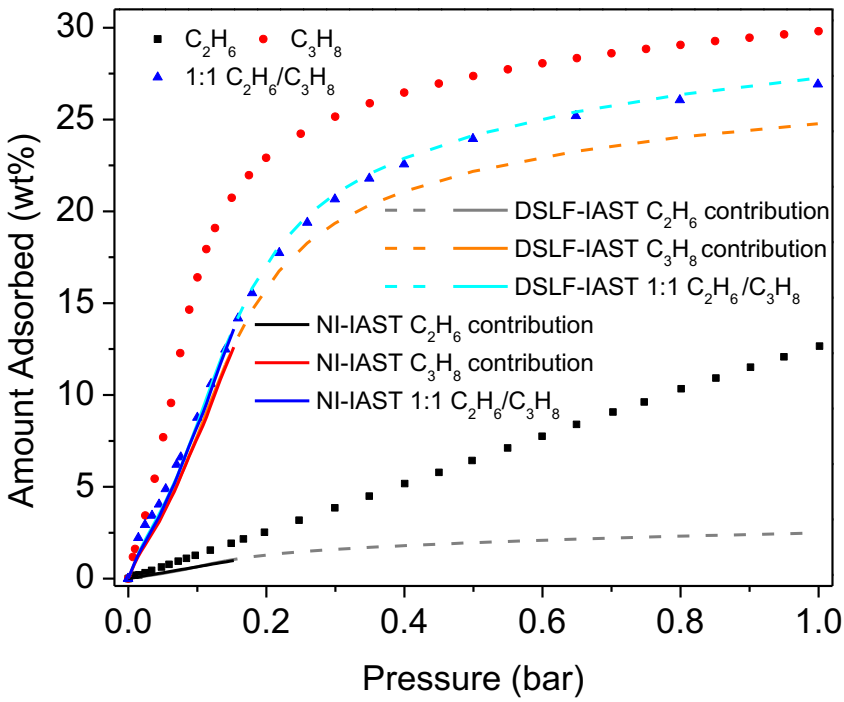



Figure 2.17 Comparison between experimental equimolar binary hydrocarbons mixture uptakes and theoretical (IAST) prediction from the pure components of $C_2H_6$ and $C_3H_8$.

Table 2.8 Summary of the discrepancies by the DSLF-IAST prediction.

| | $C_2H_4/C_2H_6$ | | $C_2H_4/C_3H_6$ | | $C_2H_6/C_3H_8$ | |
|---|---|---|---|---|---|---|
| **Pressure (bar)** | ~0.8 | 1 | 0.2 | 1 | ~0.15 | 1 |
| **Experimental uptake (wt%)** | 7.84 | 9.67 | 11.97 | 26.58 | 13.33 | 26.92 |
| **NI-IAST prediction (wt%)** | 8.45 | - | 12.67 | - | 13.24 | - |
| **NI-IAST discrepancies (%)** | 7.8 | - | 5.8 | - | -0.7 | - |
| **DSLF-IAST prediction (wt%)** | 8.42 | 10.20 | 12.66 | 26.95 | 13.43 | 27.26 |
| **DSLF-IAST discrepancies (%)** | 7.4 | 5.5 | 5.8 | 1.4 | 0.8 | 1.3 |

For the two isotherms with significant difference in uptakes, for example, between $C_2$s or $C_3$s and $CH_4$ (approximately 6–16 times higher than the uptake of $CH_4$), the NI-IAST method is not applicable because of the extremely low spreading pressure from $CH_4$. However, the DSLF-IAST method is applicable and its extrapolation shows superiorities here for the calculations of $CH_4/C_2$s and $CH_4/C_3$s since it allows the prediction of uptake at any pressure. Five sets of equimolar binary mixture isotherms were examined to show the selectivity against $CH_4$. For the equimolar binary gas mixture of $CH_4/C_2H_2$, $CH_4/C_2H_4$, $CH_4/C_3H_6$ and $CH_4/C_3H_8$, the isotherms were recorded up to 1 bar, whereas $CH_4/C_2H_6$ mixture isotherm was carried out up to 10 bar.

In comparison with the equimolar uptakes, all the extrapolated predictions of DSLF-IAST show good agreement with the experimental binary mixture uptakes at 293 K and 1 bar. In terms of two isotherms both with near-linear shaped uptakes, the $CH_4/C_2H_2$ and $CH_4/C_2H_4$ mixture isotherms lie in the middle of the two single components uptakes, which is unlike the case of $C_2H_4/C_2H_6$ mixture uptake. The DSLF-IAST calculation results for $CH_4/C_2H_2$ and $CH_4/C_2H_4$ are consistent with the experimental measurements, with extrapolation prediction discrepancies of -1.7% for $CH_4/C_2H_2$ and 3.3% for $CH_4/C_2H_4$ at 1 bar. The predicted isotherm shape of $CH_4/C_2H_6$ is similar to the experimental. However, it shows higher uptake values than the experimental data, especially at high pressure. At 1 bar, the discrepancy is calculated to be 2.5% for $CH_4/C_2H_6$ and increases as the pressure increases. At 10 bar, the prediction shows a discrepancy of 9.4% higher than the experimental data. The DSLF-IAST

calculation results for $CH_4/C_3H_6$ and $CH_4/C_3H_8$ are also consistent with the experimental measurements with the prediction discrepancies of 2.1% for $CH_4/C_3H_6$ and -0.4% for $CH_4/C_3H_8$ at 293 K and 1 bar. The equimolar uptakes and the predicted data are detailed in the Table 2.9, together with the prediction discrepancies.

In conclusion, compared with the experimental equimolar binary mixture uptake data, the prediction in the extrapolation of DSLF-IAST could show positive and negative discrepancies, and generally it shows good agreement at low pressure range and could show large inaccuracy in the extrapolation.

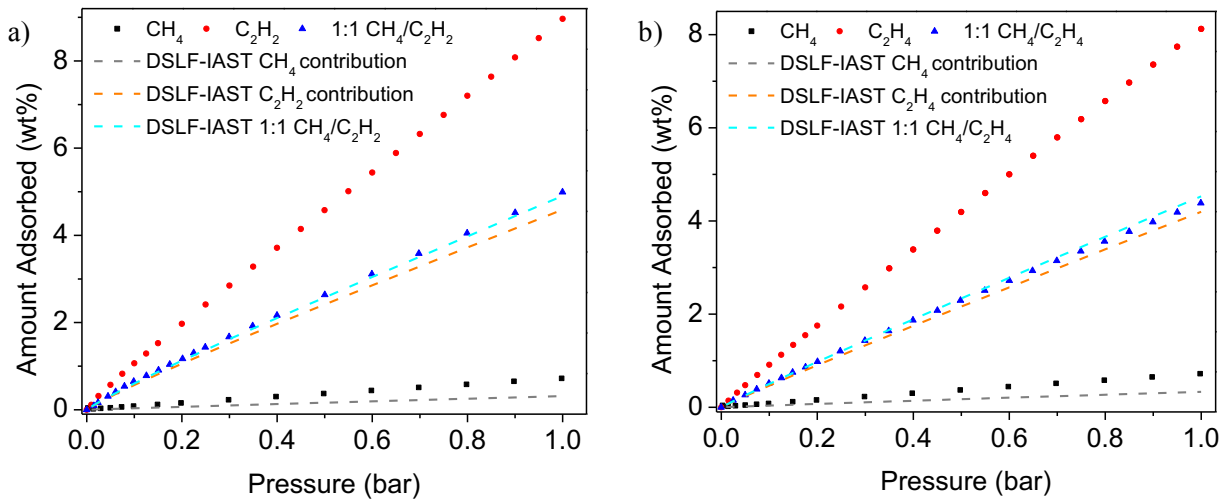



Figure 2.18 Comparison between experimental equimolar binary hydrocarbons mixture uptakes of $CH_4/C_2H_2$ and DSLF-IAST prediction from the pure components (a), $CH_4/C_2H_4$ and DSLF-IAST prediction from the pure components (b). Solid symbols: experimental gas uptake; dashed cyan lines: extrapolation of the DSLF-IAST predicted equimolar binary gases uptake beyond the isotherm experimental range; dashed grey/orange lines: extrapolations of the calculated contribution of pure gas in the predicted binary gases uptakes beyond the isotherm experimental range.

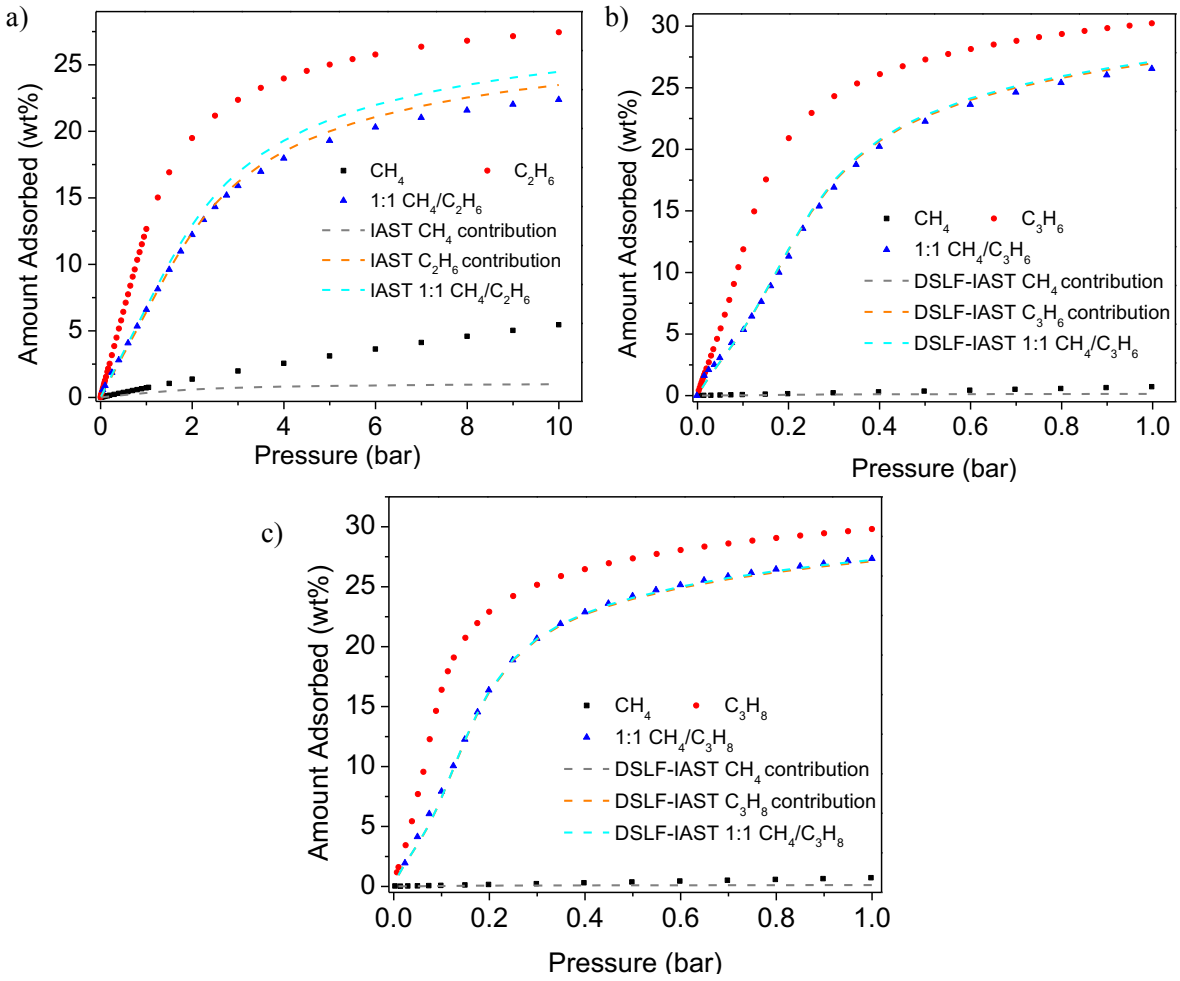



Figure 2.19 Comparison between experimental equimolar binary hydrocarbons mixture uptakes of $CH_4/C_2H_6$ and DSLF-IAST prediction from the pure components (a), $CH_4/C_3H_6$ and IAST prediction from the pure components (b), $CH_4/C_3H_8$ and IAST prediction from the pure components (c). Solid symbols: experimental gas uptake; dashed cyan lines: extrapolation of the DSLF-IAST predicted equimolar binary gases uptake beyond the isotherm experimental range; dashed grey/orange lines: extrapolations of the calculated contribution of pure gas in the predicted binary gases uptakes beyond the isotherm experimental range.

Table 2.9 Summary of the discrepancies by the DSLF-IAST prediction.

| | $CH_4/C_2H_2$ | $CH_4/C_2H_4$ | $CH_4/C_2H_6$ | | $CH_4/C_3H_6$ | $CH_4/C_3H_8$ |
|---|---|---|---|---|---|---|
| **Pressure (bar)** | 1 | 1 | 1 | 10 | 1 | 1 |
| **Experimental (wt%)** | 4.99 | 4.39 | 6.60 | 22.38 | 26.55 | 27.34 |
| **DSLF-IAST prediction (wt%)** | 4.91 | 4.53 | 6.77 | 24.48 | 27.12 | 27.24 |
| **Discrepancies (%)** | -1.7 | 3.3 | 2.5 | 9.4 | 2.1 | -0.4 |

The selectivity data for MFM-202a is calculated by DSLF-IAST method based upon the six single pure hydrocarbon isotherms carried out at 293 K.[2] In terms of methane separation, the three $C_2$ hydrocarbons show moderate selectivity values which are in the range of 7–12 below 1 bar. In contrast, the $C_3H_8/CH_4$ selectivity is ~105 at 0.01 bar and is followed by gradual decrease to 87 at 1 bar (Figure 2.19). The $C_3H_6/CH_4$ selectivity has been estimated to lie in the range of 63–75 at pressure below 1 bar. These values are comparable to the best-performing MOFs reported to date (Table 2.10a). Combined with high adsorption capacities and selectivities of $C_3H_6$ and $C_3H_8$ at 293 K, MFM-202a shows excellent potential for $C_3H_6/CH_4$ and $C_3H_8/CH_4$ separations.

In terms of $C_3H_8/C_2H_6$ separation, MFM-202a shows moderate selectivity of 7–8, which is similar to the selectivity (8–9) for $C_3H_6/C_2H_4$ separation. Interestingly, MFM-202a shows an inverse selectivity for $C_2H_4/C_2H_6$, estimated to 0.7 at 1 bar (*i.e.,* $C_2H_6/C_2H_4$ selectivity = 1.4), compared with other reported MOFs. For example, $Fe_2$(dobdc), PAF-1-$SO_3$Ag and MFM-300 show selectivities of ~13, ~27 and ~49, respectively.[1,11,15] This result indicates that MFM-202a has stronger interaction with the saturated hydrocarbons under ambient conditions and may have potential for the selective removal of saturated hydrocarbons (propane and ethane) from unsaturated hydrocarbons.

Direct comparisons of the absolute uptake difference and absolute uptake ratio difference between two hydrocarbons are detailed in Table 2.10b. The absolute uptake differences between $C_3$s and $CH_4$ of MFM-202a are much higher than those of $Fe_2$(dobdc) and UTSA-35a as shown in Table 2.10.[1,16] Combined with the high selectivities of $C_3$s/$CH_4$ calculated by DSLF-IAST, MFM-202a exhibits great potential for the separation of $C_3$ hydrocarbons from $CH_4$.

On the other hand, MFM-202a shows moderate absolute uptake ratios for $C_2H_2/CH_4$ and $C_2H_4/CH_4$, but much higher absolute uptake ratios for $C_2H_6/CH_4$, $C_3H_6/CH_4$ and $C_3H_8/CH_4$ at 1 bar than the other best-performing MOFs.[1,11,16-17]

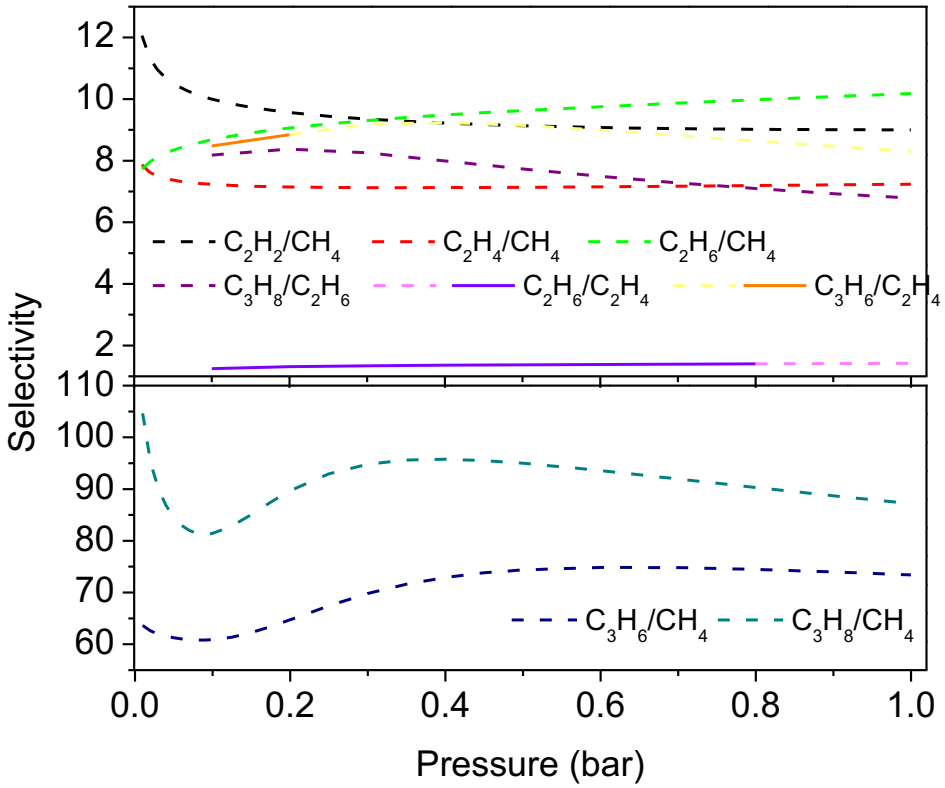



Figure 2.20 The IAST selectivity for adsorption of equimolar mixture between different hydrocarbons in MFM-202a at 293 K. These selectivity data have also been confirmed by the dual-component gas adsorption experiments as mentioned above. Solid lines: selectivities predicted by DSLF-IAST methods based on experimental data; dashed lines: extrapolations of the IAST predicted selectivities beyond the experimental range.

Table 2.10 (a) Comparison of the selectivities calculated by DSLF-IAST for light hydrocarbons for several MOFs. (b) Comparison of uptake ratios and absolute differences for a series of MOFs.

a)

| Compounds | Selectivity | | | | | | | | Ref. |
|---|---|---|---|---|---|---|---|---|---|
| | $C_2H_2$/ $CH_4$ | $C_2H_4$/ $CH_4$ | $C_2H_6$/ $CH_4$ | $C_3H_6$/ $CH_4$ | $C_3H_8$/ $CH_4$ | $C_2H_4$/ $C_2H_6$ | $C_3H_6$/ $C_2H_4$ | $C_3H_8$/ $C_2H_6$ | |
| **MFM-202a**[a] | 9.0 | 7.3 | 10.2 | 74 | 87 | 0.7 | 8.4 | 6.8 | This work |
| **$Fe_2$(dobdc)**[b] | ~950 | ~440 | ~35 | - | - | ~12.5 | - | - | 1,11 |
| **Cu-TDPAT**[c] | 82 | ~44 | ~14 | - | - | - | - | - | 17 |
| **MFM-300**[a] | >1000 | ~380 | ~5.1 | - | - | 48.7 | - | - | 11 |
| **UTSA-35a**[d] | ~20 | ~10 | ~14 | ~90 | ~83 | - | - | - | 16 |

b)

| Compounds | Ratios of uptakes | | | | | Absolute uptake differences between two hydrocarbons (mmol $g^{-1}$) | | | | | Ref. |
|---|---|---|---|---|---|---|---|---|---|---|---|
| | $C_2H_2$ /$CH_4$ | $C_2H_4$ /$CH_4$ | $C_2H_6$ /$CH_4$ | $C_3H_6$ /$CH_4$ | $C_3H_8$ /$CH_4$ | $C_2H_2$ - $CH_4$ | $C_2H_4$ - $CH_4$ | $C_2H_6$ - $CH_4$ | $C_3H_6$ - $CH_4$ | $C_3H_8$ - $CH_4$ | |
| **MFM-202a**[a] | 7.64 | 6.44 | 9.36 | 15.96 | 15.02 | 2.99 | 2.45 | 3.76 | 6.73 | 6.31 | This work |
| **$Fe_2$(dobdc)**[b] | 8.95 | 7.82 | 6.49 | 8.65 | 7.36 | 6.12 | 5.25 | 4.23 | 5.89 | 4.90 | 1,11 |
| **Cu-TDPAT**[c] | 6.29 | 5.83 | 5.47 | - | - | 6.67 | 6.08 | 5.63 | - | - | 17 |
| **MFM-300**[a] | 21.86 | 14.76 | 2.93 | - | - | 6.05 | 3.99 | 0.56 | - | - | 11 |
| **UTSA-35a**[e] | 6.74 | 5.02 | 5.65 | 7.65 | 6.91 | 2.47 | 1.73 | 2.00 | 2.86 | 2.54 | 16 |

[a] Data measured and processed at 293 K and 1 bar; [b] Data measured and processed at 318 K and 1 bar; [c] Data measured and processed at 298 K and 1 bar; [d] Data measured and processed at 296 K.

### 2.3.5 Low temperature uptake of hydrocarbons

Apart from the gas uptake measurements recorded at above 273 K, MFM-202a has also been investigated at low temperature to give an insight into the maximum capacity of hydrocarbons. Unlike the near-linear sorption isotherm at 273–303 K, all $C_2$s show inflection points of sorption at low temperature and 1 bar. Moreover, the $CH_4$ uptake again shows near-linear profiles at low temperature and 1 bar but then becomes saturated at above 10 bar. The $C_3$s adsorptions reach saturation at ~40 mbar

for $C_3H_6$ and ~10 mbar for $C_3H_8$ and thus exhibit much steeper sorption at very low pressure. Interestingly, all the three unsaturated hydrocarbons ($C_2H_2$, $C_2H_4$ and $C_3H_6$) show stepwise sorption process and hysteretic desorption process to a different extent. In contrast, the three saturated hydrocarbons ($CH_4$, $C_2H_6$ and $C_3H_8$) show fully reversible type I sorption and desorption profiles as shown in Figure 2.21.

The adsorption amounts of these hydrocarbons at low temperature are detailed in Table 2.11. First, the uptake of $CH_4$ at 195 K and 1 bar is ~6.21 mmol $g^{-1}$ (Figure 2.21), corresponding to a storage density of 104.5 kg $m^{-3}$, reaching 25% of the liquid methane density at its boiling point (422.4 kg $m^{-3}$ at 111.7 K). The uptake of $CH_4$ reaches saturation at 195 K and 16 bar, with maximum adsorption of 13.1 mmol $g^{-1}$, reaching 53% of the liquid methane density.

Interestingly, $C_2H_2$ adsorption shows a plateau starting at 27 mbar and ending at ~100 mbar, with an uptake of 5.3 mmol $g^{-1}$. An additional 11.4 mmol $g^{-1}$ of $C_2H_2$ is gained at 450 mbar, where it reaches saturation. The desorption isotherm shows very large hysteretic release of adsorbed $C_2H_2$ molecules. At the initial stage of desorption, the release of $C_2H_2$ from the material was extremely slow, with ~89% of the adsorbed $C_2H_2$ molecules maintained in the pore above 200 mbar before desorption became significant, with 37% retained at 10 mbar and 24% retained at 2 mbar, indicating a high storage capacity of adsorbed $C_2H_2$ molecules in this material at low pressure and 195 K. 100% of adsorbed $C_2H_2$ molecules were desorbed from the material upon applying high vacuum to the sample. The hysteresis phenomenon has also been observed and discussed for $CO_2$ uptakes at low temperature for MFM-202a.[9] Similar to linear $CO_2$ molecules, $C_2H_2$ also has a significant quadrupole moment, which may induce specific host-guest interactions together with other soft binding interactions and thus results in the stepwise adsorption and the hysteretic desorption. Such broad hysteretic sorption behaviour is rarely observed for $C_2H_2$ adsorption in MOFs,[1,16,17] and is particularly advantageous to practical storage and transportation because it allows $C_2H_2$ molecules to be adsorbed at high pressure but stored at relatively low pressure. This will significantly minimize the risks of $C_2H_2$ explosion by compression. Compared with the large hysteresis of $C_2H_2$ in MFM-202a, smaller hysteretic $C_2H_2$ desorption has been observed and discussed in M'MOF-3a, MOF-508 and HOF-5a, which however show much lower uptakes (6.6

mmol $g^{-1}$ at 195 K, 4.0 mmol $g^{-1}$ at 290 K and 8.1 mmol $g^{-1}$ at 273 K, respectively).[18-20] A tentative explanation for the hysteresis can be given based upon the flexible host structure of MOF-508 with a potential narrow-pore to large-pore framework phase transition triggered by the interaction of $C_2H_2$ molecule and the framwork.[18]

The uptake of $C_2H_2$ at 195 K and 1 bar gives the maximum amount of 18.3 mmol $g^{-1}$, ranking the top among all the reported $C_2H_2$ uptake capacities.[1,16-17] This adsorption capacity corresponds to a storage density of 500.0 kg $m^{-3}$ (the density of adsorbed $C_2H_2$ is 69% of the solid acetylene density at 192 K, 729 kg $m^{-3}$). The other two $C_2$ hydrocarbons, $C_2H_4$ and $C_2H_6$, also show high uptake capacities, 14.8 and 11.9 mmol $g^{-1}$, corresponding to storage densities of 435.6 kg $m^{-3}$ (the density of adsorbed $C_2H_4$ is 77% of liquid ethene density at 169 K, 568 kg $m^{-3}$) and 375.5 kg $m^{-3}$ (the density of adsorbed $C_2H_6$ is 69% of liquid ethane density at 185 K, 544 kg $m^{-3}$), respectively.

The uptake of $C_3H_6$ at 201 K and 0.2 bar gives the maximum amount of 12.1 mmol $g^{-1}$, corresponding to a storage density of 533.3 kg $m^{-3}$, reaching 87% of the liquid density (610.06 kg $m^{-3}$ at 1.013 bar and 225 K). The uptake of $C_3H_8$ at 195 K and ~0.12 bar gives the maximum amount of 9.0 mmol $g^{-1}$, equivalent to a storage density of 415.5 kg $m^{-3}$, reaching 72% of the liquid density (580.88 kg $m^{-3}$ at 1.013 bar and 231 K).

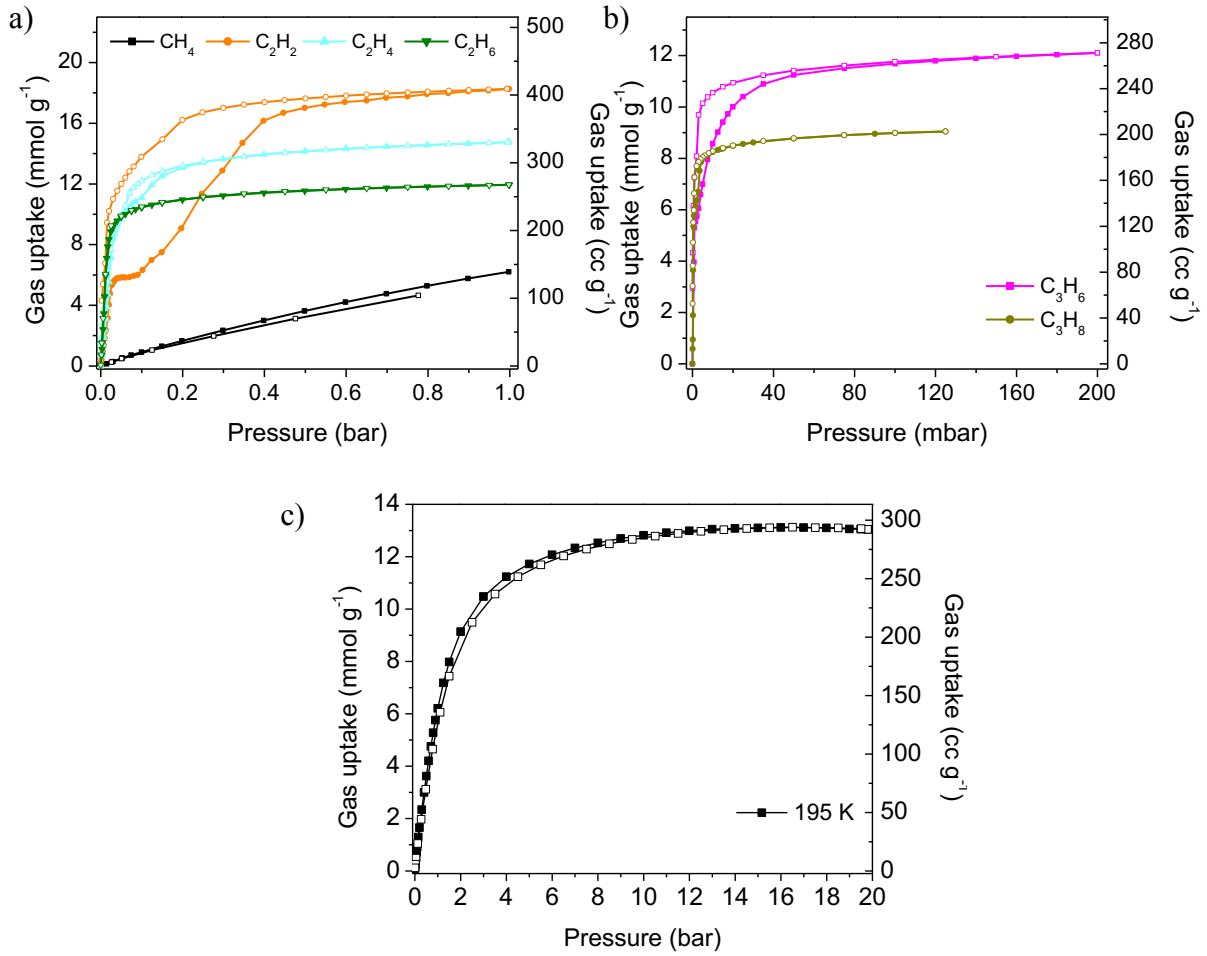



Figure 2.21 (a) $CH_4$, $C_2H_2$, $C_2H_4$ and $C_2H_6$ sorption isotherms at 195 K for MFM-202a. (b) $C_3H_6$ and $C_3H_8$ sorption isotherms at low temperature for MFM-202a. (c) $CH_4$ sorption isotherms for MFM-202a at 195 K and 20 bar. (solid symbol: adsorption; open symbol: desorption).

Table 2.11 Summary of hydrocarbon uptakes at low temperature.

| | $CH_4$ | | $C_2H_2$ | $C_2H_4$ | $C_2H_6$ | $C_3H_6$ | $C_3H_8$ |
|---|---|---|---|---|---|---|---|
| **Temperature (K)** | 195 | | 195 | 195 | 195 | 201 | 195 |
| **Pressure (bar)** | 1 | 16 | 1 | 1 | 1 | 0.2 | 0.125 |
| **Uptake (mmol $g^{-1}$)** | 6.21 | 13.1 | 18.3 | 14.8 | 11.9 | 12.1 | 9.0 |

### 2.3.6 *In situ* synchrotron powder X-ray diffraction analysis and discussions

Hysteretic isotherms have been reported widely and could be a sign for structural transition in flexible MOF materials.[6,9] To trace the structural change of MFM-202a during the sorption/desorption of $C_2$s,

*in situ* synchrotron X-ray powder diffraction (*in situ* PXRD) of MFM-202a on individual loadings of $C_2H_2$, $C_2H_4$ and $C_2H_6$ at 195 K and 1 bar have been recorded at Diamond Light Source.

The PXRD of MFM-202a shows peaks shift slightly to higher 2θ angles as $C_2H_2$ dosing pressure increases from 0 to 1 bar, suggesting a contraction of the unit cell with a slight increase of the FWHM (full width at half maximum). This is possibly due to the breakdown of MOF particles or partial framework disorder due to guest-host interactions. In contrast, the *in situ* PXRD patterns of both $C_2H_4$ and $C_2H_6$ loaded MFM-202a exhibit small shifts to lower 2θ angles as pressure increases, indicating that unit cell volumes expand on loading of $C_2H_4$ and $C_2H_6$, as shown in Figure 2.22. The PXRD patterns of all three $C_2$s loaded MFM-202a shift back to those of the desolvated MOF upon desorption, indicating an intact structure upon the sorption of the three $C_2$s.

*In situ* PXRD results confirm the absence of framework structural transition albeit with the presence of adsorption steps and hysteretic desorption for $C_2H_2$ and $C_2H_4$. In addition, there is no apparent phase change for the sorption of $C_2H_6$ at 195 K and 1 bar. This observation of *in situ* PXRD is similar to that of $CO_2$ loaded MFM-202a, but different from that of $SO_2$ loaded MFM-202a which was associated with the occurrence of a new phase.[9,21] Given that the pore size of 9 x 9 Å is much larger than the size of $C_2$s molecules (Table 2.1), no noticeable confinement effect of adsorbed gas molecules in the pores of MFM-202a was seen upon desorption. Therefore, the observed adsorption step and hysteresis are probably attributed to pore-filling effect in this flexible MOF material.[9,22-24] Owing to the complexity of the crystal structure of MFM-202a, satisfactory Rietveld refinements to extract the location of adsorbed gas molecules could not be obtained.

In summary, all three *in situ* PXRD results at $2\theta = 2–15^{o}$ show small peak shifts during the hydrocarbon uptakes from 0 to 1 bar with the degassed sample retaining the crystallinity. This suggests that MFM-202a material is intact to the interactions with $C_2$s at 195 K and 1 bar.

Analysis of the lattice parameters are shown in Figure 2.23. The top three show the unit cell parameters of *a*, *b* and *c* changes for the loadings of $C_2H_2$, $C_2H_4$ and $C_2H_6$, respectively. Interestingly, *a* axis

increases and *b*/*c* axes decrease for all $C_2$ loadings in the unit cell. The middle three exhibit the monoclinic unit cell $\beta$ angle changes with the loadings of $C_2H_2$, $C_2H_4$ and $C_2H_6$, respectively. Again, the three $C_2$s show similar decrease trend of $\beta$ in the unit cell except that $C_2H_2$-loaded unit cell experienced a fluctuation of $\beta$ at 0.064 bar. Interestingly, the cell volume for MFM-202a is reduced with $C_2H_2$ sorption whereas the cell volumes both increase with $C_2H_4$ sorption and $C_2H_6$ sorption, which is consistent to the shifts of 2θ from the *in situ* PXRD results.

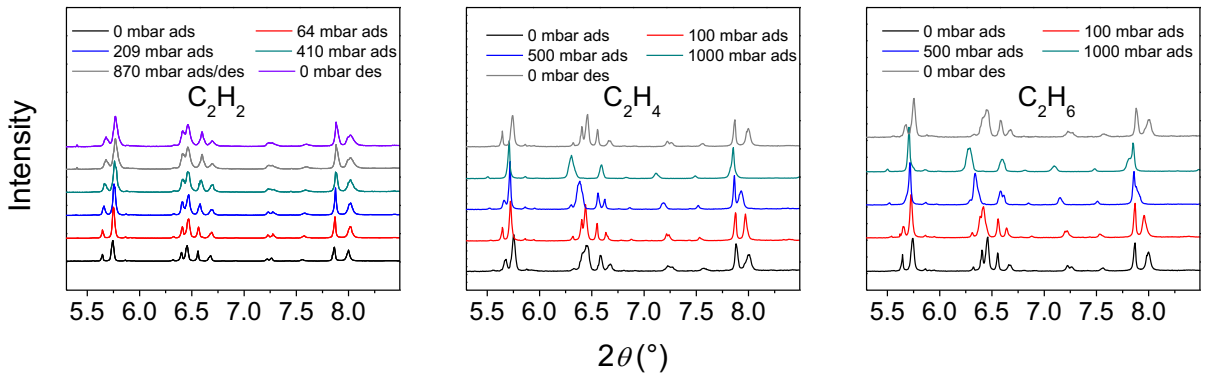



Figure 2.22 Comparison of *in situ* high resolution powder diffraction patterns for MFM-202a as a function of different $C_2H_2$ (a), $C_2H_4$ (b) and $C_2H_6$ (c) loading at 195 K (λ = 0.825774 Å).

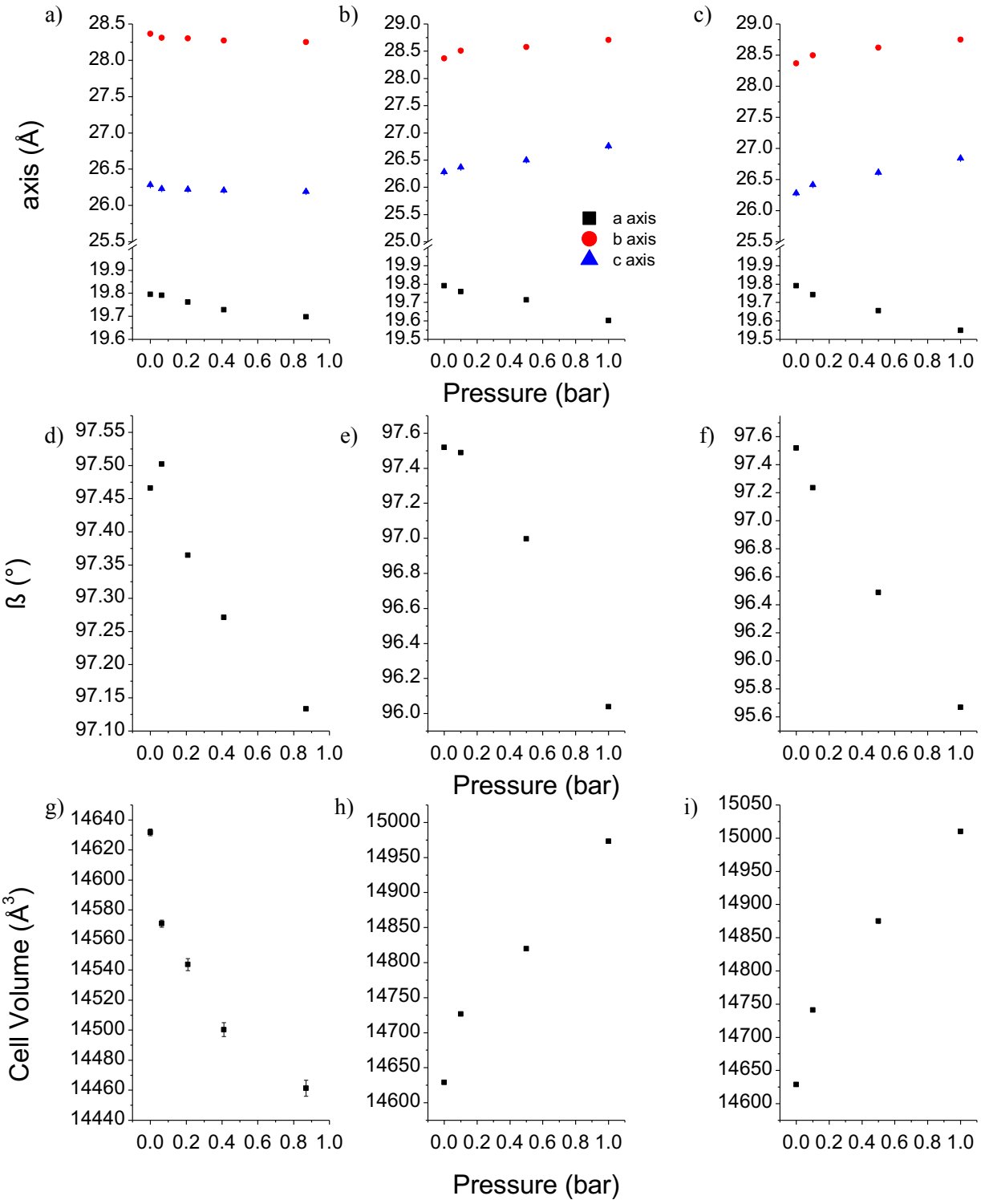



Figure 2.23 Modulation of unit cell parameters with different $C_2$s adsorption loadings for MFM-202a at 195 K. a), d), g): $C_2H_2$-loaded; b), e), h): $C_2H_4$-loaded; c), f), i): $C_2H_6$-loaded.

## 2.4 Experimental section

### 2.4.1 Materials and techniques

All reagents and solvents were used as received from commercial sources without further purification. MFM-202 was prepared using previously reported method.[9] The acetone-exchanged sample of MFM-202 was activated at 323 K and $10^{-7}$ mbar for approximately 1 day to remove the free solvents in the pore and hydrocarbon ($CH_4$, $C_2H_2$, $C_2H_4$, $C_2H_6$, $C_3H_6$ and $C_3H_8$) adsorption measurements were then carried out on an IGA-003 system (supplied by Hiden Isochema Ltd, Warrington, UK) at the University of Manchester under ultra-high vacuum from a diaphragm and turbo pumping system. The gas adsorption temperature was controlled by a water bath (for the measurements at 273−303 K), acetone-dry ice bath (for the 195 K measurements) and acetonitrile-dry ice bath (for the 201 K measurement) in separate experiments. All the hydrocarbons ($CH_4$, $C_2H_4$, $C_2H_6$, $C_3H_6$ and $C_3H_8$) except from $C_2H_2$ used for adsorption were ultra-pure research grade (> 99.99%) purchased from BOC or Air Liquide. $C_2H_2$ was purified by dual-stage cold trap systems and an activated carbon filter to remove acetone before use. The density of the desolvated MFM-202a sample used in buoyancy corrections was 1.70 g $cm^{-3}$, as estimated from the crystallographic density of the desolvated sample derived from PLATON/SOLV results.[10] The equimolar binary gases adsorption measurements were performed on the IGA system equipped with multiple identical mass flow controllers enabling mixing two different gas components to an equimolar mixture in this work. All gravimetric gas sorption data carried out and exported from IGA system have been processed using Origin 8 and Matlab_R 2014b.

### 2.4.2 *In situ* PXRD experiments

The *in situ* PXRD experiments as a function of $C_2$ hydrocarbons loadings were carried out using high-resolution synchrotron X-ray diffraction ($\lambda$ = 0.825774 Å) at Beamline I11, Diamond Light Source (Oxford, UK). The acetone-exchanged sample was gently ground and transferred into capillary gas cell and the temperature was controlled. Desolvated MFM-202a was prepared by heating the sample *in situ* at 313 K under vacuum overnight. The $C_2H_2$ was loaded first and the resultant PXRD measured at 0, 64, 209, 410 and 870 mbar loadings and then the sample was degassed in vacuum. $C_2H_4$ and $C_2H_6$ were

then loaded in sequence and the corresponding PXRD were measured at 0, 100, 500 and 1000 mbar loadings. The PXRD data and Le Bail refinements were analysed *via* TOPAS software programme.

### 2.4.3 Calculation of the isosteric heats of adsorption and entropy

The Clausius-Clapeyron equation (equation 1) was used to calculate the isosteric heats of adsorption ($Q_{st}$) and adsorption entropy ($\Delta S$), for each hydrocarbon and MFM-202a, using the isotherms carried out at 273−303 K.

$$\ln(P)_n = -\frac{Q_{st}}{R}\left(\frac{1}{T}\right) - \frac{\Delta S}{R} \quad (1)$$

Here, $P$ is the pressure (Pascal), $n$ is the amount absorbed (mmol $g^{-1}$), $T$ is the temperature (K), $R$ is the universal gas constant (J $mol^{-1}$ $K^{-1}$). The $Q_{st}$ and $\Delta S$ are obtained from the slope and intercept of the plots of $\ln(P)_n$ as a function of $1/T$.

### 2.4.4 Calculation of selectivity

The selectivity was analysed using Ideal Adsorption Solution Theory (IAST), which was developed by Myers and Prausnitz, and has been widely used to evaluate each component adsorption amount in a mixture from the single component isotherms.[2] The theory hypothesises that the adsorbed gases form an ideal solution and therefore the method is applicable at relatively low pressures and surface coverages. It uses spreading pressure to characterise the adsorbed phase and assumes that the adsorbent structure is thermodynamically inert, with its surface area being independent of the adsorbate. The pure component isotherms must be measured extremely accurately at low surface coverage because the integration to obtain spreading pressure is sensitive to this part of the isotherm. This is particularly critical for components in low gas phase concentrations.

The IAST calculations for binary mixture were carried out by the following methods. First, the measured isotherms of the pure components are non-linear fitted to appropriate equations to provide a mathematical simulation for every isotherm. Previous studies generally adopt the Langmuir and/or dual-site Langmuir Freundlich equations to describe the isotherms for the pure components.[1] These equations

are then integrated to obtain the spreading pressure as a function of amount adsorbed for each component. Alternatively and innovatively, the spreading pressures can be obtained as a function of the amount adsorbed by direct numerical trapezoidal integration of the isotherm data for the pure components. The amounts adsorbed for mixtures and gas pressures are then calculated for specific spreading pressures with the estimation of selectivity data.

In this work, the binary mixed gases isotherms were calculated by two methods using dual-site Langmuir-Freundlich (DSLF) method and Numerical Integration (NI) method combined with IAST theory.[2] DSLF is a frequently used model to fit the isotherms, which adopts the least square errors to estimate the overall error and finally gives six parameters that determine the sorption profile with the minimum residual sum of squares. The equation for DSLF[17] is given as:

$$N = P_1 \times \frac{P_2 x^{P3}}{1 + P_2 x^{p3}} + Q_1 \times \frac{Q_2 x^{Q3}}{1 + Q_2 x^{Q3}} \quad (2)$$

where $x$ is the pressure of the pure gas at equilibrium with the adsorbed phase (kPa), $N$ is the gas amount adsorbed per gram of adsorbent (mmol $g^{-1}$), $P_1$ and $Q_1$ are the simulated saturation capacities of sites $P$ and $Q$ (mmol $g^{-1}$), $P_2$ and $Q_2$ are the simulated affinity coefficients of sites $P$ and $Q$ ($kPa^{-1}$) and $\frac{1}{P3}$ and $\frac{1}{Q3}$ represent deviations from an ideal homogeneous surface. The fitted parameters were then used to predict multi-component adsorption using IAST.[2]

The parameters of DSLF fitting equation used for the IAST calculation of selectivity from the individual pure gas isotherms are listed in Table 2.12. Since the sum of the first ($P_1$) and fourth ($Q_1$) parameters (the dual binding sites) of equation (2) (Table 2.13 are relevant to the total saturated uptake, a precise estimation of these two values before applying free DSLF fitting is required. Moreover, if assigning different initial values for the six parameters, the fitted parameters may vary to some extent as shown in Table 2.13. In particular, for near-linear sorption isotherms, it is difficult to predict the knee point and the saturated adsorption capacity of the gas, and thus DSLF may not give accurate fitting parameters

and often associated with large errors in least-square fitting, which indicates the inaccuracy of the fitting and more trials are required.

The equation for the calculation of selectivity (*S*) between gas 1 and gas 2 is shown as:

$$S = \frac{x_1 / y_1}{x_2 / y_2} \quad (3)$$

where $x_i$ and $y_i$ are the mole fractions of component *i* in the adsorbed and gas phase, respectively, and *i* equals 1 or 2. In this work, selectivities for equimolar binary gases of $C_2H_2/CH_4$, $C_2H_4/CH_4$, $C_2H_6/CH_4$, $C_3H_6/CH_4$, $C_3H_8/CH_4$, $C_2H_6/C_2H_4$, $C_3H_6/C_2H_4$ and $C_3H_8/C_2H_6$ have been calculated for MFM-202a at ambient conditions (293 K and up to 1 bar).

The other method used in this work, NI, is adopted as a second means to simulate the uptake of binary gases. The application of NI method in predicting binary mixture isotherms or selectivity data precludes the uncertainty originating from the use of a certain type of adsorption model (*e.g.*, the Langmuir model). The predicted binary mixture isotherm was obtained by the numerical trapezoidal integration of the appropriate graph from each pure gas adsorption isotherm. The limits for the calculation of the spreading pressures were generated from the limits for the pure component experimental isotherms and the gas phase concentrations in the mixture. It is worth mentioning that the IAST method becomes less accurate when a) the host material surfaces contain strong binding sites and/or b) the two gases show significantly different sorption capacities.

The discrepancies of predicted selectivity values based upon DSLF-IAST and NI-IAST methods were calculated by the equation:

$$y = \frac{x_1 - x_2}{x_2} \times 100\% \quad (4)$$

where *y* is the discrepancy, $x_1$ and $x_2$ are the uptake amounts for the experimental measurement and IAST prediction (mmol $g^{-1}$), respectively, at specific pressure and temperature.

Table 2.12 The parameters for dual-site Langmuir fitting model of pure hydrocarbon sorption isotherms for MFM-202 at 293 K.

| Gas | P1 | P2 | P3 | Q1 | Q2 | Q3 | Residual | Adj. R- |
|---|---|---|---|---|---|---|---|---|
| $CH_4$ | 17.56423 | 0.06075 | 1.05913 | -6.94247 | 0.08702 | 1.14393 | 7.87E-04 | 0.99999 |
| Error | 49.70406 | 0.04361 | 0.1187 | 50.28355 | 0.08501 | 0.32964 | | |
| $C_2H_2$ | 11.37632 | 0.17115 | 1.77653 | 3.77606 | 0.89162 | 0.90693 | 1.06E-04 | 1 |
| Error | 21.61448 | 0.11021 | 1.09126 | 9.82877 | 2.234 | 0.01973 | | |
| $C_2H_4$ | 8.81584 | 0.33582 | 0.95398 | 3.36454 | 0.25312 | 2.05427 | 2.88E-05 | 1 |
| Error | 65.34024 | 2.49745 | 0.01109 | 25.89433 | 0.52758 | 2.39846 | | |
| $C_2H_6$ | 7.70646 | 0.65389 | 1.04283 | 2.3577 | 0.96226 | 2.81792 | 0.00124 | 1 |
| Error | 0.07377 | 0.00457 | 0.00772 | 0.08342 | 0.00875 | 0.05343 | | |
| $C_3H_6$ | 5.56095 | 4.54007 | 0.96421 | 2.61777 | 1184.235 | 3.30151 | 0.00151 | 0.99999 |
| Error | 0.04827 | 0.17239 | 0.0115 | 0.06691 | 164.2644 | 0.0629 | | |
| $C_3H_8$ | 2.81083 | 4592.979 | 3.34302 | 4.8745 | 4.19367 | 0.85426 | 0.00458 | 0.99996 |
| Error | 0.14457 | 1610.119 | 0.13676 | 0.07281 | 0.52108 | 0.0313 | | |

Table 2.13 $C_2H_6$ fitting by DSLF method for various initial values.

| | Initial value | Dual-site value | Dual-site error | Initial values | Dual-site value | Dual-site error | Initial value | Dual-site value | Dual-site error |
|---|---|---|---|---|---|---|---|---|---|
| P1 | 6 | 7.70646 | 0.07377 | 5.4 | 7.70647 | 0.07377 | 6.6 | 7.70629 | 0.07378 |
| P2 | 2 | 0.65389 | 0.00457 | 2 | 0.65389 | 0.00457 | 2 | 0.65389 | 0.00457 |
| P3 | 1 | 1.04283 | 0.00772 | 1 | 1.04283 | 0.00772 | 1 | 1.04281 | 0.00773 |
| Q1 | 4 | 2.3577 | 0.08342 | 4 | 2.35769 | 0.08342 | 4 | 2.35789 | 0.08342 |
| Q2 | 2 | 0.96226 | 0.00875 | 2 | 0.96226 | 0.00875 | 2 | 0.96225 | 0.00875 |
| Q3 | 1 | 2.81792 | 0.05343 | 1 | 2.81792 | 0.05343 | 1 | 2.8178 | 0.05343 |
| Residual sum of squares | 0.00124 | | | 0.00124 | | | 0.00124 | | |
| Adj. R-Square | 1 | | | 1 | | | 1 | | |
| P1 | 6 | 7.70646 | 0.07377 | 6 | 7.70638 | 0.07378 | 6 | 7.70638 | 0.07378 |
| P2 | 1.8 | 0.65389 | 0.00457 | 2.2 | 0.65389 | 0.00457 | 2 | 0.65389 | 0.00457 |
| P3 | 1 | 1.04283 | 0.00772 | 1 | 1.04282 | 0.00773 | 0.9 | 1.04282 | 0.00773 |
| Q1 | 4 | 2.3577 | 0.08342 | 4 | 2.3578 | 0.08342 | 4 | 2.3578 | 0.08342 |
| Q2 | 2 | 0.96226 | 0.00875 | 2 | 0.96226 | 0.00875 | 2 | 0.96226 | 0.00875 |
| Q3 | 1 | 2.81792 | 0.05343 | 1 | 2.81786 | 0.05343 | 1 | 2.81786 | 0.05343 |
| Residual sum of squares | 0.00124 | | | 0.00124 | | | 0.00124 | | |
| Adj. R-Square | 1 | | | 1 | | | 1 | | |
| P1 | 6 | 7.70638 | 0.07378 | 6 | 7.70637 | 0.07378 | 6 | 7.70646 | 0.07377 |
| P2 | 2 | 0.65389 | 0.00457 | 2 | 0.65389 | 0.00457 | 2 | 0.65389 | 0.00457 |
| P3 | 1.1 | 1.04282 | 0.00773 | 1 | 1.04282 | 0.00773 | 1 | 1.04283 | 0.00772 |
| Q1 | 4 | 2.35779 | 0.08342 | 4.4 | 2.35781 | 0.08342 | 3 | 2.3577 | 0.08342 |
| Q2 | 2 | 0.96226 | 0.00875 | 2 | 0.96226 | 0.00875 | 1.8 | 0.96226 | 0.00875 |
| Q3 | 1 | 2.81786 | 0.05343 | 1 | 2.81785 | 0.05343 | 1 | 2.81792 | 0.05343 |
| Residual sum of squares | 0.00124 | | | 0.00124 | | | 0.00124 | | |

| | | | | | | | | | |
|---|---|---|---|---|---|---|---|---|---|
| Adj. R-Square | 1 | | | 1 | | | 1 | | |
| P1 | 12 | 9.66982 | 3.12865 | 9 | 9.5705 | 0.09133 | 8 | 2.35793 | 0.08342 |
| P2 | 2 | 0.75918 | 0.13602 | 2 | 0.77397 | 0.01817 | 2 | 0.96225 | 0.00875 |
| P3 | 1 | 1.34515 | 0.14997 | 1 | 1.3584 | 0.02195 | 1 | 2.81777 | 0.05343 |
| Q1 | 4 | 6.75365 | 30097. | 4 | 0.07477 | 0.11736 | 2 | 7.70626 | 0.07378 |
| Q2 | 2 | -7.44E-04 | 3.42217 | 2 | 2.83E-14 | 1.63E-11 | 2 | 0.65388 | 0.00457 |
| Q3 | 1 | 1.00629 | 71.09771 | 1 | 14.54597 | 269.798 | 1 | 1.04281 | 0.00773 |
| Residual sum of squares | 0.23033 | | | 0.22684 | | | 0.00124 | | |
| Adj. R-Square | 0.99944 | | | 0.99945 | | | 1 | | |
| P1 | 7 | 7.70626 | 0.07378 | 5 | 4.80729 | -- | | | |
| P2 | 2 | 0.65388 | 0.00457 | 2 | 0.76603 | 535047.2261 | | | |
| P3 | 1 | 1.04281 | 0.00773 | 1 | 1.35011 | 1.51E+06 | | | |
| Q1 | 3 | 2.35793 | 0.08342 | 5 | 4.80729 | -- | | | |
| Q2 | 2 | 0.96225 | 0.00875 | 2 | 0.76603 | 535047.2261 | | | |
| Q3 | 1 | 2.81777 | 0.05343 | 1 | 1.35011 | 1.51E+06 | | | |
| Residual sum of squares | 0.00124 | | | 0.23072 | | | | | |
| Adj. R-Square | 1 | | | 0.99944 | | | | | |

## 2.5 Conclusions

The isotherms of a variety of small hydrocarbons have been measured for MFM-202a at both 273−303 K and low temperature (~195 K). At low temperature, MFM-202a exhibits the highest uptake of $C_2H_2$ among the reported MOFs, which is also associated with a stepwise sorption profile and broad hysteretic desorption process. This is useful for practical gas storage since it allows the $C_2H_2$ to be adsorbed at high pressure, but stored at relatively low pressure, and thus reducing the chance of accidents in terms of transportation and storage. The other two unsaturated hydrocarbons $C_2H_4$ and $C_3H_6$ exhibit smaller hysteresis loops than $C_2H_2$. In contrast, the saturated hydrocarbons of $CH_4$, $C_2H_6$ and $C_3H_8$ show fully reversible sorption/desorption at low temperature. *In situ* PXRD experiments have been carried out and show peak shifts at various gas loadings, confirming that small structural contraction and expansion were induced with the loadings of $C_2$s, but with no significant phase change. Moreover, the structure was intact after desorption of the three $C_2$s evidenced by good agreement of the PXRD patterns of MFM-202a before loading and after degassing, indicating a fully repeatable process of $C_2$s adsorption at low temperature.

MFM-202a shows high adsorption capacities for $C_3$s and moderate capacities for $C_2$s and $CH_4$ compared with other MOFs at 293 K. The adsorption of equimolar binary mixtures of light hydrocarbons have been analysed at 293 K. The NI-IAST and DSLF-IAST predictions both show good agreements with the experimental equimolar binary mixtures of light hydrocarbons within the spreading pressure range. For two isotherms with significant difference in the uptake capacity, only DSLF-IAST has been applied for the prediction of binary mixture uptakes. Generally, it shows good agreement with the experimental measurements at low pressure. However, at very high pressure range which is further away from the spreading pressure, gross errors with DSLF-IAST can be generated, which is evidenced from the comparison of $CH_4/C_2H_6$ calculation and experimental measurements at 293 K.

## References

1. Bloch, E. D.; Queen, W. L.; Krishna, R.; Zadrozny, J. M.; Brown, C. M.; Long, J. R. Hydrocarbon separations in a metal-organic framework with open iron(II) coordination sites. *Science*. **2012**, *335*, 1606−1610.

2. Myers, A. L.; Prausnitz, J. M. Thermodynamics of mixed-gas adsorption. *AIChE J.* **1965**, *11*, 121−127.

3. Gutiérrez-Sevukkabi, J. J.; Dubbeldam, D.; Rey, F.; Valencia, S.; Palomino, M.; Martín-Calvo, A. and Calero, Sofía. Analysis of the ITQ-12 zeolite performance in propane−propylene separations using a combination of experiments and molecular simulations. *J. Phys. Chem. C*. **2010**, *114*, 14907–14914.

4. Geier, S. J.; Mason, J. A.; Bloch, E. D.; Queen, W. L.; Hudson, M. R.; Brown, C. M.; Long, J. R. Selective adsorption of ethylene over ethane and propylene over propane in the metal-organic frameworks $M_2$(dobdc) (M = Mg, Mn, Fe, Co, Ni, Zn). *Chem. Sci.* **2013**, *4*, 2054–2061.

5. Webster, C. E.; Zerner, M.; Drago R. S. A multiple-process equilibrium analysis of ailica gel and HZSM-5. *J. Am. Chem. Soc*. **1998**, *120*, 538−547.

6. Trung, T. K.; Trens, P.; Tanchoux, N.; Bourrelly, S.; Llewellyn, P. L.; Loera-Serna, S.; Serre, C.; Loiseau, T.; Fajula, F. and Férey, G. Hydrocarbon adsorption in the flexible metal organic frameworks MIL-53(Al, Cr). *J. Am. Chem. Soc.* **2008**, *130*, 16926–16932.

7. Férey, G; Latroche, M.; Serre, C.; Millange, F.; Loiseau, T. and Percheron-Guégan, A. Hydrogen adsorption in the nanoporous metal-benzenedicarboxylate M(OH)($O_2C$–$C_6H_4$–$CO_2$) (M = $Al^{3+}$, $Cr^{3+}$), MIL-53. *Chem. Commun.* **2003**, 2976–2977.

8. Gao, S.; Morris, C. G.; Lu, Z.; Yan, Y.; Godfrey, H. G. W.; Murray, C.; Tang, C. C.; Thomas, K. M., Yang, S. and Schröder, M. Selective hysteretic sorption of light hydrocarbons in a flexible metal−organic framework material. *Chem. Mater.* **2016**, *28*, 2331–2340.

9. Yang, S.; Lin, X.; Lewis, W.; Suyetin, M.; Bichoutskaia, E.; Parker, J. E.; Tang, C. C.; Allan, D. R.; Rizkallah, P. J.; Hubberstey, P.; Champness, N. R.; Thomas, K. M.; Blake, A. J.; Schröder, M. A partially interpenetrated metal-organic framework for selective hysteretic sorption of carbon dioxide. *Nature Mater.* **2012**, *11*, 710−716.

10. Spek, A. L. Single-crystal structure validation with the program PLATON. *J. Appl. Crystallogr*. **2003**, *36*, 7−13.

11. Yang, S.; R-Cuesta, A. J.; Newby, R.; Garcia-Sakai, V.; Manuel, P.; Callear, S. K.; Campbell, S. I.; Tang, C. C.; Schröder, M. Supramolecular binding and separation of hydrocarbons within a functionalized porous metal-organic framework. *Nature Chem.* **2015**, *7*, 121–129.

12. Yan, Y.; Juríček, M.; Couder, F.-X.; Vermeulen, N. A.; Grunder, S.; Dailly, A.; Lewis, W.; Blake, A. J.; Stoddart, J. F.; Schröder, M. Non-interpenetrated metal-organic frameworks based on copper(II) paddlewheel and oligoparaxylene-isophthalate linkers: synthesis, structure, and gas adsorption. *J. Am. Chem. Soc.* **2016**, *138*, 3371–3381.

13. Cui, Y.; Li, B.; He, H.; Zhou, W.; Chen, B. and Qian, G. Metal−organic frameworks as platforms for functional materials. *Acc. Chem. Res.* **2016**, *49*, 483–493.

14. Llewellym, P. L.; Horcajada, P.; Maurin, G.; Devic, T.; Rosenbach, N.; Bourrelly, S.; Serre, C.; Vincent, D.; Loera-Serna, S.; Filinchuk, Y. and Férey, G. Complex adsorption of short linear alkanes in the flexible metal-organic-framework MIL-53(Fe). *J. Am. Chem. Soc.* **2009**, *131*, 13002–13008.

15. Li, B.; Zhang, Y.; Krishna, R.; Yao, K.; Han, Y.; Wu, Z.; Ma, D.; Shi, Z.; Pham, T.; Space, B.; Liu, J.; Thallapally, P. K.; Liu, J.; Chrzanowski, M.; Ma, S. Introduction of π‑complexation into porous aromatic framework for highly selective adsorption of ethylene over ethane. *J. Am. Chem. Soc*. **2014**, *136*, 8654–8660.

16. He, Y.; Zhang, Z.; Xiang, S.; Fronczek, F. R.; Krishna, R.; Chen, B. A robust doubly interpenetrated metal-organic framework constructed from a novel aromatic tricarboxylate for highly selective separation of small hydrocarbons. *Chem. Commun*. **2012**, *48*, 6493–6495.

17. Liu, K.; Ma, D.; Li, B.; Li, Y.; Yao, K.; Zhang, Z.; Han, Y.; Shi, Z. High storage capacity and separation selectivity for $C_2$ hydrocarbons over methane in the metal-organic framework Cu-TDPAT. *J. Mater. Chem. A*. **2014**, *2*, 15823–15828.

18. Xiang, S.; Zhou, W.; Gallegos, J. M.; Liu, Y.; Chen, B. Exceptionally high acetylene uptake in a microporous metal-organic framework with open metal sites. *J. Am. Chem. Soc*. **2009**, *131*, 12415–12419.

19. Wang, H.; Li, B.; Wu, H.; Hu, T.; Yao, Z.; Zhou, W.; Xiang, S.; Chen, B.; A flexible microporous hydrogen-bonded organic framework for gas sorption and separation. *J. Am. Chem. Soc*. **2015**, *137*, 9963–9970.

20. Xiang, S.; Zhang, Z.; Zhao, C.; Hong, K.; Zhao, X.; Ding, D.; Xie, M.; Wu, C.; Das, M.; Gill, R.; Thomas, K. M.; Chen, B. Rationally tuned micropores within enantiopure metal-organic frameworks for highly selective separation of acetylene and ethylene. *Nat. Commun*. **2011**, *2*, 1–7.

21. Yang, S.; Liu, L.; Sun, J.; Thomas, K. M.; Davies, A. J.; George, M. W.; Blake, A. J.; Hill, A. H.; Fitch, A. N.; Tang, C. C.; Schröder, M. Irreversible network transformation in a dynamic porous host catalyzed by sulfur dioxide. *J. Am. Chem. Soc.* **2013**, *135*, 4954–4957.

22. Wang, H.; Li, B.; Wu, H.; Hu, T.; Yao, Z.; Zhou, W.; Xiang, S.; Chen, B.; A flexible microporous hydrogen-bonded organic framework for gas sorption and separation. *J. Am. Chem. Soc*. **2015**, *137*, 9963–9970.

23. Gücüyener, C.; Bergh, J. van den.; Gascon, J.; Kateijn, F. Ethane/ethene separation turned on its head: selective ethane adsorption on the metal-organic framework ZIF-7 through a gate-opening mechanism. *J. Am. Chem. Soc.* **2010**, *132*, 17704–17706.

24. Henke, S.; Schneemann, A.; Wütscher, A.; Fischer, R. A. Directing the breathing behavior of pillared-layered metal-organic frameworks via a systematic library of functionalized linkers bearing flexible substituents. *J. Am. Chem. Soc*. **2012**, *134*, 9464–9474.

# Chapter 3 *In situ* PXRD studies for $NH_3$-loaded MFM-202a

## 3.1 Introduction

### 3.1.1 $NH_3$ sorption

Ammonia is generally produced by the reaction of hydrogen and nitrogen under high pressure in an ammonia converter. It has been considered as a very important industrial chemical and is used widely in both its pure form and as a feedstock for the production of a variety of other chemicals as shown in Figure 3.1. For instance, ammonia itself can be used as a fertiliser, household/industrial alkaline cleanser/detergent, industrial refrigerant gas and lifting gas (as it has a lower density than air); or used to produce nitric acid and cyanides (for the manufacture of other ammoniac fertilisers such as ammonium sulphate and ammonium nitrate). The annual mass output of $NH_3$ ranks second and is only behind sulfuric acid in the chemicals production over the world. However, ammonia is a corrosive and toxic chemical and is difficult to handle when transported or stored as a compressed liquid which can cause severe problems in an accident.[1] In 2010, an explosion occurred in a 65 L cylinder holding ammonia which was contaminated with another product in Laverton North, Victoria, Australia.[2] In 2014, an ammonia pipeline in a freezing and drying workshop in a food processing plant leaked and dozens of people were poisoned by inhaling the toxic gas in Harbin, China.[3] Anhydrous ammonia is regulated as a hazardous material by the United States Department of Transportation. The explosive limit of $NH_3$ gas is 16–25%.[4]

Currently the transportation of anhydrous ammonia involves pipelines, pressure tanks and refrigerated barges. The main problem is the risk of violent and toxic leaking if the container is damaged; anhydrous ammonia is usually stored in a highly pressurised state and the only protection is the container. To overcome this problem and minimize the hazard in case of dangerous leakage, many research groups in the world have started the investigation of the application of porous materials as a physical medium to adsorb this toxic and corrosive gas. By doing this, ammonia could be adsorbed and immobilized, with very slow release in case of the damage of the container. The porous materials that have been studied as an alternative to store ammonia by physical/chemical adsorption include zeolites, amberlysts, COFs

and MOFs.[1,5-12] For example, Yaghi's group have synthesised COF-10, which is constructed from hexahydroxytriphenylene and biphenyldiboroic acid building units that are connected into hexagonal layers. These boron sites in COF-10 are ready to interact with ammonia molecules in a Lewis acid-base manner as shown in Figure 3.2. Comparing its $NH_3$ uptake with other porous materials, such as zeolite 13X (9 mmol $g^{-1}$), amberlyst 15 (11 mmol $g^{-1}$) and MCM-41 (7.9 mmol $g^{-1}$), COF-10 shows much higher adsorption capacity of 15 mmol $g^{-1}$ at 298 K and 760 torr (1.01325 bar or 1 atm). In terms of the reproducibility, they also carried out the measurements for three successive cycles. Their results show that this material has a decreased uptake capacity after each sorption cycle. Between the first and third cycle, the uptake shows a decrease of 4.5%. By comparing the PXRD patterns of the as-synthesised sample and the sample after each ammonia uptake cycle, they concluded that there is an increasing disorder in packing between layers.[1]

Up to now, a series of MOFs have been reported for the application of $NH_3$ storage, for example, MOF-5, MOF-177, IRMOF-3 and M-MOF-74 (M: Zn, Cu, Ni, Co and Mg), *etc.*, with the uptake capacity shown in Table 3.1.[7,11-12]

Table 3.1 Comparison of the uptakes of $NH_3$ in reported MOFs.

| MOFs | Ammonia uptake (mmol $g^{-1}$) | Ref. |
|---|---|---|
| MOF-5 | 12.2 | 11 |
| MOF-177 | 12.2 | 11 |
| Zn-MOF-74 | 5.7 | 7 |
| Cu-BTC | 5.1 | 7 |
| DUT-6 | 12.0 | 12 |
| DUT-6 (OH) | 16.4 | 12 |

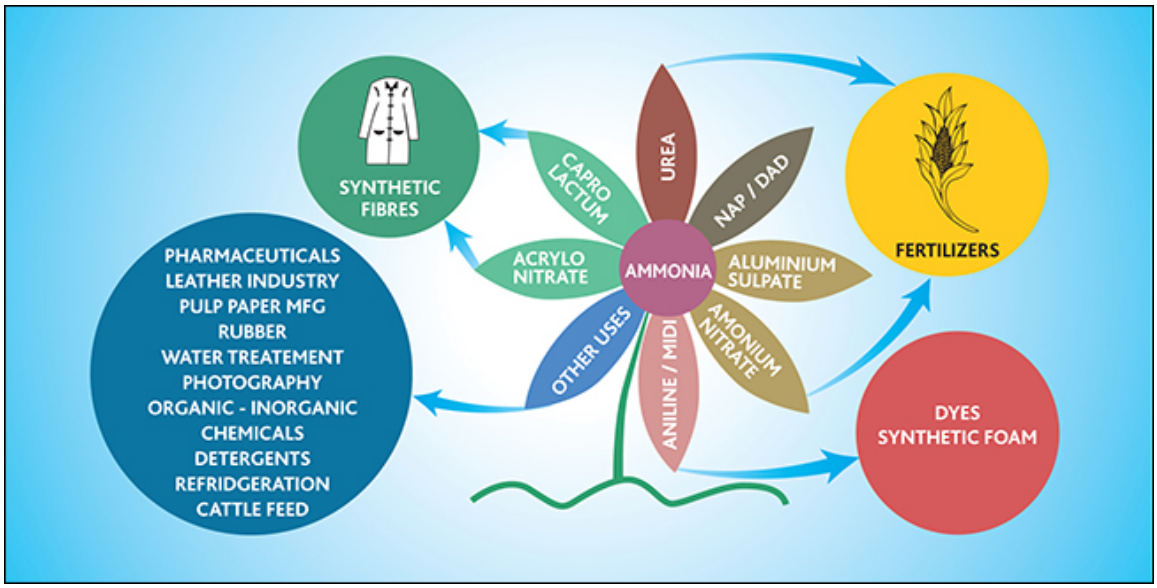



Figure 3.1 Uses of ammonia. Reproduced from http://www.gpic.com/products/Ammonia/.

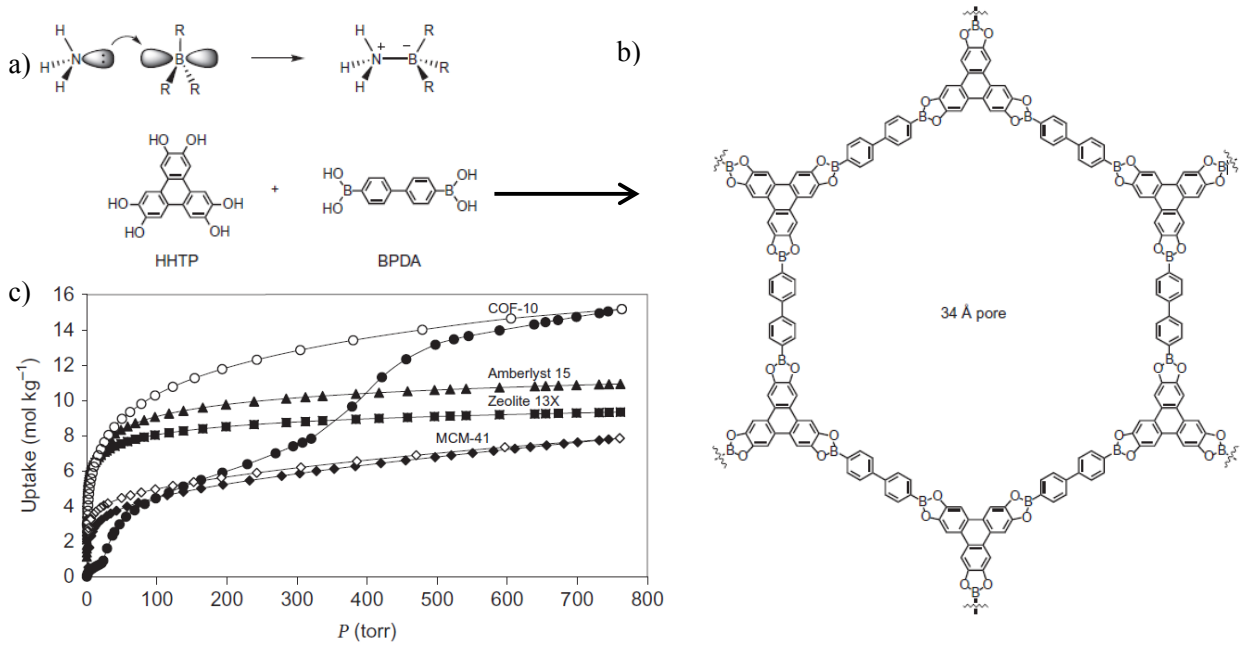



Figure 3.2 a) Ammonia-boron interactions in COF-10. b) Schematic representation of COF-10 showing its building blocks. c) Ammonia uptake in state-of-the-art materials. Figures reproduced form Ref. 1.

### 3.1.2 *In situ* PXRD studies of gas induced structural flexibility and phase change for MFM-202a with hysteretic isotherms

#### 3.1.2.1 Hysteretic uptake of $CO_2$ and *in situ* PXRD investigation

MFM-202a has been reported to exhibit a three-step $CO_2$ adsorption profile and hysteretic desorption isotherm at 195 K below 1 bar as shown in Figure 3.3a in blue triangles.[13] This rare phenomenon in MFM-202a has been found to be highly temperature-dependent and especially sensitive to the triple point (216.7 K and 5.1 bar) of $CO_2$. In other words, the isotherms carried out between 195 K and 213 K show hysteresis to different extent; however, the isotherms measured between 221 K and 303 K show complete reversible sorption/desorption profiles without any absorption steps or hysteretic loops as shown in Figure 3.3a. Interestingly, there are no apparent adsorption steps or hysteretic loops observed at the same temperature of 195 K in the uptakes of Ar, $N_2$, $H_2$, $O_2$ and $CH_4$. To probe and gain insight into the guest-host interactions with and without stepwise uptake and hysteretic desorption, *in situ* PXRD studies were carried out at both 195 K and 273 K as shown in Figure 3.3b. The phase purity of the sample was confirmed to be pure by a good agreement of the PXRD pattern for the bare material and the simulated one from SCXRD. By dosing $CO_2$ continually at increasing pressures, shifting and splitting of all the peaks were observed, confirming some degree of flexibility of the structure upon $CO_2$ loading at 195 K. Upon desorption, all the diffraction peaks shifted in the opposite direction to that of the adsorption peaks shifts, and eventually match the pattern of the activated sample, proving a reversible structural change. In contrast, the PXRD patterns show no obvious peak shifts or splitting at different $CO_2$ loadings or unloadings during the adsorption and desorption at 273 K, suggesting an intact structure under this condition.[13]

#### 3.1.2.2 Hysteretic uptake of $SO_2$ and *in situ* PXRD investigation

MFM-202a has been further analysed for $SO_2$ adsorption at various temperatures. The first three low-temperature measurements show stepwise sorption and hysteretic desorption, while the last three isotherms at higher temperatures show good reversibility of sorption and desorption.[11] Again, to probe whether a structural change is induced by the $SO_2$ sorption or not, synchrotron PXRD patterns were recorded for the hysteretic isotherm at 273 K under vacuum (the bare sample) and at various $SO_2$ loading

pressures. Figure 3.4 shows that the desolvated (black) PXRD matches the simulated PXRD from SCXRD, which confirms the phase purity. Interestingly, unlike the changes observed by *in situ* PXRD for the stepwise sorption of $CO_2$, the sorption of $SO_2$ induces the occurrence of new diffraction peaks (blue) at an adsorption pressure of 540 mbar, suggesting the formation of new phase. Meanwhile, the original phase (MFM-202a) is not absent, indicating an incomplete phase change at this stage. From 540 mbar to 1100 mbar, the diffraction peaks for the old phase disappear gradually and peaks for the new phase retain. The sample was then desolvated under vacuum to remove the adsorbed $SO_2$ from the framework. During the desolvation, *in situ* PXRD shows that the intensity of peaks for the old phase continuously decease and after the thorough desolvation, the old phase transformed completely into the pure new phase, confirming an irreversible phase change with the catalyst of $SO_2$ at 273 K.[14]

#### 3.1.2.3 Hysteretic uptakes of unsaturated hydrocarbons and *in situ* PXRD investigations

Apart from the stepwise sorption and hysteretic desorption isotherms of $CO_2$ and $SO_2$ uptakes, which trigger structural flexibility and phase change as shown by *in situ* PXRD, unsaturated hydrocarbons such as $C_2H_2$ and $C_2H_4$ also exhibit similar hysteretic isotherms at 195 K, as shown in Figure 3.5a (See chapter II for more details).[15] In contrast, $C_2H_6$ sorption shows a fully reversible type I isotherm at 195 K. To probe the structure upon the adsorption of $C_2$ hydrocarbons, *in situ* PXRD were carried out at 195 K. Interestingly, the $C_2H_2$ isotherm with obviously broad hysteresis is correlated to an "intact" structure state of MFM-202a, confirmed by the nearly unchanged diffraction peak positions of *in situ* PXRD patterns at various loading pressures and regeneration at 195 K. In contrast, the $C_2H_4$ isotherm with a much smaller hysteretic loop and the $C_2H_6$ isotherm without any hysteresis both correspond to a flexible structural disturbance upon the loadings at 195 K, confirmed by larger peak shifts in the PXRD than those loaded with $C_2H_2$ as shown in Figure 3.5b.[15]

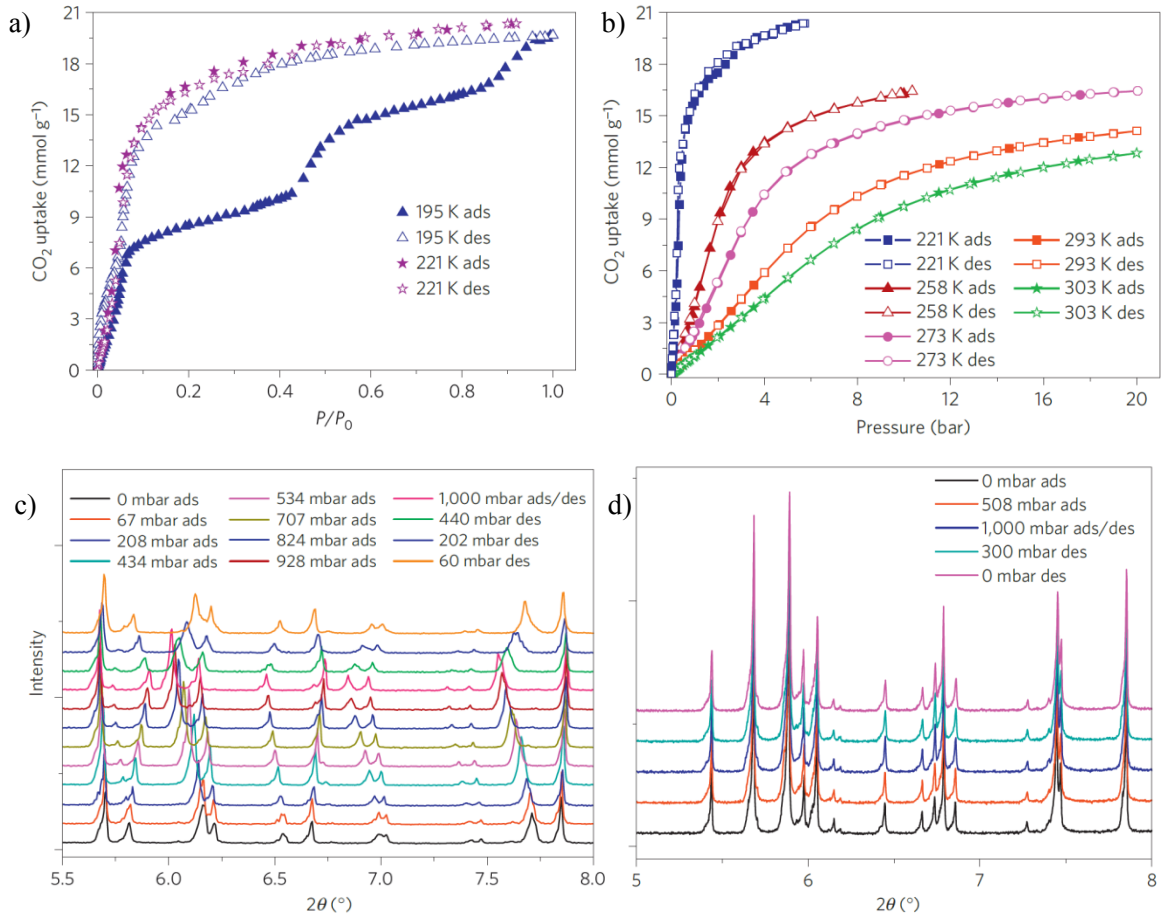



Figure 3.3 $CO_2$ uptake isotherms and *in situ* PXRD patterns of MFM-202a. $CO_2$ sorption isotherms at 195 and 221 K (a) and various temperatures between 221 and 303 K (b); comparison of *in situ* high resolution PXRD patterns for MFM-202a as a function of different $CO_2$ loading and unloading pressures at 195 K (c) and 273 K (d), $\lambda = 0.82695$ Å (Data collected at Diamond Light Source Beamline I11 using multi-analysing crystal-detectors (MACs) and monochromatic radiation. The *in situ* PXRD measurements were carried out in capillary mode and the temperature controlled by an Oxford Cryosystems open-flow nitrogen gas cryostat). Reproduced from Ref. 13.

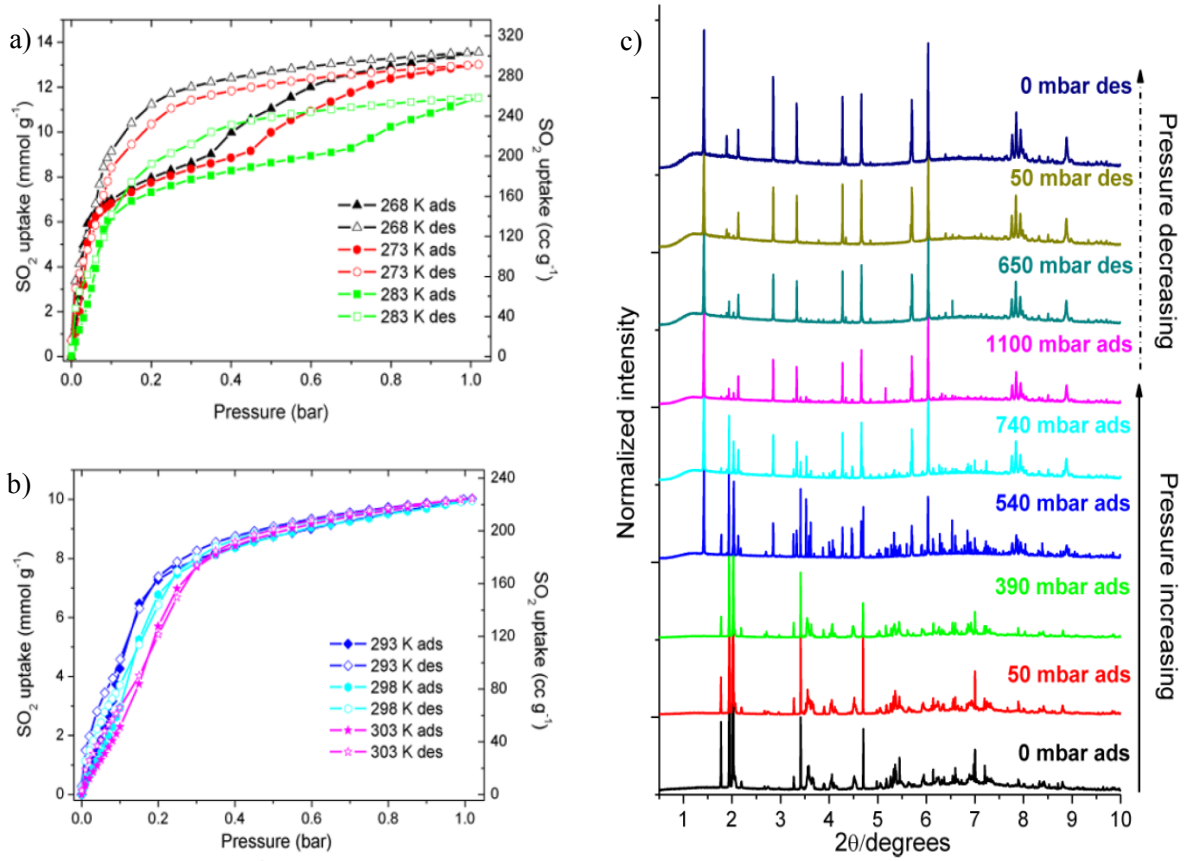



Figure 3.4 $SO_2$ uptake isotherms and *in situ* PXRD patterns of MFM-202a. $SO_2$ sorption isotherms at various temperatures between 268 K and 283 K below 1.1 bar (a) and between 293 K and 303 K below 1.1 bar (b); c) comparison of *in situ* high resolution PXRD patterns for MFM-202a as a function of different $SO_2$ loading (solid black arrow) and unloading pressures (dashed black arrow) at 273 K, $\lambda$ = 0.49581 Å (Data collected at ESRF Beamline ID31 using monochromatic radiation. The *in situ* PXRD measurements were carried out in capillary mode and the temperature controlled by an Oxford Cryosystems open-flow nitrogen gas cryostat). Reproduced from Ref. 14.

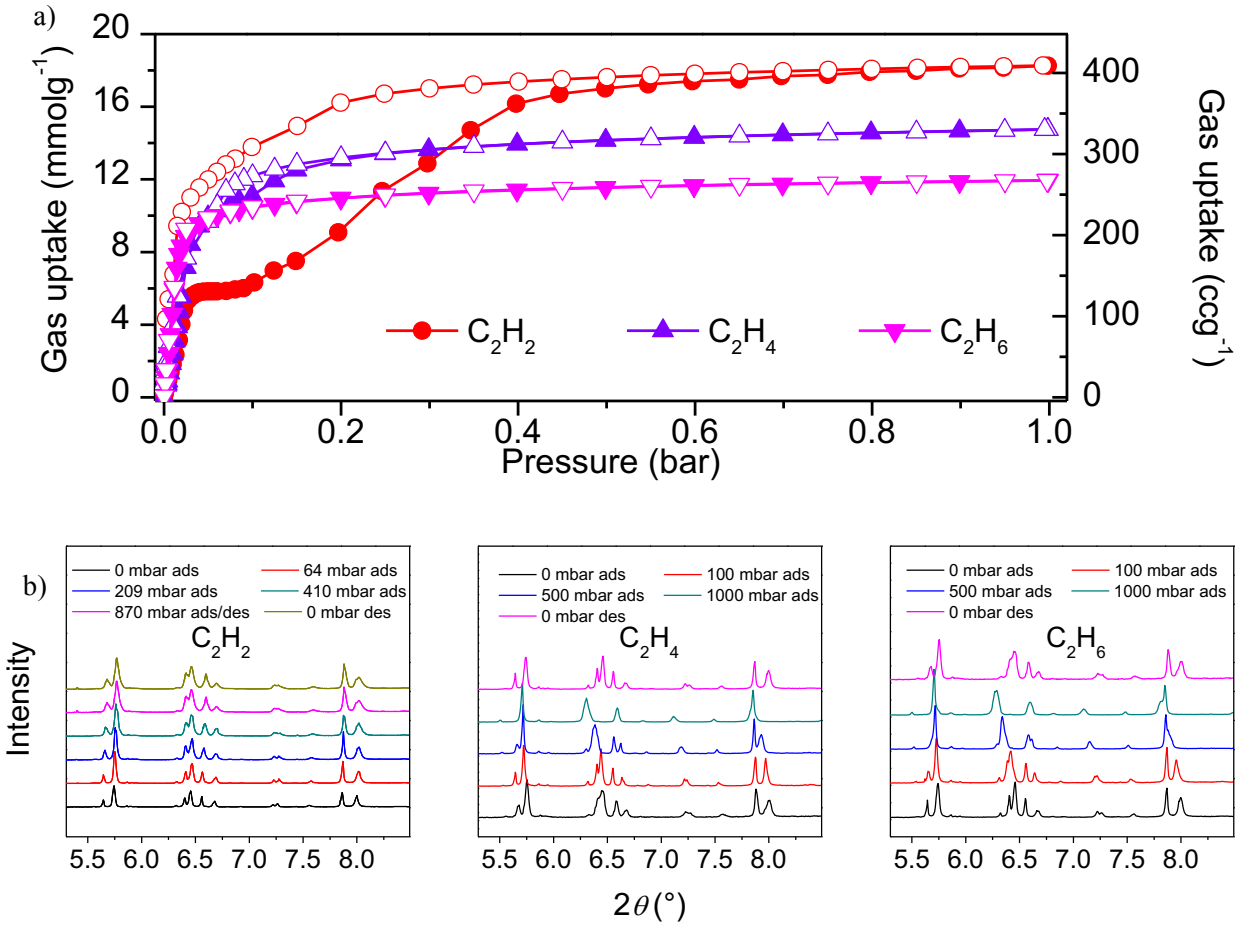



Figure 3.5 Hydrocarbon uptake isotherms and *in situ* PXRD patterns of MFM-202a. a) $C_2H_2$, $C_2H_4$ and $C_2H_6$ sorption isotherms at 195 K. (solid symbol: adsorption; open symbol: desorption). b) Comparison of *in situ* high resolution powder diffraction patterns for MFM-202a as a function of different $C_2H_2$ (left), $C_2H_4$ (middle) and $C_2H_6$ (right) loadings and regeneration at 195 K (Data collected at Diamond Light Source Beamline I11 using multi-analysing crystal-detectors (MACs) and monochromatic radiation. The *in situ* PXRD measurements were carried out in capillary mode and the temperature controlled by an Oxford Cryosystems open-flow nitrogen gas cryostat, λ = 0.825774 Å). Reproduced from Ref. 15.

## 3.2 Aims of this work

The aims of this work are to investigate the $NH_3$ uptake for a flexible MOF, MFM-202a, which has been previously studied to show structural change with the loadings of a variety of gases, such as $CO_2$ and $SO_2$.[13-14] Since $NH_3$ is a polar molecule and induces significant structural change or damage as reported,[16] the aims are also to elucidate the structural change during the process of $NH_3$ dosing and regeneration by *in situ* PXRD and *in situ* pair distribution function (PDF) experiments.

## 3.3 $NH_3$ sorption in MFM-202a

The $NH_3$ adsorption of MFM-202a at ambient condition gives the uptake of 8.49 mmol $g^{-1}$, which is comparable to the reported MOFs (Table 3.1).[1,7,11-12] However, in terms of kinetic sorption, it is very slow to reach equilibrium at a given pressure point. It takes more than 1 hour to reach equilibrium during the adsorption. For desorption, equilibrium is more difficult to reach than for adsorption and thus exhibit significant hysteresis at 298 K. However, this could be viewed as a double-edged sword in terms of application. On one hand, it decreases the release speed in case of a leakage and on the other hand, it requires high temperature and high vacuum for desorption. The regeneration was performed at 313 K and $10^{-9}$ bar for 10 hours and then a second cycle of adsorption was carried out. The comparison of the two isotherms of Cycle 1 and Cycle 2 is shown in Figure 3.6. There is an obvious decrease in uptake in the second cycle and at 0.25 bar, the difference reaches almost 1 mmol $g^{-1}$. This could be attributed to two hypotheses: one is the partial collapse of the framework due to the interaction with ammonia molecules and the other is due to a formation of a new structure which adsorbs lower amount of $NH_3$. Similar behaviour of porous materials for $NH_3$ uptake has been reported but without an *in situ* probe of the structure.[1,16] To trace the structure change in a time-resolved manner *in situ* PXRD and *in situ* PDF experiments were carried out.

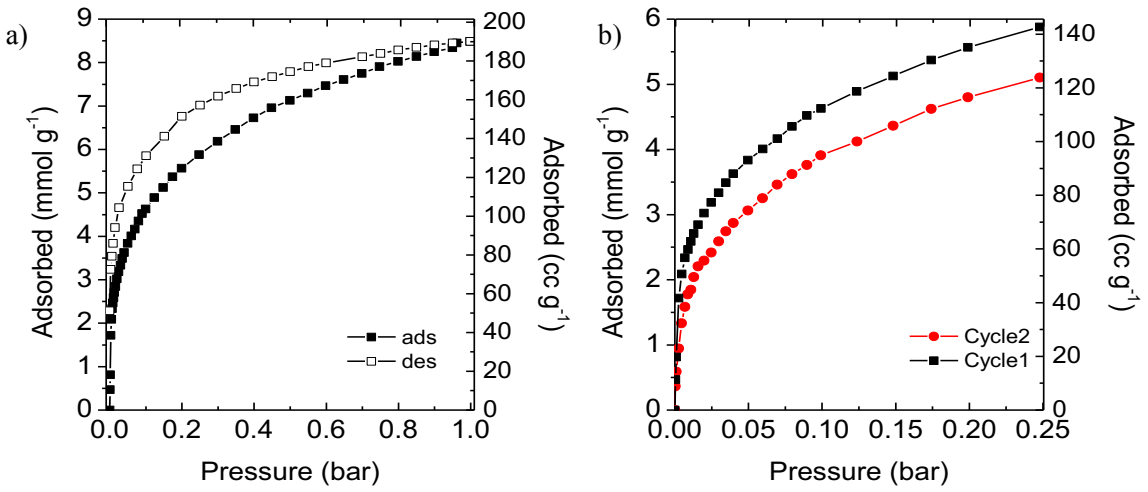



Figure 3.6 a) $NH_3$ adsorption isotherm for MFM-202a at 298 K. Solid symbols: adsorption, open symbols: desorption. b) Comparison of the uptakes in Cycle 1 and Cycle 2.

## 3.4 *In situ* PXRD and PDF studies of $NH_3$-dosed MFM-202a

### 3.4.1 *In situ* PXRD *vs in situ* PDF experiments

*In situ* PXRD has been widely utilised as a tool to investigate the structural change of crystalline materials upon various processes, such as thermal processing and gas adsorption and desorption. Owing to the high intensity and high resolution, *in situ* synchrotron PXRD can further give the detailed structural information of the crystalline material *via* Le Bail refinement and Rietveld refinement.[13-15]

For a crystalline material that does not maintain complete crystallinity or retains only short-range order during the processing, pair distribution function (PDF) analysis can be used to analyse the mechanism correlating to the structural change. It uses X-ray powder diffraction data as a powerful tool for the investigation of amorphous, crystalline and partially crystalline materials. It involves the direct Fourier transformation of X-ray diffraction data, giving the probability of finding any two atoms at a given interatomic distance.[17-19]

### 3.4.2 *In situ* PXRD studies of $NH_3$-dosed MFM-202a

To probe the activation and crystallinity, *in situ* PXRD was carried out for the activated sample, which was heated at 313 K for 2 hours. As shown in Figure 3.7, there were no apparent shifts or intensity

changes of the diffraction peaks, confirming that the crystalline material was fully activated. To gain insight into the structure after dosing $NH_3$, *in situ* PXRD data was collected immediately after the $NH_3$ loading pressure reached 2 bar at 293 K. Thus the sorption actually had not reached equilibrium in the first few minutes. Furthermore, by comparing the PXRD patterns collected in the first 20 minutes, MFM-202a showed good agreement both in the peak positions and intensities, thus confirming retention of the original crystal structure during the process to reach equilibrium. However, dramatic changes of PXRD patterns started to appear after 20 minutes. For instance, there were splits and shifts of peaks (embedded graph in Figure 3.8), significant decrease of peak intensities, broadening of FWHM (full width at half maximum) and gradual loss of weakly diffracted peaks. After 50 minutes of adsorption, the *in situ* PXRD pattern exhibited a flat line (magenta plot as shown in Figure 3.8), indicating that the sample lost crystallinity completely and an amorphous material was formed upon the adsorption of $NH_3$ at 2 bar and 293 K. This result can be explained by three assumptions. First, the single-crystal structure collapsed due to the high intensity X-ray beam flux. Second, the structure collapsed due to the strong interaction between $NH_3$ and the framework. Third, MFM-202a might not really have decomposed and the amorphous phase was only an intermediate state which involved a fast rearrangement of the framework. This would be discussed further by *in situ* PDF experiments.

To probe the structural change after degassing, *in situ* PXRD experiments were carried out as shown in Figure 3.9. Interestingly, after the regeneration, there were a series of new diffraction peaks appeared, though with much weaker intensity and broader FWHM. This suggested that after the collapse of the $NH_3$-loaded MFM-202a structure, a new phase of the MFM-202a formed and gradually degraded in the beam.

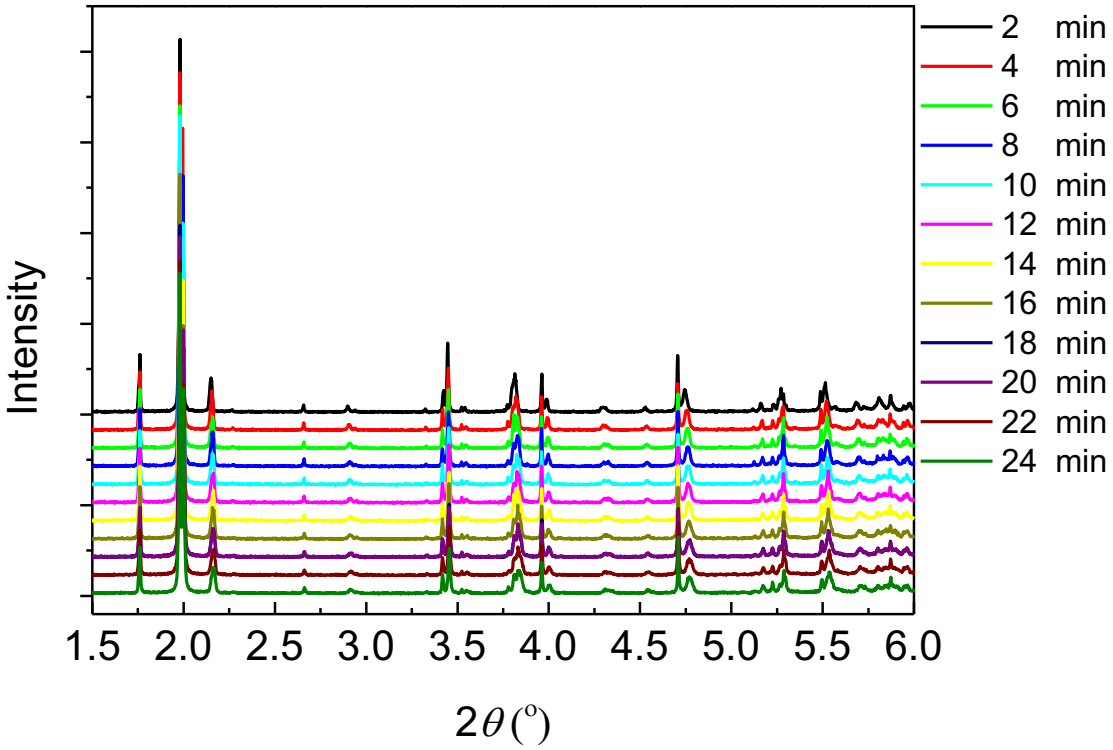



Figure 3.7 *In situ* PXRD for the activated MFM-202a, λ = 0.49593576 Å.

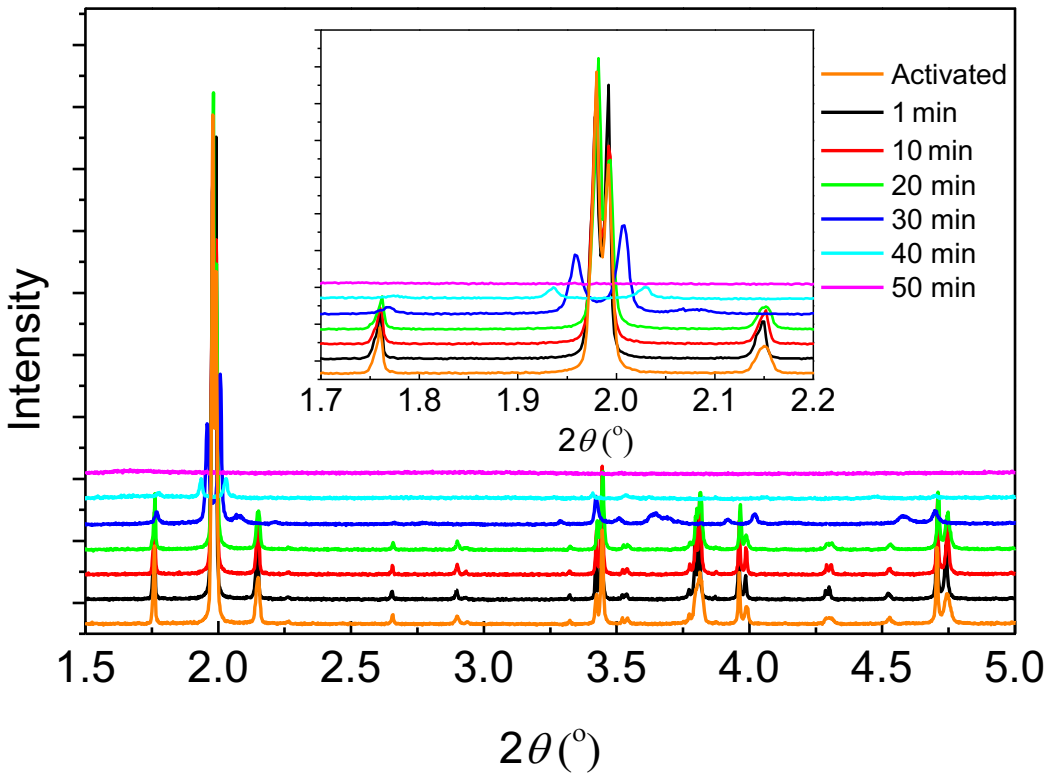



Figure 3.8 *In situ* PXRD for MFM-202a with $NH_3$ loading, λ = 0.49593576 Å.

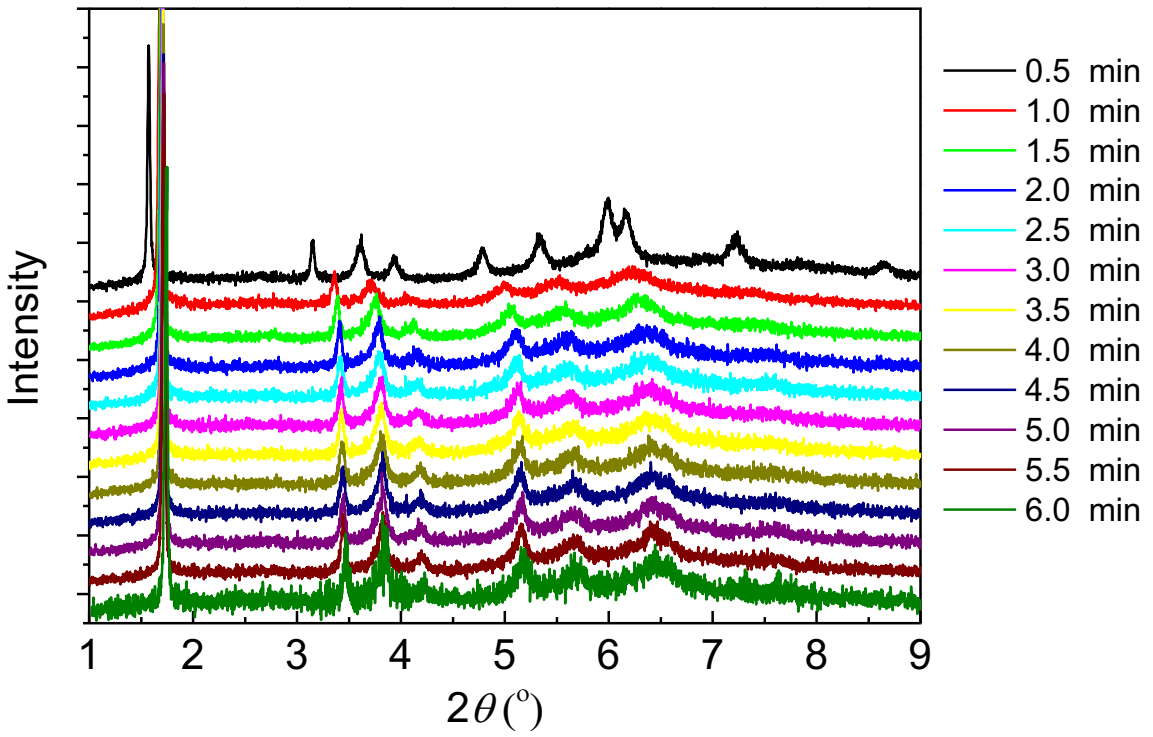



Figure 3.9 *In situ* PXRD for MFM-202a during regeneration, λ = 0.49593576 Å.

### 3.4.3 *In situ* PDF studies of $NH_3$-dosed MFM-202a

The effect of the synchrotron X-ray on the sample is determined by both photon energy (E) and photon flux ($\varphi$), which are given by the equation 1 and 2,

$$E = \frac{hc}{\lambda} \tag{1}$$

where $E$ is the photon energy, $h$ is the Planck constant, $c$ is the speed of light in vacuum and λ is the photon's wavelength;

$$\varphi = \frac{Number\ of\ photons}{s\ m^2} \tag{2}$$

where $\varphi$ is the photon flux, which is defined as the number of photons per second (s) per square meter ($m^2$). By comparing the effect of the *in situ* synchrotron X-ray in the two experiments, we found that although the X-ray wavelength (λ = 0.49593576 Å) used in the *in situ* PXRD experiment is longer than that (λ = 0.19057 Å) in the *in situ* PDF experiment, the exposure time (0.5–2 min) of the former was

much longer than that (1–5 sec) of the latter. In a word, the effect of the beam damage on the sample in the *in situ* PDF experiment is weaker than that in the *in situ* PXRD experiment.

Figure 3.10 shows the integrated *in situ* PXRD patterns from PDF experiments for the activated MFM-202a sample. The diffraction patterns at 2 sec and 80 sec are considered as identical, confirming the retention of the crystallinity and the completion of the activation. The sample was then treated with $NH_3$ at 293 K and 2 bar. The integrated *in situ* PXRD patterns of the $NH_3$-loaded MFM-202a were unchanged in the starting 120 seconds as shown in Figure 3.11, suggesting the retention of crystallinity. However, the intensity of peaks started to drop dramatically very soon after that. At 180 seconds, the PXRD pattern nearly became a flat line (indicated in blue), corresponding to the collapse of the crystalline structure. Interestingly, after 240 seconds, new peaks started to appear and grow with the absence of all the previously observed peaks, indicating the absence of the original phase and formation of a new phase. At 1800 seconds, the new structure stabilised as evidenced by the appearance of the sharp peaks. In addition, the new phase was retained upon desorption and regeneration despite a slight decrease of peak intensity.

To gain insights into the new phase of MFM-202a, a second cycle for the $NH_3$ sorption was carried out. Following the same procedure as the first cycle, 2 bar of $NH_3$ was dosed to the sample at 293 K. At the beginning, the integrated *in situ* PXRD peaks of the $NH_3$-loaded sample matched those of the regeneration in the first cycle, indicating the retention of the new phase. During the process of adsorption, the diffraction peaks grew sharper and sharper with an increase of intensity, indicating the new phase was "robust" to the exposure of $NH_3$. In addition, after the second regeneration, this new phase was also retained.

In conclusion, with the evidence from *in situ* PXRD and *in situ* PDF experiments, it is probably the formation of a new phase of MFM-202a that gives lower uptake of $NH_3$ in the second cycle of the sorption. Due to the quality of the *in situ* PDF data obtained, a full examination of the spectra was not able to be carried out.

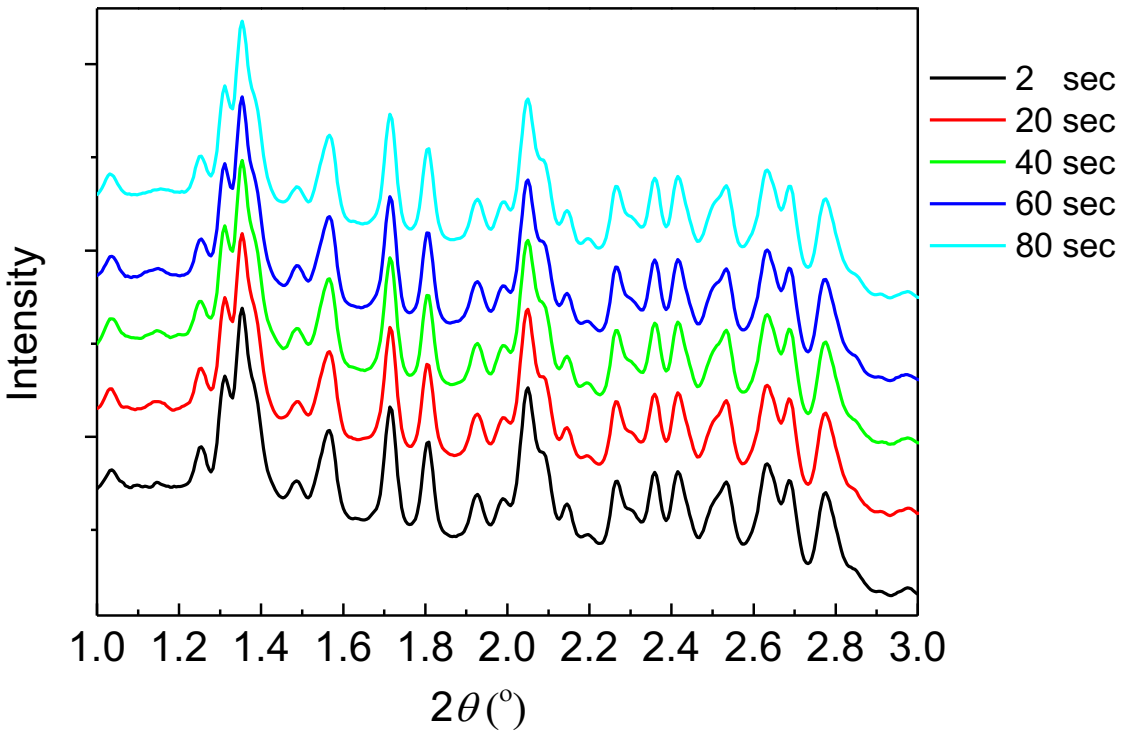



Figure 3.10 Time-dependent in situ PXRD patterns integrated from PDF experiment for the activation of MFM-202a. (λ = 0.19057 Å)

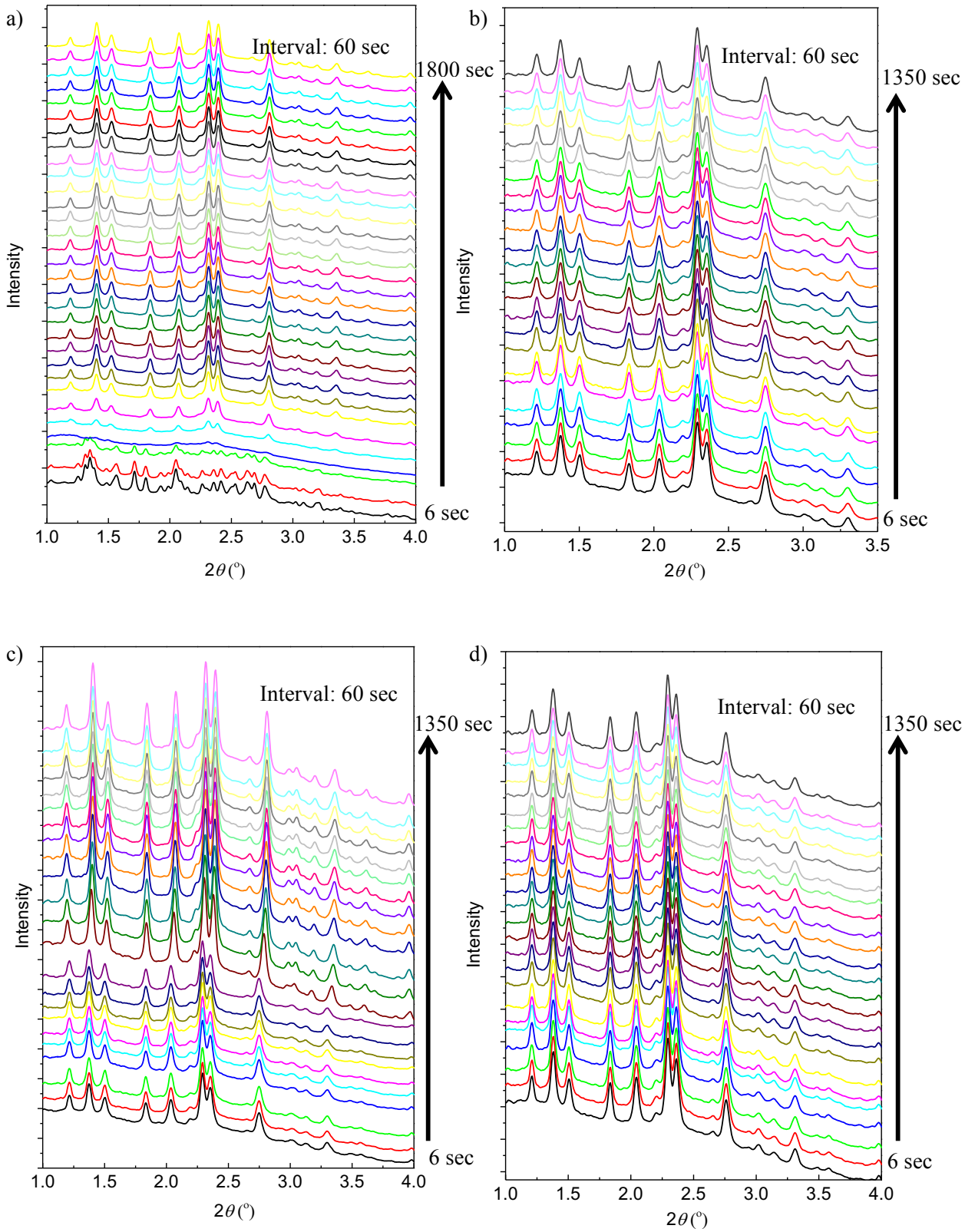



Figure 3.11 Time-dependent *in situ* PXRD patterns integrated from PDF experiment for $NH_3$-dosed MFM-202a in the first cycle a) and second cycle c), time-dependent *in situ* PXRD for the regeneration in the first cycle b) and the second cycle d), $\lambda = 0.19057$ Å.

## 3.5 Experimental section

### 3.5.1 Materials and techniques

All reagents and solvents were used as received from commercial suppliers without further purification. MFM-202a was synthesised and prepared as described previously.[10]

### 3.5.2 High resolution synchrotron X-ray powder diffraction

High resolution *in situ* synchrotron X-ray powder diffraction (PXRD) data were collected at ESRF Beamline ID22 using monochromatic radiation ($\lambda$ = 0.49593576 Å) and the temperature was controlled by an Oxford Cryosystems open-flow nitrogen gas cryostat. High resolution *in situ* PDF experiments were carried out at ESRF Beamline ID22 using monochromatic radiation ($\lambda$ = 0.19057 Å) and the temperature was controlled by an Oxford Cryosystems open-flow nitrogen gas cryostat.

For the *in situ* PXRD experiment, MFM-202a was ground gently with an agate pestle and mortar for 10 minutes to give a uniform small particle size for obtaining high resolution X-ray diffraction patterns. The sample was then immediately transferred and sealed with porous cotton wool to isolate the sample from the air. It was fitted into a brass holder with superglue to ensure that no vibration occurred during the rapid spinning of the sample on the diffractometer. Finally, the brass holder was attached to the holder base and then mounted on the diffractometer and activated under vacuum (~$1 \times 10^{-6}$ bar) at 313 K for 1 hour to remove the solvent molecules. All *in situ* PXRD patterns were collected at 293 K. The activated sample was firstly measured with 2$\theta$ from 0 to 30 degrees and a scan speed of 15 degrees per minute. $NH_3$ was then loaded into the capillary at 293 K and 2 bar. When the pressure reached 2 bar, the $NH_3$ supply was cut off and the scan was then immediately initiated. The $NH_3$-loaded sample was measured with 2$\theta$ from 0 to 15 degrees and a scan speed of 15 degrees per minute. The sample was then reactivated at 313 K for 1 hour to remove $NH_3$. To probe the structural change after regeneration, the sample was measured with 2$\theta$ from 0 to 10 degrees and a scan speed of 20 degrees per minute. After $NH_3$-dosing measurements, the sample was reactivated at 313 K for ~20 minutes.

### 3.5.3 High resolution synchrotron PDF experiment

For the PDF experiment, the sample of MFM-202a was treated in the same way as in the PXRD experiments. The activated sample was measured for 40 scans and each scan takes 1 seconds. The $NH_3$ was then loaded into the capillary at 293 K and 2 bar. When the pressure reached 2 bar, the $NH_3$ supply was cut off and PDF scan was then immediately initiated. The $NH_3$-loaded sample was measured for 300 scans and each scan takes 5 seconds. The sample was then reactivated at 313 K for 1 hour to remove $NH_3$. To probe the structural change after regeneration, the sample was measured for 225 scans and each scan takes 5 seconds. To gain insight into the reversibility of the sample, it was measured for two cycles. After the second cycle of loading $NH_3$, the sample was again reactivated at 313 K for ~20 minutes.

## 3.6 Conclusions

The $NH_3$ adsorption capacity measured at 298 K and 1 bar for MFM-202a is 8.49 mmol $g^{-1}$, which is comparable to those of reported MOFs.[1] To gain an insight into the stability of the structure for $NH_3$ uptake, a second cycle of adsorption has been carried out, which shows significant decrease of ~1 mmol $g^{-1}$ at 0.25 bar. *In situ* PXRD confirms that the structure of the MFM-202a collapses upon sorption of $NH_3$ at 293 K and 2 bar. However, new diffraction peaks were found after regeneration, indicating the occurrence of a new phase.

Integrated PXRD from *in situ* PDF studies of $NH_3$-loaded MFM-202a carried out at the ESRF confirms that $NH_3$ shows a strong interaction with the framework and induces an irreversible rearrangement of the initial structure upon sorption at 293 K and 2 bar. The new phase is retained after the regeneration in the first cycle of sorption and is robust to the exposure of $NH_3$ in the second cycle. Therefore, the lower uptake of $NH_3$ in the second cycle is probably due to the collapse of the original structure and the formation of a new phase.

In terms of the stability of the new phase of MFM-202a upon exposure to X-ray irradiation, the structure retained during *in situ* PDF experiments but collapsed during *in situ* PXRD experiments.

## References

1. Doonan, C. J.; Tranchemontagne, D. J.; Glover, T. G.; Hunt, J. R. and Yaghi, O. M. Exceptional ammonia uptake by a covalent organic framework. *Nature. Chem*. **2010**, *2*, 235–238.

2. Deery, S. and Harris, A. Gas factory explosion forces evacuation in Laverton North. *Herald Sun.* 14 Sep. **2010**. Available at: http://www.heraldsun.com.au/news/victoria/gas-factory-explosion-forces-evacuation-in-laverton-north/story-e6frf7kx-1225922103427.

3. Zhang, Q. 26 people poisoned in a Harbin food company by $NH_3$ leakage. *Xinhua website*. 14 March, **2014**. Available at: http://news.xinhuanet.com/local/2014-03/14/c_119780578.htm.

4. Hattenbach, R. Transportation & delivery of anhydrous ammonia. **2012**, 5. Available at: https://nh3fuel.files.wordpress.com/2012/05/chemicalmarketingservices.

5. Petit, C. and Bandosz, T. J. Synthesis, characterization, and ammonia adsorption properties of mesoporous metal-organic framework (MIL(Fe))-graphite oxide composites: exploring the limits of materials fabrication. *Adv. Funct. Mater.* **2011**, *21*, 2108–2117.

6. Glover, T. G.; Peterson, G. W.; Schindler, B. J.; Britt, D. and Yaghi, O. MOF-74 building unit has a direct impact on toxic gas adsorption. *Chem. Eng. Sci.* **2011**, *66*, 163–170.

7. DeCoste, J. B. and Peterson, G. W. Metal-organic frameworks for air purification of toxic chemicals. *Chem. Rev.* **2014**, *114*, 5695–5727.

8. Katz, M. J.; Howarth, A. J.; Moghadam, P. Z.; DeCoste, J. B.; Snurr, R. Q.; Hupp, J. T. and Farha, O. M. High volumetric uptake of ammonia using Cu-MOF-74/Cu-CPO-27. *Dalton Trans.* **2016**, *45*, 4150–4153.

9. Petit, C. and Bandosz, T. J. Exploring the coordination chemistry of MOF-graphite oxide composites and their applications as adsorbents. *Dalton Trans.* **2012**, *41*, 4027–4035.

10. Tan, K.; Zuluaga, S.; Gong, Q.; Gao, Y.; Nijem, N.; Li, J.; Thonhauser, T. and Chabal, T. J. Competitive coadsorption of $CO_2$ with $H_2O$, $NH_3$, $SO_2$, NO, $NO_2$, $N_2$, $O_2$, and $CH_4$ in M-MOF-74 (M = Mg, Co, Ni): the role of hydrogen bonding. *Chem. Mater.* **2015**, *27*, 2203–2217.

11. Saha, D. and Deng, S. Ammonia adsorption and its effects on framework stability of MOF-5 and MOF-177. *J. Colloid. Interface. Sci.* **2010**, *348*, 615–620.

12. Spanopoulos, I.; Xydias, P.; Malliaka, C. D. and Trikalitis, N. A straight forward route for the development of metal-organic frameworks functionalized with aromatic -OH groups: synthesis, characterization, and gas ($N_2$, Ar, $H_2$, $CO_2$, $CH_4$, $NH_3$) sorption properties. *Inorg. Chem.* **2013**, *52*, 855−862.

13. Yang, S.; Lin, X.; Lewis, W.; Suyetin, M.; Bichoutskaia, E.; Parker, J. E.; Tang, C. C.; Allan, D. R.; Rizkallah, P. J.; Hubberstey, P.; Champness, N. R.; Thomas, K. M.; Blake, A. J.; Schröder, M. A partially interpenetrated metal-organic framework for selective hysteretic sorption of carbon dioxide. *Nature Mater.* **2012**, *11*, 710−716.

14. Yang, S.; Liu, L.; Sun, J.; Thomas, K. M.; Davies, A. J.; George, M. W.; Blake, A. J.; Hill, A. H.; Fitch, A. N.; Tang, C. C.; Schröder, M. Irreversible network transformation in a dynamic porous host catalyzed by sulfur dioxide. *J. Am. Chem. Soc.* **2013**, *135*, 4954−4957.

15. Gao, S.; Morris, C. G.; Lu, Z.; Yan, Y.; Godfrey, H. G. W.; Murray, C.; Tang, C. C.; Thomas, K. M., Yang, S. and Schröder, M. Selective hysteretic sorption of light hydrocarbons in a flexible metal−organic framework material. *Chem. Mater.* **2016**, *28*, 2331−2340.

16. Kajiwara, T.; Higuchi, M.; Watanabe, D.; Higashimura, H.; Yamada, T. and Kitagawa, H. A systematic study on the stability of porous coordination polymers against ammonia. *Chem. Eur. J.* **2014**, *20*, 15611−15617.

17. Chapman, K. W.; Sava, D. F.; Halder, G. J.; Chupas, P. J. and Nenoff, T. M. Trapping guests within a nanoporous metal-organic framework through pressure-induced amorphization. *J. Am. Chem. Soc.* **2011**, *133*, 18583−18585.

18. Cliffe, M. J.; Wan, W.; Zou, X.; Chater, P. A.; Kleppe, A. K.; Tucker, M. G.; Wilhelm, H.; Funnell, N. P.; Couder, F.-X. and Goodwin, A. L. Correlated defect nanoregions in a metal-organic framework. *Nat. Commun.* **2014**, *5*, 1−8.

19. Allan, P. K.; Chapman, K. W.; Chupas, P. J.; Hriljac, J. A.; Renouf, C. L.; Lucas, T. C. A. and Morris, R. E. Pair distribution function-derived mechanism of a single-crystal to disordered to single-crystal transformation in a hemilabile metal-organic framework. *Chem. Sci.* **2012**, *3*, 2559−2564.

# Chapter 4 Gas uptake and selectivity studies on Zr- and Hf-based MOFs

## 4.1 Introduction

### 4.1.1 Development of Zr(IV)- and Hf(IV)-based MOFs

The high oxidation of Zr(IV)- and Hf(IV)-based MOFs generally have an enhanced stability in organic solvent or water.[1-5] Compared with conventional M(II)-based MOFs, MOFs derived from M(III) and M(IV) generally have higher thermal stability. For example, the M(II)- and M(III)-based MOFs generally decompose at ~250–400 °C[6-11] and Zr(IV)- and Hf(IV)-based MOFs up to ~400–540 °C measured by thermogravimetric analysis (TGA).[2,12-13] Furthermore, six Zr(IV) centres generally form $Zr_6$ clusters, which can avoid the occurrence of interpenetration and thus give materials with very high porosity, high BET surface areas and low density. For example, NU-1101, NU-1102, NU-1103 and NU-1104 were reported to have high BET surface areas of 4340, 4830, 6550 and 6230 $m^2\ g^{-1}$, respectively.[13] UiO-66, UiO-67 and UiO-68 have BET surface areas of 1187, 3000 and 4170 $m^2\ g^{-1}$, respectively.[2] Additionally, M(IV)-based carboxylate MOFs have excellent chemical and mechanical resistance associated with low toxicity.[5] Based on these advantages, the Zr- and Hf-based MOFs have been investigated in the applications of catalysis, gas sorption and separation, and drug delivery.[1,3,14]

In this project, the main focus is on the studies of gas sorption and separation for Zr- and Hf-based MOFs. Currently the gas sorption studies for Zr- and Hf-based MOFs have only concentrated on $H_2$, $N_2$, $CH_4$, $CO_2$ and water vapour.[3-5] For example, NU-1100, constructed from $Zr_6O_4(OH)_4^{12+}$ clusters and a pyrene-based tetratopic ligand (4-[2-[3,6,8-tris[2-(4-carboxyphenyl)-ethynyl]-pyren-1-yl]ethynyl]-benzoic acid ($H_4L$)), is a highly porous framework (pore volume: 1.53 cc $g^{-1}$; BET surface area: 4020 $m^2\ g^{-1}$) and therefore has been studied for $H_2$, $N_2$, $CH_4$, $CO_2$ and water uptakes, with isotherms shown in Figure 4.1. The excess $H_2$ isotherm of this material at 77 K showed a shallow maximum uptake of 0.062 g $g^{-1}$ at ~45 bar, which corresponds to a volumetric uptake of 43 g $L^{-1}$, which is amongst the highest values reported to date for $H_2$ storage.[3] The $N_2$ uptake at 77 K also shows approximately 40.2 mmol $g^{-1}$. In addition, the $CO_2$ uptake at room temperature and 30 bar is approximately 26.2 mmol $g^{-1}$, corresponding to 70% of the total pore volume. It shows the maximum sorption of $CH_4$ of ~38.6 mmol

$g^{-1}$ (corresponding to 404 $v_{STP}/v$) at 125 K. Both $CO_2$ and $CH_4$ sorption give pore volume values comparable to that calculated from $N_2$ measurements. The repeatable sorption capacity of $CH_4$ was tested by multiple cycles, which again proved its highly stable structure.[3]

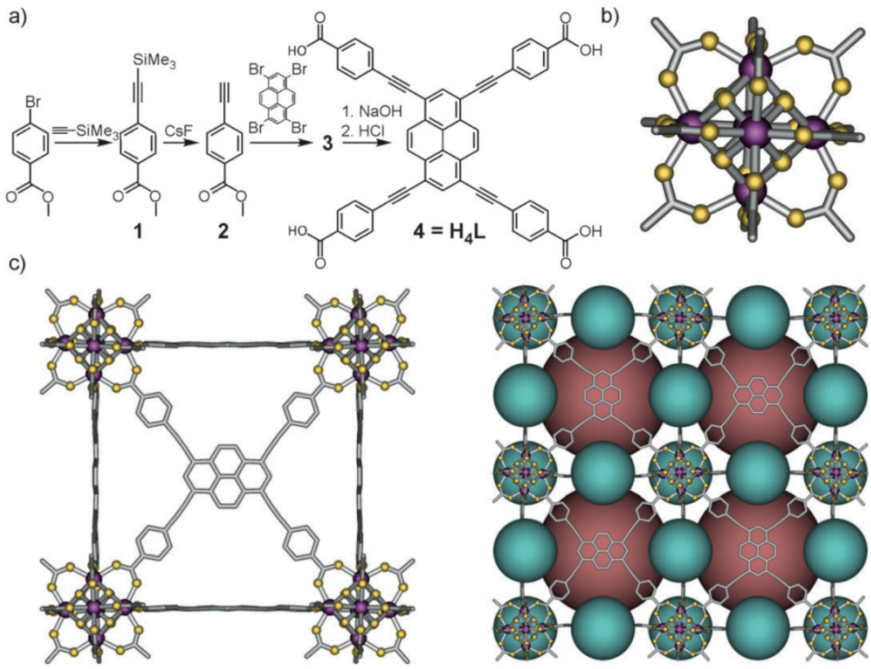



Figure 4.1 a) Scheme for $H_4L$ synthesis. b) SBU of the structure, c) Structural elements and crystal packing of NU-1100 (Zr atoms are shown as purple spheres, O atoms as yellow spheres, and carbon skeleton as grey sticks. Dark pink and light blue spheres occupy two major pore types in the crystal. Reproduced from Ref. 3.

Another well-known branch of Zr-based MOFs are the Zr-UiO-xx (xx: 66, 67 and 68) series. Zr-UiO-66, Zr-UiO-67 and Zr-UiO-68 are constructed from similar $Zr_6O_4(OH)_4$ nodes, but bridged by 1,4-benzene-dicarboxylate (BDC), 4,4'-biphenyl-dicarboxylate (BPDC) and terphenyl dicarboxylate (TPDC), respectively. These three MOFs have isoreticular structures as shown in Figure 4.2. UiO-66 and UiO-67 have also been functionalized by adding functional groups, such as $NH_2$, $NO_2$, Br, OH, sulfone, *etc*.[15-18] Among these functional groups, the sulfone-functionalised Zr-UiO-67 shows a remarkable 122% enhancement in $CO_2$ uptake at 1 bar and 273 K, reaching 4.8 mmol $g^{-1}$ (2.16 mmol $g^{-1}$ for Zr-UiO-67). Compared with Zr-UiO-67 in terms of the selectivity of $CO_2/CH_4$ (~4) at 273 K and 100–450 torr, the sulfone-functionalised Zr-UiO-67 exhibits more than 100% increase in the selectivity of $CO_2/CH_4$.[17] The enhancement was attributed to the increased interaction of $CO_2$ with the polar

sulfone groups.[17]

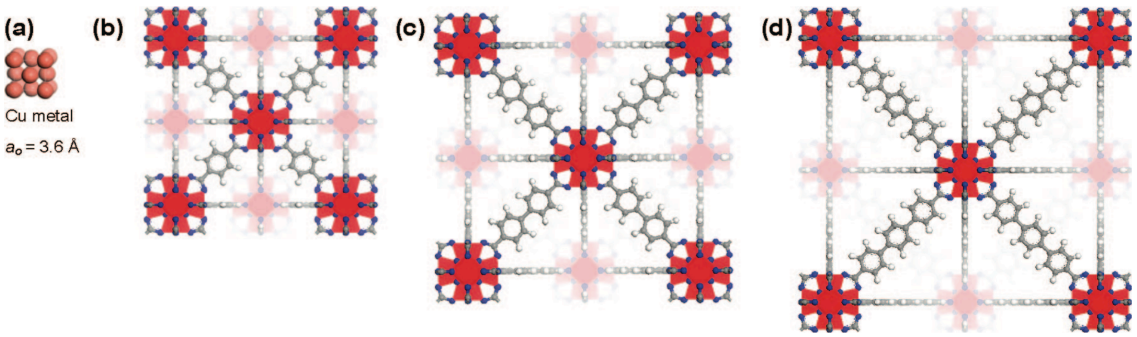



Figure 4.2 a) One unit cell of copper drawn to scale with, b) Zr-MOF with 1,4-benzene-dicarboxylate (BDC) as linker, UiO-66, c) Zr-MOF with 4,4′-biphenyl-dicarboxylate (BPDC) as linker, UiO-67, d) Zr-MOF with terphenyl dicarboxylate (TPDC) as linker, UiO-68. Zirconium, oxygen, carbon, and hydrogen atoms are red, blue, grey, and white, respectively. Reproduced from Ref. 2.

### 4.1.2 Introduction of a flexible ligand

The biphenyl-3,3',5,5'-tetra-(phenyl-4-carboxylic acid) linker has been reported to form ZJU-30, $[Ba_5(L)_3(H_2O)_6]\cdot 25H_2O\cdot 10DMF\cdot 2Me_2NH_2^+$ and MFM-202 with metal ions of Cu(II), Ba(II) and In(III), respectively.[7-8,11,19] Here, it is noteworthy that by changing the pH modifier from *conc.* HCl to $HBF_4$, the doubly-interpenetrated ZJU-30 has been modified to a non-interpenetrated framework UTSA-68, and exhibits higher uptake capacities for $N_2$ and $C_2H_2$.[7-8] The doubly interpenetrated ZJU-30 adopts a flat geometry whereas UTSA-68 adopts a twisted geometry for the two internal phenyl rings, as shown in Figure 4.3. Interestingly, this linker in $[Ba_5(L)_3(H_2O)_6]\cdot 25H_2O\cdot 10DMF\cdot 2Me_2NH_2^+$ shows a flat geometry whereas in MFM-202 shows a twisted geometry.[11,19]

The high flexibility of the linker leads to the possibility of forming structures of different conformations and geometries under different synthetic conditions. This shows great potential for the specific design of structures. For example, to obtain **ftw** topology of a Zr(IV)-based MOF, a targeted ligand with four carboxylates showing planar geometry can significantly enhance the probability of its formation.[3]

MFM-202 has been reported to show excellent gas sorption and separation properties with a range of different gases (Ar, $H_2$, $N_2$, $O_2$, $CO_2$, $SO_2$, $CH_4$, $C_2H_2$, $C_2H_4$, $C_2H_6$, $C_3H_6$ and $C_3H_8$).[11,20,21] Synthesised

with the same tetracarboxylate linker, the resulting Zr- and Hf-based MOF materials, along with amine-functionalised Zr- and Hf-based MOFs have been investigated for their gas adsorption properties.

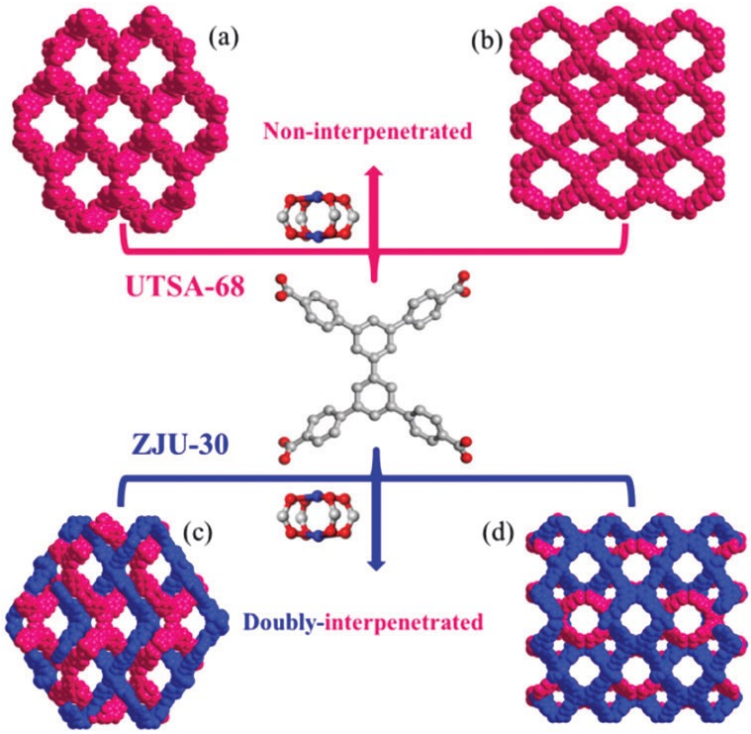
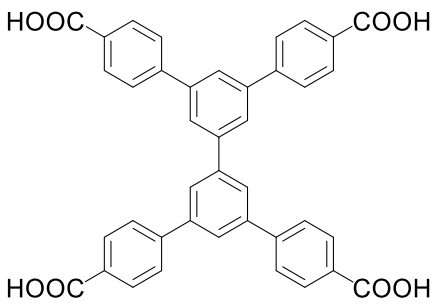


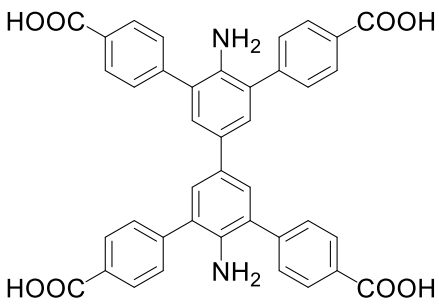

Figure 4.3 Comparison of the single crystal structures of UTSA-68 and ZJU-30 synthesised from a flexible linker, viewed along *a* (a) (c) axis and *c* (b)(d) axis. Reproduced from Ref. 7.

## 4.2 Aims of the work

Two new Zr-based MOFs and two new Hf-based MOFs based on the two tetracarboxylate ligands ($H_4L^1$ and $H_4L^2$) shown below were successfully synthesised and comprehensive characterisation of the materials were carried out with single crystal XRD, PXRD of both as-synthesised and acetone-exchanged samples, TGA, FTIR and elemental analyses. A series of hydrocarbon gas sorption and selectivity studies were also carried out on the amine-functionalised derivative of Zr-based MOF material. In addition, *in situ* PXRD experiments of $CO_2$ were carried out to investigate the mechanism for the stepwise adsorption at low temperature.




$H_4L^1$




$H_4L^2$

Scheme 4.1 Linkers used in the synthesis of Zr- and Hf-based in this Chapter.

## 4.3 Studies of Zr- and Hf-based MOFs

### 4.3.1 Crystallographic studies of Zr- and Hf-based MOFs

#### 4.3.1.1 Crystallographic study of $Zr_6(L^1)_2(\mu_3\text{-}O)_4(\mu_3\text{-}OH)_4(OH)_4(H_2O)_4$ and $Hf_6(L^1)_2(\mu_3\text{-}O)_4(\mu_3\text{-}OH)_4(OH)_4(H_2O)_4$

The $Zr_6(L^1)_2(\mu_3\text{-}O)_4(\mu_3\text{-}OH)_4(OH)_4(H_2O)_4$ is synthesised from $H_4L^1$ and $ZrCl_4$ anhydrate in DMF with benzoic acid as the modulator at 120 °C for three days. The product crystallises in space group *Fmmm* with a **flu** topology. In the framework, six Zr metal centres form an octahedral $Zr_6$ cluster which coordinates to thirty-two O centres, with sixteen from eight carboxylate groups of eight distinct linkers and the other sixteen O centres from solvent molecules. There are two crystallographically independent Zr centres in the $Zr_6$ clusters, with the ratio of Zr1:Zr2 = 1:2. The Zr1 centre in the cluster binds to four deprotonated O centres from four distinct carboxylate groups of four different linkers and the other four bridging O groups from the solvent. In contrast, the Zr2 centre binds to two deprotonated O centres from two distinct carboxylate groups of two linkers, two mono-dentate O groups and four bridging O groups from the solvent, which in total also give eight coordinates. As a result of the different coordinate environments, the six Zr centres form a slightly compressed octahedron instead of the normal octahedral cluster, with Zr1–Zr1 = 4.879(2) Å, Zr1–Zr2 = 3.495(2) Å, two adjacent Zr2–Zr2 = 3.541(2) Å and 3.536(2) Å, as shown in Figure 4.4b. The Zr–O distances range from 2.129(4) to 2.264(5) Å. The linker adopts a twisted geometry between the two internal phenyl rings, with the dihedral angle of 56°. The framework contains tetrahedral cages, with the size of approximately 12 Å × 23 Å × 25 Å. The total void volume available to guest molecules in $Zr_6(L^1)_2(\mu_3\text{-}O)_4(\mu_3\text{-}OH)_4(OH)_4(H_2O)_4$ was estimated by PLATON/SOLV calculations to be 75.6%.

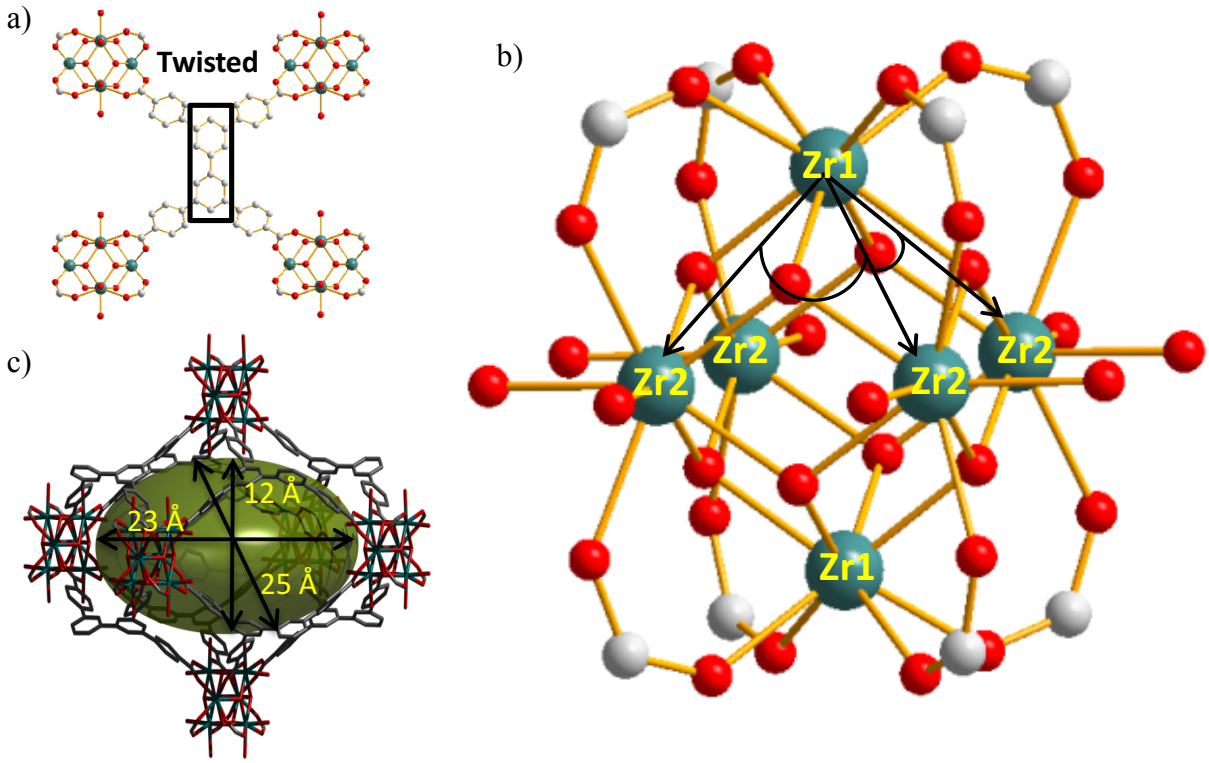



Figure 4.4 View of the single crystal structure of $Zr_6(L^1)_2(\mu_3\text{-}O)_4(\mu_3\text{-}OH)_4(OH)_4(H_2O)_4$. a) View of the coordination environment at the linker, b) View of the geometry of $Zr_6$ nodes. c) View of the polyhedral cage in the structure (olive ellipsoid). Oxygen: red; carbon: grey; zirconium: green.

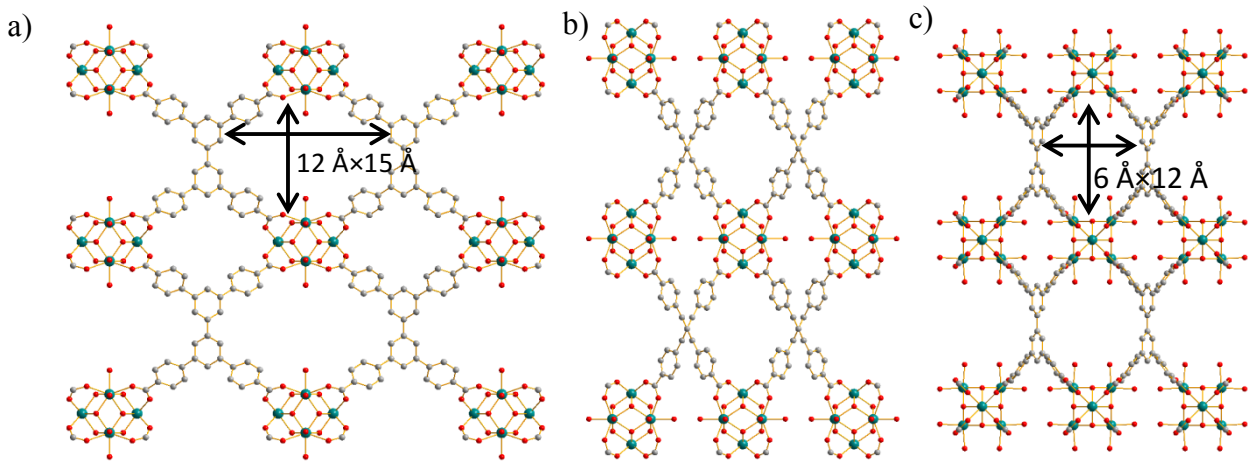



Figure 4.5 View of the pore and channel in the network of $Zr_6(L^1)_2(\mu_3\text{-}O)_4(\mu_3\text{-}OH)_4(OH)_4(H_2O)_4$. a) View along *a* axis; b) view along *b* axis; c) view along *c* axis. Oxygen: red; carbon: grey; zirconium: green, hydrogen atoms are omitted for clarity.

The $Hf_6(L^1)_2(\mu_3\text{-}O)_4(\mu_3\text{-}OH)_4(OH)_4(H_2O)_4$ is synthesised following a similar route to that of $Zr_6(L^1)_2(\mu_3\text{-}O)_4(\mu_3\text{-}OH)_4(OH)_4(H_2O)_4$. $H_4L^1$ was reacted with $HfCl_4$ in DMF at 120 °C for three days with benzoic acid as the modulator. The product is an isostructural with $Zr_6(L^1)_2(\mu_3\text{-}O)_4(\mu_3\text{-}OH)_4(OH)_4(H_2O)_4$. The six Hf centres form a slightly compressed octahedron, with Hf1–Hf1 = 4.861(2) Å, Hf1–Hf2 = 3.478(2) Å, Hf2–Hf2 = 3.524(2), as shown in Figure 4.6. Compared with the $Zr_6$ octahedral cluster, the $Hf_6$ cluster exhibits shorter bond lengths and smaller bond angles correspondingly. The total void volume available to guest molecules in $Hf_6(L^1)_2(\mu_3\text{-}O)_4(\mu_3\text{-}OH)_4(OH)_4(H_2O)_4$ was estimated by PLATON/SOLV calculations to be 73.6%.

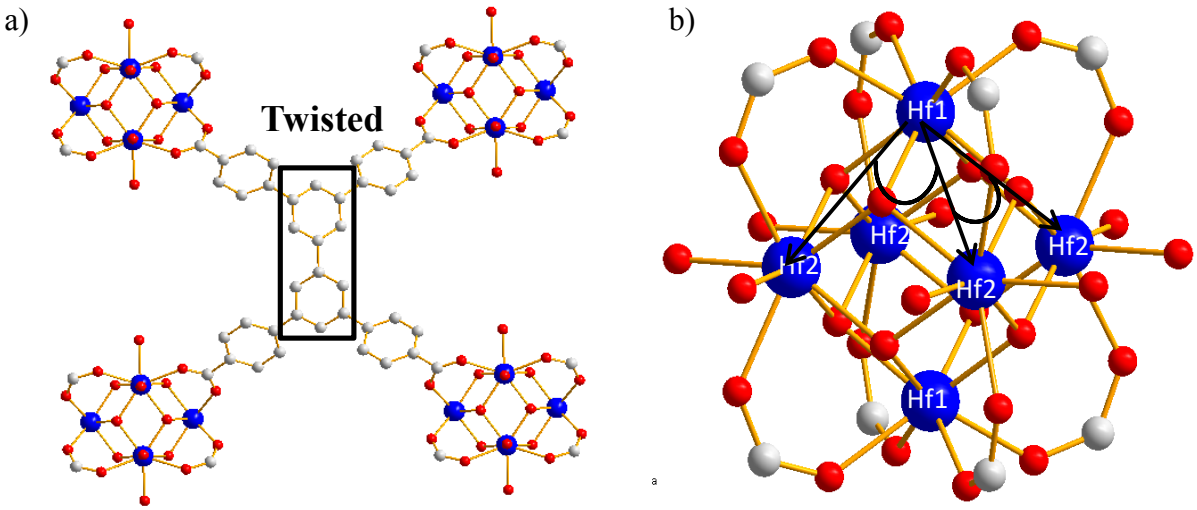



Figure 4.6 View of the single crystal structure of $Hf_6(L^1)_2(\mu_3\text{-}O)_4(\mu_3\text{-}OH)_4(OH)_4(H_2O)_4$. a) View of the coordination environment at linker. b) View of the geometry of $Hf_6$ nodes. Oxygen: red; carbon: grey; hafnium: blue, hydrogen atoms are omitted for clarity.

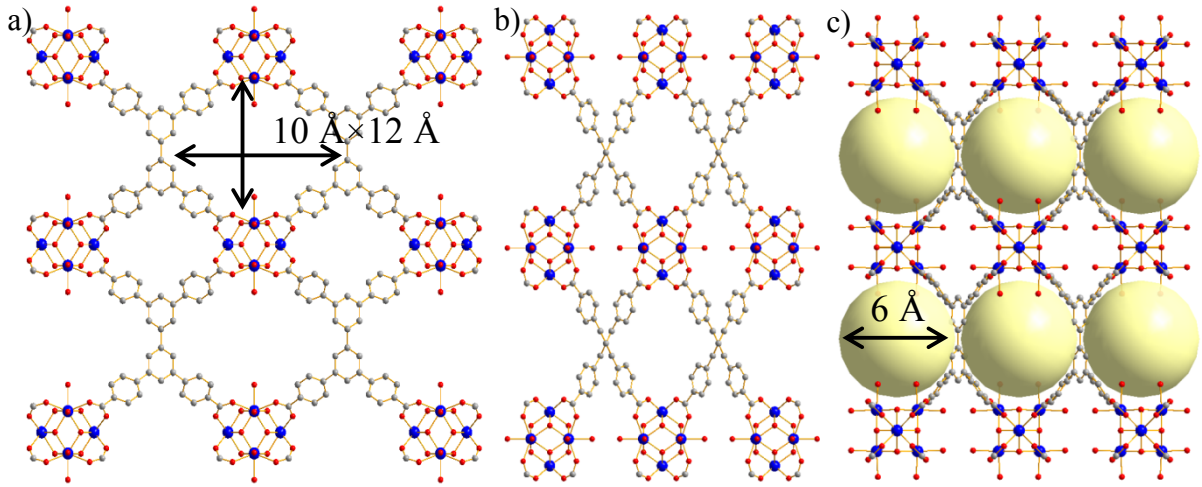



Figure 4.7 View of the pore and channel structure for $Hf_6(L^1)_2(\mu_3\text{-}O)_4(\mu_3\text{-}OH)_4(OH)_4(H_2O)_4$. a) View along *a* axis; b) view along *b* axis; c) view along *c* axis. Oxygen: red; carbon: grey; hafnium: blue, hydrogen atoms are omitted for clarity.

#### 4.3.1.2 Crystallographic study of MFM-601 and $Hf_6(L^2)_2(\mu_3\text{-}O)_4(\mu_3\text{-}OH)_4(OH)_4(H_2O)_4$

By adopting a similar synthetic route to prepare $Zr_6(L^1)_2(\mu_3\text{-}O)_4(\mu_3\text{-}OH)_4(OH)_4(H_2O)_4$, the amine-functionalised linker, $H_4L^2$, was reacted with $ZrCl_4$ anhydrate in DMF with benzoic acid as the modulator at 120 °C for three days. It crystallises in space group *Cmmm* with a point symbol for net of {3ˆ78.4ˆ98.5ˆ14}, which is different from the $Zr_6(L^1)_2(\mu_3\text{-}O)_4(\mu_3\text{-}OH)_4(OH)_4(H_2O)_4$. In the framework, the Zr metal centres also form $Zr_6$ clusters and each $Zr_6$ cluster coordinates to thirty-two O centres, with sixteen O centres from eight separate carboxylate groups of eight distinct linkers, and the other sixteen O centres from the solvent molecules, which is similar to that of $Zr_6(L^1)_2(\mu_3\text{-}O)_4(\mu_3\text{-}OH)_4(OH)_4(H_2O)_4$. In addition, the $Zr_6$ cluster forms a slightly compressed octahedron instead of a regular one, with Zr1–Zr1 = 4.867(2) Å, Zr1–Zr2 = 3.495(2) Å, Zr2–Zr2 = 3.550(2) Å and 5.017(2) Å. There are two types of windows along the *a* axis, one features an open Zr site and the other features amine-functional groups, with sizes ca. 4 × 14 Å and 2 × 12 Å, respectively. The window along the *b* axis also features open Zr site, with a size of ca. 6 × 7 Å. The size of the diamond shaped window along the *c* axis is ca. 14 Å, which is the largest amongst the windows in the framework. The total void volume available to guest molecules in MFM-601 was estimated by PLATON/SOLV calculations to be 75.8%. Unlike the twisted conformation of the linker in $Zr_6(L^1)_2(\mu_3\text{-}O)_4(\mu_3\text{-}OH)_4(OH)_4(H_2O)_4$, the amine-functionalised linker adopts a coplanar style for the two internal phenyl rings, making the entire linker flat. Thus when

viewing along the *c* axis, the linker shows a "linear" geometry to the $Zr_6$ clusters through the deprotonated carboxylate groups as shown in Figure 4.8c. Furthermore, the amine groups are pointing along the edge of the channels, which are expected to enhance the uptake of $CO_2$.

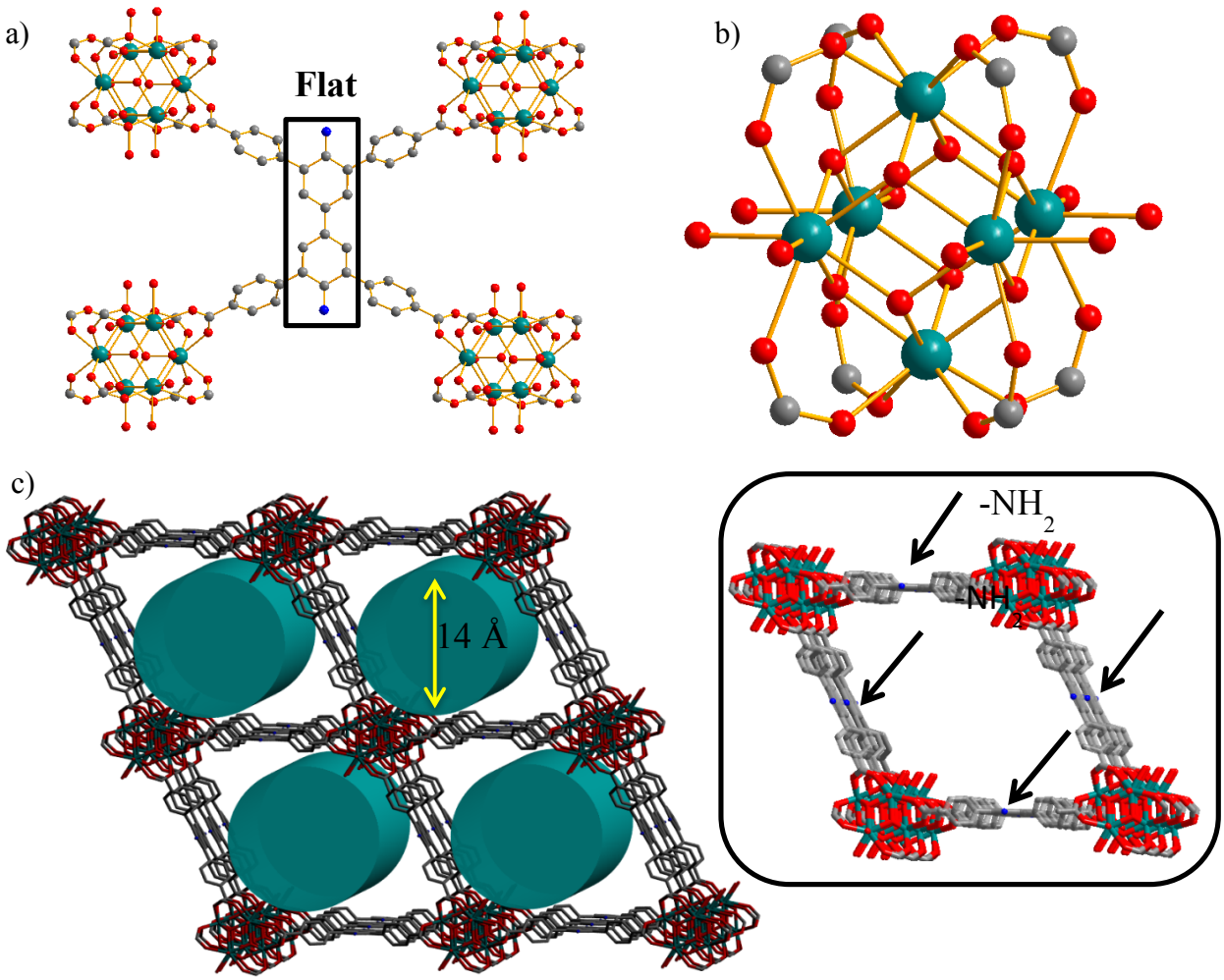



Figure 4.8 View of the single crystal structure of MFM-601. a) View of the coordination environment at the $Zr_6$ nodes and linker. b) View of the geometry of $Zr_6$ nodes. c) View of the channels running along the *c* axis. Oxygen: red; carbon: grey; nitrogen: blue; zirconium: green, hydrogen atoms are omitted for clarity.

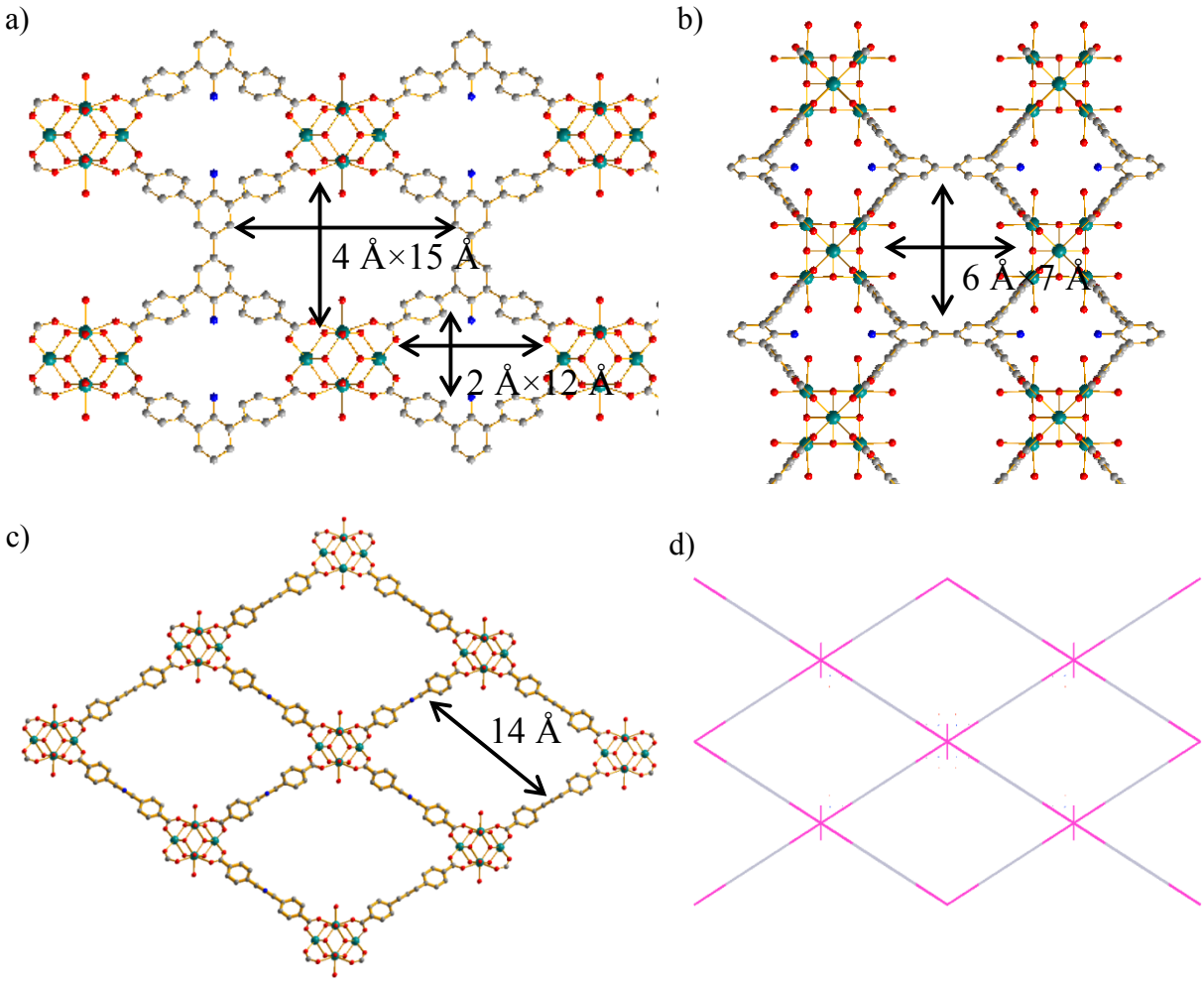



Figure 4.9 View of the pore and channel structure for MFM-601. a) View along *a* axis; b) view along *b* axis; c) view along *c* axis. d) Schematic representation of the unprecedented (4,8)-connected net for MFM-601 framework along *c* axis, in which $Zr_6$ cluster and $H_4L^2$ ligand are simplified as purple and grey nodes, respectively. Oxygen: red; carbon: grey; nitrogen: blue; zirconium: green, hydrogen atoms are omitted for clarity.

#### 4.3.1.3 Comparison of ligands conformation for $L^1$ and $L^2$ in $Zr_6(L^1)_2(\mu_3\text{-}O)_4(\mu_3\text{-}OH)_4(OH)_4(H_2O)_4$ and MFM-601, respectively

The $H_4L^1$ linker and amine-functionalised linker $H_4L^2$ are both flexible with rotational C–C bonds labelled as R1 and R2 shown below. R1 is the C–C bond between the two internal phenyl rings; R2 is the C–C bond between the internal and external phenyl rings. When constructing $Zr_6(L^1)_2(\mu_3\text{-}O)_4(\mu_3\text{-}OH)_4(OH)_4(H_2O)_4$, the two internal phenyl rings show a dihedral angle of ca. 56° with respect to each other. However, in the framework of MFM-601, the two internal phenyl rings show a dihedral angle of 180° with each other. In contrast with the different conformation of R1 bonds, the four R2 bonds in the two MOFs rotate similar angles, with the dihedral angle of ca. 40–50°. With the two distinct

conformation of linkers, $Zr_6(L^1)_2(\mu_3\text{-}O)_4(\mu_3\text{-}OH)_4(OH)_4(H_2O)_4$ and MFM-601 form totally different structures.

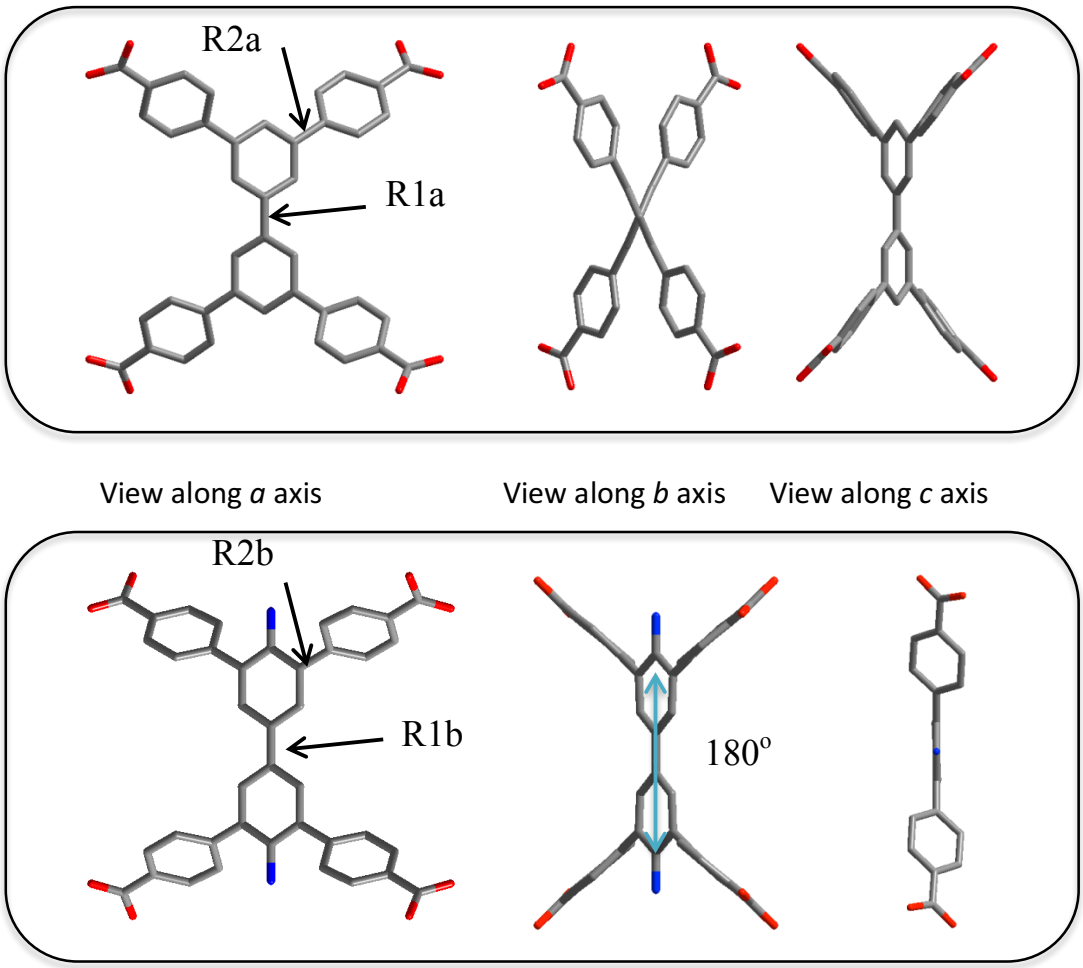



Figure 4.10 Wireframe representation of the linkers $L^1$ and $L^2$ in $Zr_6(L^1)_2(\mu_3\text{-}O)_4(\mu_3\text{-}OH)_4(OH)_4(H_2O)_4$ (top) and MFM-601 (bottom).

### 4.3.2 PXRD and TGA results

#### 4.3.2.1 PXRD and TGA discussions for $Zr_6(L^1)_2(\mu_3\text{-}O)_4(\mu_3\text{-}OH)_4(OH)_4(H_2O)_4$ and $Hf_6(L^1)_2(\mu_3\text{-}O)_4(\mu_3\text{-}OH)_4(OH)_4(H_2O)_4$

The retention of crystallinity and thermostability of $Zr_6(L^1)_2(\mu_3\text{-}O)_4(\mu_3\text{-}OH)_4(OH)_4(H_2O)_4$ and $Hf_6(L^1)_2(\mu_3\text{-}O)_4(\mu_3\text{-}OH)_4(OH)_4(H_2O)_4$ were investigated by combined PXRD and TGA. The phase purity of the as-synthesised sample of $Zr_6(L^1)_2(\mu_3\text{-}O)_4(\mu_3\text{-}OH)_4(OH)_4(H_2O)_4$ has been confirmed by good match between the experimental and the simulated PXRD from single-crystal data. However, the

peaks in the PXRD pattern of the acetone-exchanged sample show significant broadening, suggesting a certain degree of loss of crystallinity of the material.

TGA of the as-synthesised $Zr_6(L^1)_2(\mu_3\text{-}O)_4(\mu_3\text{-}OH)_4(OH)_4(H_2O)_4$ material under $N_2$ showed a two-step weight loss between 30 °C and 150 °C, which corresponds to the solvent molecules in the pores of the framework. It then reached a plateau between 150 °C and 500 °C. Compared with the TGA of the linkers, the retention of weight at 150–500 °C indicates no linker molecules trapped in the material. A sharp weight loss started to occur at ca. 500 °C, indicating the decomposition of the structure. The weight percentage eventually stabilised to ca. 17% at 550 °C which is associated to the formation of $Zr(OH)_2CO_3 \cdot ZrO_2$. The TGA of the acetone-exchanged sample of $Zr_6(L^1)_2(\mu_3\text{-}O)_4(\mu_3\text{-}OH)_4(OH)_4(H_2O)_4$ carried out under an $N_2$ atmosphere suggests a similar thermostability to that of the as-synthesised. It started to decompose at 500 °C and completely converted to $Zr(OH)_2CO_3 \cdot ZrO_2$ at 545 °C.

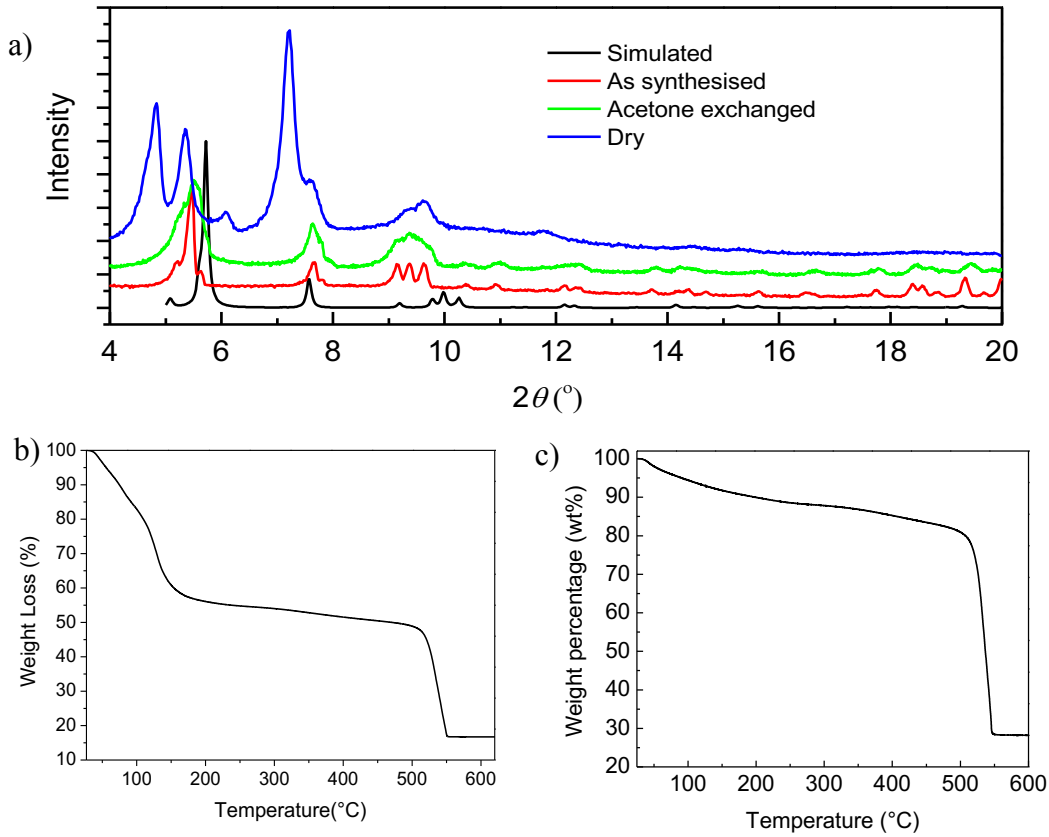



Figure 4.11 PXRD and TGA for $Zr_6(L^1)_2(\mu_3\text{-}O)_4(\mu_3\text{-}OH)_4(OH)_4(H_2O)_4$. a), comparison of simulated, as-synthesised and acetone-exchanged PXRD patterns; b) TGA of as-synthesised sample; c) TGA of acetone-exchanged sample.

The phase purity of the as-synthesised sample of $Hf_6(L^1)_2(\mu_3\text{-}O)_4(\mu_3\text{-}OH)_4(OH)_4(H_2O)_4$ has been confirmed by PXRD analysis which exhibits good agreement with the simulated pattern from single crystal data. However, the PXRD of the acetone-exchanged sample showed significant peak broadening, reduction of intensity and loss of high angle diffraction peaks, suggesting a certain degree of loss of crystallinity of the material. The TGA of both as-synthesised and acetone-exchanged sample have been carried out and confirm the decomposition point at ca. 480 °C.

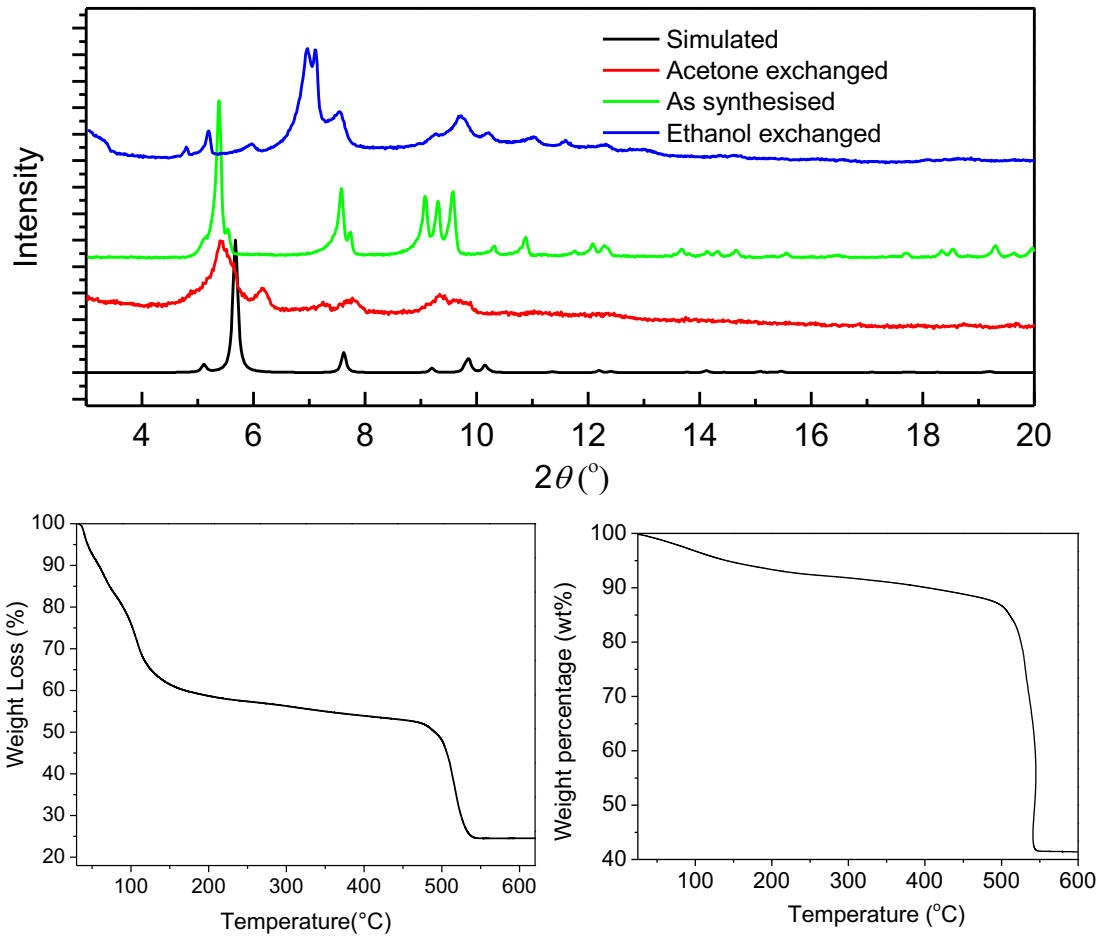



Figure 4.12 PXRD and TGA for $Hf_6(L^1)_2(\mu_3\text{-}O)_4(\mu_3\text{-}OH)_4(OH)_4(H_2O)_4$. a) Comparison of simulated, as-synthesised and acetone-exchanged PXRD patterns; b) TGA of as-synthesised sample; c) TGA of acetone-exchanged sample.

#### 4.3.2.2 PXRD and TGA results for MFM-601 and $Hf_6(L^2)_2(\mu_3\text{-}O)_4(\mu_3\text{-}OH)_4(OH)_4(H_2O)_4$

The retention of crystallinity and thermostability of MFM-601 and $Hf_6(L^2)_2(\mu_3\text{-}O)_4(\mu_3\text{-}OH)_4(OH)_4(H_2O)_4$ have been investigated by combined PXRD and TGA. The phase purity of bulk MFM-601 material is confirmed by excellent agreement with the simulated one from single-crystal data. The thermostability of as-synthesised MFM-601 is similar to that of $Zr_6(L^1)_2(\mu_3\text{-}O)_4(\mu_3\text{-}OH)_4(OH)_4(H_2O)_4$, which decomposes at ca. 500 °C. However, the acetone-exchanged MFM-601 shows a plateau in the temperature range of ca. 150–300 °C, with a further weight loss above 300 °C, which is due to the removal of framework coordinated solvents. The material is consequently confirmed to be thermally stable up to ca. 400 °C.

The product of $Hf_6(L^2)_2(\mu_3\text{-}O)_4(\mu_3\text{-}OH)_4(OH)_4(H_2O)_4$ is microcrystalline and we could not obtain crystals large enough for single-crystal X-ray diffraction analysis. Thus the PXRD of bulk material of $Hf_6(L^2)_2(\mu_3\text{-}O)_4(\mu_3\text{-}OH)_4(OH)_4(H_2O)_4$ is compared with the simulated one from MFM-601. The PXRD of the as-synthesised $Hf_6(L^2)_2(\mu_3\text{-}O)_4(\mu_3\text{-}OH)_4(OH)_4(H_2O)_4$ shows good agreement with the simulated one of MFM-601, indicating $Hf_6(L^2)_2(\mu_3\text{-}O)_4(\mu_3\text{-}OH)_4(OH)_4(H_2O)_4$ is most likely an isostructure of MFM-601. However, the PXRD for acetone-exchanged sample show obvious peak shifts and absence of high-angle peaks compared with that of the as-synthesised sample, indicating a certain degree of loss of crystallinity of this material upon solvent exchange. TGA of the acetone-exchanged sample confirms this material is thermally stable up to 400 °C.

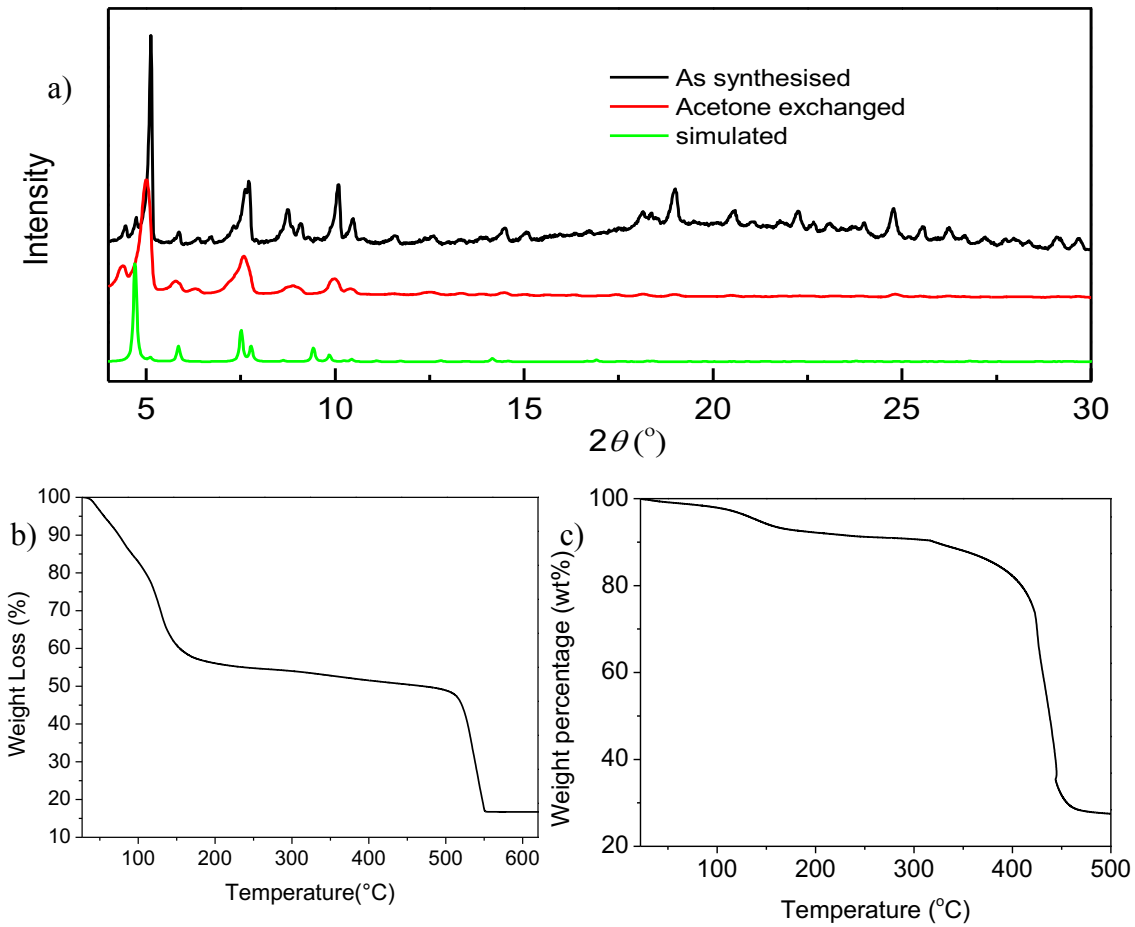



Figure 4.13 PXRD and TGA for MFM-601. a) comparison of simulated, as-synthesised and acetone-exchanged PXRD patterns; b) TGA of as-synthesised MFM-601; c) TGA of acetone-exchanged MFM-601.

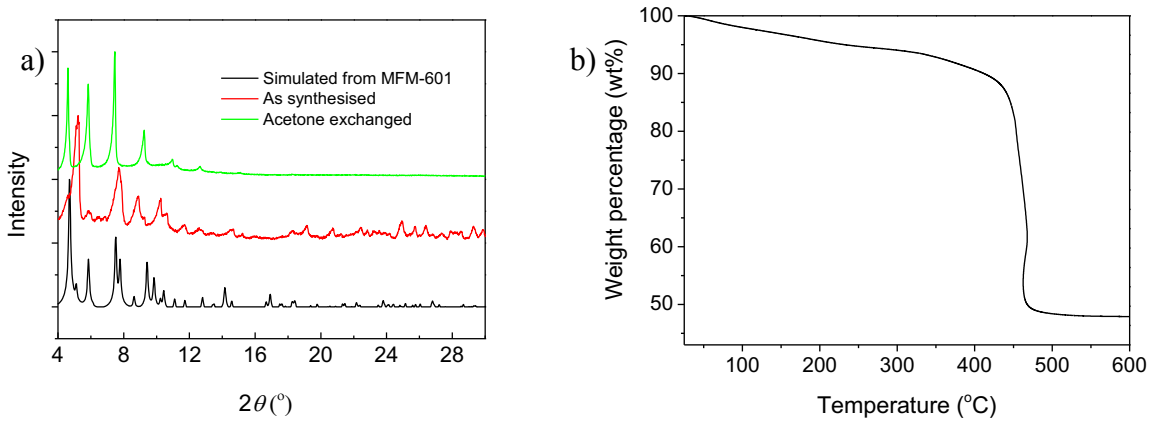



Figure 4.14 PXRD and TGA for $Hf_6(L^2)_2(\mu_3\text{-}O)_4(\mu_3\text{-}OH)_4(OH)_4(H_2O)_4$. a) Comparison of simulated, as-synthesised and acetone-exchanged PXRD patterns; b) TGA of acetone-exchanged sample.

## 4.4 Gas sorption and separation investigations

### 4.4.1 Activation for $Zr_6(L^1)_2(\mu_3\text{-}O)_4(\mu_3\text{-}OH)_4(OH)_4(H_2O)_4$/ $Hf_6(L^1)_2(\mu_3\text{-}O)_4(\mu_3\text{-}OH)_4(OH)_4(H_2O)_4$/ $Hf_6(L^2)_2(\mu_3\text{-}O)_4(\mu_3\text{-}OH)_4(OH)_4(H_2O)_4$

$Zr_6(L^1)_2(\mu_3\text{-}O)_4(\mu_3\text{-}OH)_4(OH)_4(H_2O)_4$, $Hf_6(L^1)_2(\mu_3\text{-}O)_4(\mu_3\text{-}OH)_4(OH)_4(H_2O)_4$ and $Hf_6(L^2)_2(\mu_3\text{-}O)_4(\mu_3\text{-}OH)_4(OH)_4(H_2O)_4$ are not stable on desolvation either by traditional activation or by $scCO_2$ drying method. Thus, no apparent $N_2$ adsorption was observed for these three materials and BET areas for these samples are estimated to be ~25 $m^2\ g^{-1}$, which is close to the single surface area for the solid materials.

### 4.4.2 Gas sorption and separation investigations for MFM-601

Since MFM-601 shows high stability against solvent removal, gravimetric hydrocarbon ($CH_4$, $C_2H_2$, $C_2H_4$, $C_2H_6$, $C_3H_6$ and $C_3H_8$) and $CO_2$ isotherms have been carried out at various temperatures.

#### 4.4.2.1 $N_2$ sorption studies

From $N_2$ adsorption data collected at 77 K, the BET surface area for MFM-601 was estimated to be 2953 $m^2\ g^{-1}$. At 273–303 K and 1 bar, The $N_2$ uptakes are extremely low and lie in the range of 0.03–0.1 mmol $g^{-1}$ as shown in Table 4.1. It is noteworthy that at 283–303 K, the isotherms could not reach stable sorption equilibrium due to the very weak interaction of the guest molecules and the framework. However, at 273 K, the material starts to reach stable sorption equilibrium and give an uptake of ca. 0.10 mmol $g^{-1}$ at 1 bar as shown in Figure 4.15.

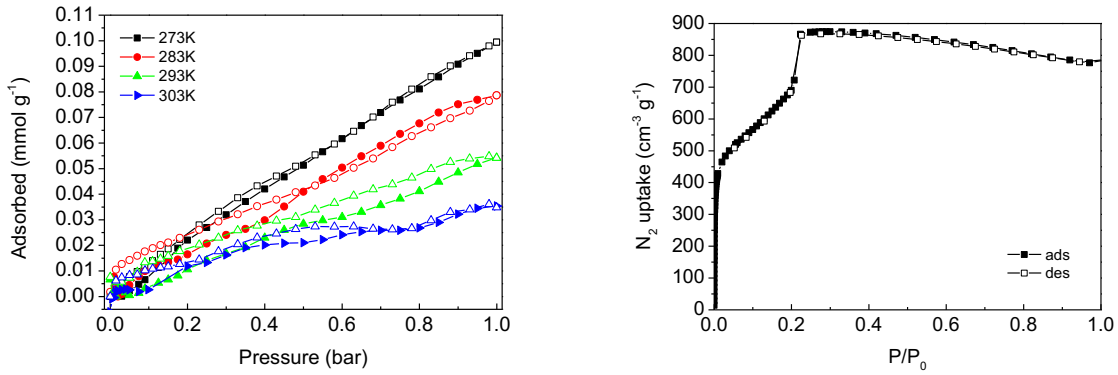



Figure 4.15 $N_2$ isotherms for MFM-601 at 273 K, 283 K, 293 K and 303 K (a) and 77 K (b). Solid symbols: adsorption; open symbols: desorption.

Table 4.1 The uptake amounts of $N_2$ for MFM-601 at 1 bar.

| **Temperature (K)** | 77 | 273 | 283 | 293 | 303 |
|---|---|---|---|---|---|
| **$N_2$ uptakes (mmol $g^{-1}$)** | 38.7 | 0.10 | 0.08 | 0.05 | 0.03 |

#### 4.4.2.2 Hydrocarbon sorption and separation investigations

##### 4.4.2.2.1 Hydrocarbon sorption and separation investigations at 273–303 K

The uptakes of $CH_4$ exhibit reversible adsorption and desorption type I isotherms at 273 K (black), 283 K (red), 293 K (green) and 303 K (blue) and 8 bar as shown in Figure 4.16. The four isotherms are near-linear below 1 bar and non-linear at 8 bar. MFM-601 shows comparable $CH_4$ uptake (ca. 3.1 mmol $g^{-1}$ at 273 K) with the reported Zr-based MOFs at 8 bar, such as NU-1100 (ca. 5 mmol $g^{-1}$ at 270 K) and dehydroxylated/hydroxylated UiO-66 (Zr) (ca. 3.9 and 4.3 mmol $g^{-1}$ at 270 K) [3,22] as shown in Table 4.10.

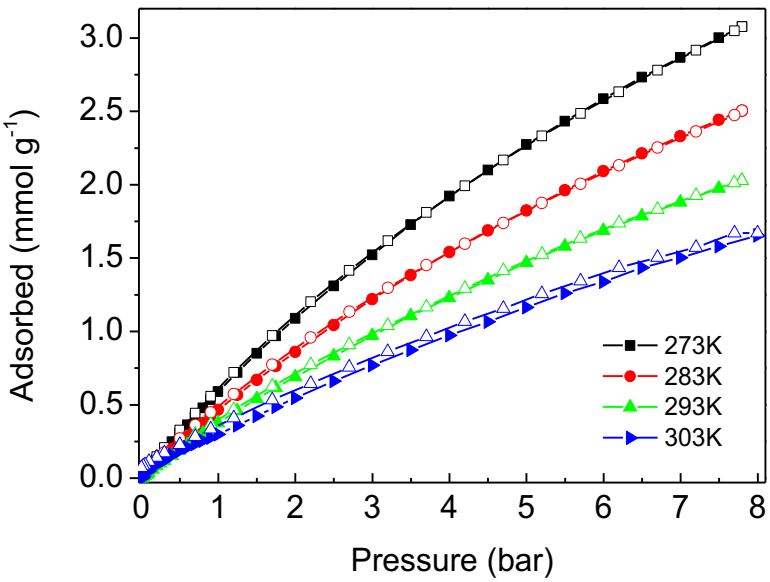



Figure 4.16 $CH_4$ isotherms for MFM-601 at 273 K, 283 K, 293 K and 303 K. Solid symbols: adsorption; open symbols: desorption.

Table 4.2 The uptake amounts of $CH_4$ at 1 bar and 8 bar from 273 K to 303 K.

| **Temperature (K)** | 273 | | 283 | | 293 | | 303 | |
|---|---|---|---|---|---|---|---|---|
| **Pressure (bar)** | 1 | 8 | 1 | 8 | 1 | 8 | 1 | 8 |
| **$CH_4$ uptake (mmol $g^{-1}$)** | 0.59 | 3.08 | 0.47 | 2.50 | 0.38 | 2.03 | 0.30 | 1.65 |

The uptakes of $C_2H_2$ exhibit fully reversible adsorption and desorption type I isotherms at 273 K (black), 283 K (red), 293 K (green) and 303 K (blue) and 1 bar. The isotherms at the four temperatures are near-linearly shaped without indications for the knee points, suggesting unsaturated uptakes for $C_2H_2$ at 1 bar. MFM-601 shows comparable $C_2H_2$ uptake (2.34 mmol $g^{-1}$) at 293 K and 1 bar with MFM-202a (3.44 mmol $g^{-1}$), which is also a highly porous material (porosity 70%).[11] Similar to MFM-202a, the gap of the uptake for MFM-601 at low temperature is larger than that at high temperature, as shown in Figure 4.17, i.e., the uptake at 273 K is 1.22 mmol $g^{-1}$ higher than that at 283 K and the uptake at 293 K is only 0.66 mmol $g^{-1}$ higher than that at 303 K.

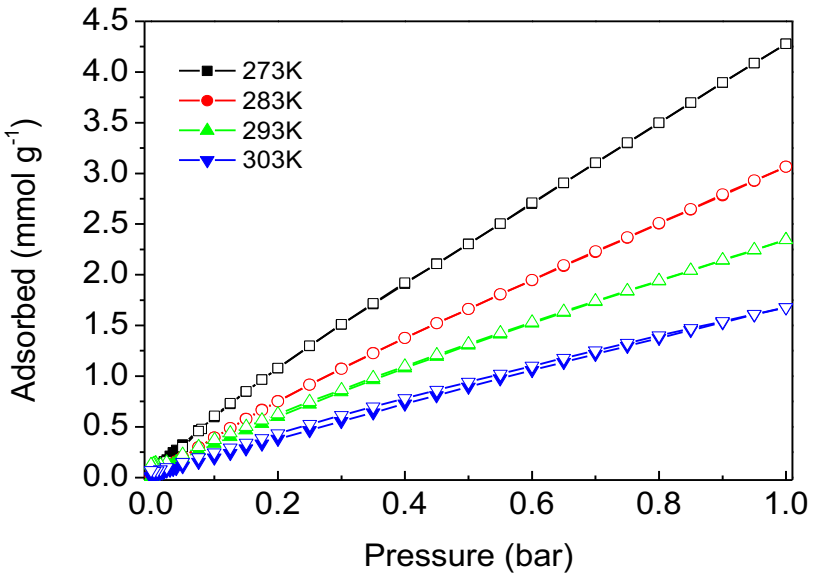



Figure 4.17 $C_2H_2$ isotherms for MFM-601 at 273 K, 283 K, 293 K and 303 K. Solid symbols: adsorption; open symbols: desorption.

Table 4.3 The uptake amounts of $C_2H_2$ at 1 bar from 273 K to 303 K.

| **Temperature (K)** | 273 | 283 | 293 | 303 |
|---|---|---|---|---|
| **$C_2H_2$ uptake (mmol $g^{-1}$)** | 4.28 | 3.06 | 2.34 | 1.68 |

The $C_2H_4$ uptakes carried out at 274 K (black), 283 K (red), 293 K (green) and 303 K (blue) and 1 bar are shown in Figure 4.18. The uptake isotherms at the four temperatures are near-linearly shaped and show reversible adsorption and desorption processes, which are similar to the isotherms of $C_2H_2$. It shows $C_2H_4$ uptake of 2.3 mmol $g^{-1}$ at 293 K and 1 bar, which is comparable to the reported MOFs (e.g. MFM-202a: 2.9 mmol $g^{-1}$).[20] In addition, the uptakes of $C_2H_2$ (2.34 mmol $g^{-1}$) and $C_2H_4$ are very close, which is due to the similar physical properties of the two molecules as shown in Table 2.2. This phenomenon has also been reported in other MOFs with large porosity.[20] The uptake capacity of MFM-601 at 274 K and 1 bar is 3.9 mmol $g^{-1}$, which is more than five times higher than the $CH_4$ uptake at the same condition.

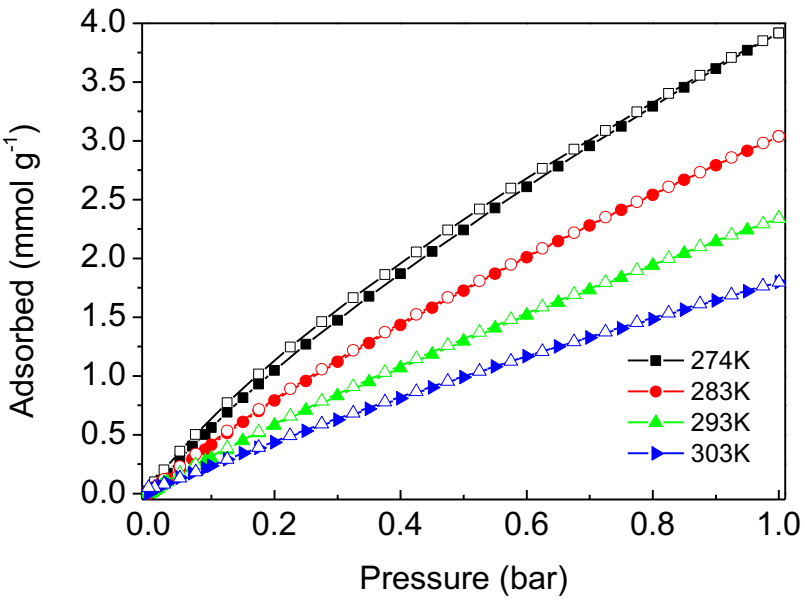



Figure 4.18 $C_2H_4$ isotherms for MFM-601 at 273 K, 283 K, 293 K and 303 K. Solid symbols: adsorption; open symbols: desorption.

Table 4.4 The uptake amounts of $C_2H_4$ at 1 bar from 274 K to 303 K.

| **Temperature (K)** | 274 | 283 | 293 | 303 |
|---|---|---|---|---|
| **$C_2H_4$ uptake (mmol $g^{-1}$)** | 3.92 | 3.04 | 2.34 | 1.80 |

The $C_2H_6$ uptakes carried out at 273 K (black), 283 K (red), 293 K (green) and 303 K (blue) and up to 4 bar are shown in Figure 4.19. The isotherms at the four temperatures exhibit near-linear profiles below 1 bar, which are similar to $C_2H_2$ and $C_2H_4$. However, these isotherms show fully reversible adsorption and desorption processes with obvious inflection points upon high-pressure sorption. Its uptake at 293 K and 1 bar is 3.1 mmol $g^{-1}$ and at 4 bar is 6.9 mmol $g^{-1}$, which are comparable to the reported MOFs.[20] The differences of $C_2H_6$ uptake capacities at every 10 K increase show a similar increment of 1 mmol $g^{-1}$ at the four temperatures. Compared with $C_2H_4$ and $C_2H_2$, MFM-601 shows higher uptake of $C_2H_6$ at a given temperature and pressure.

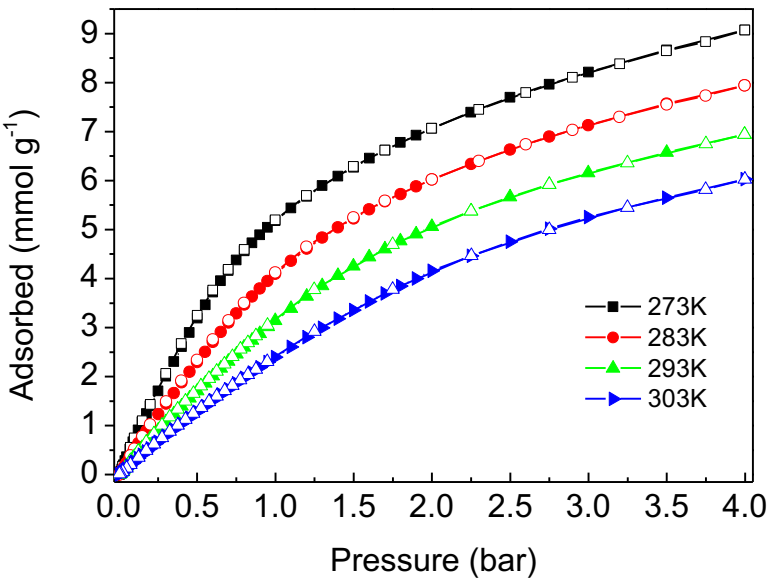



Figure 4.19 $C_2H_6$ isotherms for MFM-601 at 273 K, 283 K, 293 K and 303 K. Solid symbols: adsorption; open symbols: desorption.

Table 4.5 The uptake amounts of $C_2H_6$ at 1 bar and 4 bar from 273 K to 303 K.

| **Temperature (K)** | 273 | | 283 | | 293 | | 303 | |
|---|---|---|---|---|---|---|---|---|
| **Pressure (bar)** | 1 | 4 | 1 | 4 | 1 | 4 | 1 | 4 |
| **$C_2H_6$ uptake (mmol $g^{-1}$)** | 5.18 | 9.07 | 4.10 | 7.94 | 3.14 | 6.94 | 2.40 | 6.03 |

Apart from the $CH_4$ and $C_2$ hydrocarbons, the $C_3H_6$ and $C_3H_8$ uptakes were also carried out at 273 K (black), 283 K (red), 293 K (green) and 303 K (blue) and 1 bar as shown in Figure 4.20 and Figure 4.21, respectively. Their uptake isotherms at the four temperatures show fully reversible adsorption and desorption processes and reach near saturation at 1 bar. The uptake of $C_3H_6$ at 293 K and 1 bar is 7.1 mmol $g^{-1}$, which is comparable to the MFM-202a (7.2 mmol $g^{-1}$).[20] However, the uptake capacity at 273 K and 1 bar is 9.3 mmol $g^{-1}$, which is higher than that of MFM-202a (8.6 mmol $g^{-1}$).[20] Unlike MFM-202a, which shows a sharp increase of the uptake at 273 K, MFM-601 exhibits equal uptake increase between every two measurements among the four temperatures, as shown in Table 4.6.

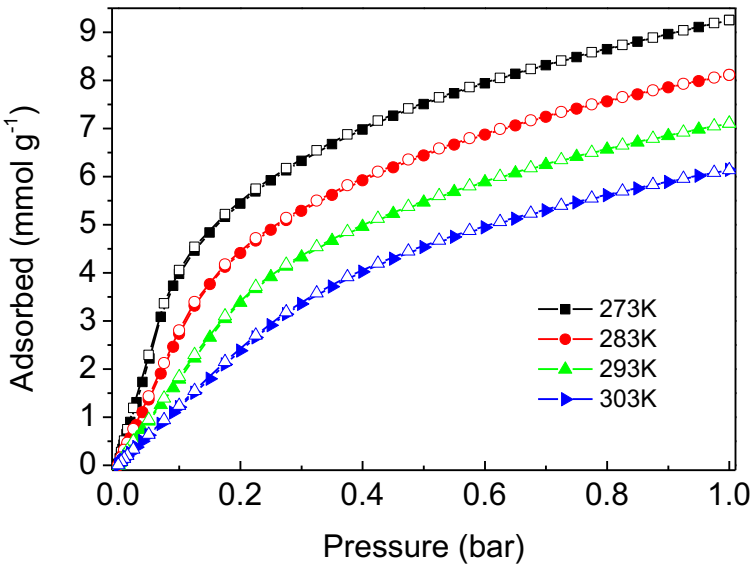



Figure 4.20 $C_3H_6$ isotherms for MFM-601 at 273 K, 283 K, 293 K and 303 K. Solid symbols: adsorption; open symbols: desorption.

Table 4.6 The uptake amounts of $C_3H_6$ at 1 bar from 273 K to 303 K.

| **Temperature (K)** | 273 | 283 | 293 | 303 |
|---|---|---|---|---|
| **$C_3H_6$ uptakes (mmol $g^{-1}$)** | 9.25 | 8.11 | 7.11 | 6.14 |

The uptake of $C_3H_8$ at 293 K and 1 bar is 7.0 mmol $g^{-1}$, which is comparable to MFM-202a (6.8 mmol $g^{-1}$). At 273 K and 1 bar, its uptake reaches 9.2 mmol $g^{-1}$, which is much higher than that of MFM-202a (7.5 mmol $g^{-1}$). However, the uptake capacity and isotherm shape of $C_3H_8$ are similar to those of $C_3H_6$, which is due to the similar physical properties of the two molecules, such as their similar polarizabilities and kinetic diameters as shown in Table 2.2.

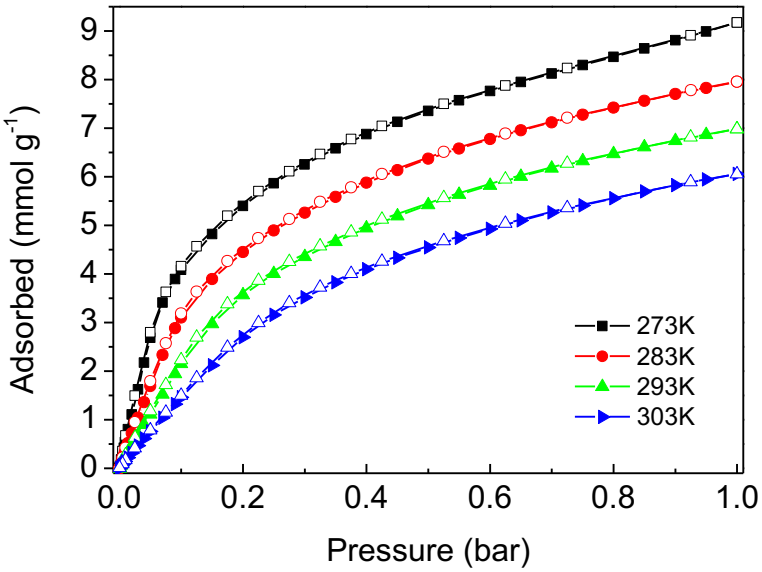



Figure 4.21 $C_3H_8$ isotherms for MFM-601 at 273 K, 283 K, 293 K and 303 K. Solid symbols: adsorption; open symbols: desorption.

Table 4.7 The uptake amount of $C_3H_8$ at 1 bar from 273 K to 303 K.

| **Temperature (K)** | 273 | 283 | 293 | 303 |
|---|---|---|---|---|
| **$C_3H_8$ uptake (mmol $g^{-1}$)** | 9.18 | 7.96 | 6.99 | 6.06 |

#### 4.4.2.2.2 Hydrocarbon sorption investigations at low temperature

The uptake isotherms of $CH_4$, $C_2$ and $C_3$ hydrocarbons have also been carried out at low temperature and 1 bar, as shown in Figure 4.22. Compared with the uptake capacities of these light hydrocarbons at 293 K, the low temperature isotherms show a similar trend below 0.1 bar, i.e., $C_3$s > $C_2$s > $CH_4$, corresponding to molecular size and polarizability. However, compared with the uptake amount sequence among the $C_2$ hydrocarbons at 273–303 K, which is $C_2H_4 > C_2H_6 \approx C_2H_2$, these three $C_2$ hydrocarbons exhibit a different uptake sequence of $C_2H_2 > C_2H_6 > C_2H_4$ at low temperature. It is notable that both $C_2H_2$ and $C_2H_6$ isotherms show stepwise adsorption at ca. 0.4 bar and hysteretic desorption processes at ca. 0.42 bar. Similarly, the isotherms of $C_3H_6$ and $C_3H_8$ also show stepwise uptakes. Additionally, their desorption isotherms show slight hysteresis compared with the adsorption isotherms. In contrast, the uptakes of $CH_4$ and $C_2H_4$ show fully reversible type I isotherms at low temperature.

Compared with the uptakes of light hydrocarbons in MFM-202a, MFM-601 shows slightly lower uptake of $CH_4$ but much higher uptakes of $C_2H_2$, $C_2H_4$, $C_2H_6$, $C_3H_6$ and $C_3H_8$ at low temperature, as shown in Table 4.8. Interestingly, the uptake of $C_2H_2$ exhibits the highest capacity than the other light hydrocarbons in both MFM-601 and MFM-202a. The uptake of $C_2H_2$ (26.4 mmol $g^{-1}$) in MFM-601 is approximately 1.5 times of that in MFM-202a (18.3 mmol $g^{-1}$). In particular, the uptake amount of $C_2H_6$ (20.6 mmol $g^{-1}$) is much higher than that in MFM-202a (11.9 mmol $g^{-1}$). The uptake amount of $C_3H_6$ (18.0 mmol $g^{-1}$) is 1.5 times of that in MFM-202a (12.1 mmol $g^{-1}$) and the uptake capacity amount of $C_3H_8$ (16.5 mmol $g^{-1}$) is approximately 1.8 times of that in MFM-202a (9.0 mmol $g^{-1}$).

The PXRD of MFM-601 after the hydrocarbon sorption experiments was carried out to give insight into the crystallinity of the material, as shown in Figure 4.23. The PXRD pattern after hydrocarbon gases sorption shows good agreement with the as-synthesised sample, with sharp diffraction peaks at low angles and the presence of a series of peaks at high angles, confirming the retention of crystallinity.

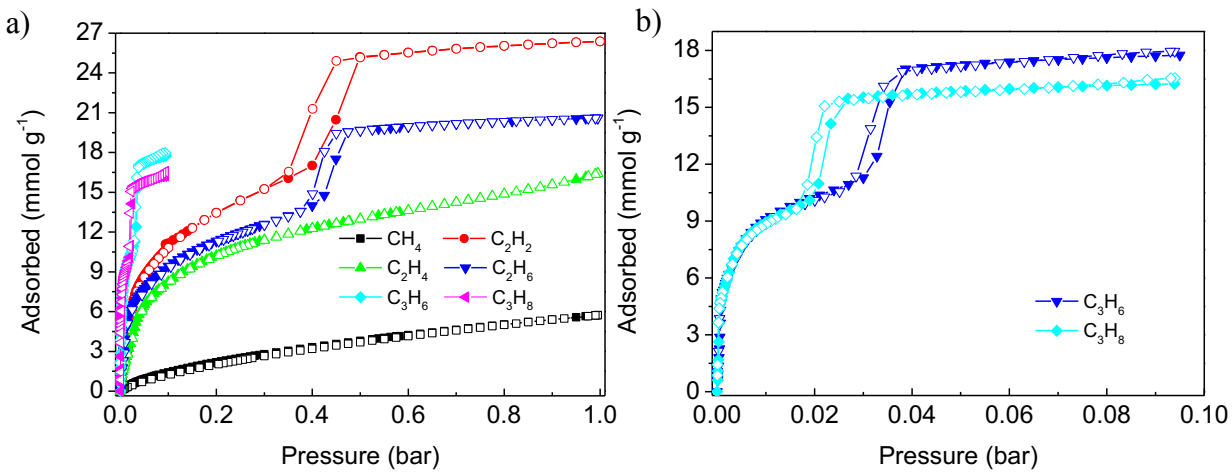



Figure 4.22 a) Hydrocarbon isotherms for MFM-601 at 195 K. b) Rescaled representation of the isotherms of $C_3H_6$ and $C_3H_8$ at low temperature. Solid symbols: adsorption; open symbols: desorption.

Table 4.8 Comparison of the hydrocarbon uptakes in MFM-601 with MFM-202a at low temperature.

| Sample | Gas uptake (mmol $g^{-1}$) | | | | | |
|---|---|---|---|---|---|---|
| | $CH_4$ | $C_2H_2$ | $C_2H_4$ | $C_2H_6$ | $C_3H_6$ | $C_3H_8$ |
| **MFM-202a** | 6.21 | 18.3 | 14.8 | 11.9 | 12.1 | 9.00 |
| **MFM-601** | 5.73 | 26.4 | 16.4 | 20.6 | 18.0 | 16.5 |

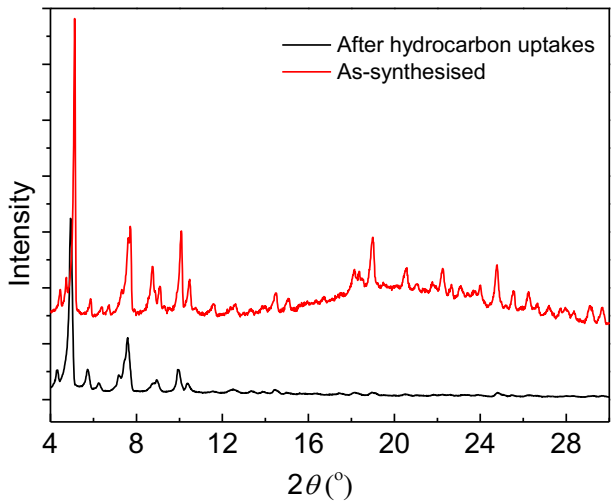



Figure 4.23 Comparison of the as-synthesised and the post-hydrocarbon-sorption-measurements PXRD patterns for MFM-601.

#### 4.4.2.3 Other gas sorption and separation investigations

##### 4.4.2.3.1 $CO_2$ sorption

Apart from the isotherms of hydrocarbons, $CO_2$ uptakes of MFM-601 have also been carried out, as shown in Figure 4.24. The four isotherms were performed at 273 K, 283 K, 293 K and 303 K and show fully reversible type I sorption and desorption processes. The uptake of $CO_2$ at 293 K and 15 bar is ca. 10.1 mmol $g^{-1}$ and the uptake at 273 K and 15 bar is ca. 15.1 mmol $g^{-1}$. These values are both comparable to those in MFM-202a (~13 mmol $g^{-1}$ at 293 K, ~16 mmol $g^{-1}$ at 273 K).

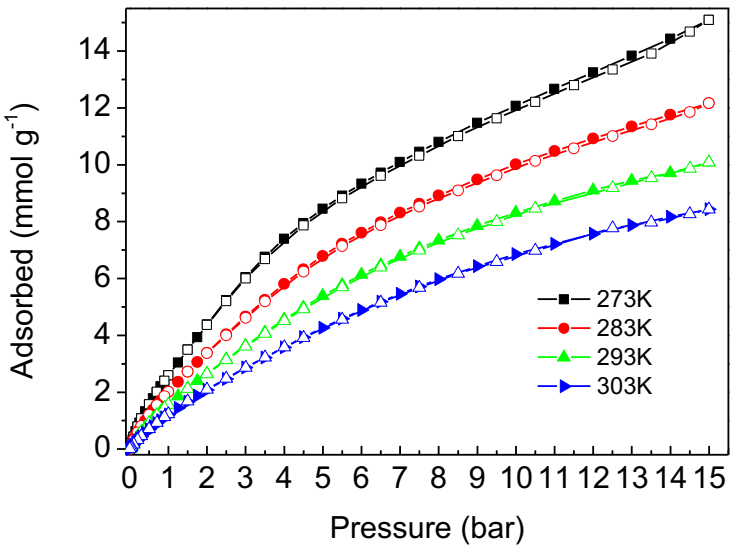



Figure 4.24 $CO_2$ isotherms for MFM-601 at 273 K, 283 K, 293 K and 303 K. Solid symbols: adsorption; open symbols: desorption.

Table 4.9 The uptake amounts of $CO_2$ at 1 bar and 15 bar from 273 K to 303 K.

| **Temperature (K)** | 273 | | 283 | | 293 | | 303 | |
|---|---|---|---|---|---|---|---|---|
| **Pressure (bar)** | 1 | 15 | 1 | 15 | 1 | 15 | 1 | 15 |
| **$CH_4$ uptake (mmol $g^{-1}$)** | 2.6 | 15.1 | 2.0 | 12.2 | 1.6 | 10.1 | 1.2 | 8.4 |

The uptakes of $CO_2$ at low temperature were measured in two cycles and both show stepwise sorption process and hysteretic desorption process, as shown in Figure 4.25. However, the hysteretic loop

becomes smaller in the second uptake cycle. Furthermore, the starting pressure for the stepwise sorption during the first cycle is at 0.65 bar and then reaches saturation at 0.85 bar; the hysteretic desorption starts at 0.85 bar and then shows a sharp decrease at 0.68 bar, finally the desorption isotherm overlaps with the sorption isotherm at 0.53 bar. In the second cycle, the starting pressure of the stepwise sorption also occurs at 0.65 bar. However, the sorption reaches saturation at 0.75 bar which is a lower pressure than that in the first cycle. The hysteretic desorption occurs at 0.75 bar and then exhibits a sharp decrease at similar pressure to the first cycle, i.e., 0.68 bar, but rapidly overlaps with the sorption isotherm at 0.6 bar, which is a higher pressure than that in the first cycle. Furthermore, the uptakes of $CO_2$ at low temperature during the two cycles show exactly the same capacity of 31.3 mmol $g^{-1}$, which is amongst the best-performing MOFs.[3]

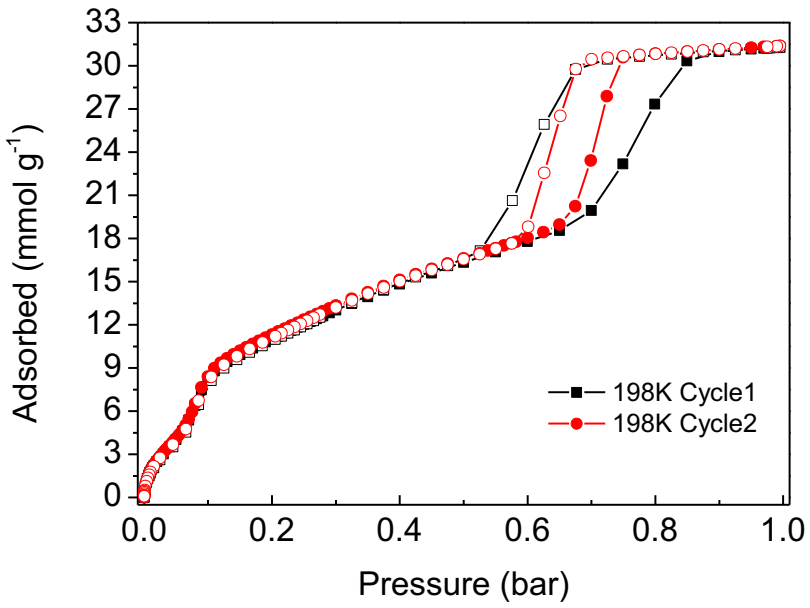



Figure 4.25 $CO_2$ isotherms for MFM-601 at low temperature. Solid symbols: adsorption; open symbols: desorption.

#### 4.4.2.3.2 *In situ* PXRD investigations of $CO_2$-loaded MFM-601

To gain insights into the structure of MFM-601 upon $CO_2$ adsorption at 195 K, *in situ* PXRD experiments have been carried out. Compared with the PXRD of the bare sample at 298 K, the PXRD pattern at 195 K shows obvious peak shifts as shown in Figure 4.26, which indicates a certain degree of structural flexibility with temperature. Interestingly, when dosed with 1 bar of $CO_2$, the PXRD of MFM-601 exhibits a decrease of intensity combined with significant peak shifts in comparison with that of the bare material at 195 K. Given that there was no change in the experimental settings of the sample or the synchrotron beam before and after $CO_2$ loading, the reduced diffraction intensity confirms the microscopic host-$CO_2$ disordering at 195 K. Furthermore, this material underwent a structural change upon adsorption of $CO_2$, which is similar to that of the $CO_2$-loaded MFM-202a.[11]

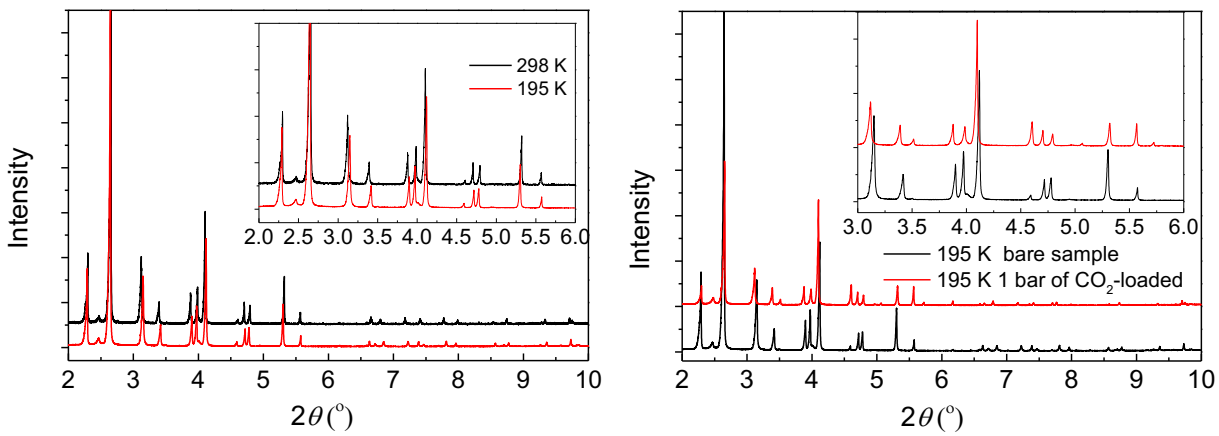



Figure 4.26 Comparisons of *in situ* synchrotron PXRD patterns for the bare sample collected at 298 K and 195 K (a), bare sample and $CO_2$-loaded MFM-601 at 195 K (b), λ = 0.82617 (2) Å.

#### 4.4.2.3.3 $NH_3$ sorption

The $NH_3$ isotherms were carried out at 298 K and 1 bar for three cycles to gain insights into the stability of the framework upon sorption. In the first cycle, the uptake at 1 bar reaches 6.5 mmol $g^{-1}$ and shows a slightly hysteretic desorption profile due to the strong interaction of $NH_3$ with the framework. In addition, this continuous increase in the adsorption isotherm of $NH_3$ for MFM-601 indicates that it does not reach saturation at 1 bar and shows storage potential at higher pressure. The regeneration after cycle 1 was carried out at 80 °C for 2 hours. However, the uptake during the second cycle is ca. 1 mmol $g^{-1}$ less than that in the first cycle at 1 bar. In the third cycle, the uptake reaches ca. 6.0 mmol $g^{-1}$, which is higher than that in the second cycle but lower than that in the first cycle.

PXRD was carried out for MFM-601 after the $NH_3$ uptake as shown in Figure 4.27. Compared with the PXRD of the as-synthesised sample, there are only two broad and weak diffraction peaks at low angle with the absence of high angle peaks for the sample after $NH_3$ sorption, indicating the loss of crystallinity after the $NH_3$ sorption.

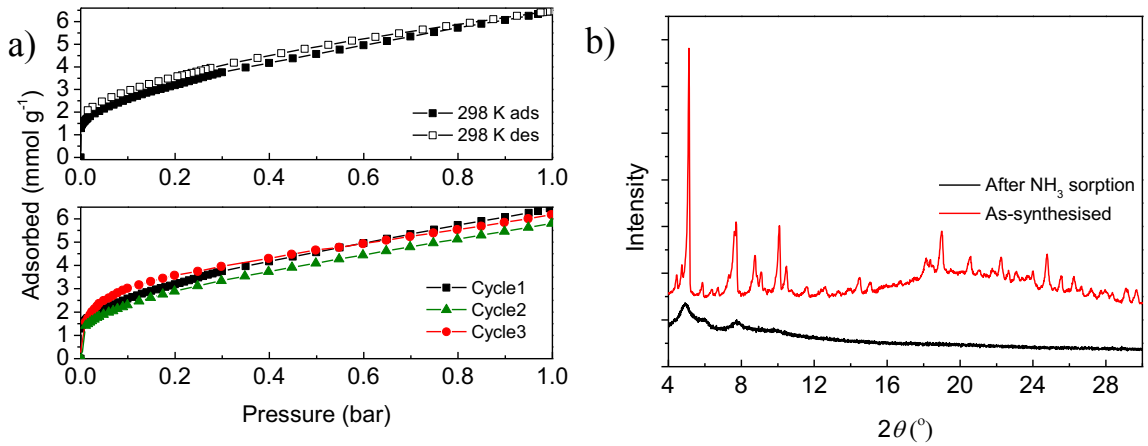



Figure 4.27 $NH_3$ isotherms for MFM-601. a) and PXRD pattern after sorption, b) Solid symbols: adsorption; open symbols: desorption.

### 4.4.3 Selectivity between hydrocarbons

Figure 4.28 shows the sorption and desorption isotherms of the six hydrocarbons at 293 K and 1 bar. In terms of uptake capacity difference, it is obvious that the isotherms show a trend of $C_3H_6 \approx C_3H_8 > C_2H_6 > C_2H_4 \approx C_2H_2 > CH_4$ at 1 bar which correlates to the trends of the gas molecule kinetic diameters and polarizability (Table 2.1). The $C_3$ hydrocarbons reach near-saturation at 1 bar whereas $C_2$s and $CH_4$ show unsaturated near-linear uptake profiles, indicating potential selectivity between $C_3$s and $C_2$s and between $C_3$s and $CH_4$. Based on the uptakes at 293 K, the selectivities among the hydrocarbons have been calculated *via* DSLF-IAST method.

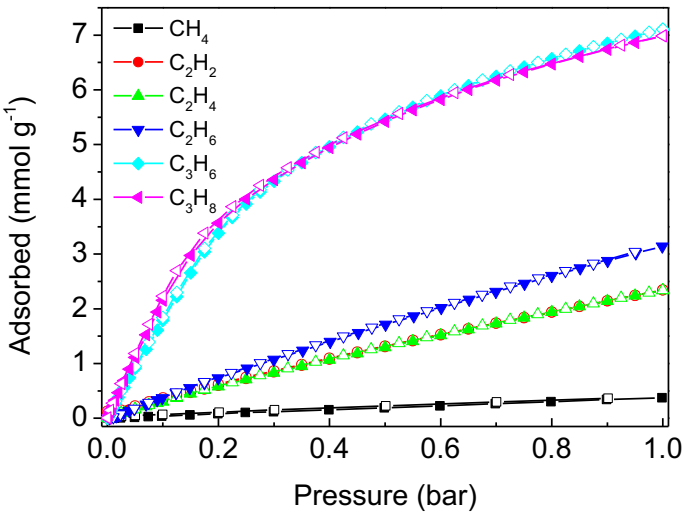



Figure 4.28 Hydrocarbon isotherms for MFM-601 at 293 K. Solid symbols: adsorption; open symbols: desorption.

The selectivity of $C_2H_2/CH_4$ at 1 bar and 293 K is shown in Figure 4.29. Since the uptake of $CH_4$ is much lower than $C_2H_2$ at 1 bar, the predicted equimolar binary mixture uptake (dashed blue line) lies in the extrapolation region of the calculation, with the total uptake of ca. 3.48 mg $g^{-1}$ at 1 bar. The $C_2H_2$ component contribution is 3.25 mg $g^{-1}$ and the $CH_4$ contribution is 0.23 mg $g^{-1}$.

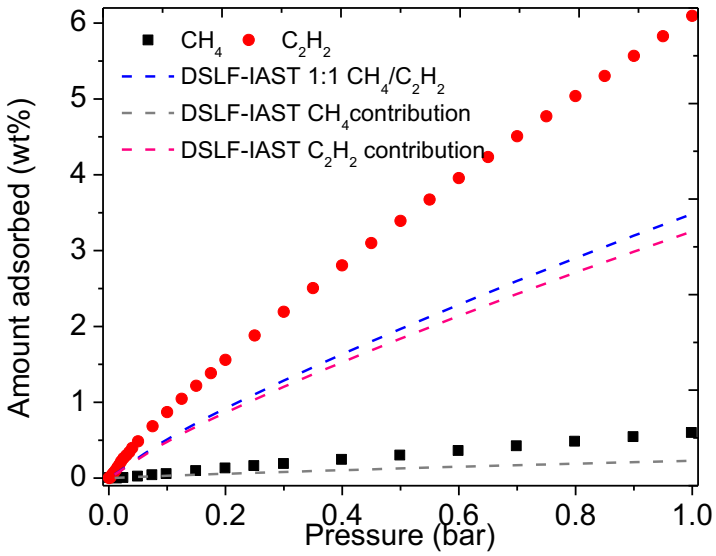



Figure 4.29 DSLF-IAST predicted equimolar binary mixture uptake of $CH_4$ and $C_2H_2$.

Owing to the similar uptake of $C_2H_4$ and $C_2H_2$ at 1 bar, the selectivity for $C_2H_4/CH_4$ is close to that for $C_2H_2/CH_4$, as shown in Figure 4.30. The predicted uptake of the equimolar binary mixture of $C_2H_4/CH_4$ (dashed blue line) lies in the extrapolation region of the calculation, with the total uptake of ca. 3.71 mg $g^{-1}$ at 1 bar. The $C_2H_4$ component contribution is 3.47 mg $g^{-1}$ and the $CH_4$ contribution is 0.24 mg $g^{-1}$.

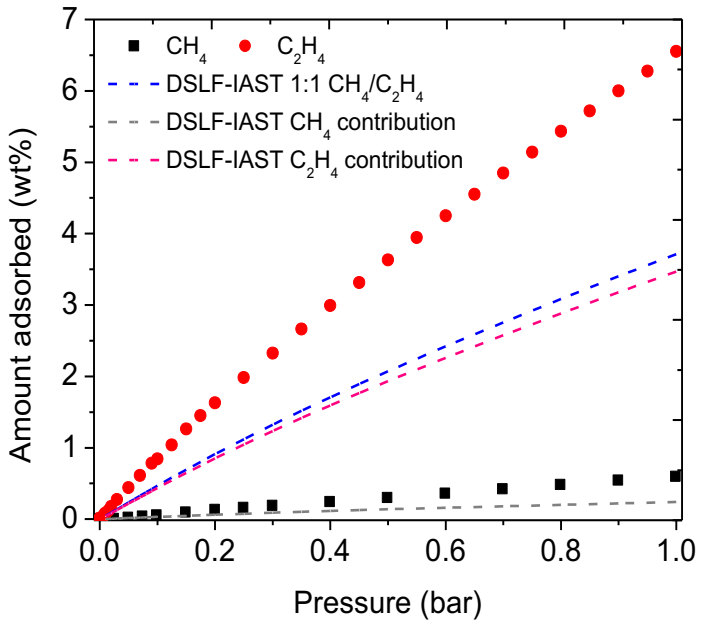



Figure 4.30 DSLF-IAST predicted equimolar binary mixture uptake of $CH_4$ and $C_2H_4$.

The selectivity of $C_2H_6/CH_4$ at 1 bar exhibits near-linear shape as shown in Figure 4.31. Since the uptake of $CH_4$ is much lower than $C_2H_6$ at 1 bar, the predicted equimolar binary mixture uptake (dashed blue line) lies in the extrapolation region of the DSLF-IAST calculation, with the uptake of ca. 5.15 mg $g^{-1}$ at 1 bar. The $C_2H_6$ contributes 4.91 mg $g^{-1}$ and the $CH_4$ contributes 0.24 mg $g^{-1}$.

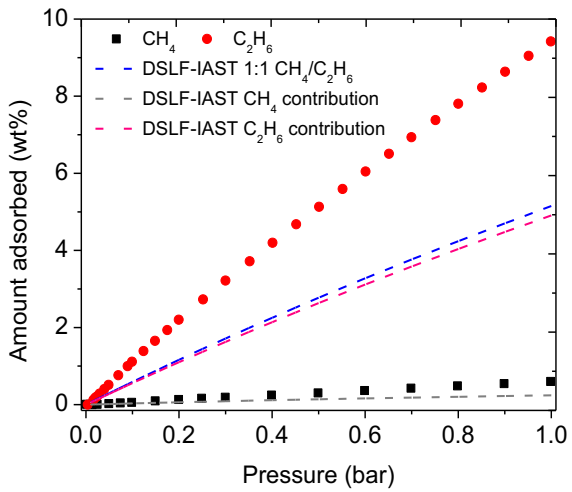



Figure 4.31 DSLF-IAST predicted equimolar binary mixture uptake of $CH_4$ and $C_2H_6$.

Figure 4.32 shows the selectivity of $C_3H_6/CH_4$. Since the uptake of $CH_4$ is much lower than $C_3H_6$ at 1 bar, the predicted equimolar binary mixture uptake (dashed blue line) is in the extrapolation region of the calculation and the total uptake at 1 bar is ca. 22.66 mg $g^{-1}$, of which 22.57 mg $g^{-1}$ comes from $C_3H_6$ and 0.09 mg $g^{-1}$ comes from $CH_4$.

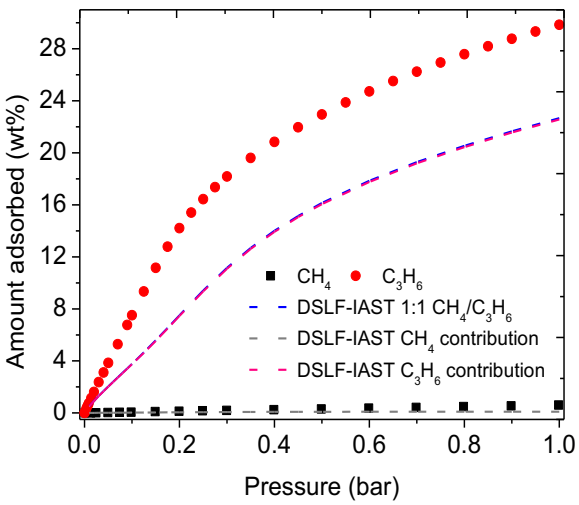



Figure 4.32 DSLF-IAST predicted equimolar binary mixture uptake of $CH_4$ and $C_3H_6$.

Figure 4.33 shows the selectivity of $C_3H_8/CH_4$. Since the uptake of $CH_4$ is much lower than $C_3H_8$ at 1 bar, the predicted equimolar binary mixture uptake (dashed blue line) is in the extrapolation region of DSLF-IAST calculation, with the uptake of ca. 23.60 mg $g^{-1}$ at 1 bar. The $C_3H_8$ component contribution is 23.52 mg $g^{-1}$ and the $CH_4$ contribution is 0.08 mg $g^{-1}$.

Compared with $C_2s/CH_4$, the selectivities for $C_3H_6/CH_4$ and $C_3H_8/CH_4$ exhibit inflection points, with much lower contributions from $CH_4$. In addition, all the predicted equimolar mixtures of $C_2s/CH_4$ and $C_3s/CH_4$ show similar isotherm shapes to the component with higher uptakes.

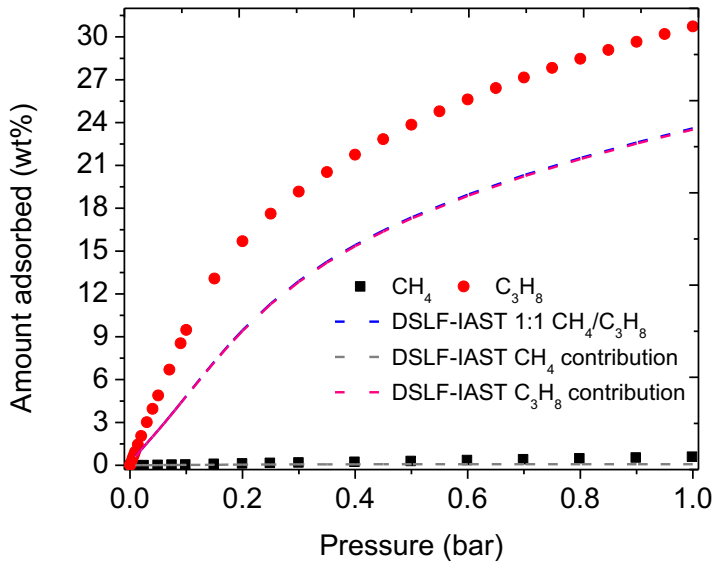



Figure 4.33 DSLF-IAST predicted equimolar binary mixture uptake of $CH_4$ and $C_3H_8$.

The selectivity of $C_3H_6/C_2H_4$ at 1 bar is shown in Figure 4.34. Since the uptake of $C_2H_4$ is much lower than $C_3H_6$ at 1 bar, the predicted equimolar binary mixture uptake (dashed blue line) lies in the extrapolation region of the calculation, with the total uptake of ca. 22.91 mg $g^{-1}$ at 1 bar. The $C_3H_6$ contribution to the total uptake is 20.99 mg $g^{-1}$ and $C_2H_4$ is 1.92 mg $g^{-1}$.

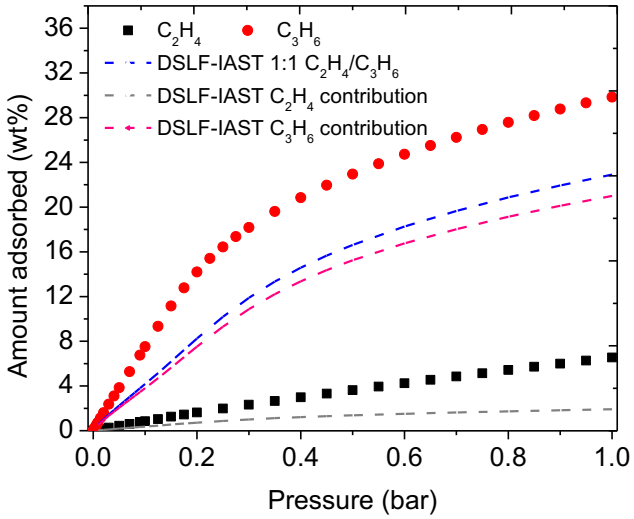



Figure 4.34 DSLF-IAST predicted equimolar binary mixture uptake of $C_2H_4$ and $C_3H_6$.

Figure 4.35 shows the selectivity between $C_2H_2$ and $C_2H_4$. The predicted equimolar uptake of $C_2H_4$ and $C_2H_2$ is shown by the dashed blue line. Since the uptake of $C_2H_4$ is similar with that of $C_2H_2$ at 1 bar and the DSLF fittings show acceptable agreement (Table 4.12) and the isotherms comply with the conditions of IAST method. However, this predicted isotherm does not lie in between the two isotherms at low pressure region (0–0.6 bar) but above the two isotherms. This is different from the predicted equimolar binary gases uptake isotherms discussed above. The reason for this feature is probably due to the high affinity of the gas molecules for the framework at low pressure.

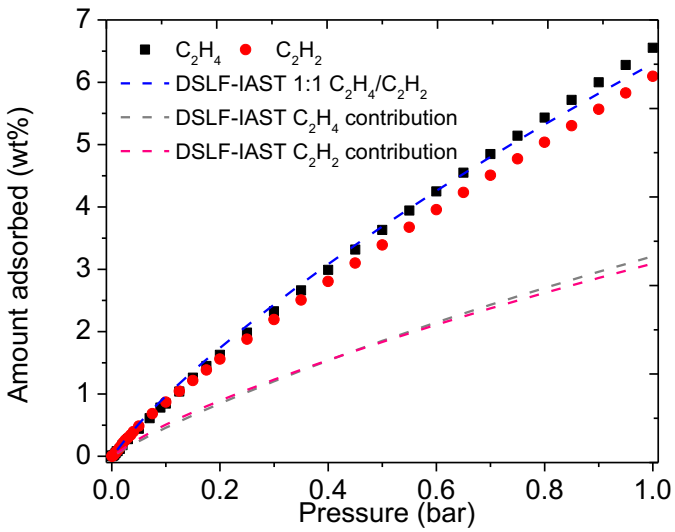



Figure 4.35 DSLF-IAST predicted equimolar binary mixture uptake of $C_2H_4$ and $C_2H_2$.

Figure 4.36 shows the selectivity of $C_3H_8/C_2H_6$ at 1 bar. Since the uptake of $C_2H_6$ is much lower than $C_3H_8$ at 1 bar, the predicted equimolar binary mixture uptake (dashed blue line) lies in the extrapolation region of DSLF-IAST calculation and the uptake value at 1 bar is ca. 25.05 mg $g^{-1}$, of which 22.25 mg $g^{-1}$ comes from $C_3H_8$ and 2.80 mg $g^{-1}$ comes from $C_2H_6$.

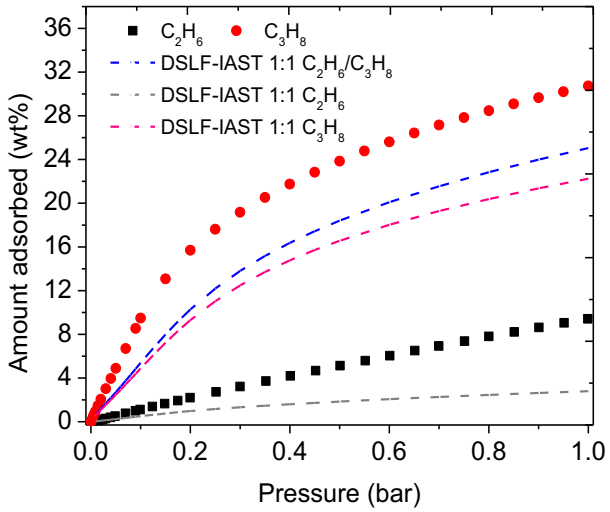



Figure 4.36 DSLF-IAST predicted equimolar binary mixture uptake of $C_2H_6$ and $C_3H_8$.

Figure 4.37 exhibits the selectivity of $C_2H_6/C_2H_4$. Compared with the extrapolated uptakes of equimolar mixtures with significant uptake differences between the two components, the $C_2H_4$ and $C_2H_6$ exhibit similar uptakes at 1 bar, giving a more accurate prediction for the total uptake of 7.89 mg $g^{-1}$ at 1 bar, of which 4.64 mg $g^{-1}$ comes from $C_2H_6$ and 3.24 mg $g^{-1}$ comes from $C_2H_4$.

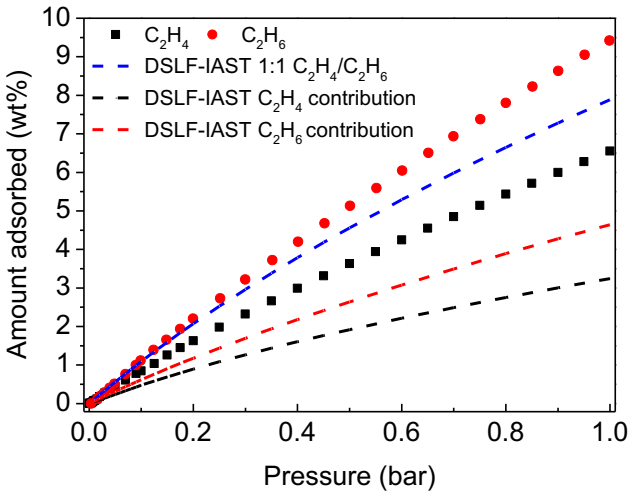



Figure 4.37 DSLF-IAST predicted equimolar binary mixture uptake of $C_2H_4$ and $C_2H_6$.

Figure 4.38 exhibits the selectivity between $C_3H_6$ and $C_3H_8$. The uptake of $C_3H_6$ is similar to $C_3H_8$ at 1 bar, indicating that the isotherms meet the conditions of IAST model. In addition, both of the isotherms exhibit inflection points, suggesting excellent fits by DSLF method. Upon this, the predicted equimolar binary mixture shows an uptake (dashed blue line) of ca. 30.26 mg $g^{-1}$ at 1 bar, of which 14.16 mg $g^{-1}$ comes from $C_3H_6$ and 16.10 mg $g^{-1}$ comes from $C_3H_8$.

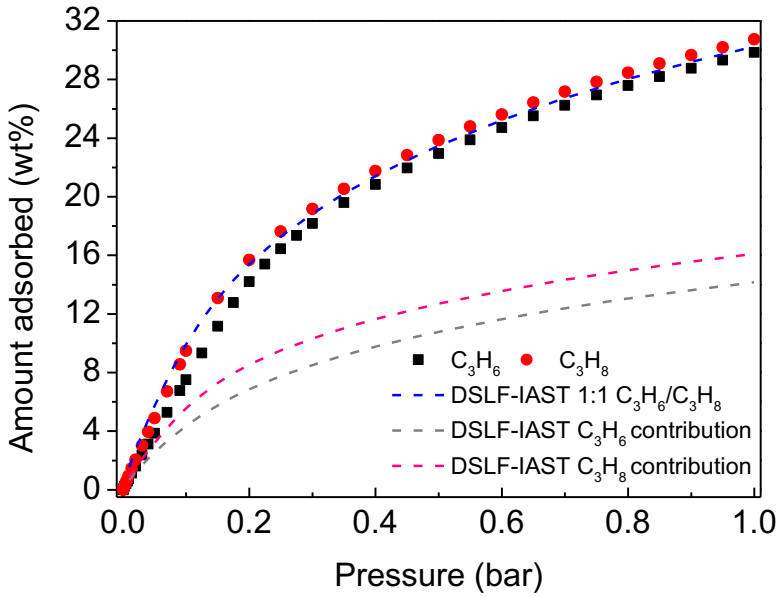



Figure 4.38 DSLF-IAST predicted equimolar binary mixture uptake of $C_3H_6$ and $C_3H_8$.

The selectivity at various pressures (0.01−1bar) for the hydrocarbon uptakes have been calculated by DSLF-IAST. Figure 4.39 shows the selectivity values between $C_2H_6$ and $CH_4$ (black), $C_2H_4$ and $CH_4$ (red), $C_2H_6$ and $C_2H_4$ (blue). For the separation between $C_2H_4$ and $CH_4$ and between $C_2H_2$ and $CH_4$, the selectivity below 1 bar lies in the range 8−14. Compared with the selectivity of $C_2H_2/CH_4$ or $C_2H_4/CH_4$, $C_2H_6$ and $CH_4$ exhibits higher selectivity values below 1 bar, which is consistent with the single gas uptake isotherms. The selectivity between $C_2H_6$ and $CH_4$ at low pressure is ca. 14 and shows an increasing trend as the pressure goes up, eventually reaching a selectivity of ca. 24 at 1 bar. For the separation of $C_2H_6$ and $C_2H_4$, the two isotherms show similar near-linear shapes and uptake capacities.

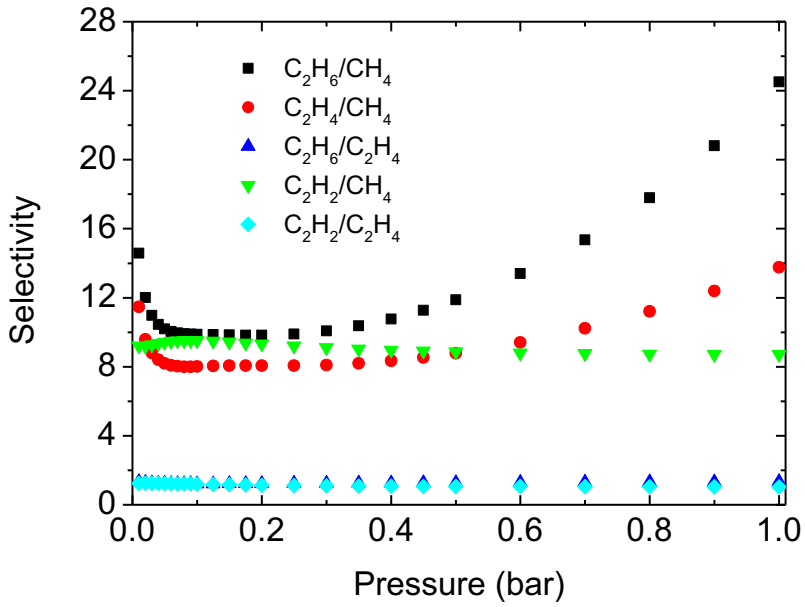



Figure 4.39 DSLF-IAST predicted selectivity of equimolar binary mixture of $C_2H_4/CH_4$, $C_2H_6/CH_4$ and $C_2H_6/C_2H_4$.

Figure 4.40 shows the selectivity values between $C_3H_8$ and $CH_4$ (black), $C_3H_6$ and $CH_4$ (red). Compared with the selectivities (8–24) between $C_2$s and $CH_4$, the $C_3$s shows much higher selectivity (55–110) over $CH_4$. Specifically, the selectivity of $C_3H_8/CH_4$ is higher than that of $C_3H_6/CH_4$. Furthermore, the selectivities of $C_3H_8/CH_4$ and $C_3H_6/CH_4$ for MFM-601 are comparable to those of MFM-202a.

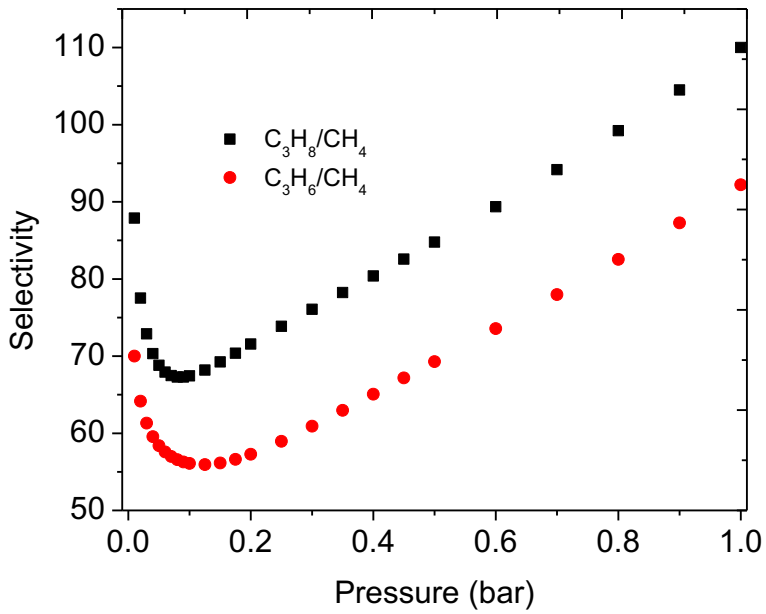



Figure 4.40 DSLF-IAST predicted selectivity of equimolar binary mixture of $C_3H_6/CH_4$ and $C_3H_8/CH_4$.

Figure 4.41 shows the selectivity between $C_3H_6$ and $C_2H_4$ (black), $C_3H_8$ and $C_2H_6$ (red), $C_3H_8$ and $C_3H_6$ (blue). For the separation between $C_3H_8$ and $C_2H_6$, the selectivity below 1 bar lies in the range 5–9. Compared with the selectivity of $C_3H_8$ and $C_2H_6$, $C_3H_6$ and $C_2H_4$ exhibits similar selectivity values at low pressure, but higher selectivity values above 0.01 bar, which is consistent with the single gas uptake isotherms. The selectivity between $C_3H_6$ and $C_2H_4$ at low pressure is ca. 9 and reaches equilibrium above 0.4 bar and eventually gives a selectivity value of ca. 7 at 1 bar. For the separation of $C_3H_8$ and $C_3H_6$, since the two isotherms show similar non-linear shape and uptake capacities, the selectivity is slightly higher than 1 below 1 bar.

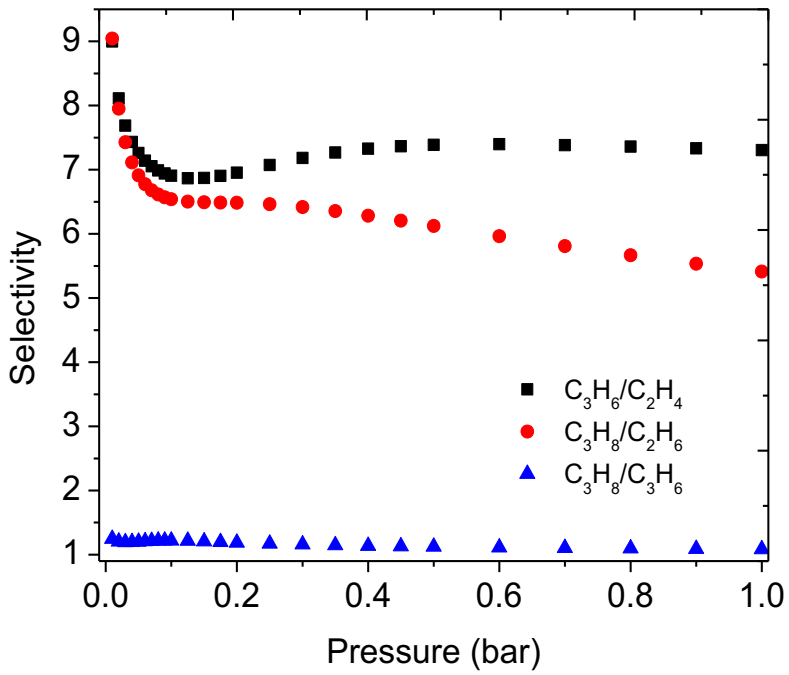



Figure 4.41 DSLF-IAST predicted selectivity of equimolar binary mixture of $C_3H_6/C_2H_4$, $C_3H_8/C_2H_6$ and $C_3H_8/C_3H_6$.

Apart from the calculations of selectivity among hydrocarbons, the selectivity of $CO_2$ over $CH_4$ is also calculated as shown in Figure 4.42. The sharp decrease below 0.5 bar is due to the uncertainty of the DSLF-IAST method. The average selectivity below 8 bar is approximately 6, which is comparable to other Zr-based MOFs (Table 4.10).

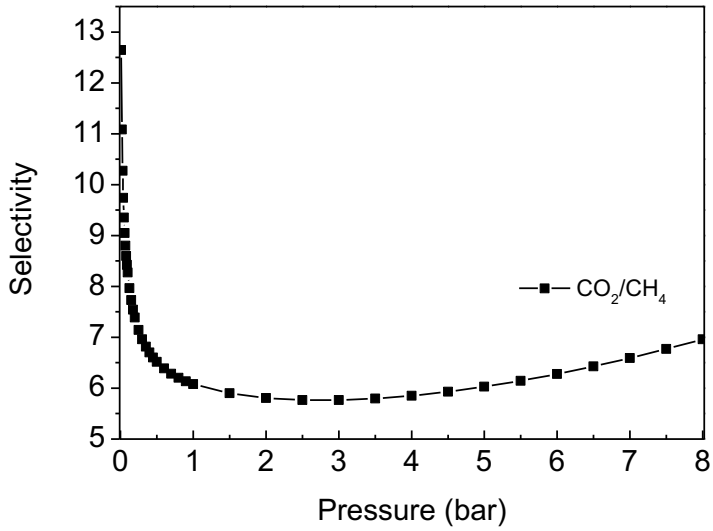



Figure 4.42 DSLF-IAST predicted selectivity of equimolar binary mixture of $CO_2/CH_4$.

Table 4.10 Summary of gas uptakes, selectivity and heats of adsorption ($Q_{st}$) for Zr-based MOFs.

| | **$CH_4$ uptake (mmol $g^{-1}$)** | **$CO_2$ uptake (mmol $g^{-1}$)** | **Selectivity $CO_2/CH_4$** | **$CH_4$ $Q_{st}$ (kJ $mol^{-1}$)** | **$CO_2$ $Q_{st}$ (kJ $mol^{-1}$)** | **Ref.** |
|---|---|---|---|---|---|---|
| **MFM-601** | 3.1[1] | 15[1] | 6 | 15 | 22 | This work |
| **NU-1100** | 5[2] | 29[2] | - | 14 | 25 | 6 |
| **Dehydroxylated UiO-66** | 3.9[2] | 9.3[2] | - | 17 | 22 | 22 |
| **Hydroxylated UiO-66** | 4.3[2] | 9.6[2] | 2.2–3.6 | 17 | 28 | 22 |
| **Zr-MOF-NH4** | 2.5[1] | 7.8[3] | 2.8–4.3 | - | - | 23 |

[1] Data measured and processed at 273 K and 8 bar; [1] data measured and processed at 273 K and 15 bar; [2] data measured and processed at 270 K and 8 bar; [2] data measured and processed at 270 K, 15 bar; [3] data measured and processed at 270 K and 10 bar.

### 4.4.4 Calculations of isosteric heats of adsorption and entropy

Figure 4.43 shows the isosteric heats of adsorption ($Q_{st}$) values and adsorption entropies ($\Delta S$) at various $CH_4$ uptake amounts. The $Q_{st}$ at low coverage is ca. 15.5 kJ $mol^{-1}$, which is comparable to the reported $Q_{st}$ values of MOFs for $CH_4$ adsorption,[20,24] with an increasing trend at higher uptake amounts. The adsorption entropy shows a decreasing trend with surface coverage and range from -148 to -180 J $K^{-1}$ $mol^{-1}$, corresponding to an increasing structural order of the system.

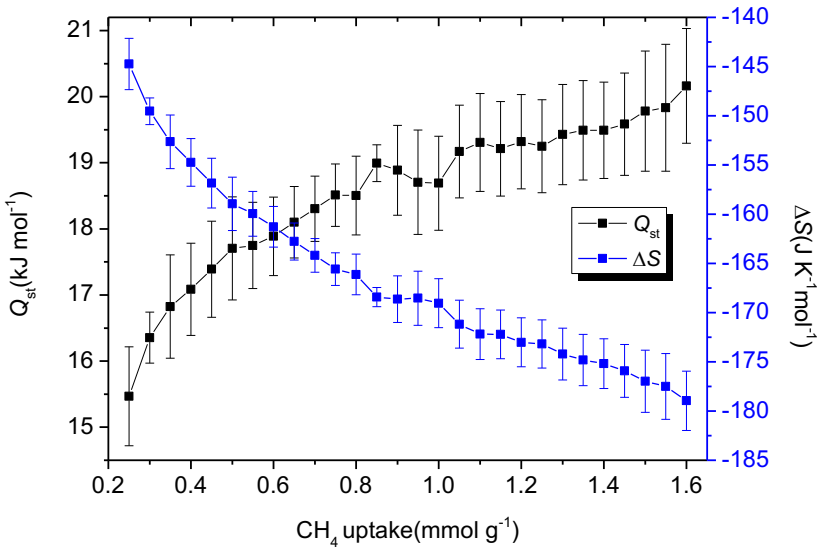



Figure 4.43 Variation of the thermodynamic parameters $Q_{st}$ and $\Delta S$ with error bars for MFM-601 as a function of $CH_4$ uptakes. The errors of the calculated heats of adsorption are within ±1 kJ $mol^{-1}$.

Figure 4.44 shows the $Q_{st}$ and $\Delta S$ values at various $C_2H_2$ uptake amounts. The $Q_{st}$ at low coverage is ca. 27.6 kJ $mol^{-1}$, with a decreasing trend as the uptake increases. The adsorption entropies also show a decreasing trend with the increasing of $C_2H_2$ coverage and range from -170 to -175 J $K^{-1}$ $mol^{-1}$. Furthermore, the errors of the calculated heats of adsorption and entropy at low coverage are much larger than those at high coverage.

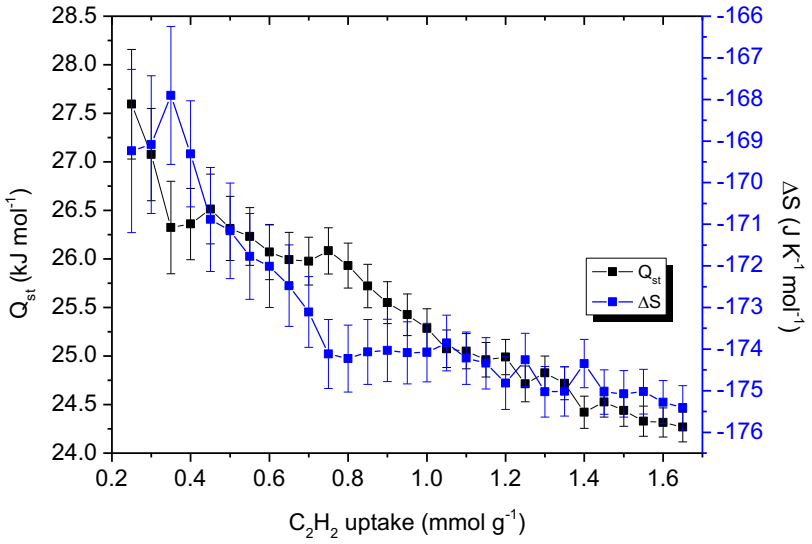



Figure 4.44 Variation of the thermodynamic parameters $Q_{st}$ and $\Delta S$ with error bars for MFM-601 as a function of $C_2H_2$ uptakes. The errors of the calculated heats of adsorption are within ±1 kJ mol$^{-1}$.

Figure 4.45 shows the $Q_{st}$ and $\Delta S$ values at various $C_2H_4$ uptake amounts. The $Q_{st}$ at low coverage is ca. 20.8 kJ mol$^{-1}$, which is comparable to the $Q_{st}$ values of the reported MOFs for $C_2H_4$ adsorption,[20,24] with an increasing trend as the loadings increase. The adsorption entropies show a decreasing trend with $C_2H_4$ coverage and range from -146 to -170 J K$^{-1}$ mol$^{-1}$, indicating an increasing structural ordering of the system.

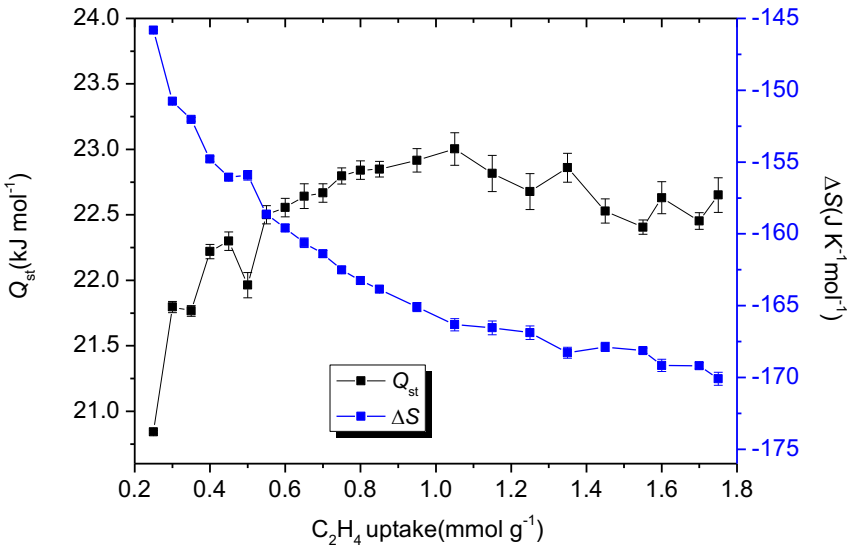



Figure 4.45 Variation of the thermodynamic parameters $Q_{st}$ and $\Delta S$ with error bars for MFM-601 as a function of $C_2H_4$ uptakes. The errors of the calculated heats of adsorption are within ±0.5 kJ mol$^{-1}$.

Figure 4.46 shows the $Q_{st}$ and $\Delta S$ values at various $C_2H_6$ uptake amounts. The $Q_{st}$ at low coverage is ca. 21.8 kJ $mol^{-1}$, which is comparable to the $Q_{st}$ values of the reported MOFs for $C_2H_6$ adsorption. [20,24] It initially shows an increasing trend for $C_2H_6$ uptakes from 0.001 to 1 mmol $g^{-1}$, where a decrease occurred for $C_2H_6$ uptakes in the range from 1 to 2 mmol $g^{-1}$ and thereafter shows an increasing trend as the loadings increase. The adsorption entropies show a decreasing trend with the increase of $C_2H_6$ coverage and range from -147 to -188 J $K^{-1}$ $mol^{-1}$, suggesting an ordering of the structure.

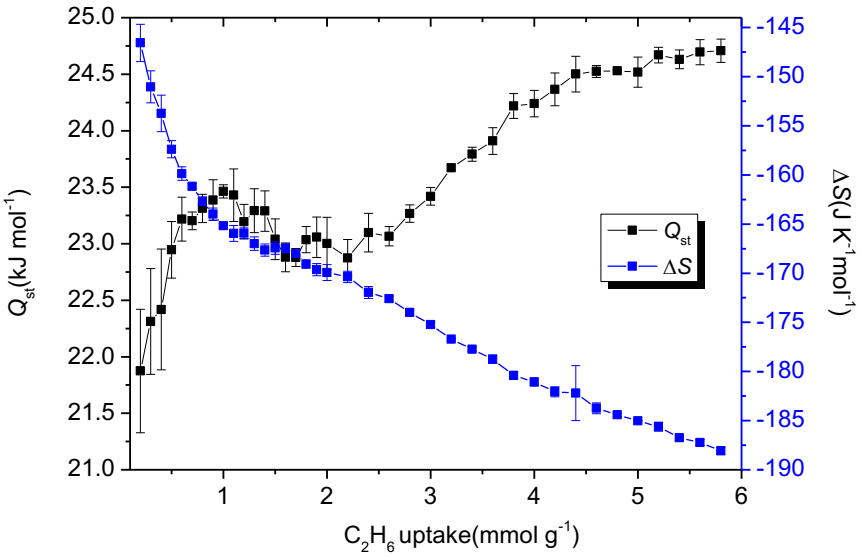



Figure 4.46 Variation of the thermodynamic parameters $Q_{st}$ and $\Delta S$ with error bars for MFM-601 as a function of $C_2H_6$ uptakes. The errors of the calculated heats of adsorption are within ±1 kJ $mol^{-1}$.

Figure 4.47 shows the $Q_{st}$ and $\Delta S$ values at various $C_3H_6$ uptake amounts. The $Q_{st}$ at low coverage is ca. 29.8 kJ $mol^{-1}$, which is comparable to the $Q_{st}$ values of the reported MOFs for $C_3H_6$ adsorption, [20,24] with a zigzag shaped trend for higher surface coverage, which is distinct from those of $CH_4$ and $C_2$s. The adsorption entropy shows a decreasing trend with the $C_3H_6$ coverage and range from -158 to -193 J $K^{-1}$ $mol^{-1}$, corresponding to an increasing structural order of the system.

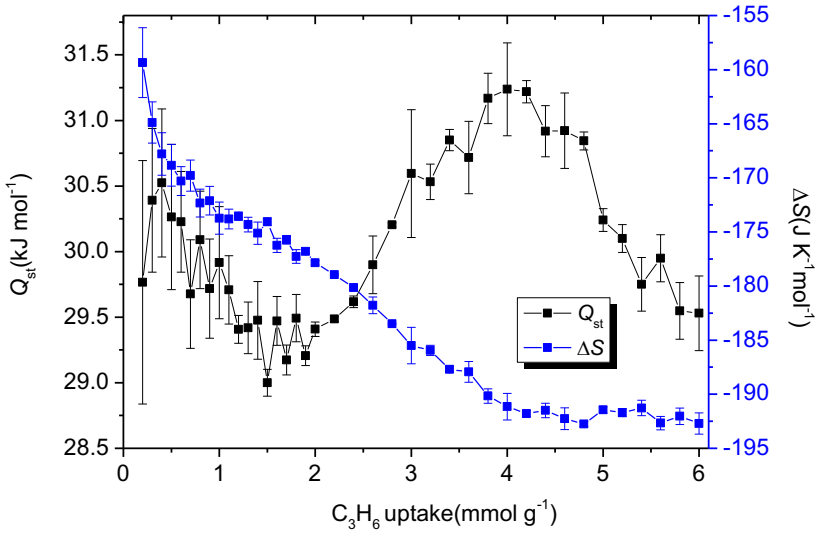



Figure 4.47 Variation of the thermodynamic parameters $Q_{st}$ and ΔS with error bars for MFM-601 as a function of $C_3H_6$ uptakes. The errors of the calculated heats of adsorption are within ±1 kJ mol$^{-1}$.

Figure 4.48 shows the $Q_{st}$ and ΔS values at various $C_3H_8$ uptake amounts. The $Q_{st}$ at low coverage is ca. 30.8 kJ mol$^{-1}$, which is comparable to the $Q_{st}$ values of the reported MOFs for $C_3H_8$ adsorption, [20,24] with a zigzag shaped trend as the loadings increase, which is similar to that of $C_3H_6$. The adsorption entropies show a decreasing trend ranging from -162 to -193 J K$^{-1}$ mol$^{-1}$ at $C_3H_8$ loadings of 0.001–6 mmol g$^{-1}$, suggesting an ordering of the structure.

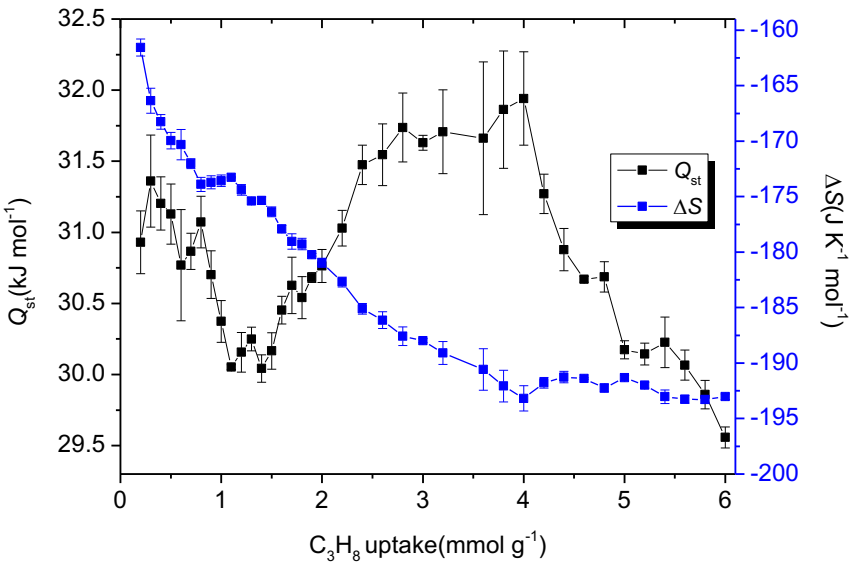



Figure 4.48 Variation of the thermodynamic parameters $Q_{st}$ and ΔS with error bars for MFM-601 as a function of $C_3H_8$ uptakes. The errors of the calculated heats of adsorption are within ±1 kJ mol$^{-1}$.

Figure 4.49 shows the $Q_{st}$ and $\Delta S$ values as a function of $CO_2$ uptake amounts. The $Q_{st}$ at low coverage is ca. 22.0 kJ $mol^{-1}$, which is comparable to the $Q_{st}$ values of the reported MOFs for $CO_2$ adsorption.[11,20,24] The adsorption entropies show a decreasing trend as the $CO_2$ loadings increase, ranging from -145 to -200 J $K^{-1}$ $mol^{-1}$, suggesting an ordering of the system.

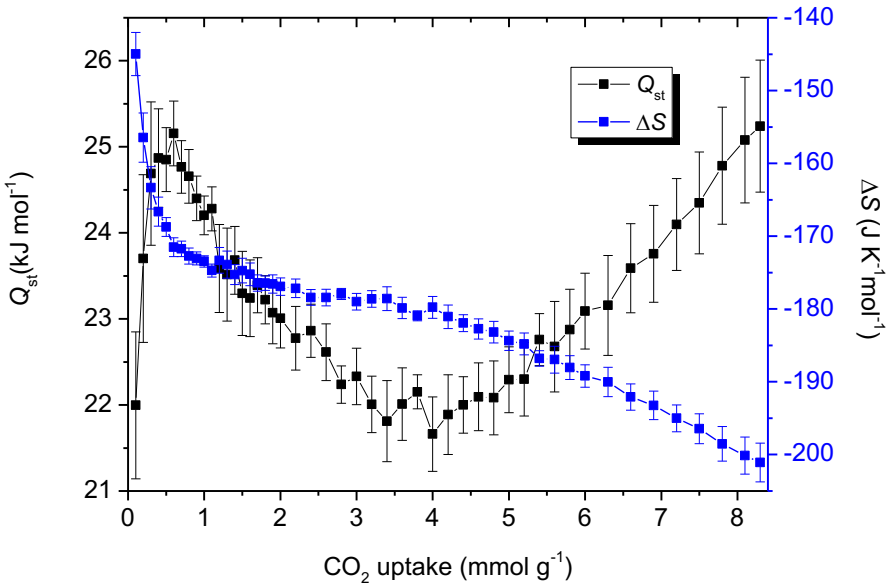



Figure 4.49 Variation of the thermodynamic parameters $Q_{st}$ and $\Delta S$ with error bars for MFM-601 as a function of $CO_2$ uptakes. The errors of the calculated heats of adsorption are within ±0.5 kJ $mol^{-1}$.

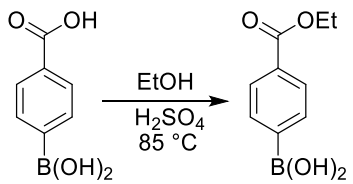
## 4.5 Experimental section

### 4.5.1 Materials and techniques

All reagents and solvents were used as received from commercial sources without further purification. Elemental analyse for C, H and N were carried out on a CE-440 elemental analyser (Exeter Analytical Company). Thermal gravimetric analyses (TGA) were recorded under an air or $N_2$ flow (100 mL/min) with a heating rate of 5 °C/min using a TA SDT-Q600 thermogravimetric analyser (TA Company) or Perkin Elmer Pyris thermogravimetric analyser. IR spectra were recorded using a Nicolet Avatar 360 FT-IR spectrometer. $^{1}$H NMR and $^{13}$C NMR spectra were collected on a JEOL EX270 NMR spectrometer. Mass Spectra were recorded on a Bruker micro-TOF spectrometer (Bruker Company) in ESI model. PXRD data were recorded on a PANalytical X'pert diffractometer using Cu-*K*$\alpha$1 radiation (Chemistry school, the University of Manchester). Single crystal XRD data were obtained at the chemistry school of the University of Nottingham. High resolution *in situ* synchrotron X-ray powder diffraction (PXRD) data were collected at Diamond Light Source beamline I11 using multi-analysing crystal-detectors (MACs) and monochromated radiation [$\lambda$ = 0.82617 (2) Å]. The temperature of *in situ* PXRD was controlled by an Oxford Cryosystems open-flow nitrogen gas cryostat.

### 4.5.2 Ligand preparation

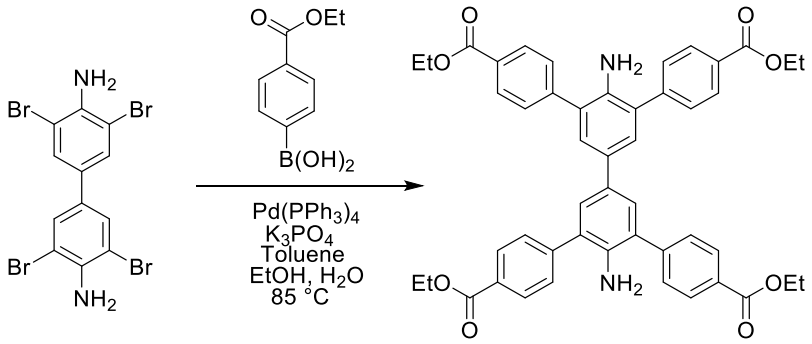
**Preparation of (4-(ethoxycarbonyl)phenyl)boronic acid**




4-Carboxyphenylboronic acid (30.0 g, 180 mmol) was dissolved in ethanol (600 mL), with dropwise addition of concentrated sulfuric acid (98%, 18.0 mL). The resulting solution was stirred under reflux at 85 °C for 1 day. The solvent was reduced under vacuum to ~100 mL, and deionised water (900 mL) was added to precipitate a white solid, which was filtered and washed with deionised water until the filtrate was neutralised. The solid product was dried in air to give 4-ethoxycarbonylphenylboronic acid

(26.4 g, 76%) as a white powder. Elemental analysis: (Found: C, 55.7; H, 5.7 %. Calc. for $C_9H_{11}BO_4$: C, 55.1; H, 5.6 %); IR $\nu_{max}$(neat)/$cm^{-1}$ 3344 (br), 2985 (w), 1689 (s), 1342 (s), 1271 (s), 705 (s); $^1$H NMR $\delta_H$ (270 MHz; DMSO): 7.90 (4H, m,), 4.31 (2H, q, *J* 7.2 Hz), 1.31 (3H, t, *J* 7.2 Hz); $^{13}$C NMR $\delta_C$ (270 MHz; DMSO): 166.5, 134.8, 131.6, 128.5, 61.3, 14.7; Mass (ESI+) m/z (M+Na): 217.07.

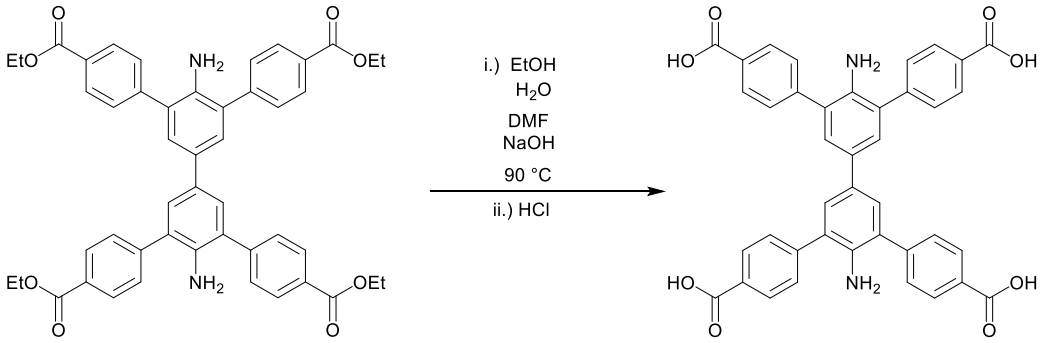
**Preparation of diethyl 4'',6'-diamino-5',5''-bis(4-(ethoxycarbonyl)phenyl)-[1,1':3',1'':3'',1'''-quaterphenyl]-4,4'''-dicarboxylate**




4,4'-Diamino-3,3',5,5'-tetrabromobiphenyl (4.00 g, 8.00 mmol), 4-carboxyphenylboronic acid (9.32 g, 48.0 mmol) and tripotassium phosphate (32.3 g, 152 mmol) were mixed in toluene (200 mL), ethanol (80 mL) and water (80 mL). The mixture was then purged with argon for 15 mins. Tetrakis(triphenylphosphine)palladium(0) (1.84 g, 1.60 mmol) was added into the mixture, which was then heated to 85 °C and stirred under argon for 3 days. The resultant mixture was filtered and the filtrate was reduced under vacuum to give yellowish oil. This oil was dissolved in dichloromethane (400 mL) and extracted into deionised water (3 x 300 mL). The organic layer was combined, dried ($MgSO_4$), filtered and then the filtrate was reduced under vacuum. The resultant yellow solid was dissolved in dichloromethane (64 mL) and refluxed at 40 °C. Hot petroleum ether (240 mL) was added to precipitate a brown solid, which was collected by filtration. The crude solid was purified by column chromatography (silica gel), eluting with petroleum ether: ethyl acetate (2:1), to yield 4,4'-diamino-3,3',5,5'-tetra(4-ethoxycarbonylphenyl)biphenyl (3.20 g, 51%) as a yellow powder. Elemental analysis: (Found: C, 71.5; H, 5.4, N, 3.5 %. Calc. for $C_{48}H_{44}N_2O_8$: C, 74.2; H, 5.7; N, 3.6 %); IR $\nu_{max}$(neat)/$cm^{-1}$ 3389 (w), 2978 (w), 1712 (s), 1606 (m), 1270 (s), 1099 (s), 1018 (m); $^1$H NMR $\delta_H$ (270 MHz; $CDCl_3$): 8.13 (8H, d, *J* 8.4 Hz), 7.61 (8H, d, *J* 8.4 Hz), 7.35 (4H, s), 4.39 (8H, q, *J* 7.2 Hz), 3.83 (4H, br s), 1.40

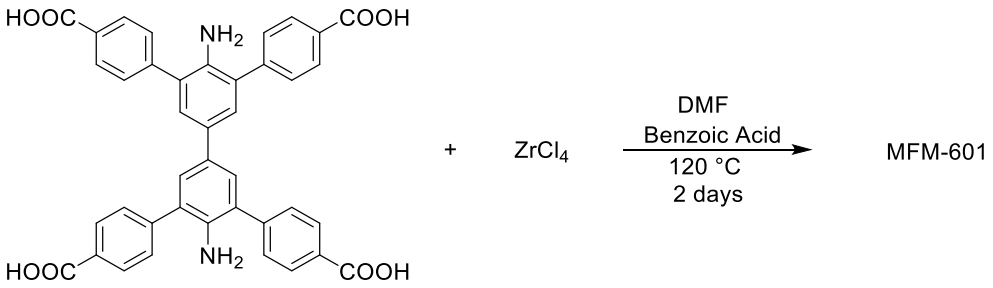
(12H, *J* 7.2 Hz); $^{13}$C NMR $\delta_C$ (270 MHz; $CDCl_3$): 166.4, 144.2, 130.3, 129.7, 129.4, 128.1, 61.2, 14.4; Mass (ESI+) m/z (M+H): 777.32.

**Preparation of 4'',6'-diamino-5',5''-bis(4-carboxyphenyl)-[1,1':3',1'':3'',1'''-quaterphenyl]-4,4'''-dicarboxylic acid**

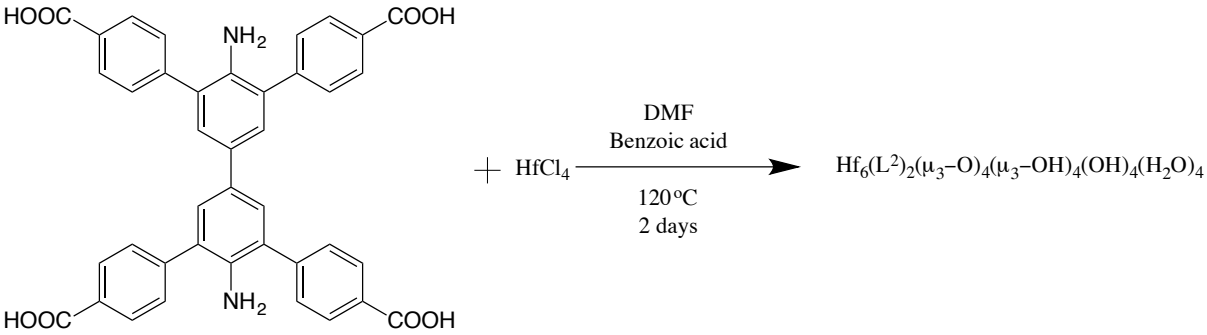



4,4'-diamino-3,3',5,5'-tetra(4-ethoxycarbonylphenyl)biphenyl (1.40 g, 1.80 mmol) and sodium hydroxide (0.42 g, 10.7 mmol) were mixed in tetrahydrofuran (50 mL), ethanol (50 mL) and water (50 mL) and then refluxed at 90 °C for 1 day. The solvent was then removed under reduced pressure, and the resultant solid salt was dissolved in deionised water (50 mL). To this, hydrochloric acid (2M) was added dropwise until the solution was mildly acidic (pH ~2) such that a yellow solid precipitated. The product was collected by filtration, washed with deionised water, and dried in air to give 4,4'-diamino-3,3',5,5'-tetra(4-carboxyphenyl)biphenyl (1.02 g, 85%) as yellow flakes. Elemental analysis: (Found: C, 65.2; H, 4.4, N, 4.1 %. Calc. for $C_{40}H_{28}N_2O_8$: C, 72.3; H, 4.3; N, 4.2 %); IR $\nu_{max}$(neat)/cm$^{-1}$: 3071 (br), 2531 (w), 1694 (s), 1607 (s), 1236 (s), 780 (s); $^1$H NMR $\delta_H$ (270 MHz; DMSO): 8.03 (8H, d, *J* 8.4 Hz), 7.66 (8H, d, *J* 8.4 Hz), 7.37 (4H, s), 4.42 (4H, br s); $^{13}$C NMR $\delta_C$ (270 MHz; DMSO): 167.7, 144.4, 140.6, 130.3, 130.1, 129.8, 128.0, 127.3; Mass (ESI+) m/z (M+H): 665.19.

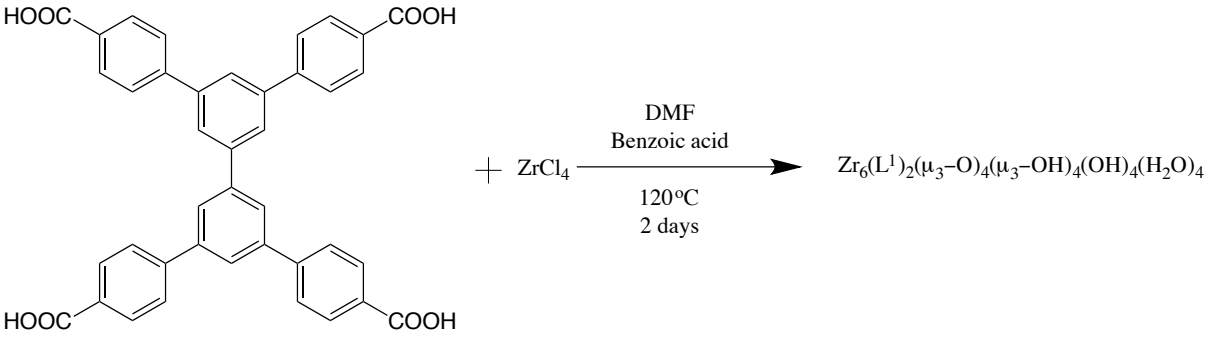
### 4.5.3 Syntheses of MOFs



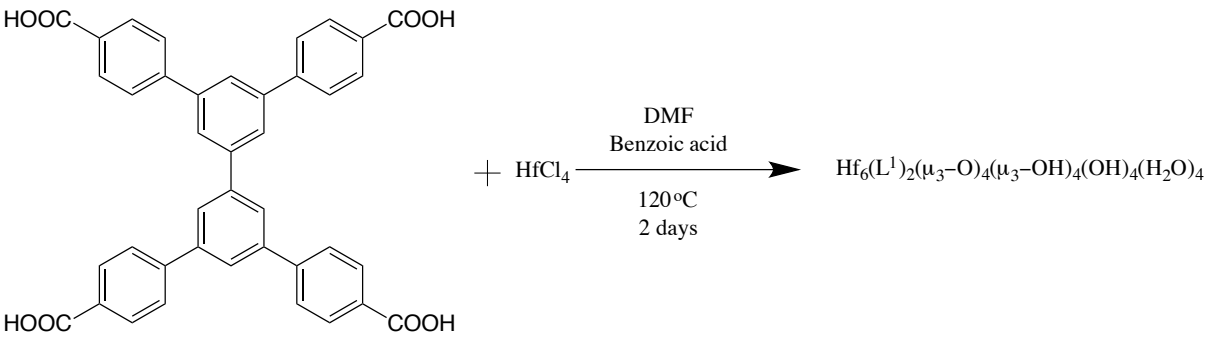

$H_4L^2$ (25.4 mg, 0.04 mmol) and $ZrCl_4$ (25.0 mg, 0.12 mmol) were dissolved in dimethylformamide (DMF) (5.0 mL), and then benzoic acid (0.9 g, 7.38 mmol) was added. The solution was heated at 120 °C for 2 days, and the resulting crystals were washed with hot DMF to give $Zr_6(L^2)_2(\mu_3\text{-}O)_4(\mu_3\text{-}OH)_4(OH)_4(H_2O)_4$ upon drying. Elemental analysis: (Found: C, 45.2; H, 2.7, N, 2.9 %. Calc. for $C_{80}H_{68}O_{32}N_4Zr_6$: C, 44.9; H, 3.0; N, 2.6 %). IR $\nu_{max}$(neat)/cm$^{-1}$: 2929 (w), 1660 (s), 1602 (m), 1553 (m), 1406 (s), 1385 (s),1091 (m), 787 (m), 655 (m).




$H_4L^2$ (25.4 mg, 0.04 mmol) and $HfCl_4$ (35.0 mg, 0.12 mmol) were dissolved in dimethylformamide (DMF) (5.0 mL), and then benzoic acid (0.9 g, 7.38 mmol) was added. The solution was heated at 120 °C for 2 days, and the resulting crystals were washed with hot DMF to give $Hf_6(L^2)_2(\mu_3\text{-}O)_4(\mu_3\text{-}OH)_4(OH)_4(H_2O)_4$ upon drying. Elemental analysis: (Found: C, 31.2; H, 2.3, N, 2.1 %. Calc. for $C_{80}H_{68}O_{32}N_4Hf_6$: C, 31.8; H, 2.1; N, 1.9 %). IR $\nu_{max}$(neat)/cm$^{-1}$: 2926 (w), 1656 (s), 1601 (m), 1561 (m), 1401 (s), 1381 (s), 1091 (m), 783 (m), 655 (m).




$H_4L^1$ (25.0 mg, 0.04 mmol) and $ZrCl_4$ (25.0 mg, 0.12 mmol) were dissolved in dimethylformamide (DMF) (5.0 mL), and then benzoic acid (0.9 g, 7.38 mmol) was added. The solution was heated at 120 °C for 2 days, and the resulting crystals were washed with hot DMF to give $Zr_6(L^1)_2(\mu_3\text{-}O)_4(\mu_3\text{-}OH)_4(OH)_4(H_2O)_4$ upon drying. Elemental analysis: (Found: C, 45.1; H, 3.2 %. Calc. for $C_{80}H_{60}O_{32}Zr_6$: C, 46.2; H, 2.9 %). IR $\nu_{max}$(neat)/cm$^{-1}$: 3064 (w), 2927 (w), 2860 (w), 1671 (s), 1610 (m), 1561 (m), 1409 (s), 1386 (s), 1256 (m), 1091 (m), 860 (w), 787 (m), 720 (m), 659 (s).




$H_4L^1$ (25.0 mg, 0.04 mmol) and $HfCl_4$ (35.0 mg, 0.12 mmol) were dissolved in dimethylformamide (DMF) (5.0 mL), and then benzoic acid (0.9 g, 7.38 mmol) was added. The solution was heated at 120 °C for 2 days, and the resulting crystals were washed with hot DMF to give $Hf_6(L^1)_2(\mu_3\text{-}O)_4(\mu_3\text{-}OH)_4(OH)_4(H_2O)_4$ upon drying. Elemental analysis: (Found: C, 35.5; H, 2.7 %. Calc. for $C_{80}H_{60}O_{32}Hf_6$: C, 36.9; H, 2.3 %). IR $\nu_{max}$(neat)/cm$^{-1}$: 3062 (w), 1604 (m), 1543 (m), 1403 (s), 1177 (w), 1013 (w), 1091 (m), 848 (m), 781 (s), 714 (s), 655 (s).

### 4.5.4 Single crystal X-ray structure

Table 4.11 Single crystal data for the MOFs in this chapter.

| | $Zr_6(L^1)_2(\mu_3\text{-}O)_4(\mu_3\text{-}OH)_4(OH)_4(H_2O)_4$ | $Hf_6(L^1)_2(\mu_3\text{-}O)_4(\mu_3\text{-}OH)_4(OH)_4(H_2O)_4$ | $Zr_6(L^2)_2(\mu_3\text{-}O)_4(\mu_3\text{-}OH)_4(OH)_4(H_2O)_4$ **(MFM-601)** |
|---|---|---|---|
| Formula | $C_{80}H_{60}O_{32}Zr_6$ | $C_{80}H_{60}O_{32}Hf_6$ | $C_{80}H_{68}O_{32}N_4Zr_6$ |
| Formula weight | 2080.2 | 2604.2 | 2138 |
| Temperature (K) | 120(2) | 120(2) | 120(2) |
| Wavelength (Å) | 1.54184 | 1.54184 | 1.54184 |
| Space group | *Fmmm* | *Fmmm* | *Cmmm* |
| *a* (Å) | 20.5772(12) | 20.959(3) | 22.334 (2) |
| *b* (Å) | 31.4950(9) | 31.284(2) | 34.5440 (16) |
| *c* (Å) | 34.7392(9) | 34.553(2) | 15.0846 (4) |
| *V* (Å$^3$) | 22513.7(16) | 22656(3) | 11637.9 |
| Z | 4 | 4 | 1 |
| $D_{cal}$ (g cm$^{-3}$) | 0.596 | 0.763 | 0.738 |
| μ (mm$^{-1}$) | 2.464 | 5.172 | 2.510 |
| *F*(000) | 3911.9 | 4778.3 | 2582.4 |
| $R_{int}$ | 0.0418 | 0.1224 | 0.0662 |
| $R_1$ [$F > 4\sigma(F)$]/$wR_2$ [all $F^2$ ] | 0.1111/0.3062 | 0.1169 | 0.1063 |
| GOF | 2.0137 | 1.4477 | 1.8430 |
| Diffraction map extrema (e Å$^{-3}$) | 1.8, -1.2 | 6.2, -3.0 | 2.3, -1.7 |
| Total potential solvent accessible void volume per unit cell vol | 75.6% | 73.6% | 75.8% |

### 4.5.5 Calculation of selectivities

For the calculation of selectivity, we adopt DSLF-IAST method (See 2.4.3 for details), with the parameters shown in Table 4.12.

Table 4.12 The simulated parameters for dual-site Langmuir fitting model of pure hydrocarbon sorption isotherms for MFM-601 at 293 K.

| | P1 | P2 | P3 | Q1 | Q2 | Q3 | Residual Sum of Squares | Adj. R-Square |
|---|---|---|---|---|---|---|---|---|
| **$CH_4$** | 2.0390 | 0.2105 | 1.0340 | 1.7477 | 0.0115 | 2.0103 | 0.0000 | 0.9999 |
| **Error** | 1.5453 | 0.1627 | 0.0219 | 1.6650 | 0.0143 | 0.7034 | | |
| **$C_2H_2$** | 19.8970 | 0.1284 | 0.9634 | 0.0746 | 288.0468 | 1.7590 | 0.0002 | 1.0000 |
| **Error** | 5.9932 | 0.0412 | 0.0457 | 0.0396 | 633.8432 | 0.5828 | | |
| **$C_2H_4$** | 0.8943 | 3.5289 | 1.0416 | 8.0509 | 0.2564 | 1.3591 | 0.0002 | 1.0000 |
| **Error** | 0.7912 | 1.9062 | 0.0258 | 5.8147 | 0.1322 | 0.4196 | | |
| **$C_2H_6$** | 9.2312 | 0.2049 | 1.0022 | 9.2312 | 0.2049 | 1.0022 | 0.00228 | 0.9999 |
| **Error** | 1780790 | 17499.89 | 2698.21 | 1780720 | 17503.4 | 2688.6 | | |
| **$C_3H_6$** | 10.5577 | 1.2152 | 0.8800 | 1.3015 | 450.9742 | 3.1254 | 0.0068 | 1.0000 |
| **Error** | 0.3406 | 0.1582 | 0.0245 | 0.1717 | 274.2999 | 0.2861 | | |
| **$C_3H_8$** | 11.4063 | 0.8648 | 0.8051 | 1.7073 | 127.5699 | 2.1626 | 0.0060 | 1.0000 |
| **Error** | 0.7031 | 0.1712 | 0.0248 | 0.2659 | 67.5777 | 0.1951 | | |
| **$CO_2$** | 20.9439 | 0.0805 | 0.8353 | 0.9641 | 0.0038 | 3.3736 | 0.0067 | 1.0000 |
| **Error** | 0.5040 | 0.0020 | 0.0073 | 0.1374 | 0.0019 | 0.3364 | | |

## 4.6 Conclusions

By adopting similar synthetic routes, two new Zr-based MOFs have been successfully synthesised. The organic ligands in the two MOFs show completely different geometries and thus form two distinct structures. Each Zr-based MOF has an Hf-based isostructure synthesised with the same method using Hf(IV) salts. Phase purity has been confirmed by good agreement of the PXRD patterns between the as-synthesised MOFs and the simulated one from SCXRD. The PXRD of MFM-601 after IGA measurements of hydrocarbons and $CO_2$ still shows higher quality diffraction peaks which confirms the highly stable structure of this framework. TGA results indicate the two Zr-based MOFs could be thermally stable up to 500 °C and the two Hf-based MOFs could be thermally stable up to 480 °C.

Hydrocarbons and $CO_2$ isotherms for MFM-601 have been carried out at various temperatures. Among those isotherms, $CH_4$, $C_2H_2$, $C_2H_4$ and $C_2H_6$ and $CO_2$ show unsaturated near-linear uptakes below 1 bar; however, $C_3H_6$ and $C_3H_8$ show near-saturated non-linear uptakes below 1 bar. Additionally, the $C_2H_6$ isotherms reach near-saturations at the four temperatures when increasing the pressure to 4 bar. It shows similar uptake capacity to MFM-202a for $C_2H_6$ at 4 bar and 273–303 K, but lower uptake capacity at 1 bar. Low temperature (194–198 K) isotherms of the small hydrocarbons and $CO_2$ have been carried out to show the maximum capacities of the MFM-601 for $CH_4$ to $C_3$s gases. Interestingly, the $CH_4$ and $C_2H_4$ sorption process show type I isotherm whereas the $C_2H_2$, $C_2H_6$, $C_3$s gases and $CO_2$ show type IV isotherms at low temperatures. Specifically, the $C_2$s and $C_3$s uptakes at low temperature and 1 bar exhibit the highest amounts ($C_2H_2$: 26.4 mmol $g^{-1}$, $C_2H_4$: 16.4 mmol $g^{-1}$; $C_2H_6$: 20.6 mmol $g^{-1}$; $C_3H_6$: 18.0 mmol $g^{-1}$ and $C_3H_8$: 16.5 mmol $g^{-1}$) among all the reported MOFs. The $CO_2$ uptake at 198 K also gives an extraordinary high value of 32 mmol $g^{-1}$ at 1 bar and is ca. 12 mmol $g^{-1}$ higher than that of MFM-202a (19.4 mmol $g^{-1}$ at 1 bar and 195 K).

The selectivities for MFM-601 between the small hydrocarbons and between $CO_2$ and $CH_4$ have been calculated via DSLF-IAST method based on the isotherms carried out at 293 K. MFM-601 exhibits similar selectivities of $C_2H_2/CH_4$, $C_2H_4/CH_4$ and $C_2H_6/CH_4$, ranging from 7 to 11. Compared with the $C_2$s/$CH_4$, it shows higher selectivities of $C_3H_6/CH_4$ and $C_3H_8/CH_4$ ranging from 55 to 110. The

selectivity of the unsaturated $C_3H_6/C_2H_4$ ranges 7–9, which is similar to that of saturated $C_3H_8/C_2H_6$ (5–9) below 1 bar. It also shows moderate selectivity of $CO_2/CH_4$ (ca. 6) below 8 bar.

The heats of adsorption ($Q_{st}$) and entropies as a function of the uptake amounts for the small hydrocarbons and $CO_2$ of MFM-601 have been calculated *via* Clausius-Clapeyron equation from the isotherms carried out at 273–303 K. Compared with MFM-202a, which is also a porous MOF, the MFM-601 shows similar values of $Q_{st}$ at low coverage for $CH_4$ (14 kJ $mol^{-1}$) and $CO_2$ (22 kJ $mol^{-1}$), but higher values of $Q_{st}$ for $C_2H_2$ (MFM-601: 27.6 kJ $mol^{-1}$, MFM-202a: 23.3 kJ $mol^{-1}$), $C_2H_4$ (MFM-601: 21 kJ $mol^{-1}$, MFM-202a: 18 kJ $mol^{-1}$) , $C_2H_6$ (MFM-601: 22 kJ $mol^{-1}$, MFM-202a: 18 kJ $mol^{-1}$) and $C_3H_8$ (MFM-601: 31 kJ $mol^{-1}$, MFM-202a: 27 kJ $mol^{-1}$). In contrast, the $Q_{st}$ at low coverage for $C_3H_6$ of MFM-601 (30 kJ $mol^{-1}$) is lower than that of MFM-202a (33 kJ $mol^{-1}$).

MFM-601 exhibits moderate uptakes of $NH_3$ at RT during three cycles, with the uptake capacity of ca. 6.5 mmol $g^{-1}$ at 1 bar. *In situ* PXRD carried out at 195 K confirms the structural flexibility of the framework upon the $CO_2$ uptake.

## References

1. Bai, Y.; Dou Y.; Xie, L., Rutledge, W.; Li, J. and Zhou, H. Zr-based metal–organic frameworks: design, synthesis, structure, and applications. *Chem. Soc. Rev.* **2016**, *45*, 2327–2367.

2. Cavka, J. H.; Jakobsen, S.; Olsbye, U.; Guilou, N.; Lamberti, C.; Bordiga, S. and Lillerud, K. P. A new zirconium inorganic building brick forming metal organic frameworks with exceptional stability. *J. Am. Chem. Soc.* **2008**, *130*, 13850–13851.

3. Gutov, O. V.; Bury, W.; Gomez-Gualdron, D. A.; Krungleviciute, V.; Fairen-Jimenez, D.; Mondloch, J. E.; Sarjeant, A. A.; Al-Juaid, S. S.; Snurr, R. Q.; Hupp, J. T.; Yildirim, T. and Farha, O. K. Water-stable zirconium-based metal–organic framework material with high-surface area and gas-storage capacities. *Chem. Eur. J.* **2014**, *20*, 12389–12393.

4. Furukawa, H.; Gándara, F.; Zhang, Y.; Jiang, J.; Queen, W. L.; Hudson, M. R. and Yaghi, O. M. Water adsorption in porous metal−organic frameworks and related materials. *J. Am. Chem. Soc.* **2014**, *136*, 4369−4381.

5. Yang, Q.; Vaesen, S.; Ragon, F.; Wiersum, A. D.; Wu, D.; Lago, A.; Devic, T.; Martineau, C.; Taulelle, F.; Llewellyn, P. L.; Jobic, H.; Zhong, C.; Serre, C.; Weireld, G. D. and Maurin, G. A water stable metal–organic framework with optimal features for $CO_2$ capture. *Angew. Chem. Int. Ed.* **2013**, *52*, 10316 –10320.

6. Qiu, L.; Lin, J. and Xu, Y. Synthesis, characterization and luminescent property of a novel zinc(II) 1,2,3,4-tetra(4-pyridyl)thiophene metal–organic framework. *Inorg.Chem.Commun*. **2009**, *12*, 986–989.

7. Chang, G.; Li, B.; Wang, H.; Hu, T.; Bao, Z. and Chen, B. Control of interpenetration in a microporous metal–organic framework for significantly enhanced $C_2H_2/CO_2$ separation at room temperature. *Chem. Commun.* **2016**, *52*, 3494-3496.

8. Cai, J.; Yu, J.; Xu, H.; He, Y.; Duan, X.; Cui, Y.; Wu, C.; Chen, B. and Qian, G. A doubly interpenetrated metal−organic framework with open metal sites and suitable pore sizes for highly selective separation of small hydrocarbons at room temperature. *Cryst. Growth Des.* **2013**, *13*, 2094−2097.

9. Yang, S.; Sun, J.; Ramirez-Cuesta, A. J.; Callear, S. K.; David, W. I. F.; Anderson, D. P.; Newby, R.; Blake, A. J.; Parker, J. E.; Tang, C. C. and Schröder, M. Selectivity and direct visualization of carbon dioxide and sulfur dioxide in a decorated porous host. *Nature Chem.* **2012**, *4*, 887-894.

10. Zhong, R.; Xu, Z.; Bi, W.; Han, S.; Yu, X. and Zou, R. A charged metal–organic framework for $CO_2/CH_4$ and $CO_2/N_2$ separation. *Inorganica.* Chimica. *Acta*. **2016**, *443*, 299-303.

11. Yang, S.; Lin, X.; Lewis, W.; Suyetin, M.; Bichoutskaia, E.; Parker, J. E.; Tang, C. C.; Allan, D. R.; Rizkallah, P. J.; Hubberstey, P.; Champness, N. R.; Thomas, K. M.; Blake, A. J.; Schröder, M. A partially interpenetrated metal-organic framework for selective hysteretic sorption of carbon dioxide. *Nature Mater.* **2012**, *11*, 710-716.

12. Liu, T.; Feng, D.; Chen, Y.; Zou, L.; Bosch, M.; Yuan, S.; Wei, Z.; Fordham, S.; Wang, K. and Zhou, H. Topology-guided design and syntheses of highly stable mesoporous porphyrinic zirconium metal−organic frameworks with high surface area. *J. Am. Chem. Soc.* **2015**, *137*, 413−419.

13. Wang, T. C.; Bury, W.; Gómez-Gualdrón, D. A.; Vermeulen, N. A.; Mondloch, J. E.; Deria, P.; Zhang, K.; Moghadam, P. Z.; Sarjeant, A. A.; Snurr, R. Q.; Stoddart, J. F.; Hupp, J. T. and Farha, O. K. Ultrahigh surface area zirconium MOFs and insights into the applicability of the BET theory. *J. Am. Chem. Soc.* **2015**, *137*, 3585−3591.

14. Beyzavi, M. H.; Klet, R. C.; Tussupbayev, S.; Borycz, J.; Vermeulen, N. A.; Cramer, C. J.; Stoddart, J. F.; Hupp, J. T. and Farha, O. K. A hafnium-based metal−organic framework as an efficient andmultifunctional catalyst for facile $CO_2$ fixation and regioselective and enantioretentive epoxide activation. *J. Am. Chem. Soc.* **2014**, *136*, 15861−15864.

15. Garibay, S. J. and Cohen, S. M. Isoreticular synthesis and modification of frameworks with the UiO-66 topology. *Chem. Commun.* **2010**, *46*, 7700–7702.

16. Katz, M. J.; Brown, Z. J.; Colón, Y. J.; Siu, P. W.; Scheidt, K. A.; Snurr, E. Q.; Hupp, J. T. and Farha, O. K. A facile synthesis of UiO-66, UiO-67 and their derivatives. *Chem. Commun.* **2013**, *49*, 9449-9451.

17. Xydias, P.; Spanopoulos, I.; Klontzas, E.; Froudakis, G. E. and Trikalitis, P. N. Drastic enhancement of the $CO_2$ adsorption properties in sulfone-functionalized Zr- and Hf-UiO-67 MOFs with hierarchical mesopores. *Inorg. Chem.* **2014**, *53*, 679−681.

18. Biswas, S. and Van Der Voort, P. A general strategy for the synthesis of functionalised UiO-66 frameworks: characterisation, stability and $CO_2$ adsorption properties. *Eur. J. Inorg. Chem.* **2013**, 2154–2160.

19. Chen, X.; He, S.; Chen, F. and Feng, Y. Synthesis, characterization, and luminescence modulation of a rare barium-tetracarboxylate framework with $I^2O^1$ connectivity. *CrystEngComm.* **2014**, *16*, 8706-8709.

20. Gao, S.; Morris, C. G.; Lu, Z.; Yan, Y.; Godfrey, H. G. W.; Murray, C.; Tang, C. C.; Thomas, K. M., Yang, S. and Schröder, M. Selective hysteretic sorption of light hydrocarbons in a flexible metal−organic framework material. *Chem. Mater.* **2016**, *28*, 2331−2340.

21. Yang, S.; Liu, L.; Sun, J.; Thomas, K. M.; Davies, A. J.; George, M. W.; Blake, A. J.; Hill, A. H.; Fitch, A. N.; Tang, C. C.; Schröder, M. Irreversible network transformation in a dynamic porous host catalyzed by sulfur dioxide. *J. Am. Chem. Soc.* **2013**, *135*, 4954−4957.

22 Wu, H.; Chua, Y. S.; Krungleviciute, V.; Tyagi, M.; Chen, P.; Yildirim, P. and Zhou, W. Unusual and highly tunable missing-linker defects in zirconium metal−organic framework UiO-66 and their important effects on gas adsorption. *J. Am. Chem. Soc.* **2013**, *135*, 10525−10532.

23 H. R. Abid, G. H. Pham, H-M, Ang, M. O. Tade and S. Wang. Adsorption of $CH_4$ and $CO_2$ on Zr-metal organic frameworks. *J. Colloid. Interface. Sci*. **2012**, *366*, 120−124.

24. Bloch, E. D.; Queen, W. L.; Krishna, R.; Zadrozny, J. M.; Brown, C. M.; Long, J. R. Hydrocarbon separations in a metal-organic framework with open iron(II) coordination sites. *Science* **2012**, *335*, 1606−1610.

# Chapter 5 Conclusions

The work in this thesis describes the design, preparation and characterisation of a series of MOF materials: MFM-202a, $Zr_6(L^1)_2(\mu_3\text{-}O)_4(\mu_3\text{-}OH)_4(OH)_4(H_2O)_4$ ($L^1$: 5',5''-bis(4-carboxylatophenyl)-[1,1':3',1'':3'',1'''-quaterphenyl]-4,4'''-dicarboxylate) and its isostructural $Hf_6(L^1)_2(\mu_3\text{-}O)_4(\mu_3\text{-}OH)_4(OH)_4(H_2O)_4$, $Zr_6(L^2)_2(\mu_3\text{-}O)_4(\mu_3\text{-}OH)_4(OH)_4(H_2O)_4$ (denoted MFM-601, $L^2$: 4'',6''-diamino-5',5''-bis(4-carboxylatophenyl)-[1,1':3',1'':3'',1'''-quaterphenyl]-4,4'''-dicarboxylate) and its Hf-based isostructure. Single crystal XRD measurements have been carried out to reveal the microstructures of these MOFs. The Zr- and Hf-based MOFs show high porosities of 73.6–75.8% by PLATON/SOLV. However, the solvents inside the pores play a crucial role in the stability of the highly porous structures which have been confirmed by the activation process.

Comprehensive gas uptake and separation analyses have been studied for MFM-202a, which is known as a flexible porous MOF. In this work, it has been studied for the sorption of $CH_4$, $C_2H_2$, $C_2H_4$, $C_2H_6$, $C_3H_6$ and $C_3H_8$ at 273–303 K and ~195 K. The isotherms of these hydrocarbons at 273–303 K show fully reversible adsorption and desorption. In particular, the uptakes of $CH_4$ and $C_2$ hydrocarbons exhibit near-linear isotherms below 1 bar, whereas the $C_3$ hydrocarbons show curved isotherms and reach saturation at ~1 bar. Since the isotherms of $CH_4$ and $C_2$ hydrocarbons have not reached saturation at 1 bar and 273–303 K, MFM-202a shows moderate uptake capacities for them. In contrast, the uptakes of $C_3$ hydrocarbons are comparable to the best-performing MOFs. Additionally, the uptakes of $C_2H_6$ have been further measured up to 10 bar at 273–303 K, with high saturated uptake amounts compared with other MOFs. The heats of adsorption, $Q_{st}$, for these hydrocarbons have been calculated using the Clausius-Clapeyron equation. For the saturated hydrocarbons, the sequence order is $C_3H_8$ (27 kJ mol$^{-1}$) > $C_2H_6$ (18 kJ mol$^{-1}$) > $CH_4$ (14 kJ mol$^{-1}$) at low coverage, which is consistent with the increased molecular size and polarizability that contributes to the molecular interaction with the framework. The $Q_{st}$ sequence for the unsaturated hydrocarbons is calculated as $C_3H_6$ (33 kJ mol$^{-1}$) > $C_2H_2$ (23 kJ mol$^{-1}$) > $C_2H_4$ (19 kJ mol$^{-1}$), corresponding to the order of their uptake capacities at 273–303 K.

A significant difference in the uptake capacities among these hydrocarbons at 293 K and 1 bar makes MFM-202a a potential candidate for the separation of light hydrocarbons. Comprehensive calculations of selectivity between each two hydrocarbons have been performed in this work. In summary, MFM-202a exhibits high selectivity values for $C_2$s/$CH_4$, $C_3$s/$CH_4$ with an interesting inverse selectivity for $C_2H_4/C_2H_6$. Equimolar binary mixture uptakes have also been predicted by both DSLF-IAST and NI-IAST methods, which give the contributions of each component in their total uptakes.

The uptakes of these hydrocarbons have also been carried out at low temperature to give insights into their maximum capacities for MFM-202a. Interestingly, MFM-202a exhibits broad hysteresis for the sorption of $C_2H_2$, with very high storage of ~18.3 mmol $g^{-1}$, which is the highest among the reported MOFs. Such hysteresis also occurs for the adsorption of $C_2H_4$ and $C_3H_6$, but with much smaller hysteretic loops. *In situ* PXRD experiments have been carried out to monitor structural changes upon different loadings of $C_2H_2$, $C_2H_4$ and $C_2H_6$, respectively. The *in situ* PXRD patterns for $C_2H_2$-, $C_2H_4$- and $C_2H_6$-loaded MFM-202a show continuous peak shifts as loadings increase, indicating MFM-202a exhibits flexibility during gas adsorption. Upon desorption, the shifted diffraction peaks shift back to their original positions, suggesting retention of crystallinity and reversible structural change upon adsorption of $C_2H_2$, $C_2H_4$ and $C_2H_6$ at low temperature.

MFM-202a has also been investigated for $NH_3$ adsorption at 293 K. The uptake of $NH_3$ exhibits a continuous increasing trend below 1 bar, with a maximum uptake of ~8.5 mmol $g^{-1}$. Owing the strong interaction with the polar gas molecule, it shows very slow release of $NH_3$ upon desorption with an apparent hysteresis. The decrease in uptake in the second cycle indicates a possible structural change caused by the strong interaction with $NH_3$ in the first cycle. Thus *in situ* PXRD and *in situ* PDF experiments have been carried out to gain insights into the structure upon $NH_3$ sorption. Time-dependent *in situ* PXRD patterns of the $NH_3$-loaded MFM-202a show dramatic peaks shifts and splittings compared with the bare material, confirming the structural change during the sorption. The retention of peaks in the new phase upon desorption confirm an irreversible phase change, which is likely to explain the decrease in uptake in the second cycle.

MFM-601 has also been investigated for a series of gas storage and separations. The uptakes of $N_2$, $CH_4$, $C_2H_2$, $C_2H_4$, $C_2H_6$, $C_3H_6$, $C_3H_8$ and $CO_2$ have been carried out at 273−303 K and ~195 K. The $NH_3$ uptake of MFM-601 has been carried out at 293 K in multiple cycles, which is a pioneering study for Zr-based MOFs. Similarly to MFM-202a, MFM-601 also exhibits fully reversible isotherms for the uptakes of $N_2$, $CH_4$, $C_2H_2$, $C_2H_4$, $C_2H_6$, $C_3H_6$, $C_3H_8$ and $CO_2$ at 273−303 K. The selectivities between the hydrocarbons and $CO_2/CH_4$ have been calculated and analysed using DSLF-IAST. MFM-601 shows high selectivity values for $C_2$s/$CH_4$, $C_3$s/$CH_4$ and moderate selectivity values in the separation of $C_3H_6/C_2H_4$, $C_3H_8/C_2H_6$ and $CO_2/CH_4$. Remarkably, MFM-601 shows higher adsorption in the storages of $C_2H_2$, $C_2H_4$, $C_2H_6$, $C_3H_6$, $C_3H_8$ and $CO_2$ than MFM-202a at low temperature. In addition, the uptakes of $C_2H_2$, $C_2H_6$, $C_3H_6$, $C_3H_8$ and $CO_2$ show significant stepwise adsorption and desorption at low temperature, which is probably attributed to the mesopore effect. PXRD of MFM-601 after gas sorption measurements shows good agreement with the as-synthesised sample, confirming retention of crystallinity and high stability of the MOF. *In situ* PXRD of the $CO_2$-loaded MFM-601 reveals the structural flexibility evidenced from the shifts of diffraction peaks compared with the bare sample.

The main highlights of this work are the investigations of a series of MOFs with high porosities in the applications of gas storage and separation, combined with *in situ* PXRD experiments to reveal the structural flexibility upon sorption of a variety of gases. Future work will focus on structural refinement for the gas-loaded frameworks with high resolution PXRD data.

# Appendices

1. Full range diffraction of *in situ* high resolution powder diffraction patterns for MFM-202a.

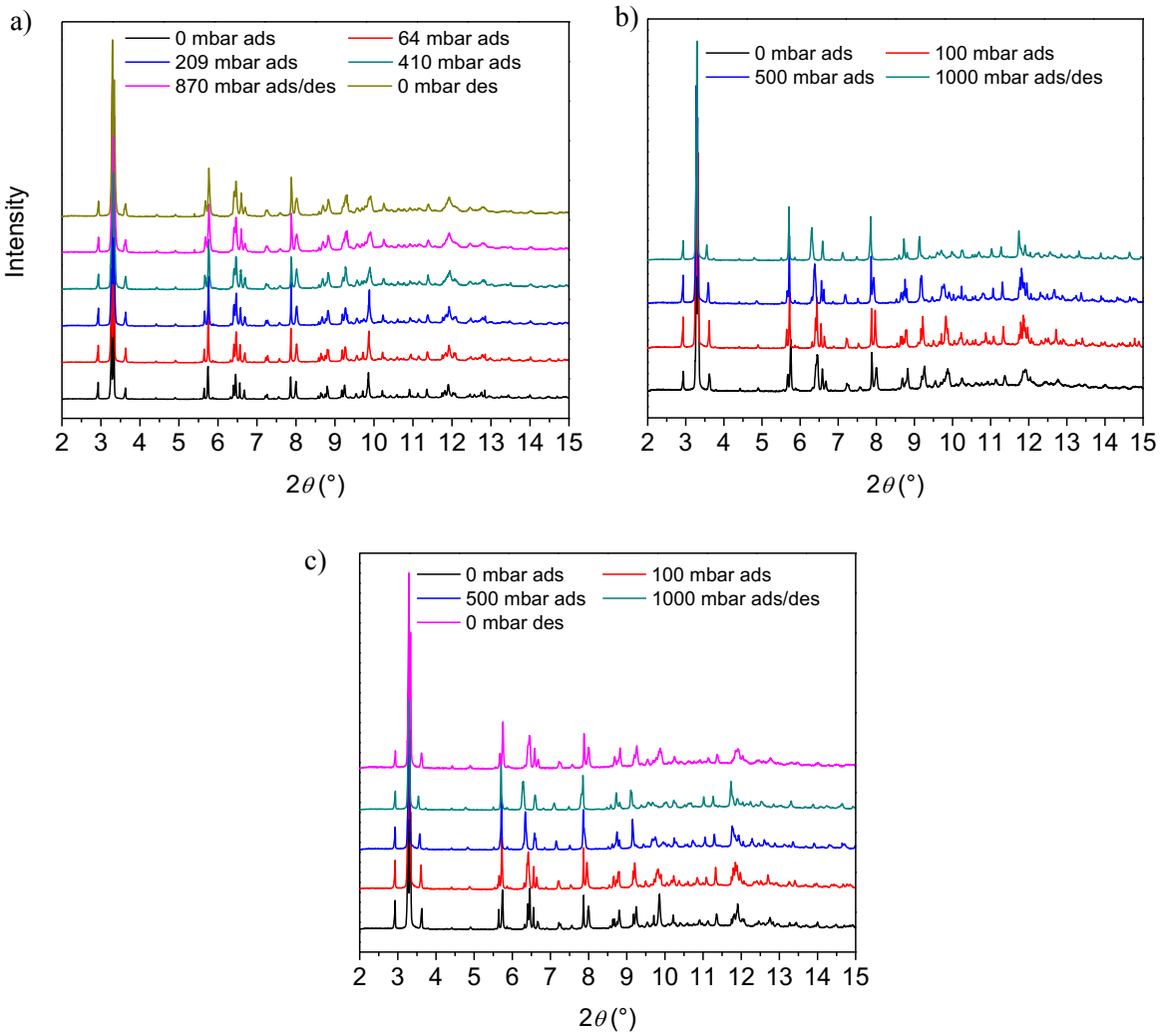



Figure A1. Comparison of *in situ* high resolution powder diffraction patterns for MFM-202a as a function of different $C_2H_2$ (a), $C_2H_4$ (b) and $C_2H_6$ (c) loadings at 195 K ($\lambda$ = 0.825774 Å).

# Publications

1. **Gao, S**.; Morris, C. G.; Lu, Z.; Yan, Y.; Godfrey, H. G. W.; Murray, C.; Tang, C. C.; Thomas, K. M.; Yang, S. and Schröder, M. Selective hysteretic sorption of light hydrocarbons in a flexible metal−organic framework Material. *Chem. Mater.* **2016**, *28*, 2331−2340.